STRUCTURAL AND ECONOMIC EVALUATION OF SELF-ANCHORED DISCONTINUOUS HYBRID CABLE BRIDGES

by

DEVIN JAMES SAUER

A THESIS SUBMITTED IN PARTIAL FULFILLMENT
OF THE REQUIREMENTS FOR THE DEGREE OF

DOCTOR OF PHILOSOPHY
in
THE FACULTY OF GRADUATE AND POSTDOCTORAL STUDIES

(Civil Engineering)

THE UNIVERSITY OF BRITISH COLUMBIA

(Vancouver)

April, 2017

ABSTRACT

A self-anchored discontinuous hybrid cable bridge is a novel type of bridge system which has the potential to overcome many of the deficiencies of conventional cable bridge structures while preserving their advantages. Nonetheless, self-anchored discontinuous hybrid cable bridges have been largely overlooked by designers and researchers. Research on the system is extremely limited. In addition, only one bridge in the world currently utilizes a self-anchored discontinuous hybrid cable system, and from its relatively short span, it appears that the system was chosen mainly for its originality rather than its technical merits. Accordingly, this thesis focuses on studying the structural and economic attributes of the system as well its constructability. These areas of research are vital in evaluating the utility of the system and in advancing its development.

The structural attributes of self-anchored discontinuous hybrid cable bridges were methodically studied in this thesis using a systematic, step-by-step approach. The behaviour of each of the two basic cable types found in hybrid cable bridges, namely stay cables and suspension cables, was first studied under a wide range of parameters. Then, starting with a bare model of a self-anchored discontinuous hybrid cable bridge, a series of analyses was performed while progressively expanding the model so that the influence of various parameters and bridge components could be isolated, and accurately assessed. The model parameters were further refined through a cost analysis which yielded important information on the economic attributes and optimum proportions of the system. Thereafter, upon reaching a complete and detailed model, the influence of various structural parameters was re-assessed, the structural benefits of employing various supplemental design components were appraised, and the constructability of the system was addressed.

This work is significant in that it provides a highly generalized and robust model of a self-anchored discontinuous hybrid cable bridge. Using this model, it is possible to ascertain how various design parameters such as geometric factors, material properties, and loading conditions affect the structural behaviour, cost, and constructability of the system. As a result, designers may quickly evaluate the viability of employing a self-anchored discontinuous hybrid cable bridge for their unique situational and design requirements. Alternatively, the model can be used to confirm the competence of a specific design. Many insights were also obtained from the research which led to the formation of a recommended design space for the system. Through a number of sensitivity studies it was found that the design space can be universally applied, and through its use, the conceptual design process can be significantly optimized and accelerated. The design space can also be used to accelerate site specific optimization studies as it provides a vital starting point and focus for more rigorous methods of investigation. In addition, the practicality and adaptability of the system were demonstrated through

the development of several innovative construction schemes which aim to reduce construction duration and costs through the creation of multiple work fronts and the elimination of large temporary works.

PREFACE

This dissertation is the original, unpublished, independent work of the author, D. J. Sauer.

TABLE OF CONTENTS

LIST OF TABLES

LIST OF FIGURES

LIST OF SYMBOLS

a	Projected length of stay cable; Length of cable array
a_o	Initial projected length of stay cable
A	Constant of integration (refer to Section 3.1)
A_{sa}	Area of superstructure required for longitudinal axial demands
A_{sao}	Area of superstructure required for longitudinal axial demands in reference bridge
A_c	Cross-sectional area of cable
A_{cm}	Cross-sectional area of suspension cable
A_g	Cross-sectional area of girder/superstructure
A_h	Cross-sectional area of hanger
A_{sb}	Area of superstructure required for longitudinal bending demands
A_{sbo}	Area of superstructure required for longitudinal bending demands in reference bridge
A_{sm}	Area of superstructure required for miscellaneous transverse members
A_{smo}	Area of superstructure required for miscellaneous transverse members in reference bridge
A_t	Cross-sectional area of bridge tower
b	Height above deck level of first stay cable-tower connection
B	Constant of integration (refer to Section 3.1)
c	Distance from neutral axis of superstructure to extreme fibre of cross-section
c_{cm}	Unit cost of suspension cable material
c_f	Unit cost of foundation material
c_h	Unit cost of hanger material
c_s	Unit cost of superstructure material
c_{st}	Unit cost of stay cable material
c_t	Unit cost of bridge tower material
C	Stressed length of cable
C_H	Cost of a self-anchored discontinuous hybrid cable bridge
C_{Ho}	Cost of reference bridge
C_o, C_f	Initial, and final stressed length of stay cable
d	Depth of superstructure
E	Elastic modulus
E_c	Elastic modulus of cable
E_{eff}	Effective modulus of cable
E_{sec}	Secant modulus of cable
E_{tan}	Tangent modulus of cable
f	Cable sag; Global cable sag for partially-laden suspension cable
f_h	Local cable sag for partially-laden suspension cable (refer to Section 4.1.1.1)
f_o	Initial stay cable sag
f_p	Parabolic stay cable sag
f_y	Vertical suspension cable sag (refer to Appendix A)
F_c	Chord component of stay cable force
Fh	Hanger force
Fh_x, Fh_y, Fh_z	Component of hanger force in x, y, and z direction
F_s	Axial force in superstructure due to self-weight
F_p	Axial force in superstructure due to live load
g	Standard acceleration due to gravity
h	Projected height of stay cable
h_B	Height of bridge tower below deck level

h_o	Initial projected height of stay cable
h_T	Height of bridge tower above deck level
h_{TR}	Tower height-to-main span length ratio ($h_T : L_m$)
h_{TRo}	Tower height-to-main span length ratio of reference bridge
h_x, h_y, h_z	Coordinates for end node of hanger (refer to Appendix A)
H	Horizontal component of cable force
H_{cm}, H_{cs}	Horizontal reaction at bridge tower from suspension cable, and anchor cable
H_{SR}	Frictional resistance provided at base of side span piers
I_g	Moment of inertia of girder/superstructure
I_t	Moment of inertia of bridge tower
K	Non-dimensional suspension cable parameter (refer to Section 3.2.2.6)
K_r	Non-dimensional parameter (refer to Section 4.2.1.7)
L_c	Chord length of stay cable
L_{cm_1}	Length of suspension cable in stayed region
L_{cm_2}	Length of suspension cable in suspended region
L_{co}	Initial chord length of stay cable
L_h	Length of suspended region (length of superstructure supported via hangers)
L_m	Main span length of bridge; Span length of suspension cable
L_{mo}	Main span length of reference bridge
L_p	Length of uniformly distributed live load
L_R	Suspension ratio ($L_h : L_m$)
L_s	Side span length of bridge
L_{SR}	Side-to-main span length ratio ($L_s : L_m$)
L_{SRo}	Side-to-main span length ratio of reference bridge
M	Bending moment (general)
M^{SO}	Bending moment obtained from second order analysis
n	Number of suspension cable segments
N_v	Axial force at top of bridge tower
N_f	Axial force at top of foundation
p, q	Non-dimensional suspension cable parameters (refer to Appendix A)
Q	Quantity of material (general)
Q_{cm}, Q_{cs}	Quantity of suspension cable, and anchor cable material
Q_f	Quantity of foundation material
Q_{Fan}, Q_{Harp}	Quantity of stay cable material in pure fan, and harp system
Q_h	Quantity of hanger material
Q_s	Quantity of superstructure material
Q_{st}	Quantity of stay cable material
Q_{stm}, Q_{sts}	Quantity of stay cable material in main span, and side spans
Q_t	Quantity of bridge tower material
R_p	Reaction at anchor pier
Rx, Ry, Rz	Force component at start of suspension cable segment in x, y, and z direction
S_R	Sag-to-span ratio of suspension cable ($f : L_m$)
T	Tension force (general)
T_{cs}	Chord force of anchor cable
T_A, T_B	Tensile force in stay cable at lower, and upper end
USL	Unstressed length of cable
USL_c, USL_p	Unstressed length of cable for catenary, and parabolic solution
USL_o, USL_f	Initial, and final unstressed length of stay cable
V_A, V_B	Vertical component of stay cable force at lower, and upper end
V_{cm}, V_{cs}	Vertical reaction at bridge tower from suspension cable, and anchor cable

V_{pf}	Total vertical force acting on side span pier foundations from dead load
V_s	Vertical component of suspension cable force at end
V_T	Vertical force in bridge tower
VOL_{sa}	Volume of superstructure material required for longitudinal axial demands
W_t	Self-weight of bridge tower
x_p	Position of uniformly distributed live load
x_{pi}	Position of intermediate pier
y_B	Projected height of stayed region (refer to Section 4.1.1.3)
y_c, y_p	Cable ordinates for catenary, and parabolic solution
z	Vertical distance from top of bridge tower
α_p	Live load factor
α_{sdl}	Load factor for superimposed dead load
β_t	Reduction coefficient for bridge tower to account for out-of-plane loading
γ_c	Unit weight of cable material
γ_{cm}	Unit weight of suspension cable material
γ_s	Unit weight of superstructure material
γ_{st}	Unit weight of stay cable material
γ_t	Unit weight of bridge tower material
δ	Deflection (general)
δ^{SO}	Deflection obtained from second order analysis
$(\delta)_{FL}, (\delta)_{PL}$	Deflection in a fully-laden, and partially-laden suspension cable
δ_c	Component of stay cable deflection along cable chord
δ_e	Elastic component of deflection
δ_h, δ_v	Horizontal, and vertical deflection
δ_r	Rigid component of deflection
δ_{sf}	Strain-free component of suspension cable deflection
δa	Change in projected length of stay cable
δC	Change in stressed length of cable
δf	Change in cable sag
δh	Change in projected height of stay cable
$\delta h_x, \delta h_y, \delta h_z$	Projected length of hanger in x, y, and z direction
δL_c	Change in chord length of stay cable
$\delta \theta_c$	Change in stay cable chord inclination
$\delta \sigma_c$	Change in stay cable chord stress
Δ_e	Elastic elongation of cable
Δ_{eo}, Δ_{ef}	Initial, and final elastic elongation of stay cable
$\Delta x, \Delta y, \Delta z$	Projected length of suspension cable segment in x, y, and z direction
$\Delta X_T, \Delta Y_T, \Delta Z_T$	Projected length of suspension cable in x, y, and z direction
$\Delta \omega_s$	Variation in self-weight of superstructure
ϵ_c	Stay cable strain
η	Non-dimensional parameter (refer to Section 5.2.2)
θ_A, θ_B	Tangential angle of stay cable at lower, and upper end
θ_c	Stay cable chord inclination
$\theta_x, \theta_y, \theta_z$	Tangential angle at end of suspension cable with respect to x, y, and z axis
λ	Uniform spacing of hangers
Λ	Non-dimensional parameter (refer to Section 5.3.2)
μ	Coefficient of static friction
ξ	Non-dimensional suspension cable parameter (refer to Section 3.2.2)
ρ_{cm}, ρ_{cs}	Density of suspension cable, and anchor cable material
ρ_h	Density of hanger material

ρ_{st}	Density of stay cable material
ρ_t	Density of bridge tower material
σ_{allow}	Design/Allowable stress of cable material
$\sigma_{a,DL}, \sigma_{a,LL}$	Axial stress in superstructure due to dead, and live load
$\sigma_{b,LL}$	Bending stress in superstructure at extreme fibre of cross-section due to live load
σ_c	Stay cable chord stress (F_c/A_c)
σ_{co}, σ_{cf}	Initial, and final state of stay cable chord stress
σ_{cm}, σ_{cs}	Design/allowable stress of suspension cable, and anchor cable material
σ_h	Design/allowable stress of hanger material
σ_{st}	Design/allowable stress of stay cable material
σ_s	Design/allowable stress of superstructure material
σ_t	Design/allowable stress of tower material
$\Sigma H_{sts}, \Sigma V_{sts}$	Cumulative horizontal, and vertical reaction from stay cables in side span
Ψ_c	Non-dimensional cable parameter ($\omega_c a/H$)
Ψ_{cp}	Non-dimensional cable parameter ($\omega_{cp} a/H$)
$\bar{\Psi}_p$	Non-dimensional suspension cable parameter (($\omega_c + \omega_s)L_m/H$)
ω_c	Distributed self-weight of cable
ω_{cm}	Uniformly distributed self-weight of suspension cable
ω_{cp}	Uniformly distributed self-weight of cable
ω_p	Uniformly distributed live load
ω_s	Uniformly distributed self-weight of superstructure
ω_{sm}, ω_{ss}	Uniformly distributed self-weight of superstructure in main span, and side spans
ω_{so}	Uniformly distributed self-weight of superstructure of reference bridge
ω_R	Live load ratio ($\omega_p : \omega_s$)
ω_{Rm}	Live load ratio in main span ($\omega_p : \omega_{sm}$)
ω_{Ro}	Live load ratio of reference bridge ($\omega_p : \omega_{so}$)
Ω	Non-dimensional cable parameter (refer to Sections 3.1.1 and 4.1.1)

ACKNOWLEDGMENTS

can say with certainty that this thesis would not have been completed without them.

DEDICATION

To my family

Chapter 1

INTRODUCTION

The most common forms of cable supported bridges are the self-anchored cable-stayed bridge and the earth-anchored suspension bridge. Since their conception, both have been used extensively all over the world. This is clearly due to the advantages cable structures exhibit for medium to long spans which stem from their ability to efficiently carry dead load forces axially, as opposed to in shear or in bending. Nonetheless, these common cable bridge forms are hampered by a variety of design characteristics which limit their cost efficiency and long term durability. With the current rate of population growth, urban expansion, and third world development, it will become increasingly more important to further optimize their design.

A hybrid is, by definition, an object contrived by the merging of two or more distinct subsystems into a single collaborative entity. As opposed to optimizing each subsystem independently, the creation of a hybrid system provides an alternative and effective means of optimization because hybrid systems have the capability of assimilating the positive attributes of each subsystem whilst bypassing some, or all, of the negative attributes. For this reason, different forms of hybrid cable bridges have been proposed throughout history.

This thesis is focused on the development and evaluation of a novel type of hybrid cable bridge which employs a self-anchored discontinuous cable system. Further details of the system, along with supplementary information regarding the limitations of conventional cable bridges, are provided in this chapter. The reasons for carrying out the research are also included in addition to the objectives, scope, and organization of the thesis.

1.1   Limitations of Conventional Cable Bridges

1.1.1   Self-Anchored Cable-Stayed Bridges

The primary components of a self-anchored cable-stayed bridge are illustrated in Figure 1.1. As the term self-anchored implies, in a self-anchored cable-stayed bridge the horizontal component of all cable forces are transferred to the superstructure as opposed to the earth, and any unbalanced vertical components are resisted by the end/anchor piers. Consequently, a simplified axial force diagram for the superstructure under dead load resembles that shown in Figure 1.2.
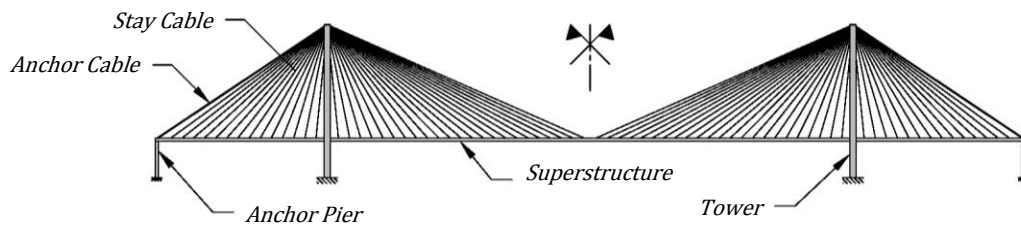
Figure 1.1: Self-Anchored Cable-Stayed Bridge Components
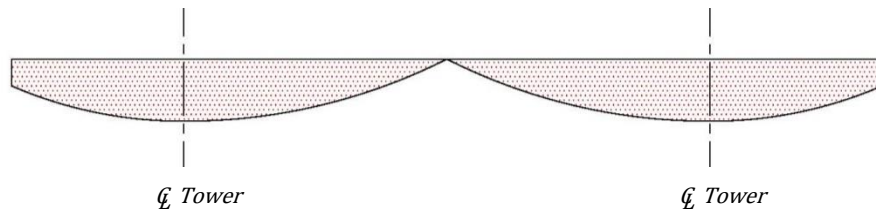
Figure 1.2: Idealized Axial Force Diagram for Superstructure in a Cable-Stayed Bridge

To avoid the use of costly temporary supports, cable-stayed bridges are normally constructed using the cantilever method. With the cantilever method, construction of the superstructure commences at the towers and progresses outwards through the sequential addition of segments of superstructure and their adjoining stay cables. One major drawback is that relative to the speed of erection of the superstructure in suspension bridges, the cantilever method is a slow process. Moreover, more often than not multiple cable tensioning operations are required in order to limit construction induced stresses in the towers and in the superstructure. This further lengthens the overall construction time. The effect is compounded for longer spans which are also subject to stability concerns due to the great length at which the cantilever must extend prior to closure of the main span.

Additional limitations of cable-stayed bridges relate to how their behavior changes as their span length is increased. In general, cable-stayed bridges have shown to be competitive in spans ranging from 100

metres to just over 1000 metres (Svensson, 2012). However, as their span length is increased, the effective stiffness of the cable system decreases (this is explained in more detail in Chapter 3). Consequently, larger deflections/forces need to be accommodated, and the stay cables themselves become increasingly prone to damaging vibration phenomena. In addition, the optimum height of the towers in cable-stayed bridges has long been established to be within the range of 0.17 to 0.25 times the main span length. This is relatively tall in comparison to suspension bridges which are generally constructed with a tower height of roughly 0.1 times the main span length. (Gimsing & Georgakis, 2012; Farquhar, 2008; Svensson, 2012) Thus, as the main span length is increased, the height of the towers in cable-stayed bridges becomes increasingly lofty. This, combined with the larger compressive and bending forces generated from the added length of the main span, leads to notable second order p-delta effects which must be counteracted more often than not through increased section properties. As a result, the costs of both towers and the foundations are adversely affected.

1.1.2 Earth-Anchored Suspension Bridges

In earth-anchored suspension bridges, all loads from the superstructure are imparted to the main cables before being transferred to the earth via large anchorage structures (see Figure 1.3). At the top of each tower, horizontal cable forces are inherently balanced and thus bending forces can be minimized. In addition, no compressive forces are typically introduced into the superstructure as a result of the cable system. The superstructure is also quasi moment-free under dead load, and due to these differences, all of the issues previously described for cable-stayed bridges are more or less resolved in earth-anchored suspension bridges. However, there are also numerous issues associated with earth-anchored suspension bridges which do not apply to self-anchored cable-stayed bridges.
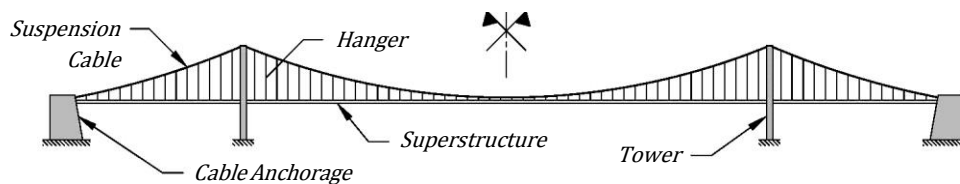
Figure 1.3: Earth-Anchored Suspension Bridge Components

During the construction of earth-anchored suspension bridges the superstructure is typically erected using a crane mounted on top of the suspension cables. This is a great advantage because similar to the balanced cantilever method for cable-stayed bridges, temporary supports are not required. However, although the erection of the superstructure can be done expeditiously, the erection of the suspension cables is a lengthy procedure which lies on the critical construction path. As a result, the

overall construction time required for a suspension bridge is often longer than that required for a cable-stayed bridge of equal span. Also, following years of service, whereas it is now common practice to design cable-stayed bridges so that individual stay cables can be easily replaced, replacement of the standard parallel wire type main cable in suspension bridges is generally not feasible unless the entire superstructure is temporarily supported or rebuilt. Neither option is acceptable for the vast majority of suspension bridges which are either long spanning, and/or have spans overlying deep waterways. Accordingly, the lifespan of most suspension bridges is typically confined to the lifespan of the suspension cables. As such, corrosion of the suspension cables must be avoided insofar as possible. This can be an expensive task considering the numerous challenges in current maintenance and inspection procedures.

In terms of performance, the four-point mesh configuration of the cable system in a suspension bridge is much more flexible than the triangular configuration achieved in a cable-stayed bridge. This leads to larger deflections and makes suspension bridges particularly susceptible to aerodynamically induced instabilities during construction and operation. As a result, construction of the suspension cables is generally prone to weather delays and additional material is often added to the main girder to increase its stiffness, or supplemental fairings are incorporated to provide a more streamlined profile.

Lastly, there are large costs associated with the construction of the anchorages required for the suspension cables. This feature in itself limits the economical span range of suspension bridges, and also makes them unsuitable for construction in locations where the soil composition contains thick layers of silt and clay deposits. As a solution, engineers have proposed self-anchored suspension systems on several occasions; however, few have been selected for construction. This is because to erect a self-anchored suspension bridge the superstructure needs to be temporarily supported during construction or, alternatively, the horizontal component of the suspension cable force needs to be temporarily restrained. Consequently, any benefits gained are often outweighed by the added construction time and cost associated with the temporary support structures. Also, due to the introduction and concentration of large axial forces at the cable anchorages, only moderate spans are practicable. For more information on historic and modern self-anchored suspension bridges the reader is referred to Ochsendorf & Billington (1999), Goolen (2006), and Zhang et al. (2006).

1.2 Hybrid Cable Bridges

A hybrid cable bridge in the context of this thesis refers to a bridge which contains both a cable-stayed and a suspension cable system. As shown in Figure 1.4, the suspension cables and hangers in hybrid cable bridges may be designed to act cooperatively with the stay cables throughout the structure in a

continuous arrangement, or they can be designed so that their support is segregated and discontinuous with respect to the stay cables. The continuous arrangement is most well-known from the designs of famed bridge engineer John A. Roebling (1806-1869). The Covington-Cincinnati Bridge (renamed in 1983 and now known by his namesake) and the Brooklyn Bridge are two examples of Roebling's designs which are still in service today. In contrast, a French engineer by the name of Ferdinand Arnodin (1845-1924) is generally considered the pioneer of the discontinuous arrangement. His work can be viewed at present in France when crossing the Saint-Ilpize Bridge.

(Continuous Arrangement)

(Discontinuous Arrangement)
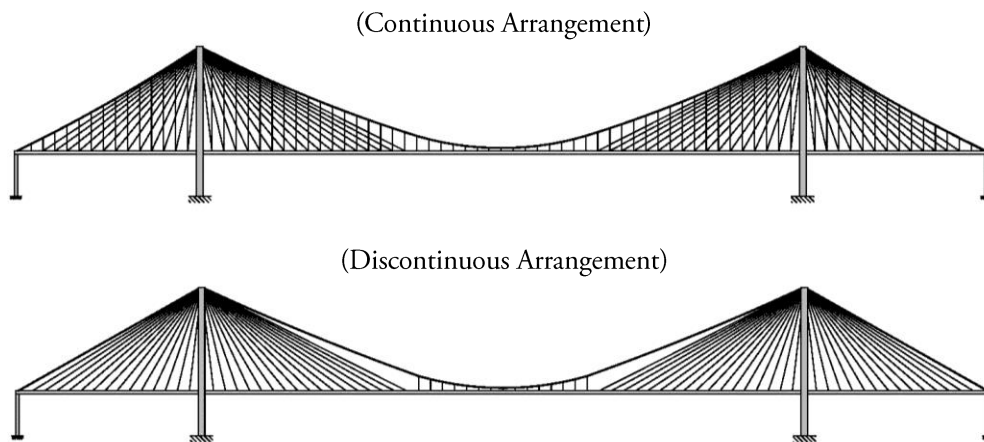
Figure 1.4: Continuous and Discontinuous Hybrid Cable Bridges

The fact that the cable-stayed supports are generally much stiffer than those provided via the suspension cable and hangers presents numerous challenges for hybrid cable bridges arranged in a continuous configuration. This is mainly because in a continuous arrangement the different cable elements behave much more collectively, and when two systems are arranged in such a way as to compete for the same load, the internal distribution of the load will be determined according to the stiffness ratio of the two systems. Consequently, erection becomes both challenging and time consuming, and during operation the stays and suspension systems are not efficient partners. For these reasons, the continuous system is excluded from study in this thesis.

In addition to the different cable arrangements, hybrid cable bridges can also be classified according to the primary load path chosen for the structure. Three different types are illustrated in Figure 1.5. Articulation schemes which may exist for each type are shown in idealized form in the figure in order to better illustrate the load path for each case. Axial force diagrams for the superstructure under dead load are also included underneath for added clarity.

(Earth-Anchored)

(Partially Earth-Anchored)
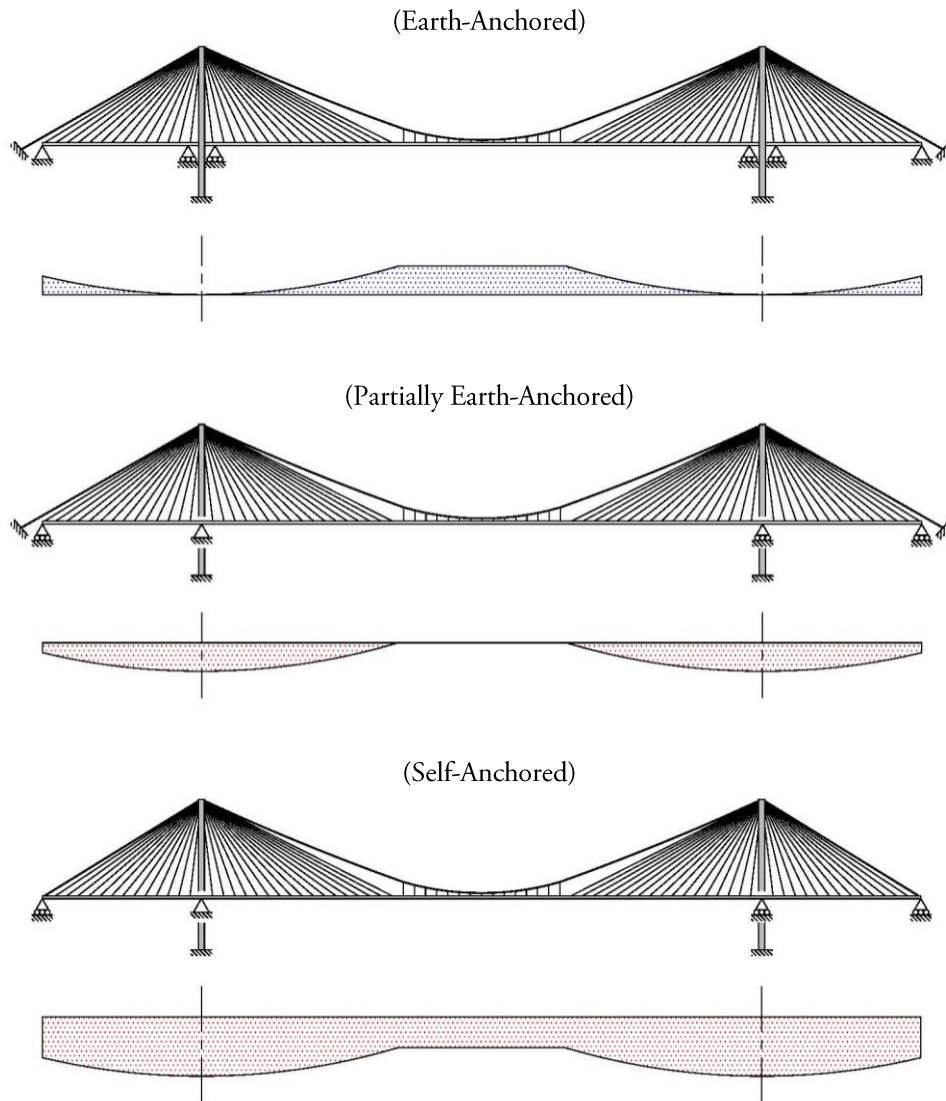
(Self-Anchored)

Figure 1.5: Different Forms of Hybrid Cable Bridges
*Axial Force Diagram Shown Underneath

Self-anchored hybrid cable bridges have a significant advantage over earth-anchored and partially-earth anchored hybrid cable bridges in that they do not require external anchorage structures for the suspension cable. The elimination of this costly component makes self-anchored systems potentially very competitive in the 250 to 1000 metres span range in which cable-stayed and suspension bridges currently compete.

1.3   Motivation

Many hybrid cable bridges were constructed in the 19th and early 20th centuries before their behaviour was well understood. As a consequence, hybrid cable bridges quickly fell out of favour in response to increasing popularity of pure suspension and cable-stayed bridges which were at the time, much simpler to analyze and construct. At present, attention is starting to shift back towards hybrid cable systems. Engineers are beginning to realize the advantages such systems possess and numerous studies have already been conducted to investigate their behavioural characteristics. However, the majority of these studies deal with earth-anchored and partially earth-anchored systems. This is because the hybrid cable bridges which were constructed in the 19th and early 20th centuries were either earth-anchored, or partially earth-anchored and, therefore, there is historical context for such a design. In addition, a large amount of attention has recently been directed towards bridging vast waterways previously considered to be untraversable, such as the Messina and Gibraltar Straits. Due to the large compressive forces exerted on the superstructure in self-anchored systems, for ultra-long spans, self-anchored systems cannot compete with earth-anchored or partially earth-anchored systems. Thus, self-anchored hybrid cable bridges have for the most part been overlooked.

In North America, the North Avenue Bridge in Chicago, Illinois (USA), which opened to traffic in 2008, is the only vehicular bridge in operation which utilizes a self-anchored hybrid cable system. However, with a main span of only just over 77 metres, the bridge was selected largely based on aesthetics rather than cost. This is because the city of Chicago desired a signature structure unlike any ordinary bridge (Brown, 2006; Powers, et al., 2005). All other continents are devoid of self-anchored hybrid cable bridges with the exception of Asia. Within the last decade, China has begun to investigate self-anchored hybrid cable bridges and proposals have already been made on numerous occasions for various crossings in the provinces of Hubei, and Liaoning (Wang, et al., 2010). Still, despite the advances made in China, literature pertaining to self-anchored hybrid cable bridges is scarce. Moreover, only one self-anchored hybrid cable bridge has been constructed in China, and similar to the North Avenue Bridge, the 110 metre span length of the bridge is relatively small.

Clearly, more research is required in order to provide decision makers with sufficient information to determine whether or not the merits of self-anchored hybrid cable systems outweigh the added risk which naturally accompanies the construction of a novel system. Research on the static design and economics of self-anchored hybrid cable bridges is vital. The constructability of the system also needs to be addressed since self-anchored hybrid cable bridges and suspension bridges are subject to similar erection issues. The research objectives may, therefore, be stated as follows in Section 1.4.

1.4   Research Objectives

The objectives of this research are multifaceted:

1) To evaluate the structural and economic attributes of self-anchored discontinuous hybrid cable bridges;

2) To develop and optimize the general design of self-anchored discontinuous hybrid cable bridges; and

3) To address and resolve the foremost concerns regarding the constructability of self-anchored discontinuous hybrid cable bridges.

1.5   Scope of Research

To limit the scope of research so that it may be completed within a reasonable timeframe, this thesis is limited to vehicular bridges. Rail and pedestrian bridges are not considered as they are, by comparison, relatively uncommon and have substantially different loading and serviceability requirements. In addition, only static loads are considered. Dynamic loading is a complex and specialized topic that requires its own treatise.

1.6   Organization of Thesis

To achieve the aforementioned research objectives within the established scope of work, this thesis is organized as follows:

Chapter 2 provides a comprehensive literature review on the current state of development of self-anchored discontinuous hybrid cable bridges. Past designs and proposals are discussed along with the related research that has been conducted to date.

Chapter 3 studies the basic behaviour of stay cables and suspension cables. Cable behaviour, as it relates to bridge design, is a highly specialized topic. Therefore, the purpose of this chapter is to expand on the existing literature while providing context for when the hybrid cable system is examined.

Chapter 4 studies the fundamental characteristics of discontinuous self-anchored hybrid cable bridges. This chapter is considered necessary in order to obtain a global perspective of how various design parameters affect the behaviour of hybrid cable bridges. The studies are also designed to validate some of the assumptions made in Chapter 5.

Chapter 5 collectively examines the economic attributes and optimum proportions of self-anchored discontinuous hybrid cable bridges. This includes, but is not limited to, an examination of the standard ratios typically applied during the conceptual design of conventional cable bridges. In addition, the effect of different design parameters on the overall bridge cost is discussed.

Chapter 6 involves a more detailed examination into the behaviour of self-anchored discontinuous hybrid cable bridges. This is achieved by utilizing the results from Chapter 5 to narrow the number and range of design parameters involved. Specifically, the sensitivity of demand values to different design parameters is discussed in addition to the effect of various design configurations. In regard to the design configurations, the effect of the articulation scheme is examined in detailed. In addition, the consequences of employing intermediate piers, cross stays, and a suspension cable clamp are also investigated.

Chapter 7 addresses the constructability of self-anchored discontinuous hybrid cable bridges through the preliminary development of an innovative construction scheme which increases the number of work fronts and eliminates the need for large temporary works.

Chapter 2

CURRENT STATE OF DEVELOPMENT

The purpose of this chapter is to familiarize the reader with the current state of research and development of self-anchored discontinuous hybrid cable bridges. The first part of the chapter is dedicated to the examination of the technical details of self-anchored hybrid cable vehicular bridges currently in service. As previously mentioned, apart from the Jianshe Bridge in Zhuanghe, China, the North Avenue Bridge in Chicago, USA, is the only other vehicular self-anchored hybrid cable bridge in the world. In contrast to the Jianshe Bridge, the cables in the North Avenue Bridge follow a semi-continuous type of arrangement. Although hybrid bridges employing this type of cable arrangement fall outside the scope of this research, due to the limited number of self-anchored hybrid bridges in operation, pertinent technical details relating to the design of the North Avenue Bridge are also included to provide supplementary information.

In addition to the bridges in service, there have been a number of proposals for self-anchored discontinuous hybrid cable bridges. Details of these proposals are provided for two reasons. Firstly, bridge proposals are typically developed through a number of preliminary analyzes and much can be learned regarding the various design configurations which have been considered. Secondly, a certain degree of context is required since a great deal of the research literature concerns one of the proposed concepts.

The research literature itself is reviewed in the latter part of the chapter. Emphasis is placed on articles which directly relate to the focus of this research; specifically, articles which discuss the static behaviour and economics of self-anchored discontinuous hybrid cable bridges. For each article, the conclusions and limitations of the research are discussed in detail. At the end of the chapter, as well as at the end of all consecutive chapters, a brief summary of the information presented is provided for convenience.

2.1 Bridges in Operation

2.1.1 The Jianshe Bridge

Opened to traffic in 2008, the Jianshe Bridge (also referred to as the Zhuanghe Jianshe Bridge) spans 110 metres across the Xiaosi River in the east of Zhuanghe city, Liaoning province, China. Overall structural dimensions of the bridge are given in Figure 2.1. All technical information presented regarding the details of the design components was obtained from Li & Zhang (2010).
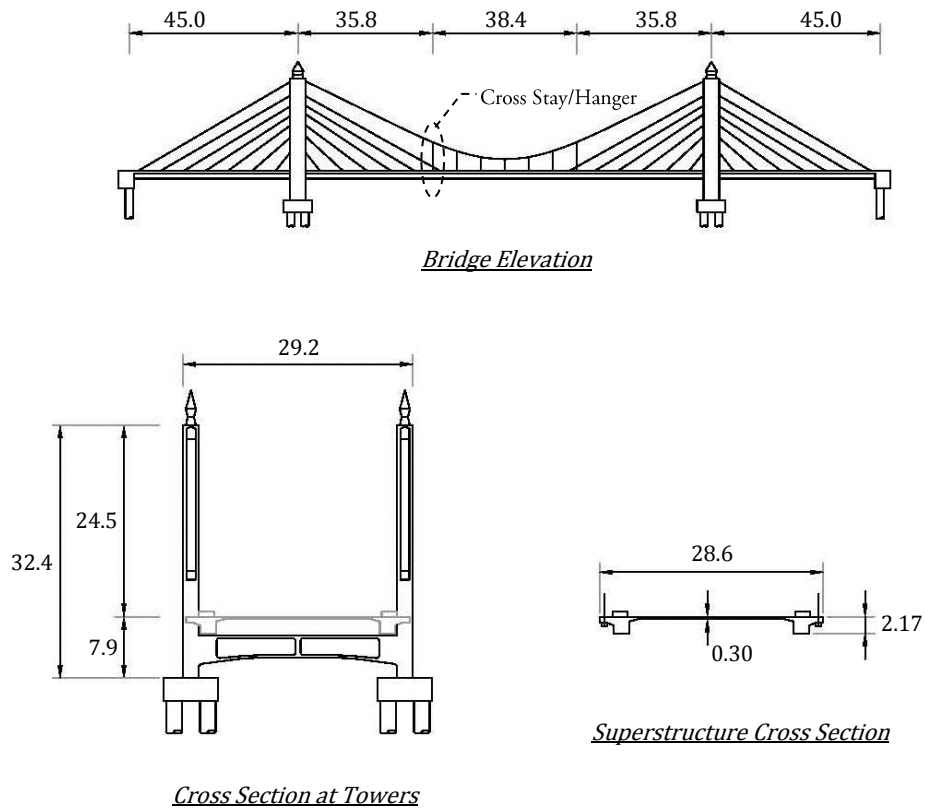
Figure 2.1: Structural Dimensions of the Jianshe Bridge
*All dimensions are in metres

In terms of the cable system, the suspension cable for the Jianshe Bridge is fully continuous over the towers and was erected using the prefabricated parallel wire strand (PPWS) method. A cable sag-to-span ratio of 0.2 was selected for the geometry of the cable based on prior experience with self-anchored suspension bridges (the cable sag is measured with respect to the cable attachment point at

the top of the towers). The adjoining hangers and the stay cables are also shop assembled and are spaced at 6.4 metres along the deck. For reasons which will be later discussed, as shown in Figure 2.1, a cross stay/hanger is provided at the junction between the stay cables and hangers.

Supporting the cable-system are two H-frame concrete towers. The tower legs have a 2 x 4 metre rectangular cross-section at their base and an I-shaped cross section at their tops. A prestressed concrete box girder is used to connect each set of legs. The superstructure is also a concrete structure and has a relatively low span-to-depth ratio of 51:1. Eight spherical bearings provide additional vertical support. According to Li & Zhang (2010), the articulation scheme can be described as 'semi-floating' and, therefore, presumably, the spherical bearings have an added sliding mechanism which does not provide any longitudinal restraint.

At the ends of the bridge, the superstructure transitions into a 21.5 ton concrete anchor block which rests atop of the end piers. The individual strands of the suspension cable are anchored into the blocks after passing through a splay saddle. The large weight of the anchorage blocks maintains compression in the end piers under all design load cases.

Erection of the bridge followed that of a conventional self-anchored suspension bridge. The towers were first constructed and then the superstructure was cast-in-place while being temporarily supported by falsework. After the concrete reached its design strength, the cable system was installed and tensioned, thereupon lifting the superstructure from the falsework.

The total cost of the bridge is reported to be 4.3 million USD which gives a unit cost of $1000 USD/m², measured from curb-to-curb. Comparing the design against a traditional self-anchored suspension bridge, Li & Zhang (2010) state that total mass of the cables is reduced by 39%, the volume of concrete in the anchorages is reduced by 57%, and the weight of the prestressed tendons is increased by 160%. In comparison to a traditional cable-stayed bridge, the mass of the cables is increased by 18%, and the height of the pylons is reduced by 7 metres. It should be noted though that no specific details are given as to how these values were determined.

Details regarding the structural performance of the Jianshe Bridge are provided in a different article by Wang et al. (2011); however, it appears that the bridge model used is from an earlier design which has since been refined. Major changes in comparison to the information presented above include a shortening of the main span by 10 metres, and the addition of another cross hanger at the junction between the stay cables and hangers. There is also a small variance in the side-to-main span length as a result of the additional cross hanger.

The imposed traffic loading for the bridge is not directly defined by the authors but is specified as 'City-A grade (China)'. Under this traffic loading, the maximum superstructure displacement occurs at mid-span and is shown to be only 32 millimetres. Furthermore, the positive (sagging) moment envelope for the superstructure appears fairly uniform over the length of the bridge. At mid-span, the moment is 11.1 meganewton metres, whereas at the towers the moment is reduced to 9.89 meganewton metres. The negative moment envelope for the superstructure is also fairly uniform; the tower locations are the only exception. At the towers, the moment spikes from on average -11 meganewton metres to -14 meganewton metres. No information is provided on how the moment envelopes were generated.

Wang et al. (2011) also presents a fatigue study conducted on the hangers. Special emphasis was placed on the effect of the cross hanger at the junction between the stay cables and hangers. Cable configurations with a double cross hanger, single cross hanger, and no cross hanger were examined. For each case, the stress ranges of the hangers are given in Table 2.1. Hanger #5 represents the middle hanger, and because of symmetry, only half of the hangers are included. Since no other load case is specified it is presumed that 'City-A grade (China)' is applied.

Table 2.1: Stress Range of Hangers (Jianshe Bridge)
(units: MPa)

Hanger #	Double Cross Hanger	Single Cross Hanger	No Cross Hanger
1	26.9	n/a	n/a
2	22.1	42.6	n/a
3	95.4	93.3	121.0
4	119.0	116.5	108.9
5	113.6	111.2	104.4

Based on Table 2.1, Wang et al. (2011) note that the stress range in the outermost hanger (hanger # 1, 2, or 3 depending on the number of cross hangers) can be reduced by a factor of almost 1/5 if double cross hangers are employed in lieu of no cross hangers. However, it would appear from the results that when considering all of the hangers, the maximum stress range only reduces from 121 MPa in the case of no cross hangers to 119 MPa when employing double cross hangers. Also, the maximum reduction occurs for the single cross hanger configuration; nevertheless, the maximum stress range is only reduced to 116.5 MPa. This puts into question the efficacy of employing cross stays/hangers. It should be noted though that the relatively stiff superstructure and small live-to-dead load ratio of the Jianshe Bridge likely have a significant effect on reducing the stress range in the hangers. Li & Zhang (2010) briefly note that the cross hangers have the added beneficial effect of enhancing the load carrying capacity of the superstructure at the stay cable-hanger junction and, therefore, this could be the reason why a single cross stay/hanger was adopted in the final design. It is interesting though that Wang et al. (2011) chose to study the fatigue stress range of the hangers

instead of the stay cables. The stay cables being the stiffer of the two, logic would suggest that the stay cables would be more prone to fatigue and thus more deserving of further study.

2.1.2 The North Avenue Bridge

The North Avenue Bridge, pictured in Figure 2.2, was opened to traffic in 2008. Unless otherwise noted, all technical information regarding its design was obtained from Powers et al. (2005).
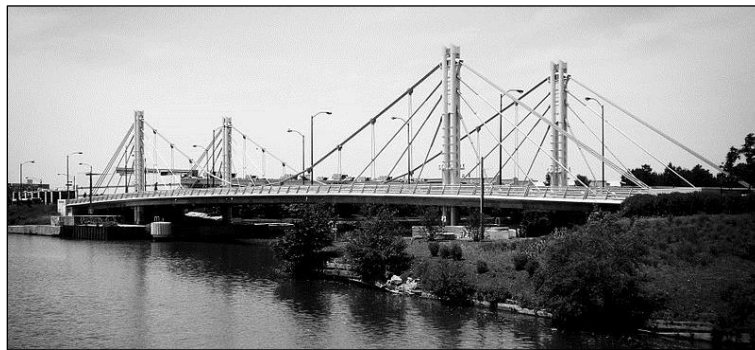
Figure 2.2: The North Avenue Bridge, Chicago, Illinois, USA
Photo By Vxla (Own work)
[CC BY 3.0 (http://creativecommons.org/licenses/by/3.0)], via Wikimedia Commons

The layout of the bridge is symmetric and consists of a 76.8 metre main span flanked by 25.6 metre side spans. As previously noted, the hybrid cable system for the North Avenue Bridge follows a semi-continuous arrangement. In other words, only the main span follows a continuous arrangement. Stay cables provide the sole support for the side spans. The suspension cable is continuous over the towers and all stay cables and hangers are longitudinally spaced along the bridge deck at 6.4 metres. The suspension cables and hangers are composed of galvanized structural strands, whereas epoxy-coated seven-wire strands are used for the stay cables.

The towers of the North Avenue Bridge are uniquely constructed from steel pipes. Two elliptical pipes offset from one another form the base of each tower, and at deck level the pipes are divided to form a section of four interconnected partial ellipsoids. Above deck, the height of the towers is configured to achieve a tower height-to-span ratio of 0.19. At the upper end where the stay cables and suspension cable attach, the tower section is integrated with the stay housing box and saddle. During design, the housing box controlled the overall dimensions of the towers and is said to be the reason for their relatively stocky appearance.

The superstructure carries four lanes of traffic and two sidewalks over a 24.7 metre wide bridge deck.

The support structure consists of two high performance concrete (HPC) edge girders and a series of tapered steel box floor beams made composite with the overlying HPC deck slab. Spacing of the floor beams matches that of the hangers and stay cables. Clearance limitations limited the depth of the superstructure to 1.17 metres; however, this still yields a fairly small span-to-depth ratio of roughly 66:1. Similar to the Jianshe Bridge, only a vertical connection is provided between the towers and the superstructure. Thus, the superstructure is free to translate in the longitudinal direction. Also, heavy concrete anchor blocks at the ends of the bridge serve as abutments and resist the vertical pull from the suspension cable.

Initially, due to requirements for uninterrupted river navigation, it was planned to construct the cable-stayed portions of the bridge using the conventional free cantilever method. Next, the two opposite sides of the bridge were to be joined through steel pipes integrated into the concrete edge girders. The steel pipes would then serve as compression struts during the erection of the suspension cables. However, for unspecified reasons, a different construction scheme was adopted. The land portions of the superstructure were first constructed on falsework around the towers and the remaining central 33.2 metre portion of the main span was shored and formed on three barges. The 33.2 metre long, 800 ton central segment of superstructure was then floated up the river and jacked into position using temporary trusses situated on top of the already cast land portions of the superstructure. With the superstructure temporarily supported along its length, the cable system was then installed. Though effective under the circumstances, this construction scheme along with the one initially conceived are clearly only practical for relatively small spans. In the end, the total cost of the project is cited at 25 million USD which results in a relatively large cost per square metre of $12,815 USD/$m^2$. (Smith, 2008)

Although specific details of the analysis were not published, a parametric study was performed during design to investigate what effect longitudinal beam stiffness, stay cable size, suspension cable size, and pylon stiffness has on the maximum deflection under extreme live loading. Loading was applied in accordance with the specifications given by the American Association of State Highway and Transportation Officials (AASHTO). According to Powers et al. (2005), changes in the suspension cable size had the largest effect. However, without any information as to the range of values considered it is difficult to ascertain whether this conclusion may be applied to other bridges. Powers et al. (2005) also state that the majority of the live load forces were carried by the stay cables as opposed to the hangers. Thus, it is not surprising that fatigue forces governed the design of the stay cables. It must be remembered though that the North Avenue Bridge has a semi-continuous hybrid cable system. In a discontinuous hybrid cable system, the hangers do not take away from the dead load carried by the stay cables and, therefore, it is possible that fatigue forces may not govern the design of the stay cables when the cable system is discontinuous.

2.2 Bridge Proposals

2.2.1 North America

In North America, the recently designed Willamette River Bridge in Portland, Oregon, USA (referred to as the Tilikum Crossing since its official opening in 2015) is the only documented project to have had a proposal for a self-anchored hybrid cable bridge. The bridge currently carries light rail, buses, and pedestrians. Private vehicles are prohibited, and for that reason, the design of the Willamette River Bridge does not fall within the scope of this thesis. However, details of the project are of interest given the amount of material published regarding the bridge selection process and the paucity of information available regarding the design of self-anchored hybrid cable bridges.

As a result of the conspicuousness of the project, there were many stakeholders involved in the bridge selection process. Beyond the project steering committee, a special bridge advisory committee (BAC) was appointed to narrow down the number of bridge alternatives based on an extensive list of selection criteria, details of which can be found in (TriMet, 2009). After an 8 month study, the BAC recommended that two bridge types be advanced: a cable-stayed bridge and a self-anchored hybrid cable bridge. It is not documented how the latter came to be conceived; however, it is likely that the engineering firm responsible for the North Avenue Bridge played a role given that the same firm was engaged to participate in the selection process.

During the refinement process, also known as the preliminary engineering stage, several changes were made to both bridge concepts. All of the details and the cost estimates can be found in Willamette River Bridge Advisory Committee (2009). For the hybrid cable bridge, the size of the suspension cable was adjusted so that stay cable technology could be used in place of aerial spinning, the hybrid cable system was changed from a semi-continuous to a discontinuous configuration, and the span layout was optimized. Illustrations of the initial and the refined hybrid design concepts are given in Figure 2.3. Not clear from the figure is that the initial span layout is 330' – 860' – 330' (101 m – 262 m – 101 m). Also, the refined tower height-to-span ratio is 0.14. Two notable observations from the refined concept are that the layout of the stay cables appears roughly symmetrical about the towers and double cross stays/hangers are employed at the stay cable-hanger junction. A rendering of the refined bridge concept with the city's landscape is shown in Figure 2.4.
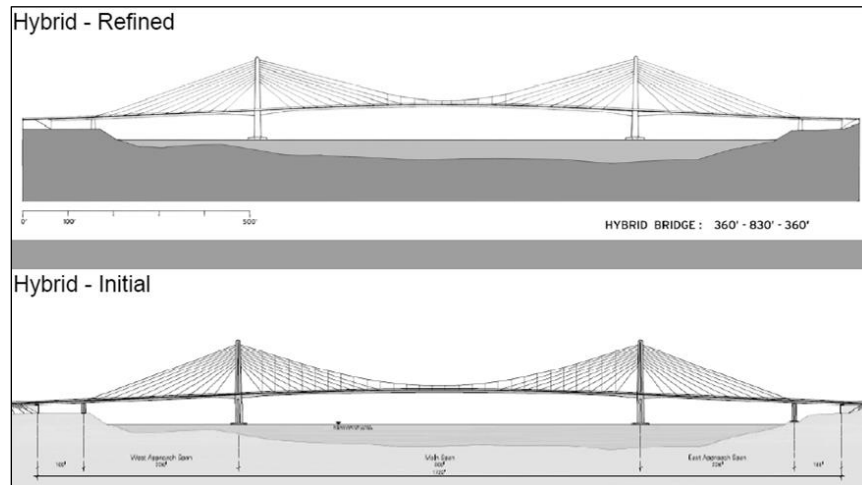
Figure 2.3: Sketches of Hybrid Concepts for Willamette River Bridge
(Willamette River Bridge Advisory Committee, 2009)

Figure 2.4: Rendering of Refined Hybrid Concept for Willamette River Bridge
(Willamette River Bridge Advisory Committee, 2009)

Estimates of the construction costs showed the refined hybrid concept to be approximately 20% more expensive in comparison to the refined cable-stayed concept. However, no specific breakdown of the costs are provided and, therefore, the primary source of the disparity cannot be ascertained. The cost for the design build contractor engineering was also set roughly 20% greater for the hybrid concept. This is the cost associated with preparing the final design. Although not specified, it is likely that this is a result of the current uncertainty in the structural behaviour of self-anchored hybrid cable bridges. Extra contingencies were also factored in to account for the uniqueness and, ergo, the assumed additional risk of the hybrid concept. After the total cost estimate was escalated to the year of expenditure, the hybrid concept came in at 3% over budget, whereas the cable-stayed concept was 18% under budget. Consequently, despite an earlier endorsement by the City of Portland Design Commission for the hybrid concept (City of Portland Design Commission, 2009), the cable-stayed concept was ultimately chosen for construction. Nonetheless, since this bridge is intended primarily for rail, it should not be inferred that the same cost discrepancy will arise in vehicular bridges. Different costs will also exist for different span lengths and site conditions.

2.2.2 Asia

The first ever documented proposal for a self-anchored discontinuous hybrid cable bridge appears to be for a 4 lane, vehicular, 600 metre span crossing in Taiwan, referred to as the 'Keelung Harbour Bridge'. Details are discussed in Wenzel (1991). For the proposed bridge site, conventional cable-stayed and suspension bridge alternatives were also studied. In developing the proposed concepts, the soil strata was assumed to be made up of a 35 metre thick layer of gravel and sand overburden resting atop of solid rock. When deriving the cost estimates, the foundations were not altered for the different bridge types.

The proposed hybrid concept is symmetric about mid-span. The tower height-to-span ratio is set at 0.15 and the side-to-main span ratio is set at 1/3. Furthermore, the stay cables are arranged symmetrically about the towers in a semi-fan configuration and double cross stays are employed at the hanger junction in the main span. In the side span, the superstructure is designed as a concrete box girder with a 5 metre depth. This design is carried forward 150 metres into the main span; however, the depth of the section is progressively reduced to 3.5 metres and at the 150 metre mark, the superstructure is transitioned into a steel box girder with a composite concrete deck slab. For the main span, this yields an average span-to-depth ratio of approximately 155:1.

Each suspension cable for the hybrid concept is comprised of a 2x6 array of single cables. Each single cable employs one hundred and eleven, PVC coated, 15.7 millimetre diameter strands. The strands are placed inside a PVC tube which is then filled with grout. Assembly of the cables is to be done on site in a similar manner to stay cables and, therefore, presumably, the same cable technology is used for the stay cables. That being stated, no other mention is made in regards to the construction scheme or schedule for the bridge.

The span layouts for the cables-stayed and suspension bridge alternatives are consistent with the hybrid concept, although their details are less clear. The cable-stayed alternative appears to employ the same superstructure design as the hybrid concept. Conversely, the suspension bridge alternative appears to employ the composite section throughout. It seems reasonable to assume that the same cable technology specified for the hybrid concept is also applied in the cable-stayed alternative. However, it is clear that the cables for the suspension alternative were designed to be aerial spun, as was the convention at the time. Apart from the cable system, included in all of the bridges concepts is a sole intermediate pier situated at the mid-point of the side span.

Based on a cost analysis of the three bridge systems, Wenzel (1991) concludes that the self-anchored hybrid concept is economically advantageous in the 500-900 metre span range. A detailed cost breakdown is not included and it is not clear how the concepts were scaled. Nevertheless, both the

cable technology and erection methods which were factored into the cost analysis are now grossly obsolete. Thus, although the details of the proposal are interesting from a structural standpoint, the results of the cost analysis can no longer be considered valid.

In Asia, apart from the Keelung Harbour Bridge, the only other documented proposals which have been made for self-anchored hybrid cable bridges have been made recently, and all are for bridge sites in China. These bridge projects are referred to in literature as the Dalian Bay Bridge, the Dalian Jingzhou Bay Bridge, the Dalian Xiaopingdao Bay Bridge, and the ErDong Bridge (Miao, 2014). Not a great deal of information has been published regarding the static behaviour of the latter; however, the Dalian Bay Bridge has been the subject of many research articles.

The Dalian Bay Bridge Project is part of the Across Sea Highway for Dalian City in Northeast China. The proposed hybrid concept is designed to carry six lanes of traffic across an 800 metre span, the central 280 metres of which is supported via hangers. The overall layout of the concept is shown in Figure 2.5. Analogous to the Jianshe Bridge, Miao et al. (2011) describe the articulation scheme as 'semi-floating'. Furthermore, the superstructure is designed with what is generally referred to in literature as a 'hybrid girder system': a concrete box girder is employed in the cable-stayed supported regions and a steel box girder is employed in the hanger supported region. With a 3.5 metre deep section, the span-to-depth ratio of the superstructure equates to roughly 229:1. In regards to the substructure, the towers are H-shaped concrete structures and the tower height-to-span ratio is configured to be approximately 0.16. In addition, similar to the Keelung Harbour Bridge proposal, a sole intermediate pier is positioned in each of the side spans.

No cost analysis has yet been presented for the proposed concept; however, there are several articles which discuss its structural behaviour. Details are presented in the following section.

(a) Elevation of bridge/m
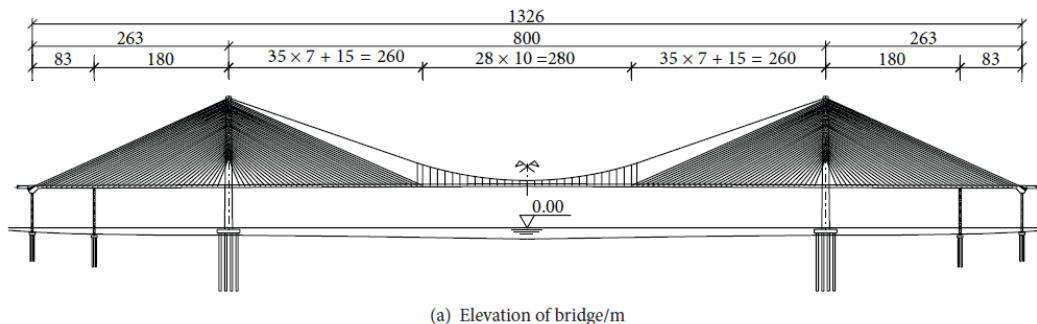
Figure 2.5: Hybrid Concept for Dalian Bay Bridge
(Wang, et al., 2013a)

(b) Standard section of steel box beam   (c) Standard section of concrete box beam
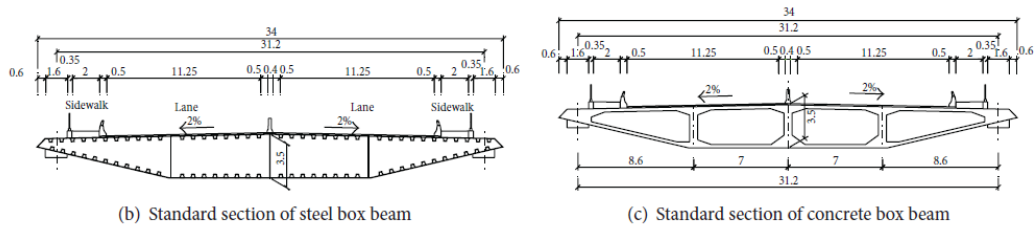
Figure 2.5 Cont'd: Hybrid Concept for Dalian Bay Bridge
(Wang, et al., 2013a)

2.3   Literature Review

As previously mentioned, most the research concerning self-anchored discontinuous hybrid cable bridges has originated from Chinese research institutions. It is important to note that this section pertains only to research articles which have been translated to, or published in English.

2.3.1   Feng et al. (2013)

Feng et al. (2013) investigate the effects on the static characteristics of the proposed Dalian Bay Bridge when carbon fibre reinforced plastic (CFRP) cables are employed in lieu of standard cables composed of steel wire. Relative to standard cables composed of steel wire, CFRP cables have only been recently developed. Their primary advantages over standard cables stem from having a smaller density, a higher ultimate stress limit, and improved fatigue resistance. In addition, CFRP cables are not subject to corrosion. However, all these advantageous come at the expense of a lower elastic modulus and a higher initial cost.

The variances in the static characteristics of the proposed Dalian Bay Bridge were assessed through a series of nonlinear finite element analyses. Two different sizing criteria for the CFRP cables were considered in the study, each based on the original proposed design and the accompanying standard steel cables. In one case, the CFRP cables were sized to have the same ultimate tensile strength as the steel cables. In the other, the CFRP cables were sized to have the same axial stiffness under zero cable sag. For all cases, the authors state that the 'bending energy minimization method' and the 'internal forces balance method' were used during analysis to optimize the cable forces.

When switching from standard cables to CFRP cables with equivalent axial stiffness, stay cable forces were consistently lower in the CFRP cables by as much as 5.3%, and little change was observed in the hanger forces and the suspension cable force. Moreover, similar axial forces and bending moments

were recorded in the superstructure; however, the maximum superstructure deflection was reduced by 56% and the maximum tower deflection by 31%. Conversely, when switching from standard cables to CFRP cables with equivalent tensile strength, cable forces were consistently greater in the CFRP cables. The maximum difference recorded for the stay cables was 23.5%. No information is provided regarding the axial forces and bending moments in the superstructure; however, the maximum superstructure deflection was increased by 161% and the maximum tower deflection by 102%.

Although the magnitude of the values reported is compelling, their derivation is unclear. For the reference case involving standard steel cables, the values reported for the maximum superstructure and tower displacement are 306 and 65 millimetres, respectively. Considering the span length, these values are remarkably small. Moreover, they do not agree with the values reported in other literature (see Section 2.3.2). In addition, the diagrams shown for the superstructure demands are not envelopes, and no mention is made with regards to the loading scenario(s) considered. The axial force diagram is particularly suspect, because the axial force at the end pier is shown to be dramatically different from the axial force at mid-span. Equilibrium dictates that the two forces be relatively similar.

Despite the ambiguity, the results are, in a general sense, not particularly surprising. With equivalent axial stiffness, the primary difference between a CFRP cable and a cable composed of steel wire is the weight ratio between the two. The CFRP cable will be substantially lighter; consequently, the cable force will be slightly lower. For stay cables, there will also be considerably less sag in a CFRP cable. Less sag translates to a greater effective stiffness which in turn leads to less deflection. With equivalent tensile strength, the area required for a CFRP cable will be notably less than that required for a standard steel cable. When combined with the relatively lower elastic modulus of the CFRP cable, the resulting axial stiffness is comparatively lower by an appreciable amount. As a consequence, the superstructure will exhibit greater deflections.

2.3.2 Wang et al. (2013a)

Wang et al. (2013a) examine the effect of geometric nonlinearities due to live load, concrete creep and shrinkage, suspension cable geometry, and girder camber for the proposed Dalian Bay Bridge crossing. The influence of nonlinear effects due to live load was assessed by performing a set of analyses by way of linear theory, second-order linear theory, and nonlinear theory. Central to the workings of linear theory is the assumption that the stiffness of the structure remains unchanged by deformation. Second-order linear theory takes into account the deformed configuration of the structure; however, only the axial forces due to dead load are considered when formulating the equations of equilibrium. Moreover, it assumes that displacements under live load are small and do not affect the magnitude of axial forces. Hence, the force-displacement relationship is effectively linearized. In contrast,

nonlinear theory takes into account these added effects. The only exception in the application of the nonlinear theory is in regard to the modelling of the stay cables where the tangent stiffness of the cables was utilized to approximate nonlinear effects.[1] Also, presumably to determine the worst-case loading scenarios, it is stated that the nonlinear analysis was conducted using the 'influence zone method'. However, no reference or description of that method is provided. Likewise, no reference or description is provided for the applied live loading which is specified as 'automobile load of grade I (China)'.

The moment/displacement envelopes for the superstructure and towers are shown in Figure 2.6 and Figure 2.7, respectively (it is presumed that the results are the same for the two towers due to symmetry). Linear theory appears to provide a reasonable approximation of the superstructure demands; however, at the same time, the moment demands in the towers are radically underestimated. In contrast, the second order linear theory is shown to accurately estimate the demands in both the superstructure and towers. The maximum difference between the second order linear theory and the nonlinear theory is only 6% for the superstructure and 3% for the towers.

Based on Figure 2.6, the authors also make note of the relatively large negative moment in the superstructure at the juncture between the stay cables and hangers and, as a consequence, remark that the section there has to be strengthened considerably to withstand the demands. Furthermore, based on the maximum deflection in the girder which roughly equates to 1/650 of the main span length, the bridge is deemed to have a greater stiffness is comparison to a suspension bridge of the same span. This is attributed to the presence of the stay cables.
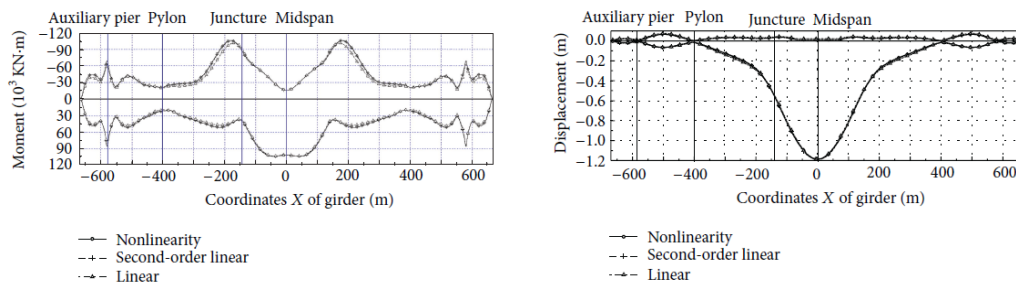
Figure 2.6: Moment/Displacement Envelope for Dalian Bay Bridge Superstructure
(Wang, et al., 2013a)

---

[1] The reader is referred to Chapter 3 for a more comprehensive explanation of the various modelling theories and approaches commonly applied in cable bridges.
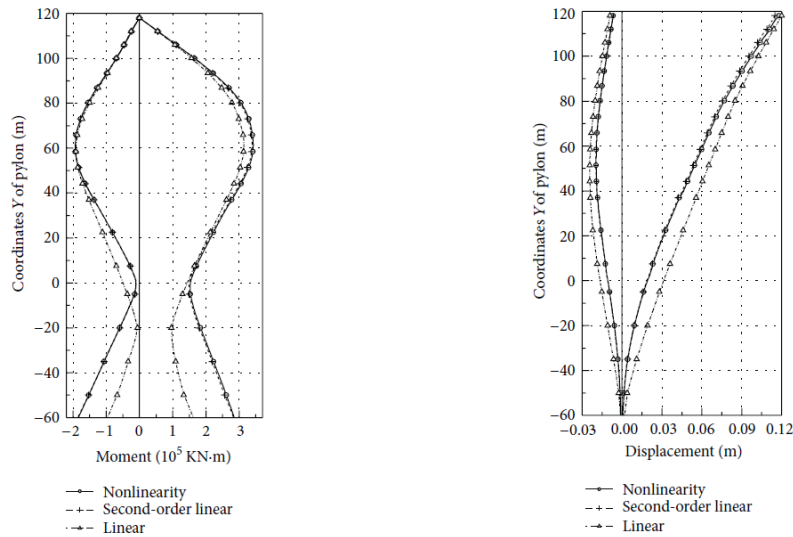
Figure 2.7: Moment/Displacement Envelope for Dalian Bay Bridge Towers
(Wang, et al., 2013a)

Creep and shrinkage effects were analyzed over a 15 year time span in accordance with the 'Bridge Criterion (China)'. No further details, such as the type of concrete employed or the age of the concrete at loading are given. The results are provided in Table 2.2. It is unclear whether the values given represent the dead load moment/displacement at the end of the 15 year time span or alternatively, the added moment/displacement due only to creep and shrinkage (i.e. the dead load moment/displacement at 15 years minus the dead load moment/displacement at the time of construction). The only remark by the authors is that creep and shrinkage have a discernable effect, and measures should be taken to reduce the impact to the structure. Of course, this cannot be contested. Nonetheless, many of the values in Table 2.2 are relatively inconsequential when compared with the live load demands. For instance, the maximum negative live load moment in the girder at midspan is -15,000 kN·m and, therefore, a moment of -358 kN·m is likely to have little impact on the design. One exception is the moment in the girder at the tower; however, it is difficult to gauge the relative importance of the value without knowing the corresponding dead load moment at the end of construction. Regardless, creep and shrinkage effects in cable bridges are normally minimized through proper design and construction practices, and are generally to a large extent offset by cambering.

Effects due to suspension cable geometry were evaluated by varying the sag-to-span ratio of the cable, where the sag is measured with respect to the top of the towers. The resulting effect on various demand parameters is plotted in Figure 2.8 (the sag-to-span ratio is on the abscissa). In the figure, all results are normalized with respect to a cable sag-to-span ratio of 0.1.

Table 2.2: Creep and Shrinkage Effects (Dalian Bay Bridge)

Location	Moment/(kN·m)	Displacement/(mm)*
Girder		
At mid-span	-358	-36.6
At tower	-11700	-1.0
Tower		
At top	n/a	27.2
At base	36150	n/a

*For superstructure, a negative value indicates a displacement in the direction of gravity.

*For tower, a positive value indicates displacement towards the main span.
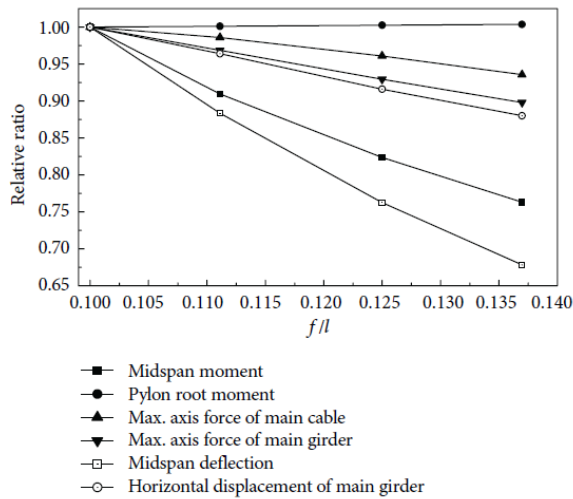
Figure 2.8: Changes in Demand Parameters versus Suspension
Cable Sag-to-Span Ratio (Dalian Bay Bridge)
(Wang, et al., 2013a)

In regards to Figure 2.8, no mention is made as to whether or not the tower height was varied in conjunction with the sag-to-span ratio of the cable, or whether the sectional properties of the bridge components were updated during the analysis to reflect the altered demands. Nevertheless, the trends exhibited for the mid-span demands and the pylon (or tower) root moment are the most intriguing. The negative trend for the mid-span demands is opposite to that which would be expected in an earth-anchored suspension bridge (Gimsing & Georgakis, 2012), whereas it is similar to trends that have been observed in self-anchored suspension bridges (Romeijn, et al., 2008). Once more, the decrease in mid-span demands seems to be accompanied by only a marginal increase in tower demands. It would be of great interest to know whether these trends occur universally, or rather if they are a manifestation of the specific design parameters chosen for the proposed Dalian Bay Bridge.

The last study conducted by the authors is aimed at measuring the effects resulting from having a 2.9 metre high 'camber' at mid-span. However, the implied meaning of the word 'camber' is unclear. Traditionally, camber is the calculated undeformed geometric profile for a bridge. It is prescribed to counteract deflections due to permanent loads in order to achieve a desired service alignment. This does not appear to be the intended meaning. Instead, Wang et al. (2013a) appear to be studying the effects resulting from the minor arch action created by the vertical alignment, in this case, a vertical alignment which rises from the towers to 2.9 metres at mid-span. Under live loading the impacts are minor with a 2% decrease in the mid-span moment in the girder and a 3% decrease in the mid-span deflection.

2.3.3 Wang et al. (2013b)

Wang et al. (2013b) discuss the design of the connection at the steel-concrete girder interface for a self-anchored discontinuous hybrid cable bridge employing a hybrid girder system. Different types of connection details are presented followed by a case study. Although not directly referenced, the bridge used in the case study appears to be of the same design as the proposed Dalian Bay Bridge crossing.

Only one type of connection detail is considered in the case study, and the joint interface is evaluated using finite element analysis. The concrete girder and steel plates are modeled using 6 node triangular elements, and shear connectors are modeled using nonlinear spring elements to account for slippage. The results show that the main girder stresses in both the steel and concrete elements are well within acceptable limits. The main conclusion following the analysis is that stress mutations at the interface can be alleviated through proper detailing.

2.3.4 Wang et al. (2010)

Wang et al. (2010) establish the basic differential equations for a three span self-anchored discontinuous hybrid cable bridge subject to vertical static loading. The derivations are carried out in two dimensions and further simplifications include:

- All loads are considered to act uniformly along the length of the bridge. Accordingly, under dead load it is assumed that the suspension cable takes the form of a parabola; in addition,

- All materials conform to Hooke's Law;

- The properties of the superstructure are assumed to remain constant along the length of the bridge;

- The superstructure is vertically supported at tower locations;

- The vertical profile of the superstructure is ignored; and

- The stay cables and hangers are idealized as homogeneous membranes with only axial resistance.

The authors first formulate the large-displacement incomplete generalized potential energy functional using the partition generalized variation principle. The basic differential equations are then obtained through constraint variation. However, due to the complexity of the equations, further simplifications are introduced so that the equations can be conveniently solved. Mainly, the effects arising from axial force-moment interaction are neglected and the hangers are assumed inextensible. With these simplifications in place, it was observed that the equations for the girder and the tower accord with that of a classical beam. Also, the equation for the suspension interval adheres to the elastic theory developed for earth-anchored suspension bridges.

The analytical solution obtained from the simplified differential equations was validated by comparing its results for a bridge with a 100 metre main span and 34.5 metre side spans against those from a nonlinear numerical analysis. The bridge used in the case study was configured to have a suspension cable sag-to-span ratio of 0.17 and a harp type arrangement for the stay cables. Only the moment demands for the girder at three locations are presented: the middle of the side span, the stay cable-hanger junction, and the middle of the main span. Furthermore, the demand values presented are for live load uniformly distributed over the entire bridge. Other loading scenarios are not considered.

The results obtained from using the analytical solution are shown to be for the most part conservative. The maximum deviation of the moments in the girder at the middle of the side span and main span are 12% and 7%, respectively. The only exception is the moment at the stay cable-hanger junction which the analytical solution underestimated by 4%. Based on these results, the authors state that the proposed simplified differential equations can be applied in preliminary analysis of simple self-anchored hybrid cable bridges, but should not be used in the design stage. Such a statement may, however, be premature.

In the case study the simplified differential equations clearly provide adequate results for preliminary design. However, it is difficult to ascertain the general accuracy of the equations based solely on the case study presented. One significant limitation of the equations is their inability to account for axial force-moment interaction. In the case study, the span length of the bridge is relatively small. Moreover, the stiffness of the towers and girder is exceedingly large in proportion to the span length of the bridge (the moment of inertial of the towers and girder is set to 7.08 m^4 and 3.06 m^4, respectively). It also follows that the magnitude of the applied live load is only 8.5% that of the

applied dead load. Intuitively, all of these factors will tend to reduce the effects of axial force-moment interaction. Therefore, more case studies are required to truly validate the accuracy of the proposed differential equations. Even so, with current computer software and technology, it is difficult for such analytical methods to compete with finite element analysis which, by comparison, can be just as readily employed for preliminary design without the same limitations.

2.3.5 Zhang et al. (2010)

Zhang et al. (2010) propose a two-stage iterative approach for cable tension optimization in self-anchored discontinuous hybrid cable bridges, the objective of which is to minimize the combined magnitude of dead and live load moments in the superstructure and towers. Rather than attempting to optimize the hybrid cable system simultaneously, the two-stage approach essentially separates the design of the suspension system from that of the stay cables. Thus, the unstrained lengths and coordinates of the suspension cables are first computed and then the tension in the stay cables is adjusted to obtain a favourable dead load state.

The optimization is performed through a combination of finite element analysis and a constraint relaxation quadratic programming method. For the constraint relaxation, several parameters are taken into account. These include: the dead and live load moments in the superstructure and towers, the cable tensions, and the support reactions at the anchor piers. Lower and upper constraint limits are imposed on each of the parameters, and in order to ensure global convergence, different relaxation coefficients are factored into each constraint condition. During the iterative process, the relaxation coefficients are updated until convergence is achieved. Moreover, different step sizes are assigned to each relaxation coefficient to account for the relative importance of each constraint condition.

A case study of the Jianshe Bridge is used to prove the merit of the proposed approach wherein a comparison is made between the design values and the results of the two-stage approach. Based on a comparison of the dead load demands, the authors note that the proposed method improved the uniformity of cable tensions and reduced the maximum superstructure moment by 53%. On the other hand, as a trade-off, the maximum moment in the towers was increased by a similar margin.

The proposed two-stage optimization approach appears to be well structured; however, it is difficult to gauge the effectiveness of the method based solely on dead load demands. Minimizing the impact of live load demands is the objective. On that account, dead load manipulation through cable tension optimization is of real benefit when the centre of the combined moment demand envelope does not coincide with the centre of the moment capacity envelope for the superstructure and/or towers. Neither of these envelopes were referenced in the article. In any case, dead load manipulation is of limited value for bridges employing concrete superstructures because any moments introduced into

the superstructure will inevitably redistribute due to concrete creep. Thus, such a method is far more applicable to bridges employing primarily steel sections.

2.3.6 Zhang et al. (2009)

Zhang et al. (2009) study the limiting span of a general three span symmetrical self-anchored discontinuous hybrid cable bridge subject to dead and live loading under the aspect of material strength. The study is carried out in two dimensions with similar assumptions to those made in Wang et al. (2010). In addition,

- Nonlinear effects are neglected;

- The stay cables are arranged in a fan type configuration; and

- The stay cables are symmetrically positioned about the centerline of each tower.

The limiting span was computed by equating the maximum cumulative horizontal force generated by the stay cables and suspension cable to the allowable stress of the superstructure. Since the algebraic solution for the corresponding span length is highly complex, numerical results are displayed graphically as a function of three parameters. The first parameter is the sag-to-span ratio of the suspension cable, where the sag of the cable is measured with respect to the top of the towers. The second parameter, which will be referred to herein as the 'cable-stayed height-to-span ratio', is the ratio of the tower height to the length of superstructure supported by the stay cables. The third parameter is the length of the superstructure supported by the stay cables. Result plots are also presented for a concrete and steel superstructure.

Initially, an 'Upper Limit Span' is considered based only on primary dead loads (superimposed dead loads and live loads are not considered). In varying each parameter, it was generally found that the upper limit span increases approximately linearly with increasing sag-to-span ratio, and a similar relationship exists with the cable-stayed height-to-span ratio. It was also found that the upper limit span increases parabolically as the length of superstructure supported by the stay cables increases. Ultimately, for a concrete superstructure with an allowable stress of 17.5 MPa, the upper limit span was computed to be 1000 metres. Conversely, for a steel superstructure with an allowable stress of 200 MPa, the upper limit span was computed to be 3500 metres.

It is somewhat curious that the authors chose to vary both the sag-to-span ratio and the cable-stayed height-to-span ratio when evaluating the upper limit span. In doing so, unrealistically large distances are permitted between the suspension cable and the superstructure at mid-span, and the suspension cable is also permitted to fall beneath the superstructure. The values reported will also be somewhat

optimistic due to the assumption that the suspension cable takes a parabolic form. Regardless, these aspects do not affect the values reported above since the upper limit span was found to occur when the length of the superstructure supported by the stay cables approaches the span length of the bridge. Thus, the upper limit span values reported are indicative of a hybrid cable bridge wherein only a minute portion of the span is supported via suspension.

As the length of the superstructure supported by the stay cables decreases, any inaccuracy deriving from the assumed parabolic form of the suspension cable will likely be over-compensated by the assumption that the properties of the superstructure are uniform along the length of the bridge. In reality, this will not be the case. The maximum axial force in the superstructure occurs at the towers, whereas at other locations along the length of the bridge the axial force is reduced. If the area of the superstructure was varied to reflect the axial force diagram, then the overall dead load would decrease resulting in a greater limit span. In this respect, the values reported may be considered conservative. That being said, given that bridges are always designed to support loading beyond their own self-weight, the authors recognize that the upper limit span has little practical value. Accordingly, additional computations were carried out to determine the effect of superimposed dead load and live load on the value of the limit span.

Assuming the same stress values as specified above, the limiting span was shown to decrease rapidly with increasing magnitude of superimposed dead load and live load. It was therefore concluded by the authors that the following measures have a beneficial impact on the limit span: increasing the sag-to-span ratio, increasing the cable-stayed height-to-span ratio, increasing the length of the superstructure supported by stay cables, increasing the cross-sectional area of the superstructure, and reducing the magnitude of the superimposed dead load.

In deriving the limit span under live load, nonlinear effects and the bending stiffness of the superstructure were neglected. For such long spans, these factors surely have an influence, as do the assumed values for the allowable stress of the stay cables, suspension cables, and superstructure. Nevertheless, these inaccuracies do not affect the overall conclusions.

2.4   End of Chapter Summary

This chapter presented the technical details of the two self-anchored hybrid cable bridges currently in service: the Jianshe Bridge and the North Avenue Bridge. Also included were the technical details of the various concepts which have been proposed for construction. Of the information published, Table 2.3 presents the design ratios employed for the in-service and proposed bridges. The latter are separated by a dashed line.

A review of the literature on self-anchored discontinuous hybrid cable bridges was also conducted. Thus far, in regards to static behaviour, the basic differential equations, cable tension optimization, and the limit span of self-anchored discontinuous hybrid cable bridges have all been investigated. The research has also addressed certain aspects of the design of one of the proposed concepts, in addition to the impact of employing CFRP cables.

Currently missing in the research is a generalized parametric study on the effect different design parameters have on the static behaviour of self-anchored discontinuous hybrid cable bridges. No study carried out thus far has been generalized. Also missing is a study into the optimum proportions of the bridge system. This is clearly needed as evidenced by the variability in the design ratios in Table 2.3 when comparing the bridges which have been constructed and those which have been proposed. Such a study would also give designers a clear idea as to which design parameters vitally affect the economy of the bridge system. Furthermore, no study thus far has endeavoured to address the constructability of the system which is currently one of the major issues hindering the development of self-anchored hybrid cable bridges. As previously stated in Chapter 1, all of these areas of research are central to the aims of this thesis.

Table 2.3: Design Ratios for Constructed/Proposed Self-Anchored Hybrid Cable Bridges

Bridge Name	Main Span Length (m)	R1	R2	R3	R4	R5	M1	M2
Jianshe	110	0.20	0.41	0.23	51	3.8	Concrete	Concrete
North Avenue	76.8	(0.19)	0.33	n/a	66	3.1	Steel	Concrete
Tilikum Crossing	253	(0.14)	0.39	0.24				
Keelung Harbour	600	(0.15)	0.33	0.36	155	25		Hybrid
Dalian Bay	800	0.14	0.33	0.35	229	24	Concrete	Hybrid
Dalian Jingzhou Bay	400	0.15	0.33	0.3	308	15	Concrete	Hybrid
Dalian Xiaopingdao Bay	350	0.14		0.23		13		Hybrid
ErDong	1100	0.1	0.27	0.36		31		Hybrid

R1 = Cable Sag-to-Span Ratio (Tower Height-to-Span Ratio)
R2 = Side-to-Main Span Ratio
R3 = Suspended Span-to-Main Span Ratio Excluding Cross Hangers
R4 = Span-to-Depth Ratio
R5 = Span-to-Width Ratio
M1 = Tower Material
M2 = Girder Material

Chapter 3

CABLE BEHAVIOUR

This chapter studies the basic behaviour of the two cardinal cable types used in bridge engineering: stay cables and suspension cables. Stay cables carry external loads acting at their end points; whereas, suspension cables carry external loads acting along their length. In addition, suspension cables may be designed to carry external load along their entire length (fully-laden), or alternatively, along a discrete portion of their length (partially-laden). Although the focus of this thesis is on the latter type of suspension cable, this chapter discusses fully-laden suspension cables in order to provide the necessary context. Partially-laden suspension cables are covered in Chapter 4.

The behaviour of a cable under the action of applied loading depends not only on the cable's function but also on its initial geometric form, or dead load condition. Near exact and approximate methods for determining the geometric shape of a cable under dead load are discussed. This information is then used to study the deformation characteristics of a single isolated cable when its loading deviates from that of its dead load state.

Equations that describe the dead load state of cables can be found in modern textbooks on the subject. However, due to their broad applicability, the equations are often presented in a form that is not tailored towards bridge design. Moreover, although cable bridge designers are aware of the general deformation characteristics of cables, other engineering professionals are not. This is because it is a subject which is rarely discussed in literature. As such, the intent of this chapter is to expand on the existing literature while providing context for later chapters. Notwithstanding, it is important to recognize that when a cable is used in conjunction with other structural components, as is the case in bridge structures, the stiffness of other major structural components will have an effect on the cable's response. As this chapter is concerned only with a cable acting as a single element, the conclusions drawn are only meant to provide a general theoretical foundation of cable bridge behaviour upon which further study is based.

3.1   Stay Cables

3.1.1   Geometric Form

Generally, the only forces acting along the length of a stay cable are those due to its own self-weight and under this condition the term 'catenary' has long been used to describe the curve that the cable forms. In deriving the mathematical expression which describes the catenary, the cable is assumed to have negligible bending stiffness and for most practical purposes, this provides a near exact solution (Irvine, 1981). The complex nature of the catenary equation can make it difficult to work with and for this reason a more approximate parabolic solution is often employed.

3.1.1.1   The Catenary Solution

Figure 3.1 illustrates a free body diagram of an inclined stay cable along with the parameters typically used to describe its geometry. Note that for clarity, the self-weight of the cable (in terms of weight per unit length), ω_c, is not depicted in the figure. Also, the sag of the cable, f is measured with respect to the cable chord.
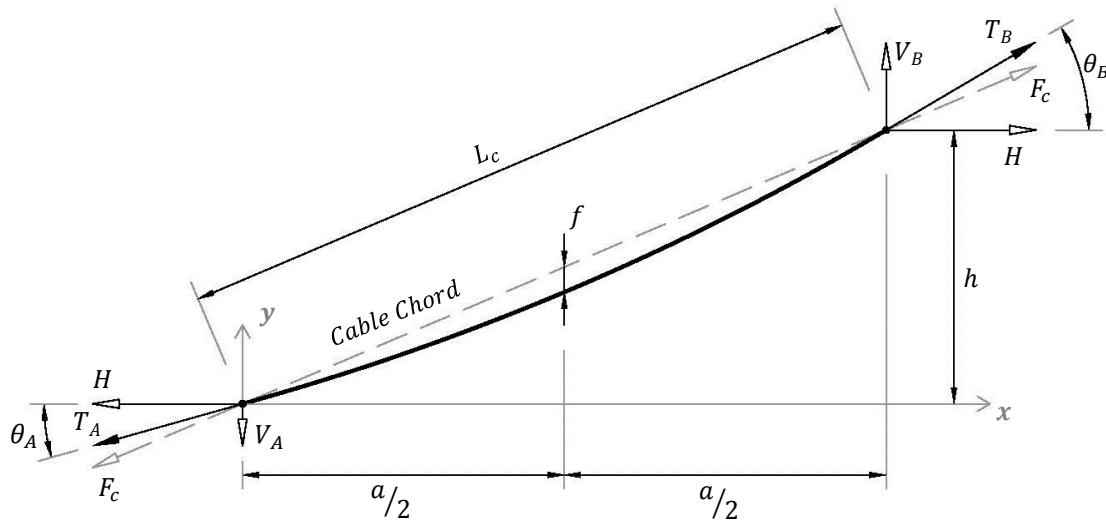
Figure 3.1: Geometric Parameters of an Inclined Stay Cable

Vertical equilibrium on a small isolated segment cable gives the following differential equation, wherein the horizontal component of the tensile force in the cable, H is constant.

$$\frac{d^2y}{dx^2} = \frac{\omega_c}{H}\sqrt{1 + \left(\frac{dy}{dx}\right)^2} \tag{3.1}$$

Utilizing two non-dimensional parameters to simplify the equations,

$$\Psi_c = \frac{\omega_c a}{H} \qquad \text{and} \qquad \Omega = \frac{h}{a}$$

the general solution to Equation (3.1) can be given by,

$$\frac{dy}{dx} = sinh\left(\frac{\Psi_c x}{a} + A\right) \tag{3.2}$$

and,

$$y = \frac{a}{\Psi_c} cosh\left(\frac{\Psi_c x}{a} + A\right) + B \tag{3.3}$$

whereupon substitution of the initial conditions, $y(x = 0) = 0$ and $y(x = a) = h$, the constants of integration are found to be,

$$A = asinh\left[\frac{\Psi_c \Omega}{2sinh\left(\frac{\Psi_c}{2}\right)}\right] - \frac{\Psi_c}{2} \qquad \text{and} \qquad B = -\frac{a}{\Psi_c} cosh(A)$$

From Equation (3.2), several other cable parameters of interest can be obtained. The y-component of the cable tension at the ends of the cable is found by multiplying the horizontal component of the cable tension with the first derivative of the cable ordinates at the supports.

$$V_A = H\frac{dy}{dx}\bigg|_{x=0} = \frac{\omega_c a}{\Psi_c} sinh(A) \tag{3.4}$$

$$V_B = H\frac{dy}{dx}\bigg|_{x=a} = \frac{\omega_c a}{\Psi_c} sinh(\Psi_c + A) \tag{3.5}$$

Using the Pythagorean Theorem, the magnitude of the tension force at the ends of the cable is simply the square root of the sum of the squares of the force components in the x and y directions. Note, for negative values of h, the maximum tension in the cable will be given by T_A; whereas, T_B provides the maximum tension for positive values of h.

$$T_A = \sqrt{H^2 + V_A{}^2} = \frac{\omega_c a}{\Psi_c} cosh(A) \tag{3.6}$$

$$T_B = \sqrt{H^2 + V_B{}^2} = \frac{\omega_c a}{\Psi_c} cosh(\Psi_c + A) \tag{3.7}$$

The two end angles measured with respect to the tangent of the cable curve and the x axis are

$$\theta_A = atan\frac{dy}{dx}\bigg|_{x=0} = atan[sinh(A)] \tag{3.8}$$

$$\theta_B = atan\frac{dy}{dx}\bigg|_{x=a} = atan[sinh(\Psi_c + A)] \tag{3.9}$$

The length of the cable in its stressed state, C can be obtained by integrating the length of a small segment of the cable curve over the cable's entire projected length.

$$C = \int_0^a \sqrt{1 + \left(\frac{dy}{dx}\right)^2}\, dx = \frac{a}{\Psi_c}[sinh(\Psi_c + A) - sinh(A)] \tag{3.10}$$

The length of the cable in its stressed state will also equal the length of the cable in its unstressed state, USL, plus the elastic elongation of the cable, Δ_e.

$$C = USL + \Delta_e \tag{3.11}$$

Assuming the cable material follows Hooke's Law and the stress in the cable is below the material's proportionality limit, integration of the strains along the length of the cable gives the cable's elastic elongation as

$$\Delta_e = \frac{H}{E_c A_c}\int_0^a \left[1 + \left(\frac{dy}{dx}\right)^2\right] dx = \frac{\gamma_c a^2}{\Psi_c E_c}\left[\frac{\Psi_c \Omega^2}{2}coth\left(\frac{\Psi_c}{2}\right) + \frac{1}{2} + \frac{1}{2\Psi_c}sinh(\Psi_c)\right] \tag{3.12}$$

where, A_c is the cross-sectional area of the cable, and E_c and γ_c are the elastic modulus and unit weight of the cable material, respectively. If C and Δ_e can be computed from known parameters, as is often the case, Equation (3.11) can then be rearranged to give the unstressed length of the cable.

$$USL = C - \Delta_e \tag{3.13}$$

Equations (3.2) through (3.13) provide a means for computing parameters related to the cable's geometry based on the horizontal force in the cable. However, the equations have been prescribed in such a way that they can also be specified in terms of a different force component simply by modifying the parameter, Ψ_c. For example, if it is desired to relate the equations to the cable chord force, F_c (see Figure 3.1), then using the relationship,

$$F_c = H\frac{L_c}{a} = H\sqrt{1 + \Omega^2} \tag{3.14}$$

Ψ_c can be written as,

$$\Psi_c = \frac{\omega_c a}{F_c}\sqrt{1 + \Omega^2} \tag{3.15}$$

Alternatively, Equation (3.15) can also be written in terms of the chord stress, σ_c.

$$\Psi_c = \frac{\gamma_c a}{\sigma_c}\sqrt{1 + \Omega^2} \tag{3.16}$$

3.1.1.2 The Parabolic Approximation

If the self-weight of the cable is assumed to act along the cable chord, as opposed to along the cable curve, then the loading becomes disassociated from the shape of the cable and the radical in Equation (3.1) can be eliminated. It is important to note that the same approximation can also be made by applying a uniform load with magnitude, ω_{cp} over the cable's projected length, as shown in Figure 3.2.
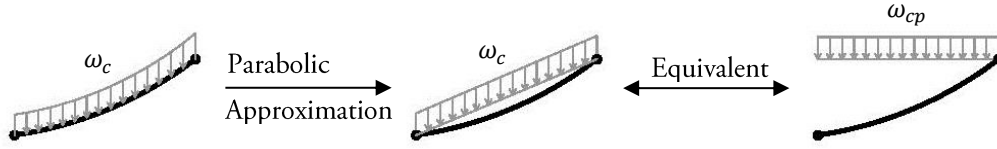
Figure 3.2: Equivalent Loading for Parabolic Approximation

where,

$$\omega_{cp} = \omega_c\sqrt{1 + \Omega^2} \tag{3.17}$$

and as before, Ω is the rise-to-span ratio of the cable. In either case, the differential equation governing the shape of the cable curve becomes

$$\frac{d^2y}{dx^2} = \frac{\omega_{cp}}{H} \tag{3.18}$$

which after integration and substitution of the same initial conditions as before in the case of the catenary,

$$\frac{dy}{dx} = \frac{\Psi_p}{2a}(2x - a) + \Omega \tag{3.19}$$

$$y = \frac{\Psi_p x}{2a}(x - a) + \Omega x \tag{3.20}$$

It is clear from Equation (3.20) that the ordinates of the cable now follow the path of a parabola. For simplicity, the non-dimensional parameter Ψ has been changed from the case of the catenary to be expressed in terms of the projected self-weight of the cable, ω_{cp}.

$$\Psi_p = \frac{\omega_{cp} a}{H}$$

Using the same methodology as in the case of the catenary, the vertical reactions at the ends of the cable are,

$$V_A = H \frac{dy}{dx}\bigg|_{x=0} = \frac{\omega_{cp} a}{\Psi_p} \left(\Omega - \frac{\Psi_p}{2} \right) \tag{3.21}$$

$$V_B = H \frac{dy}{dx}\bigg|_{x=a} = \frac{\omega_{cp} a}{\Psi_p} \left(\Omega + \frac{\Psi_p}{2} \right) \tag{3.22}$$

The magnitude of the tension at each end of the cable is,

$$T_A = \sqrt{H^2 + V_A{}^2} = \frac{\omega_{cp} a}{\Psi_p} \sqrt{1 + \left(\Omega - \frac{\Psi_p}{2} \right)^2} \tag{3.23}$$

$$T_B = \sqrt{H^2 + V_B{}^2} = \frac{\omega_{cp} a}{\Psi_p} \sqrt{1 + \left(\Omega + \frac{\Psi_p}{2} \right)^2} \tag{3.24}$$

and the two end angles measured with respect to the tangent of the cable curve and the x axis are

$$\theta_A = atan \frac{dy}{dx}\bigg|_{x=0} = atan \left(\Omega - \frac{\Psi_p}{2} \right) \tag{3.25}$$

$$\theta_B = atan \frac{dy}{dx}\bigg|_{x=a} = atan \left(\Omega + \frac{\Psi_p}{2} \right) \tag{3.26}$$

Similar to the case of the catenary, the stressed length of the cable can be calculated as,

$$C = \int_0^a \sqrt{\left[1 + \left(\frac{dy}{dx} \right)^2 \right]} \, dx \tag{3.27}$$

although contrary to the catenary, the radical in Equation (3.27) cannot be eliminated through manipulation prior to integration. Consequently, the solution to Equation (3.27), as given by Equation (3.28), is highly arduous to derive and no less cumbersome than that of its catenary

counterpart.

$$C = \frac{a}{2\Psi_p}\left[\left(\Omega + \frac{\Psi_p}{2}\right)\sqrt{1 + \Omega^2 + \Omega\Psi_p + \frac{\Psi_p^2}{4}} - \left(\Omega - \frac{\Psi_p}{2}\right)\sqrt{1 + \Omega^2 - \Omega\Psi_p + \frac{\Psi_p^2}{4}}\right.$$
$$\left. + asinh\left(\Omega + \frac{\Psi_p}{2}\right) - asinh\left(\Omega - \frac{\Psi_p}{2}\right)\right]$$

(3.28)

A simplified solution with comparable precision can, however, be derived by utilizing the first two terms of the Maclaurin series for $\sqrt{1 + k}$, where k is used to represent a generic variable. In its unabridged form, the series is given by the following summation (Stewart, 2012),

$$\sqrt{1 + k} = \sum_{m=0}^{\infty} \frac{(-1)^m (2m)!}{(1 - 2m)(m!)^2 (4^m)} k^m$$

(3.29)

The utilization of Equation (3.29) allows for the radical in Equation (3.27) to be dispensed with, thereby greatly simplifying the solution. It must be recognized though that the Maclaurin series is centered about $k = 0$ and converges for $|k| \leq 1$. As a result, the use of Equation (3.29) is only appropriate when the rise-to-span ratio of the cable, Ω, nears zero. For the case of a horizontal cable ($\Omega = 0$) the solution is given by,

$$C_{approx}\big|_{\Omega=0} = \int_0^{L_c}\left[1 + \frac{1}{2}\left(\frac{dy}{dx}\right)^2\right]dx = L_c\left[1 + \frac{1}{24}\left(\frac{\omega_c L_c}{H_{horiz}}\right)^2\right]$$

(3.30)

where, H_{horiz} is used to denote the horizontal force in a horizontal stay cable, and L_c is the chord length. To obtain a more general solution applicable for all values of Ω the limitation inherent in using the Maclaurin series can be circumvented by relating the horizontal force in Equation (3.30) to the horizontal force present in an inclined cable with equivalent geometry (Podolny & Scalzi, 1976). This relationship is shown in Figure 3.3, where the horizontal force in each cable was obtained considering the principles of static equilibrium.
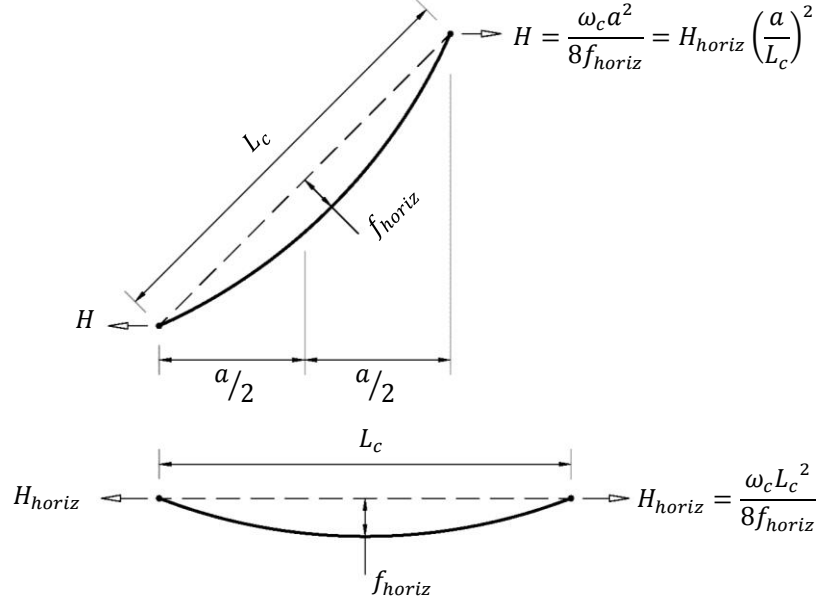
Figure 3.3: Horizontal and Inclined Stay Cables with Equivalent Geometry

Substituting the compatibility equation in Figure 3.3 into Equation (3.30) gives the general simplified solution for an inclined cable as,

$$C_{simplified} = a\sqrt{1 + \Omega^2}\left[1 + \frac{1}{24}\left(\frac{\Psi_p}{1 + \Omega^2}\right)^2\right] \tag{3.31}$$

The elastic elongation does not require any extraordinary means to derive as its formulation is comparatively simple.

$$\Delta_e = \frac{H}{E_c A_c}\int_0^a\left[1 + \left(\frac{dy}{dx}\right)^2\right]dx = \frac{\gamma_c a^2\sqrt{1 + \Omega^2}}{\Psi_p E_c}\left[1 + \Omega^2 + \frac{1}{12}\Psi_p^2\right] \tag{3.32}$$

The unstressed length can still be expressed using Equation (3.13) where the elastic elongation is given by Equation (3.32) and the stressed length of the cable is given by Equation (3.28), or alternatively via Equation (3.31). As in the case of the catenary, Ψ_p can be expressed in terms of the chord force,

$$\Psi_p = \frac{\omega_c a}{F_c}\left(1 + \Omega^2\right) \tag{3.33}$$

Or, in terms of the chord stress,

$$\Psi_p = \frac{\gamma_c a}{\sigma_c}\left(1 + \Omega^2\right) \tag{3.34}$$

As an additional measure, by taking equilibrium at a section cut through mid-span, Ψ_p can also be related to the parabolic cable sag denoted as, f_p.

$$\Psi_p = \frac{8f_p}{a} \tag{3.35}$$

3.1.1.3 Examining the Error in the Parabolic Approximation

In order to gauge the precision of the parabolic solution, its ordinates will be compared against those of the near exact catenary solution. Every point along the length of the cable is investigated and only the maximum difference is recorded. The results are shown in Figure 3.4 where the maximum difference in ordinates has been normalized with respect to the projected length of the cable and the abscissa is plotted using two equivalent non-dimensional ratios; one related to the chord stress, σ_c and the other to the parabolic cable sag, f_p. Examining once more Figure 3.2, it is evident that the error should depend strongly on these two parameters as any increase in sag, or alternatively any decrease in chord stress, results in a greater difference between the assumed action of the cable's self-weight (uniformly distributed along the cable chord) and its actual action (distributed along the cable curve).
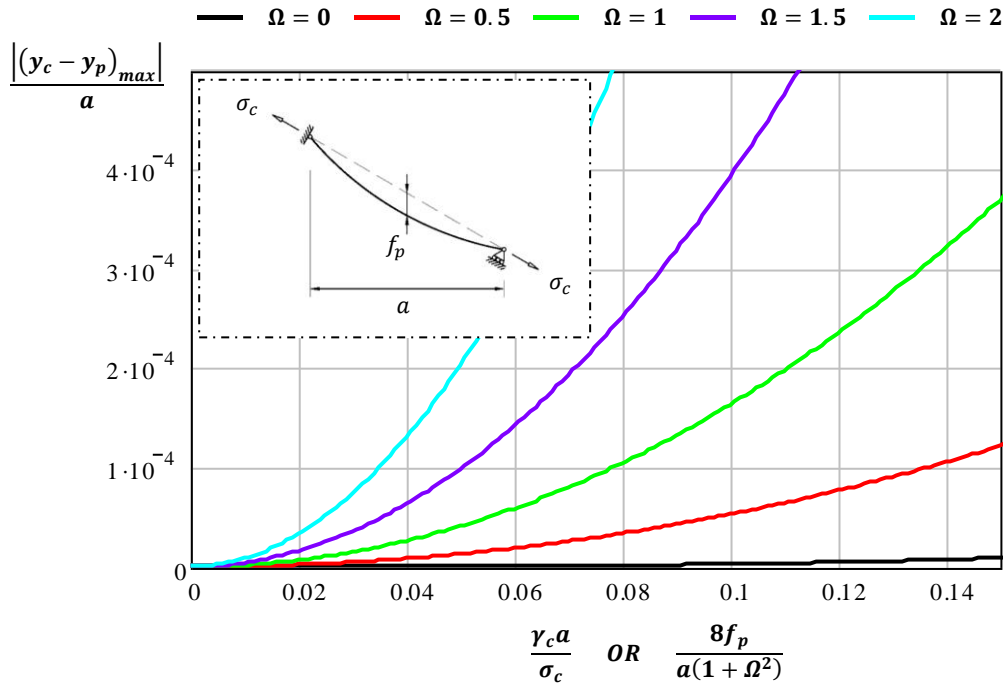
Figure 3.4: Maximum Difference in Ordinates using the Catenary and Parabolic Formulations

It is clear from Figure 3.4 that the parabolic solution has greater difficulty in approximating the shape of the cable curve as the inclination of the cable increases. In horizontal cables with equal chord

stress, the parabolic curve will always be shallower than the catenary due to the underestimation of the total magnitude of the self-weight of the cable ($a < C$). However, because the self-weight of the cable is distributed symmetrically, the shape of the parabola is able to match more closely the shape of the catenary. In contrast, for positively inclined cables, the parabolic solution overestimates the magnitude of the loading in the lower end of the cable and underestimates the loading at the upper end. As a result, the parabolic curve must traverse over top of the catenary curve in order to satisfy the boundary conditions and the error is greater in comparison. This is depicted in Figure 3.5 which shows the error profile for a horizontal cable versus that of an inclined cable, with equal projected length and equal chord stress. The exact location where the parabolic solution crosses the catenary curve varies depending upon the parameters specified.
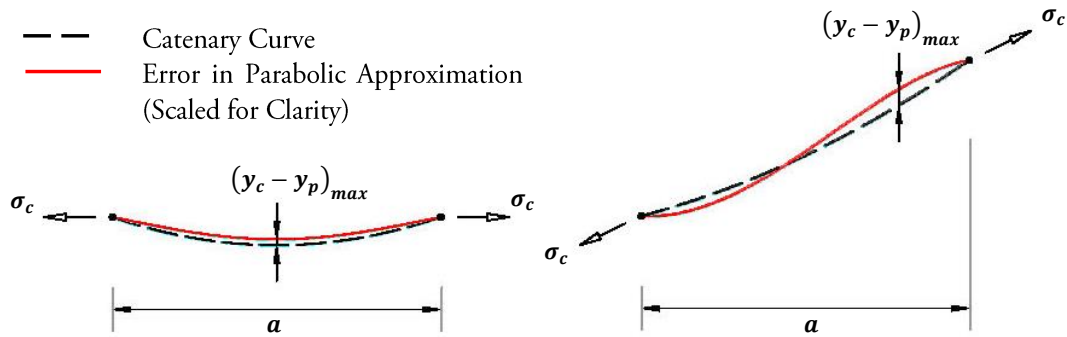
Figure 3.5: Error Profiles from Parabolic Approximation in a Horizontal and Inclined Cable
Parameters: γ_c = 0.09MN/m³, a = 100m, Ω=0.05, and σ_c = 200MPa.

Although the parabolic approximation is not as accurate for inclined cables with equal chord stress, this observation should not be misinterpreted to give the impression that large errors will be introduced for scenarios involving highly inclined cables. Rather, the error in such cables typically ends up being marginalized due to their inherently small projected length. As evidence, the maximum difference in ordinates using the catenary and parabolic formulations is given in a bar plot in Figure 3.6 for a typical cable-stayed bridge with a cable spacing of 20 metres. Note that in the figure, the difference in ordinates has been normalized with respect to the longest stay cable and the chord stress in all cables is assumed equal to 650MPa.
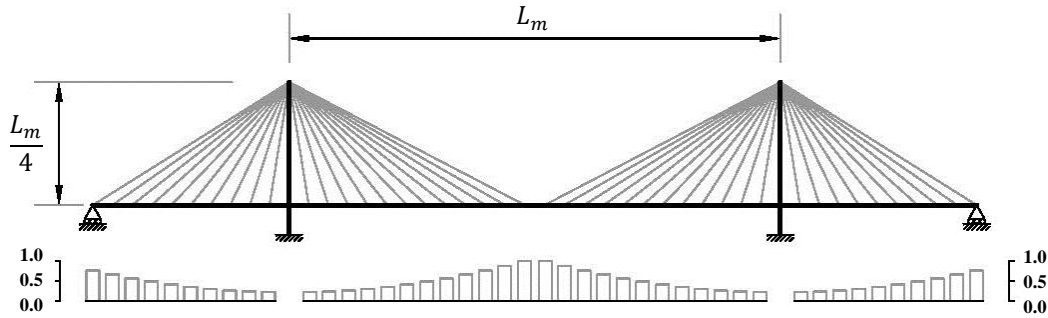
Figure 3.6: Parabolic Error in Typical Cable-Stayed Bridge Normalized to Longest Stay
Parameters: L_m= 500m, γ_c = 0.09MN/m³, σ_c = 600MPa

The ratio in Figure 3.6 remains virtually unchanged for practical values of chord stress, and so long as the tower height-to-span ratio remains within the standard interval of 0.2 to 0.25, the longest stay will always possess the greatest error (assuming that the relative chord stress in the anchor cable is not substantially lower). Given that the longest stay will have a rise-to-span ratio, Ω roughly equal to 0.5, Figure 3.4 indicates that the parabolic approximation is acceptable for most bridge engineering applications.

In addition to the ordinates of the cable, the unstressed length is often an important parameter used in design. As a final study with regard to precision of the parabolic approximation, Figure 3.7 compares the unstressed length computed using Equations (3.28) and (3.31) (denoted as USL_p), against the unstressed length obtained using the catenary solution (denoted as USL_c). Again, the difference is normalized with respect to the projected length of the cable.

Figure 3.7 reveals that the simplified parabolic equation for the stressed length derived from Equation (3.31) actually provides closer agreement with the catenary solution compared to the exact parabolic formulation based on Equation (3.28). In cable-stayed bridges, the largest error will again occur in the longest stays for which the parabolic approximation is shown to produce negligible error. So long as the elastic elongation in the cable is small compared to the stressed length, as typically is the case, the error in the unstressed length will remain virtually unaffected by adjustments to, E_c.

$$\frac{\left|USL_c - USL_p\right|}{a}$$

(Simplified Parabolic Equation)

$\Omega = 0$

$\Omega = 0.5$

$\Omega = 1$

$$\frac{\gamma_c a}{\sigma_c} \quad OR \quad \frac{8f_p}{a(1 + \Omega^2)}$$

$\Omega = 1.5$

$\Omega = 2$

(Exact Parabolic Equation)
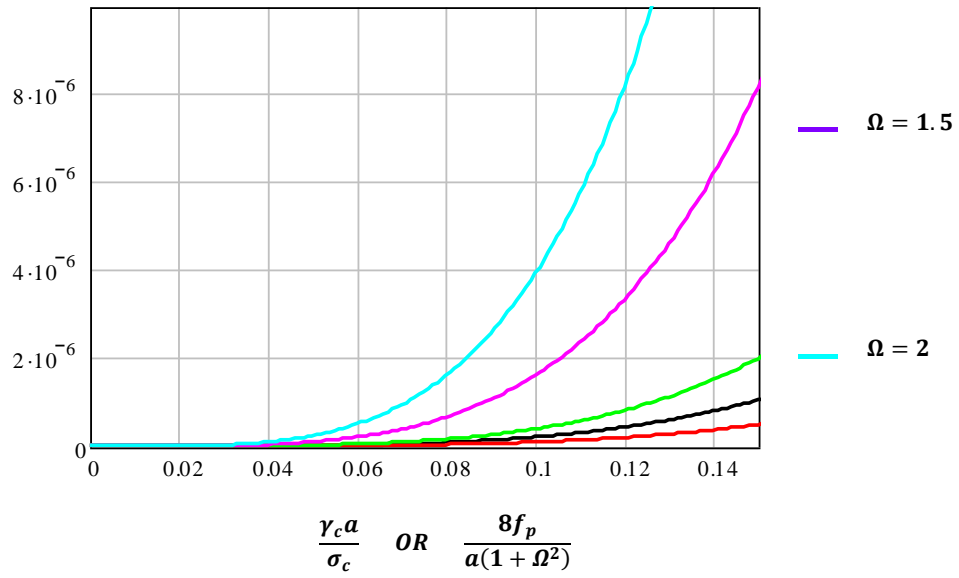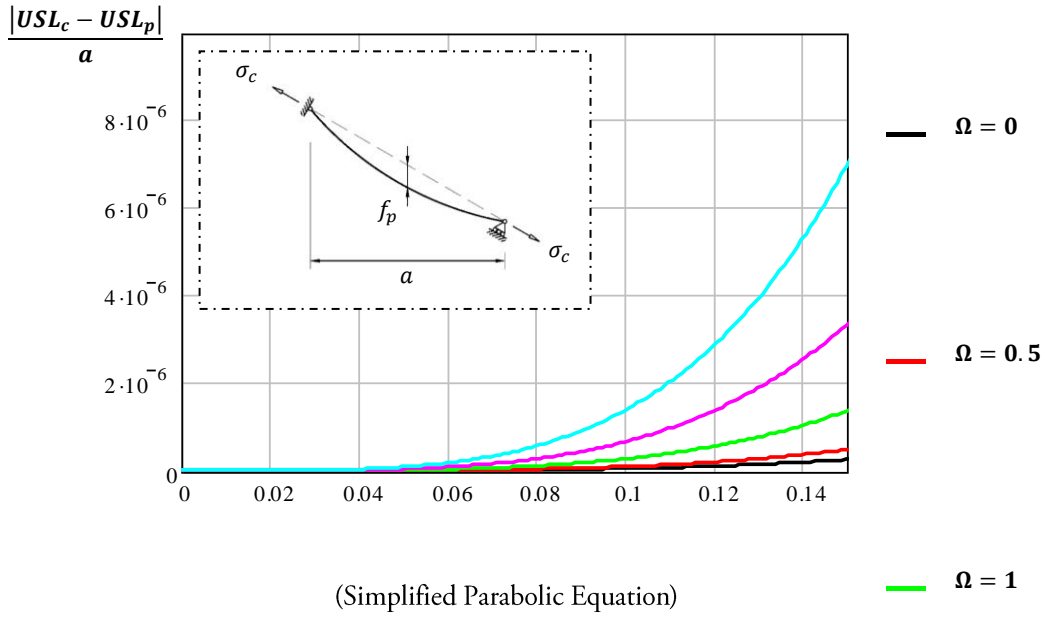
Figure 3.7: Difference in USL using the Catenary and Parabolic Solutions
Parameters: E_c= 200GPa.

3.1.2 Deformation Characteristics

To understand how a stay cable behaves under loading, Figure 3.8 shows a stay cable under two states of stress; an initial state denoted by, σ_{co} and a second or final state denoted by, σ_{cf}. In both cases the stay cable is restrained so that deformation can only occur along the cable chord.

(Initial Stress State)   (Final Stress State)
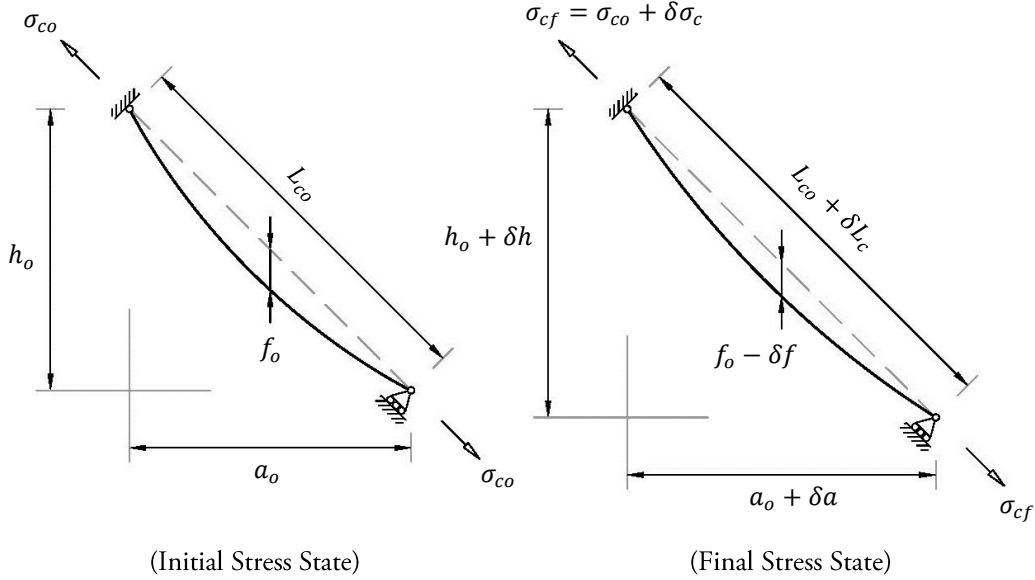
Figure 3.8: Stay Cable Subjected to Two Stress States

Assuming a parabolic curve, the stressed lengths and elastic elongations of the cable under the two different stress states may be obtained from Equations (3.31) and (3.32), respectively, as

$$C_o = L_{co}\left[1 + \frac{1}{24(1+\Omega^2)}\left(\frac{\gamma_c L_{co}}{\sigma_{co}}\right)^2\right] \tag{3.36}$$

$$\Delta_{eo} = \frac{L_{co}\sigma_{co}}{E_c} + \frac{1}{12E_c}\left(\frac{\gamma_c{}^2 L_{co}{}^3}{\sigma_{co}}\right) \tag{3.37}$$

$$C_f = L_{co} + \delta L_c + \frac{1}{24(1+\Omega^2)}\left(\frac{\gamma_c}{\sigma_{cf}}\right)^2 (L_{co} + \delta L_c)^3 \tag{3.38}$$

$$\Delta_{ef} = \frac{(L_{co} + \delta L_c)\sigma_{cf}}{E_c} + + \frac{1}{12E_c}\frac{\gamma_c{}^2}{\sigma_{cf}}(L_{co} + \delta L_c)^3 \tag{3.39}$$

Regardless of the magnitude of stress in the cable, the cable's unstressed length remains the same.

Therefore, the two stress states may be related through the following compatibility equation,

$$USL_o = USL_f \tag{3.40}$$

which after substitution of Equations (3.36) to (3.39) yields,

$$\frac{\delta L_c}{L_{co}} - \overbrace{\frac{\delta L_c}{L_{co}}\frac{\sigma_{cf}}{E_c}}^{\sim 0} = \frac{(\sigma_{cf} - \sigma_{co})}{E_c} - \frac{\gamma_c{}^2 a^2}{24}\left[\frac{1}{\sigma_{cf}{}^2}\overbrace{\frac{(L_{co} + \delta L_c)^3}{L_{co}{}^3}}^{\sim 1} - \frac{1}{\sigma_{co}{}^2}\right] \tag{3.41}$$

$$+ \overbrace{\frac{\gamma_c{}^2 L_{co}{}^2}{12 E_c \sigma_{cf}}}^{\sim 0}\left[\frac{(L_{co} + \delta L_c)^3}{L_{co}{}^3} - \frac{\sigma_{cf}}{\sigma_{co}}\right]$$

Assuming material cable properties common for bridge engineering applications, and also assuming small displacements ($\delta L_c \ll L_{co}$), many of the terms in Equation (3.41) may be neglected without introducing any appreciable error arriving at the following stress-deformation relationship (Gimsing & Georgakis, 2012),

$$\frac{\delta L_c}{L_{co}} = \underbrace{\frac{(\sigma_{cf} - \sigma_{co})}{E_c}}_{Linear\ Term} + \underbrace{\frac{\gamma_c{}^2 a^2}{24}\left(\frac{1}{\sigma_{co}{}^2} - \frac{1}{\sigma_{cf}{}^2}\right)}_{Nonlinear\ Term} \tag{3.42}$$

The first term in Equation (3.42) is recognizable from Hooke's Law; a constitutive relationship which applies to most structural materials. It characterizes the linear elastic deformations in the cable resulting from strains in the cable material. The second nonlinear term however is unique to cables and does not depend on the cable material's elasticity but rather on the cable's geometry. It arises due to strain-free deformations that occur as a result of geometric changes in the cable profile. This could also be thought of as deformations which would otherwise occur in an inextensible or axially stiff cable. Note that neither term is dependent on the inclination/rise of the cable.

As a result of the nonlinear term, the initial forces in the cable and its deformations thereafter cannot automatically be assumed to have a negligible impact on the level of stiffness exhibited. To illustrate this point, Figure 3.9 depicts a generalized stress-deformation relationship for a stay cable. The linear term in Equation (3.42) is also plotted in the figure as a dashed line.

As can be seen in the figure, the lower end of the curve is highly nonlinear and is thus controlled by strain-free deformations. In this region, the sag of the cable will be pronounced and any small change in stress will result in large deformations as the cable straightens its form. Conversely, at the upper

end of the curve, the sag in the cable will be relatively minimal and nonlinear effects start to diminish rapidly. Eventually, the stiffness of the cable will be driven almost entirely by the linear term in Equation (3.42) and the deformation behaviour of the cable will approach that of a straight bar with modulus of elasticity equal to, E_c. Where the initial stress in the cable lies on the curve is thus an important factor in determining the response of a stay cable.
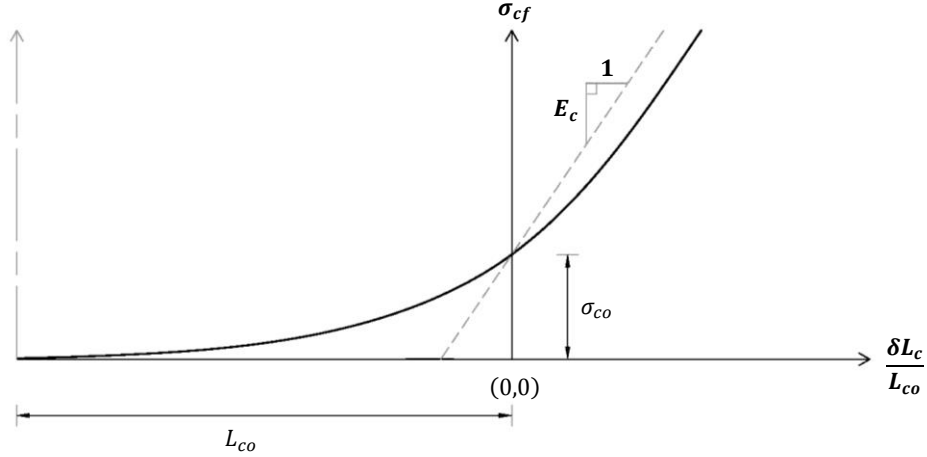
Figure 3.9: Generalized Stress-Deformation Relationship for a Stay Cable

3.1.2.1 The Sag Effect

For scenarios where nonlinear effects cannot be neglected, precisely capturing the deformation behaviour of a cable is an iterative process which can exponentially increase the amount of computations required. H.-J Ernst was the first to popularize a simplified method based upon an equivalent linear approach (Ernst, 1965). Using this method, a cable may be considered to act as a straight member with zero sag and the nonlinear stiffness associated with moving from one stress state to another (aptly referred to in literature as the 'sag effect'), is accounted for by setting the elastic stiffness of the cable member equal to a secant modulus (see Figure 3.10), E_{sec}, defined by

$$E_{sec} = \left(\sigma_{cf} - \sigma_{co}\right)\frac{L_{co}}{\delta L_c} \tag{3.43}$$

which after substitution of Equation (3.42) and rearranging terms yields,

$$E_{sec} = \cfrac{1}{\cfrac{1}{E_c} + \cfrac{\gamma_c{}^2 a^2\left(\sigma_{cf} + \sigma_{co}\right)}{24\sigma_{cf}{}^2\sigma_{co}{}^2}} \tag{3.44}$$
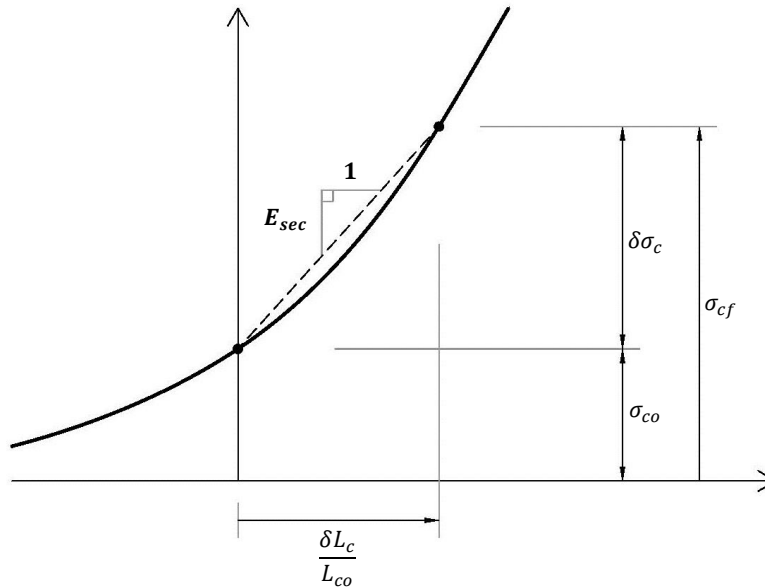
Figure 3.10: Close-up of Stress-Deformation Relationship Illustrating the Secant Modulus

The introduction of the secant modulus allows deformations to be computed with relative ease using linear analysis, and since the final deformation will be the correct one, no additional error is generated. Nevertheless, iterations are still required in order to obtain the second or final stress point. For a bridge with numerous cables, each subject to many different loading conditions, the task can still be laborious. If the variability of $\delta\sigma_c$ under all loading conditions is relatively small then it may be sufficient to compute the secant modulus corresponding to the maximum $\delta\sigma_c$ and then use this value to approximate the deformation for all other loading conditions. For anchor cables subject to relatively large load reversals, this would mean determining two different moduli; one for the maximum positive $\delta\sigma_c$ and one for the maximum negative $\delta\sigma_c$. Loading conditions may also be categorized according to different limit states in order to reduce the variability of $\delta\sigma_c$.

In addition to the secant method, H.-J Ernst also stipulated that if $\delta\sigma_c \ll \sigma_{co}$ then a further simplification could be made by considering the cable stiffness as constant with magnitude equal to the tangent stiffness at $\sigma_{cf} = \sigma_{co}$. Replacing σ_{cf} in Equation (3.44) by σ_{co} gives,

$$E_{tan} = \frac{1}{\dfrac{1}{E_c} + \dfrac{\gamma_c{}^2 a^2}{12\sigma_{co}{}^3}} \qquad (3.45)$$

As the tangent stiffness is independent of the final or second stress point, iterations are no longer necessary and deformations can be computed based on the cable's undeformed geometry. In general,

σ_{co} is linked to the stiffness of the cable in its dead load state and, therefore, by using the tangent stiffness, the stiffness of all cables at the end of construction is assumed constant for any and all additional loading.

Figure 3.11 shows the ratio of the tangent modulus to the elastic cable modulus for different values of initial stress. A ratio very near to one indicates that the cable will respond to additional load in a near linear fashion. For such cases, nonlinear effects can often be neglected completely and the cable may be modelled as a straight member with an elastic stiffness equal to its elastic modulus, E_c. For lesser values, the error introduced as a result of using the tangent modulus can be somewhat quantified by comparing the tangent and secant moduli for the load case resulting in the maximum change in cable stress. Engineering judgement must then be made with regard to the most suitable method for modelling the cable stiffness given the margin for error available. It is important to note though that for cable-stayed bridges with spans in excess of 1000 metres studies have shown that it is crucial to accurately model the sag effect of the cables through more advanced means than the tangent modulus approach (Janjic, 2008).
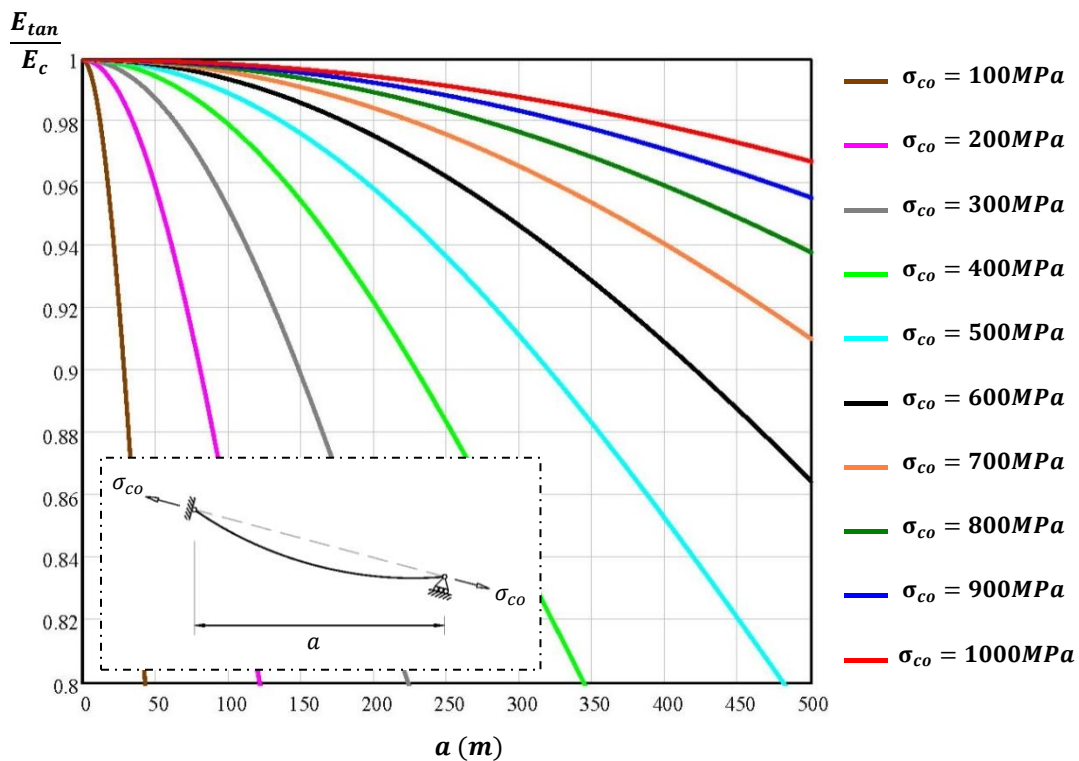
Figure 3.11: Tangent Modulus as a Ratio of the Elastic Cable Modulus
Parameters: E_c= 200GPa, γ_c = 0.09MN/m³

3.1.2.2 The Relationship between Cable Inclination and Deformation

The inclination of a stay cable affects not only the magnitude of tension in the cable, but also the length of the cable, both of which in turn oppositely impact the amount of deformation. To study the effect of inclination, Figure 3.12 illustrates the deformation components of a typical stay cable subjected to an arbitrary transitory force of magnitude, P. Note that the horizontal restraint provided is an idealization of the actual restraint which exists in a cable-stayed bridge as a result of the relatively large axial stiffness of the superstructure. Also, for the purposes of this study the bending stiffness of the superstructure has been neglected. If deformations are assumed small ($\delta\theta_c \ll \theta_c$), then the component of the deformation along the cable chord may be given by the following expression (Troitsky, 1988),

$$\delta_c = \epsilon_c L_c = \frac{\sigma_c}{E_{eff}} \frac{a}{cos\theta_c} \qquad (3.46)$$

where E_{eff} is the effective modulus of the cable (E_{sec} or E_{tan}), assuming the cable may be modelled using the equivalent linear approach described in Section 3.1.2.1. Thereafter, the vertical deflection can be obtained by dividing the chord deformation by the sine of the cable inclination,

$$\delta_v = \frac{\delta_c}{sin\theta_c} = \frac{\sigma_c}{E_{eff}} \left(\frac{1}{sin\theta_c} \frac{1}{cos\theta_c} \right) a \qquad (3.47)$$

Given Equation (3.47), it is now possible to determine how changes in inclination affect the amount of deflection. Assuming that each time the inclination is changed the cable area is updated so that the chord stress remains constant, by fixing the variable 'a', the inclination yielding the minimum vertical deflection occurs when, $\theta_c = 45°$. Intuitively, this makes sense given that as the inclination of the cable increases, the tension force in the cable decreases in direct proportion to the resulting increase in cable length. Figure 3.13 illustrates the relative amount of deflection when inclinations other than $\theta_c = 45°$ are employed. For a conventional cable stayed bridge, the inclination of the longest stay is set within the range of, $21.5° \leq \theta_c \leq 26.5°$ which means that the deflection at mid-span can be as much as 45% greater than if the optimum inclination was employed. The primary reason why the inclination in conventional cable-stayed bridges is not increased is that cost of the bridge starts to become uneconomical beyond an angle of $\theta_c = 26.5°$ as a result of the increased costs associated with the towers.

Similarly, when studying the effect the side span length has on the deformation of the anchor cable, the problem is nearly identical since the model for the anchor cable can be obtained simply by rotating Figure 3.12 ninety degrees counter clockwise. Thus, the vertical deformation is now restrained as a result of the relatively large axial stiffness of the towers and the horizontal deflection of the cable will be equal to Equation (3.47) with the parameter 'a' replaced by the height of the towers.

The only differences are that the change in the effective modulus of the cable must now be taken into account since the projected length of the cable changes when the side span length is altered. Also, the chord stress in the anchor cable generally depends on the side-to-main span length of the bridge. Consequently, increasing the side span length has the effect of increasing the chord stress. These differences produce a slightly greater optimum inclination. A more detailed discussion is provided in Chapter 4 (Section 4.2.1.5).
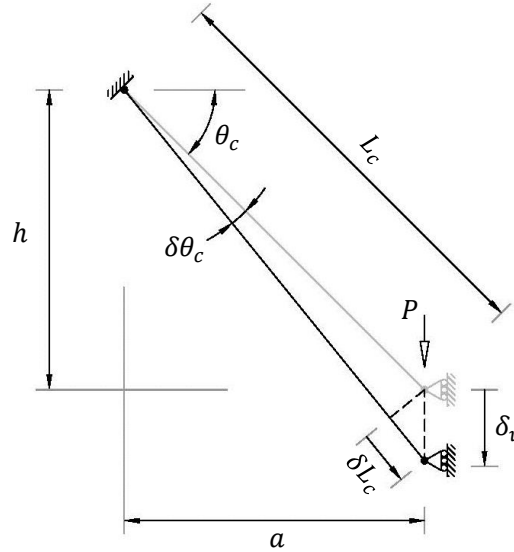
Figure 3.12: Deformation Components in a Typical Stay Cable
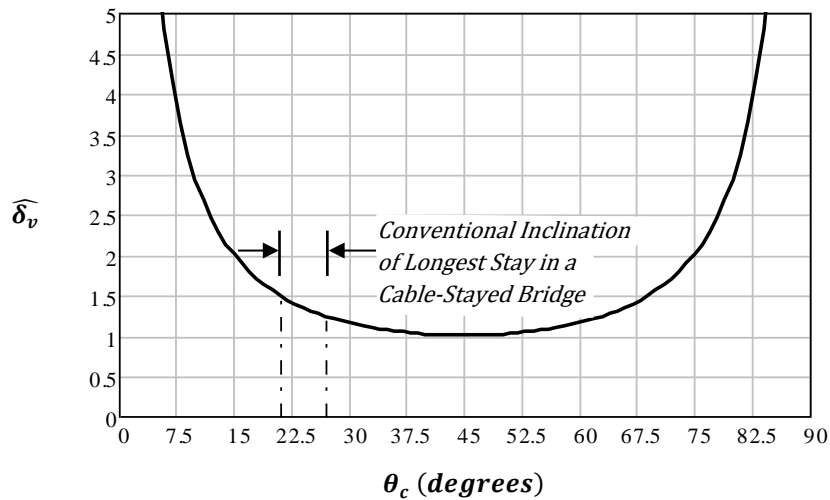
Figure 3.13: Normalized Deflection of a Stay Cable as a Function of Inclination with Fixed Projected Length

3.2   Fully-Laden Suspension Cables

3.2.1   Geometric Form

Gravity loads on suspension cables generally consist of two major components:

1. Distributed loading from the self-weight of the suspension cable; and
2. Concentrated forces due to the self-weight of the superstructure, hanger, and hanger assembly.

The self-weight of the suspension cable is uniformly distributed along the cable curve, whereas the majority of each concentrated force is derived from the self-weight of the superstructure which acts along the cable's projected length. The amalgamation of the two will therefore result in a cable shape that has both catenary and parabolic properties. The relative magnitude of the two load components will dictate the exact shape of the cable. However, because the influence of the self-weight of the suspension cable is also dependent upon the cable shape, an iterative numerical process is required to obtain the exact cable coordinates.

With decreasing span length, a diminishing proportion of the cable's overall load carrying capacity is taken up by its own self-weight, and at a certain point, the catenary effect can be neglected. Under this assumption, all gravity loads are considered to act along the projected length of the cable and closed form solutions can be derived giving the cable coordinates in the form of a parabola.

This section describes a procedure which has been adapted from Zhang et al. (2010) for obtaining the near exact shape of a fully-laden suspension cable considering the catenary effect. Equations which can be used to determine the approximate cable shape assuming a parabolic form are also provided. In both cases, it is assumed that all hanger forces are vertical and the cable is symmetric with respect to the centre of its span. The complexity of computing the geometric form of a suspension cable is greatly compounded if these assumptions are not valid. For such special cases, a procedure for determining the shape of a cable in three-dimensional space has been developed and is presented in Appendix A.

3.2.1.1   Dead Load Geometry Considering Catenary Effect

Figure 3.14 illustrates the free body diagram of a fully-laden suspension cable with a section cut placed at mid-span. The cable is further visualized as consisting of a series of cable segments, each bounded between hanger and/or sectional nodes. A free body diagram of an individual segment reveals that the only gravity forces acting on a cable segment will be those due to its own self-weight.

Accordingly, the local coordinates of each cable segment take the form of a catenary.
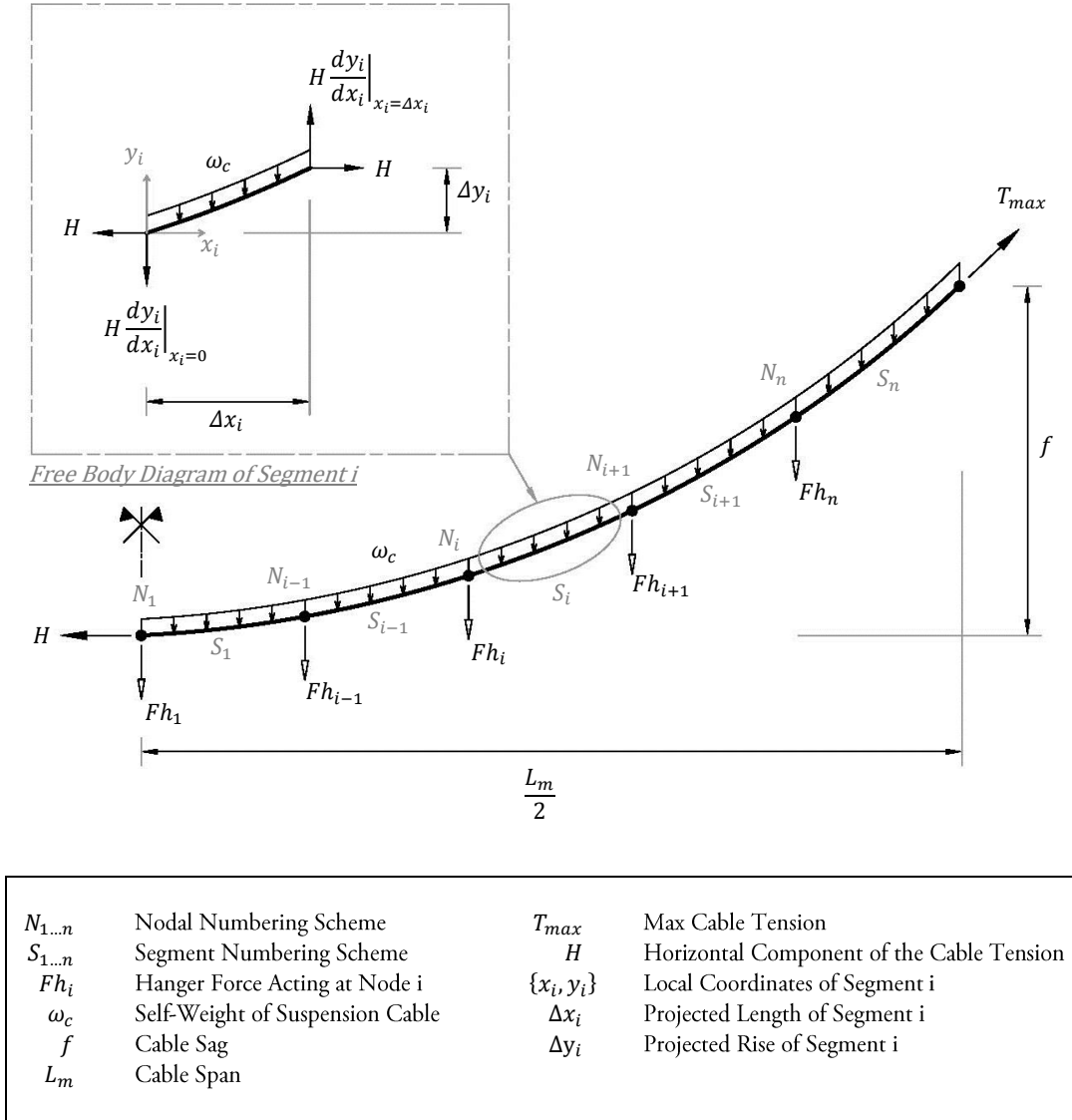
Figure 3.14: Reference Diagram for Segmented Catenary Solution

Using the equations already established in Section 3.1.1.1, the local coordinates for a segment, i, may therefore be written as,

$$y_i = \frac{H}{\omega_c} \cosh\left(\frac{\omega_c x_i}{H} + A_i\right) + B_i \tag{3.48}$$

where,

$$A_i = asinh\left[\frac{\omega_c \Delta y_i}{2Hsinh\left(\frac{\omega_c \Delta x_i}{2H}\right)}\right] - \frac{\omega_c \Delta x_i}{2H} \qquad \text{and} \qquad B_i = -\frac{H}{\omega_c}cosh(A_i)$$

Assuming the self-weight of the suspension cable and the distance between all hangers are known parameters, Equation (3.48) still contains, $n + 1$ unknowns in the form of, $\Delta y_{1...n}$ and H. However, given a value of H, $\Delta y_{1...n}$ can be obtained from the following equilibrium equations.

For joint, $i = 1$,

$$2H\frac{dy_1}{dx_1}\bigg|_{x_1=0} = Fh_1$$

$$\xrightarrow{\textit{reduces to}} \qquad Hsinh(A_1) = \frac{Fh_1}{2} \tag{3.49}$$

For joints, $i = 2 \dots n$,

$$H\frac{dy_i}{dx_i}\bigg|_{x_i=0} = H\frac{dy_{i-1}}{dx_{i-1}}\bigg|_{x_{i-1}=\Delta x_{i-1}} + Fh_i$$

$$\xrightarrow{\textit{reduces to}} \qquad H\left[sinh(A_i) - sinh\left(\frac{\omega_c \Delta x_{i-1}}{H} + A_{i-1}\right)\right] = Fh_i \tag{3.50}$$

The assumption of symmetry is utilized for Equation (3.49), and when combined with the specified nodal numbering scheme, this allows the above equations to be solved successively. Herein lays the main improvement of the aforementioned procedure: the number of unknowns is reduced to one which greatly simplifies the solution algorithm. Thus, once $\Delta y_{1...n}$ is obtained, the sag of the cable, f corresponding to the given value of H can thereafter be computed as,

$$f = \sum_{i=1}^{n} \Delta y_i \tag{3.51}$$

And, since the sag of the cable is also typically a known parameter, the correct cable coordinates may be obtained by iterating the value of H until Equation (3.51) converges to the desired target value. This is described in the following algorithm which utilizes a form of Newton's Method adapted from, Miller (1971), to optimize the iterative process.

CABLE SHAPE FINDING ALGORITHM

Assumptions:

1. The end nodes of the cable are at equal elevation.
2. Hanger forces are vertical and symmetric with respect to the centerline of the cable span.
3. The cable has negligible bending stiffness.
4. The cable material obeys Hooke's Law.
5. Infinitesimal strain theory applies.

Initial Inputs:

1. The self-weight of the suspension cable, $\omega_c = \gamma_c A_c$.
2. An array containing $\Delta x_{1\ldots n}$ ⎤
3. An array containing $Fh_{1\ldots n}$ ⎦ See Figure 3.14
4. The target value for the cable sag, denoted as f_T. Also, the tolerance accepted in achieving the target value, denoted as TOL.
5. An initial guess value for the horizontal force in the cable, denoted as H_A.

Steps:

1. Solve for $\Delta y_{1\ldots n}$ using Equations (3.49) & (3.50) with H_A set as the horizontal cable force.
2. Compute the cable sag (denoted as f_A) corresponding to H_A using Equation (3.51) combined with the $\Delta y_{1\ldots n}$ obtained from Step 1.
3. Determine the error in the computed cable sag, $f_E = f_T - f_A$.
4. Check convergence
    a. If $f_E > TOL$ advance to Step 5.
    b. If $f_E \leq TOL$ advance to Step 8.
5. Numerically compute the derivative, $\frac{dH_{AB}}{df_{AB}} = \left(\frac{H_A - H_B}{f_A - f_B}\right)$
    a. Set $H_B = (1 - TOL)H_A$
    b. Solve successively for $\Delta y_{1\ldots n}$ using Equations (3.49) & (3.50) with H_B set as the horizontal cable force.
    c. Compute the cable sag (denoted as f_B) corresponding to H_B using Equation (3.51) combined with the $\Delta y_{1\ldots n}$ obtained from Step 5b.
6. Update the guess value for the horizontal cable force, $H_{A\,NEW} = H_{A\,OLD} + f_E \left(\frac{dH_{AB}}{df_{AB}}\right)$
7. Repeat Steps 1 through 6 until the convergence criterion in Step 4b is met.
8. With H_A set as the horizontal cable force, compute the local cable coordinates for each cable segment using Equation (3.48) combined with the $\Delta y_{1\ldots n}$ from Step 1.

9. Convert the local coordinates of each cable segment to a global coordinate system.

ADDITIONAL NOTES

- All initial inputs should be entered as positive values.

- When entering $\Delta x_{1...n}$ and $Fh_{1...n}$, Node 1 should be at the mid-span of the cable regardless of the hanger locations. If there is no hanger at mid-span then Fh_1 should be set equal to zero and Δx_1 should represent the distance from mid-span to the nearest hanger.

- The convergence of Newton's Method is sensitive to the initial guess value of H provided (Epperson, 2013). For general bridge engineering applications, it is recommended that the parabolic approximation be used to provide the starting value of H_A.

- To avoid possible convergence problems, $H_{A\,NEW}$ should be prevented from becoming negative. As such, it is recommended that the limit, $H_{A\,NEW} \geq 0.5 H_{A\,OLD}$ be placed on Step 6.

GENERAL COMMENTS

- Once the correct cable shape has been established using the algorithm presented, the unstressed length of the cable may be computed as (from Equations (3.10) to (3.13)),

$$USL = 2 \left[\sum_{i=1}^{n} C_i - \Delta_i \right] \tag{3.52}$$

where,

$$C_i = \frac{H}{\omega_c} \left[sinh \left(\frac{\omega_c \Delta x_i}{H} + A_i \right) - sinh(A_i) \right] \tag{3.53}$$

and,

$$\Delta_{e\,i} = \frac{H\Delta x_i}{E_c A_c} \left[\frac{\omega_c \Delta y_i^2}{2H\Delta x_i} coth \left(\frac{\omega_c \Delta x_i}{2H} \right) + \frac{1}{2} + \frac{H}{2\omega_c \Delta x_i} sinh \left(\frac{\omega_c \Delta x_i}{H} \right) \right] \tag{3.54}$$

- In some cases, prior to computing the cable shape, the unstressed length of the cable may be known and the sag of the cable may be unknown. For such cases, using Equations (3.52) to (3.54), the algorithm presented may be easily modified to make the unstressed length of the cable the target variable.

3.2.1.2   Dead Load Geometry Using Parabolic Approximation

The self-weight of the suspension cable is now assumed to act along the cable's projected length, and as such, the cable ordinates can be determined directly. However, because the hanger loads act at discrete locations, in order to obtain accurate ordinates at intermediary locations between hangers, a piecewise/segmental solution must still be employed.

Using Figure 3.15 as a reference, the ordinates of the cable for a given segment, S_m may be obtained from sectional moment equilibrium,

$$y(x)|_{S_m} = \frac{1}{H}\left[\sum_{j=1}^{m-1} Fh_j\left(x - \sum_{i=1}^{j}\lambda_i\right) + \frac{\omega_c x^2}{2} - V_s x\right] \tag{3.55}$$

where x and y are measured with respect to a global coordinate system placed at the upper left end node of the cable and all parameters including the hanger forces are given as positive values. The vertical component of the cable tension at the supports is derived from global force equilibrium,

$$V_s = \frac{1}{2}\sum_{i=1}^{N_{hangers}} Fh_i + \omega_c \frac{L_m}{2} \tag{3.56}$$

and similarly, an expression relating the cable sag to the horizontal force in the cable is derived from sectional moment equilibrium about mid-span of the cable,

$$H = \frac{1}{f}\left[V_s\frac{L_m}{2} - \omega_c\frac{L_m^2}{8} - \sum_{j=1}^{N^*} Fh_j\left(\frac{L_m}{2} - \sum_{i=1}^{j}\lambda_i\right)\right] \tag{3.57}$$

where,

$$N^* = \begin{cases} \dfrac{N_{hangers}-1}{2}, & \text{if there is a hanger at mid-span} \\[2em] \dfrac{N_{hangers}}{2}, & \text{if there is no hanger at mid-span} \end{cases} \tag{3.58}$$

The above equations allow for the approximate determination of a cable shape with varying hanger forces so long as those forces are symmetric with respect to the centerline of the cable span. However, without the aid of a computer algorithm, the solution process for longer span suspension bridges containing an extensive number of hangers is cumbersome.

Figure 3.15: Reference Diagram of Fully-Laden Suspension Cable for Parabolic Approximation

Typically during initial stages of design, the only ordinates of interest on a suspension cable are those which correlate to points of hanger attachment. In addition,

- The cross-sectional area of the superstructure is kept constant along the cable span;

- Hangers are designed to have equal spacing and it is assumed that each hanger carries an equal distribution of the superstructure weight, and;

- The weight of the hangers and of the hanger assemblies can often be neglected relative to the combined weight of the suspension cable and superstructure, or alternatively, they may be considered as a uniform load to be included within the overall cable weight, ω_c.

Under these conditions, denoting λ as the hanger spacing, and ω_s as the uniformly distributed weight of the superstructure, Equations (3.55) to (3.58) reduce to the much simpler form,

$$H = \begin{cases} \dfrac{(\omega_c+\omega_s)L_m{}^2}{8f}, & \text{if there is a hanger at mid-span} \\[4mm] \dfrac{(\omega_c+\omega_s)L_m{}^2}{8f} - \dfrac{\omega_s\lambda^2}{8f}, & \text{if there is no hanger at mid-span} \end{cases} \tag{3.59}$$

and,

$$y(x) = \frac{(\omega_c + \omega_s)x}{2H}\left[x - L_m\right] \tag{3.60}$$

where x is defined only at hanger locations. Because they are easier to manipulate, Equations (3.59) and (3.60) are frequently cited in literature in place of Equations (3.55) to (3.58). However, when doing so, the effect the hanger configuration has on the horizontal cable force is often ignored. It is important to note though that at intermediate locations between hangers, in contrast to Equation (3.55), Equation (3.60) will yield ordinates representative of a loading scheme in which the uniform weight of the superstructure is applied continuously along the entire cable span rather than transmitted by hangers at discrete intervals. This is evident upon comparing Equation (3.60) to the parabolic expression derived for the ordinates of a stay cable (Equation (3.20)), wherein the two equations only differ in the magnitude of their respective loading coefficients. Consequently, if Equation (3.60) is used at intermediate locations between hangers, an added degree of error will be introduced (more in Section 3.2.1.3).

When computing the unstressed length of the cable, the ordinates of the cable at all locations must be considered. As opposed to deriving an expression directly from Equation (3.60), a segmental approach is best suited to properly capture the loading condition on the cable between hangers. Recognizing that the parabolic equations previously developed in the section on stay cables may be applied for the local curve of each cable segment, and introducing once more the segment/node numbering scheme shown in Figure 3.15, the stressed length and elastic elongation of an individual segment of cable can be approximated as (by way of Equations (3.31) and (3.32)),

$$C_m = \lambda_m\sqrt{1 + \Omega_m{}^2}\left[1 + \frac{1}{24}\frac{\Psi_{c_m}{}^2}{\left(1 + \Omega_m{}^2\right)}\right] \tag{3.61}$$

and,

$$\Delta_{e_m} = \frac{H\lambda_m}{E_cA_c}\left[1 + \Omega_m{}^2 + \frac{1}{12}\Psi_{c_m}{}^2\left(1 + \Omega_m{}^2\right)\right] \tag{3.62}$$

where the dimensionless coefficients are given by,

$$\Psi_{c_m} = \frac{\omega_c\lambda_m}{H} \qquad \text{and} \qquad \Omega_m = \frac{h_m}{\lambda_m}$$

For uniformly spaced hangers and hanger forces, the hanger spacing, λ_m may be replaced by a constant parameter, λ; the horizontal force in the cable, H, can be determined from Equation (3.59); and since segment boundary nodes correspond to hanger locations, the projected rise of each cable segment, h_m, may be obtained directly from Equation (3.60),

$$h_m = y_m - y_{m-1} \tag{3.63}$$

where y_m represents the cable ordinates at a given node, m. Alternatively, for non-uniform hanger forces, Equations (3.55) and (3.57) may be used for y_m, and H, respectively. Thereafter, summing the unstressed lengths of all cable segments yields the total unstressed length of the cable.

$$USL_{Total} = \sum_{m=1}^{N_{hangers}+1} (USL_m) = \sum_{m=1}^{N_{hangers}+1} \left(C_m - \Delta_{e_m} \right) \tag{3.64}$$

3.2.1.3 Examining the Error in the Parabolic Approximation

Similar to the section on stay cables, the accuracy of the parabolic approximation for fully-laden suspension cables will be measured against the near exact segmental catenary solution presented in Section 3.2.1.1. To limit the parameters involved, in all cases the cable sag is set equal to a conventional value of 10% the cable span; though as a general rule, the precision of the parabolic approximation will diminish with increasing cable sag.

Considering all values of x, the maximum deviation between the ordinates obtained using the catenary solution (denoted by y_c), and those obtained using Equation (3.60) (denoted y_p), are plotted in Figure 3.16 for a range of dead load ratios (ordinates are plotted with respect to the coordinate system defined in Figure 3.15). The error in the parabolic approximation is shown by the solid black line and the additional error generated from using Equation (3.60) at locations other than hanger positions is given by the dashed lines.

As noted in the previous section, the additional error from using Equation (3.60) at intermediate locations between hangers can be substantial depending on the ratios $\lambda : L_m$, and $\omega_c : \omega_s$. However, as the dead load of the cable increases relative to the dead load of the superstructure, the global error in the parabolic approximation supersedes the local error generated between hangers. The point at which this transition occurs is marked by the intersection of the dashed line with the solid line and depends on the hanger spacing relative to the cable span length. For cases in which this transition has occurred, Equation (3.60) may be used at all locations along the cable with a similar degree of accuracy as that provided by the piecewise approach given by Equations (3.55). This also has

implications for the computation of the unstressed length of the cable (see the final note in this section).
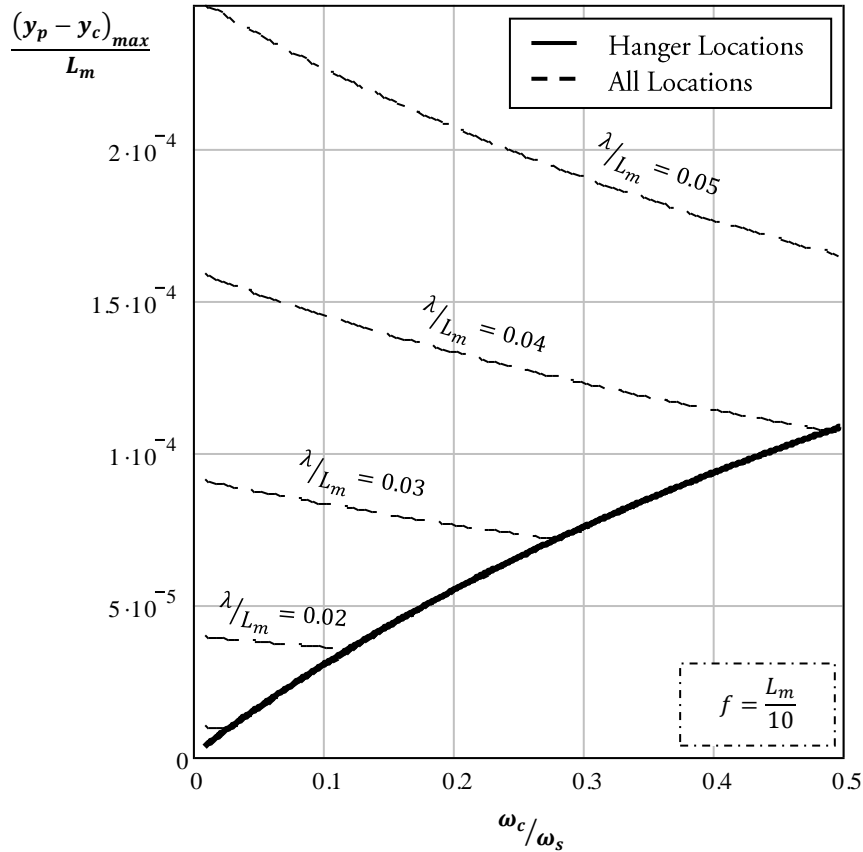
Figure 3.16: Error Produced using Simplified Parabolic Approximation versus Dead Load Ratio

To gain a sense of how the error in the ordinates varies with span length, the cable area must first be sized accordingly. In practise, the area of the cable is determined based upon the specified properties of the cable material and design procedures set out by local regulatory authorities. Since these procedures vary from region to region, a simple universal method is adopted here. Live load is considered as a uniformly distributed load, ω_p and the cable is sized under the condition that when the entire span is loaded with dead and live load (unfactored), the maximum stress in the cable equates to a specified allowable design stress, σ_{allow}. This method is commonly used for conceptual design. For standard cable types applied in cable bridges, an allowable design stress of 800MPa is conventionally employed (Gimsing & Georgakis, 2012).

Figure 3.17 plots the error in ordinates as a function of span length using a live load-to-superstructure dead load ratio of 0.6. This load ratio is representative of a typical, fully-laden suspension bridge with a steel deck, carrying vehicular traffic. For lower load ratios, the self-weight of the cable will be lower in proportion to the dead load of the superstructure, and as indicated in Figure 3.16, the error at hanger locations will decrease, whereas, the error will increase at intermediate locations between hangers.
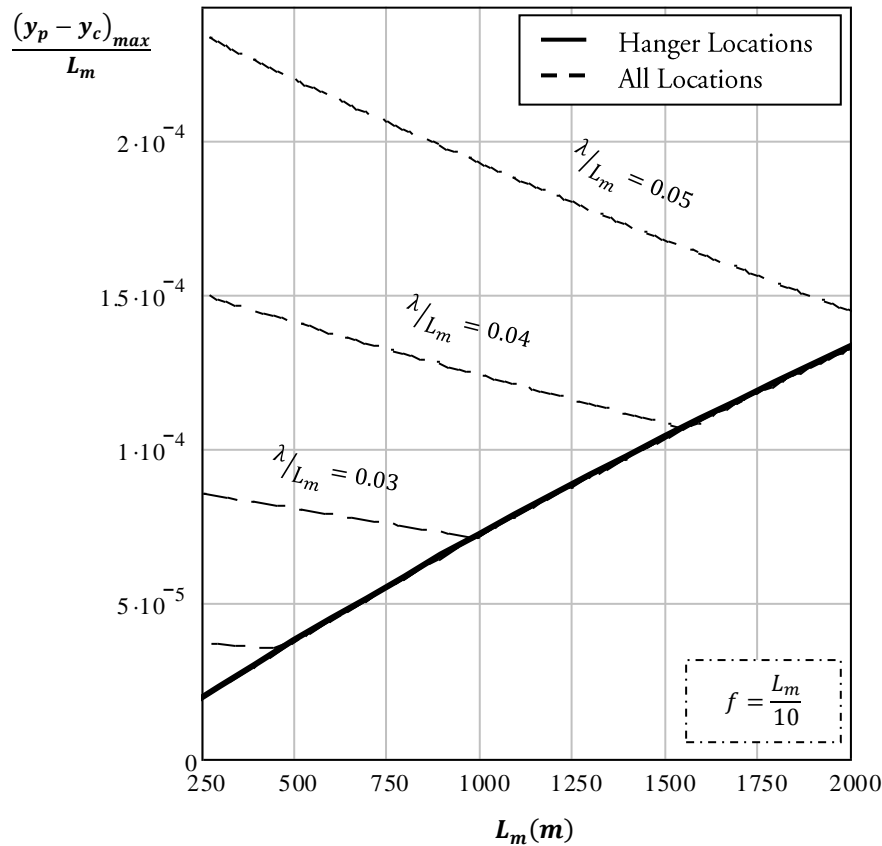
Figure 3.17: Error Produced using Simplified Parabolic Approximation versus Span Length

Parameters: $\gamma_c = 0.09 \text{MN/m}^3$, $\sigma_{allow} = 800 \text{MPa}$, $\omega_p = 0.6 \cdot \omega_s$

Using the same cable sizing parameters as in Figure 3.17, the error in the unstressed lengths are also compared in Figure 3.18, where USL_c is used to denote the unstressed length computed using the segmented catenary approach, and USL_p denotes the unstressed length computed using Equations (3.61) to (3.64).
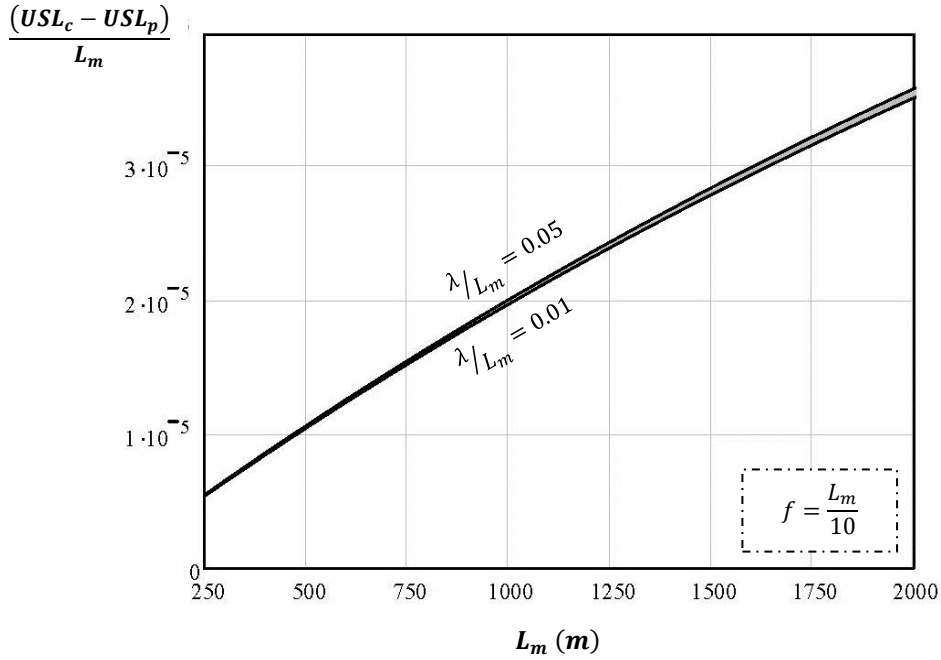
Figure 3.18: Error in USL using Simplified Parabolic Approximation
Parameters: $\gamma_c = 0.09$MN/m³, $\sigma_{allow} = 800$MPa, $\omega_p = 0.6 \cdot \omega_s$, $E_c = 200$GPa

Owing to the segmental method employed, the error in the unstressed length is for all practical purposes independent of the hanger spacing. Moreover, for small to medium spans, the error is minor and will decrease further for lower $\omega_p : \omega_s$ ratios. For long spans, the parabolic approximation may not be advisable depending on the level of accuracy desired. However, when a quick approximation is required, a simpler approach may be taken.

As the span length of the cable increases, the hanger spacing generally remains constant in order to avoid designing the superstructure for large local bending moments. Thus, for long spans the hanger spacing is relatively small in comparison to the main span length and if, according to Figure 3.17, the error from Equation (3.60) is the same at hanger and at non-hanger locations, then an expression for the unstressed length of the cable may be derived directly from Equation (3.60) without introducing any additional error. A segmental approach thereby becomes superfluous and the stressed length and elastic elongation of the cable may be reduced to,

$$C = \int_0^{L_m} \sqrt{\left[1 + \left(\frac{dy}{dx} \right)^2 \right]} \, dx = \frac{L_m}{2\overline{\Psi}_p} \left[\overline{\Psi}_p \sqrt{1 + \frac{\overline{\Psi}_p^{\,2}}{4}} + 2\sinh\left(\frac{\overline{\Psi}_p}{2} \right) \right] \qquad (3.65)$$

and,

$$\Delta_e = \frac{H}{E_c A_c} \int_0^{L_m} \left[1 + \left(\frac{dy}{dx} \right)^2 \right] dx = \frac{HL_m}{E_c A_c} \left[1 + \frac{1}{12} \bar{\Psi}_p^{\,2} \right] \tag{3.66}$$

where,

$$\bar{\Psi}_p = \frac{(\omega_c + \omega_s)L_m}{H} = 8 \left(\frac{f}{L_m} \right)$$

Note that these are the same expressions derived previously in the section on stay cables (Equations (3.28) and (3.32)), except that the loading coefficient now includes the weight of the superstructure.

3.2.2 Deformation Characteristics

This section is focused on the response of fully-laden suspension cables to vehicular loading. In comparison to stay cables, the behaviour of fully-laden suspension cables is relatively complex. As such, unless otherwise stated, the following simplifications are made in order to limit the number of parameters involved:

- The weight of the hangers and the hanger assemblies is neglected relative to the combined weight of the suspension cable, ω_c, and superstructure, ω_s.

- Dead loads are considered to act uniformly along the projected length of the cable. It is, therefore, assumed that the error in the cable ordinates under dead load (see Section 3.2.1.3) is negligible in comparison to the cable deflection under live load.

- The effects of concentrated wheel loads are neglected and live load is idealized as a uniformly distributed load with magnitude, ω_p.

- Based on standard cable types applied in bridge engineering, an effective unit weight of 0.09MN/m^3, and a modulus of elasticity of 200GPa are assumed

Similar to the previous section, the cable area will also be sized under the condition that when the entire span is loaded with dead and live load (unfactored), the maximum stress in the cable equates to an allowable design stress of, $\sigma_{allow} = 800\text{MPa}$. When nonlinear effects are neglected, this results in the following function for the self-weight of the cable (Steinman, 1911),

$$\omega_c = \frac{\left(\omega_s + \omega_p \right) \xi \sqrt{1 + 16\, S_R^{\,2}}}{1 - \xi \sqrt{1 + 16\, S_R^{\,2}}} \tag{3.67}$$

where the parameter S_R represents the ratio of cable sag-to-span length $(f:L_m)$ and the dimensionless

parameter ξ is defined by,

$$\xi = \frac{\gamma_c \, L_m}{8 \, \sigma_{allow} \, S_R}$$

Using this criterion, for general values of ω_s and ω_p, Figure 3.19 shows how the self-weight of the cable varies with increasing span length.
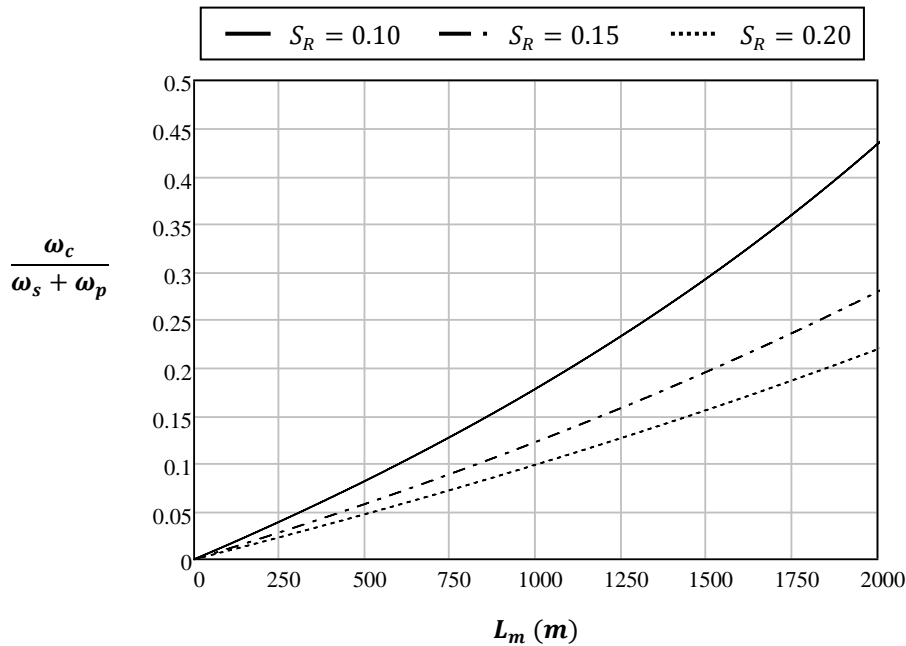
Figure 3.19: Variation of Cable Weight with Span Length in Fully-Laden Suspension Cables
Parameters: γ_c = 0.09MN/m³, σ_{allow} = 800MPa

In addition to the above simplifications, to avoid confusion, it is important to make the following distinctions:

> The term 'Live Load Scenario' will be used to describe a particular live load arrangement (i.e. the position of the load and the span length over with it acts). It is not meant to relate in any way to the magnitude of the applied loading. In that regard, the term 'Live Load Ratio' is used to describe the relative magnitude of the live load to that of the superstructure dead load ($\omega_p : \omega_s$).

> Moreover, the live load ratio may be factored or it may be unfactored. The two ratios must not be confused. Factoring the live load ratio simply implies a change in the magnitude of the applied loading without a corresponding change in the area of the cable (i.e. the properties of the applied loading have changed, whereas, the properties of the structure

remain unchanged). Conversely, a change in the unfactored live load ratio implies a change in the initial loading conditions and/or the properties of the structure.

To establish a reference case, in the following studies, the unfactored live load ratio is kept constant at a value of, $\omega_p : \omega_s = 0.6$. As mentioned previously, considering vehicular as opposed to rail or pedestrian traffic, this ratio represents more or less an upper bound value characteristic of a serviceability limit state for a bridge employing a lightweight steel superstructure. The cable sag is also kept constant at value of 10% of the cable span, which is within the narrow range conventionally employed in fully-laden suspension bridges.

The effects resulting from factoring the live load ratio are discussed in Section 3.2.2.5, and the effects resulting from changing the unfactored live load ratio are discussed in Section 3.2.2.6. In addition, variations in cable sag are addressed in Section 3.2.2.7.

3.2.2.1 General Response

The deflection of a suspension cable under a specific loading scenario may be solved in a similar manner to that of a stay cable though the general result is highly complex by comparison (Irvine, 1981; Pugsley, 1957). Ergo, by ensuring that equilibrium of forces is satisfied in the deformed state of the cable (under both dead and live load), and using the compatibility condition given by Equation (3.40), the maximum deflection of a fully-laden suspension cable was computed numerically for a variety of loaded positions, x_p, and loaded lengths, L_p. The results for a cable with a 1000m span are shown in Figure 3.20, where the position of the load is limited to,

$$\frac{L_p}{2} \leq x_p \leq L_m - \frac{L_p}{2}$$

Naturally, the recorded values of deflection will vary depending on the span of the cable; however, the general trend exhibited by Figure 3.20 will remain virtually unaffected. Thus, for all span lengths, given that the cable area is updated accordingly and the cable parameters are kept within reasonable and practical limits, the following general statements can be made:

1. As the loaded length increases, deflections in the cable will rise until a peak value is reached. Thereafter, any further increase in loaded length reduces deflections in the cable.

2. Regardless of the loaded length, the cable is most flexible when the centre of the load is placed asymmetrically with respect to the centre of the span. This becomes even more evident when Figure 3.20 is viewed from above in a 2D representation as shown in Figure 3.21.

Also, although not apparent from the figure, in nearly all cases the location of the maximum deflection along the length of the cable falls within close proximity to the center of the applied loading. Thus, deflections are greatest when the load is placed near the quarter points of the span.
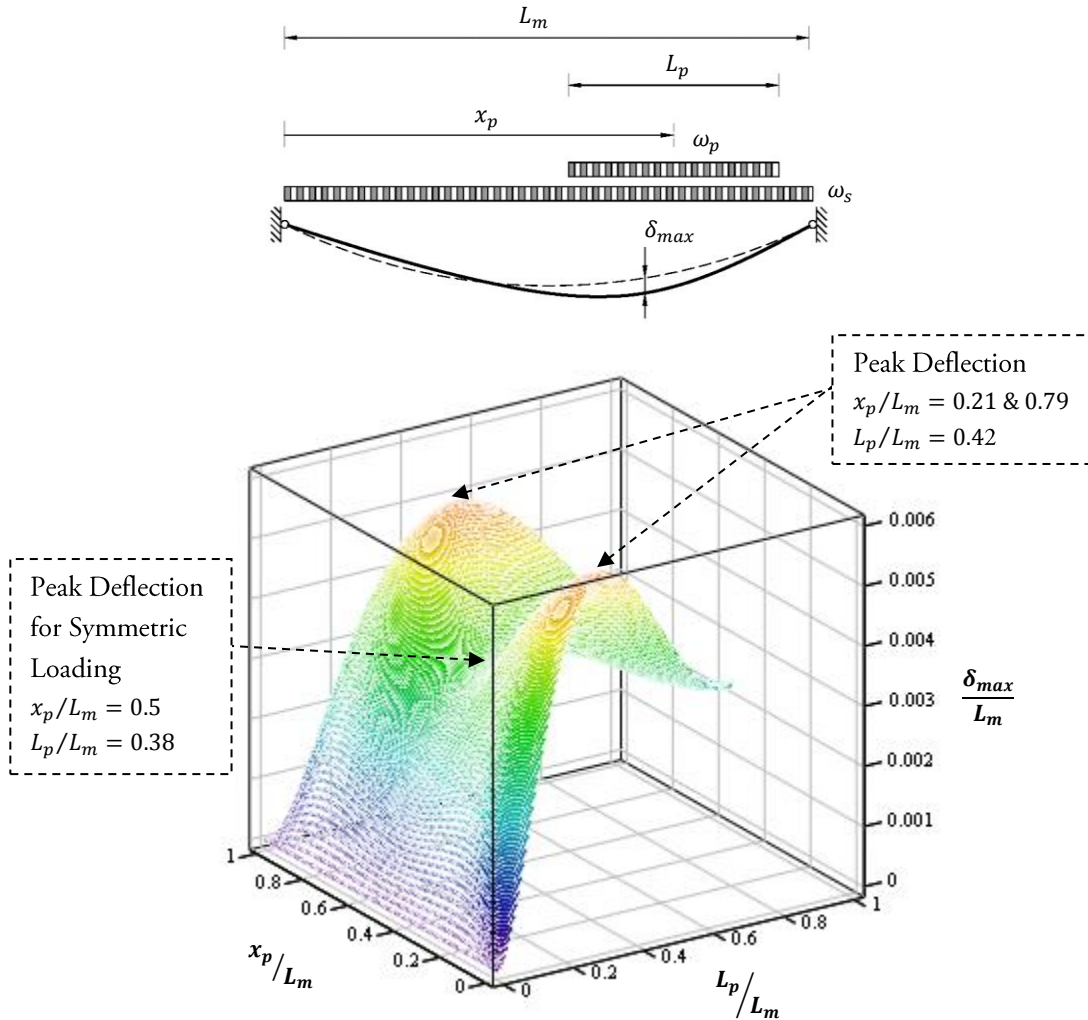
Figure 3.20: Max Deflection of Fully-Laden Suspension Cable under Live Load
Parameters: L_m = 1000m, γ_c = 0.09MN/m³, E_c = 200GPa, σ_{allow} = 800MPa, ω_p = 0.6·ω_s, S_R = 0.1

This behaviour is opposite to that which would be expected in a simple beam bridge and the cause for the distinction can be attributed to the presence of strain-free deformations. Indicative from the above observations, strain-free deformations vary in scale depending on the loaded position and loaded length. Moreover, as shall be explained later, strain-free deformations are affected by the relative magnitude of the tensile forces in the cable. As such, varying either the dead or the live load

forces can have a notable impact on the response of suspension cables, including the values of peak deflection and the corresponding loading scenarios to which they are associated. It is important to note though that the response of a suspension cable will not be impacted when the forces are varied in proportion to one another such that the unfactored live load ratio and the cable dead load-to-superstructure dead load ratio remain constant.
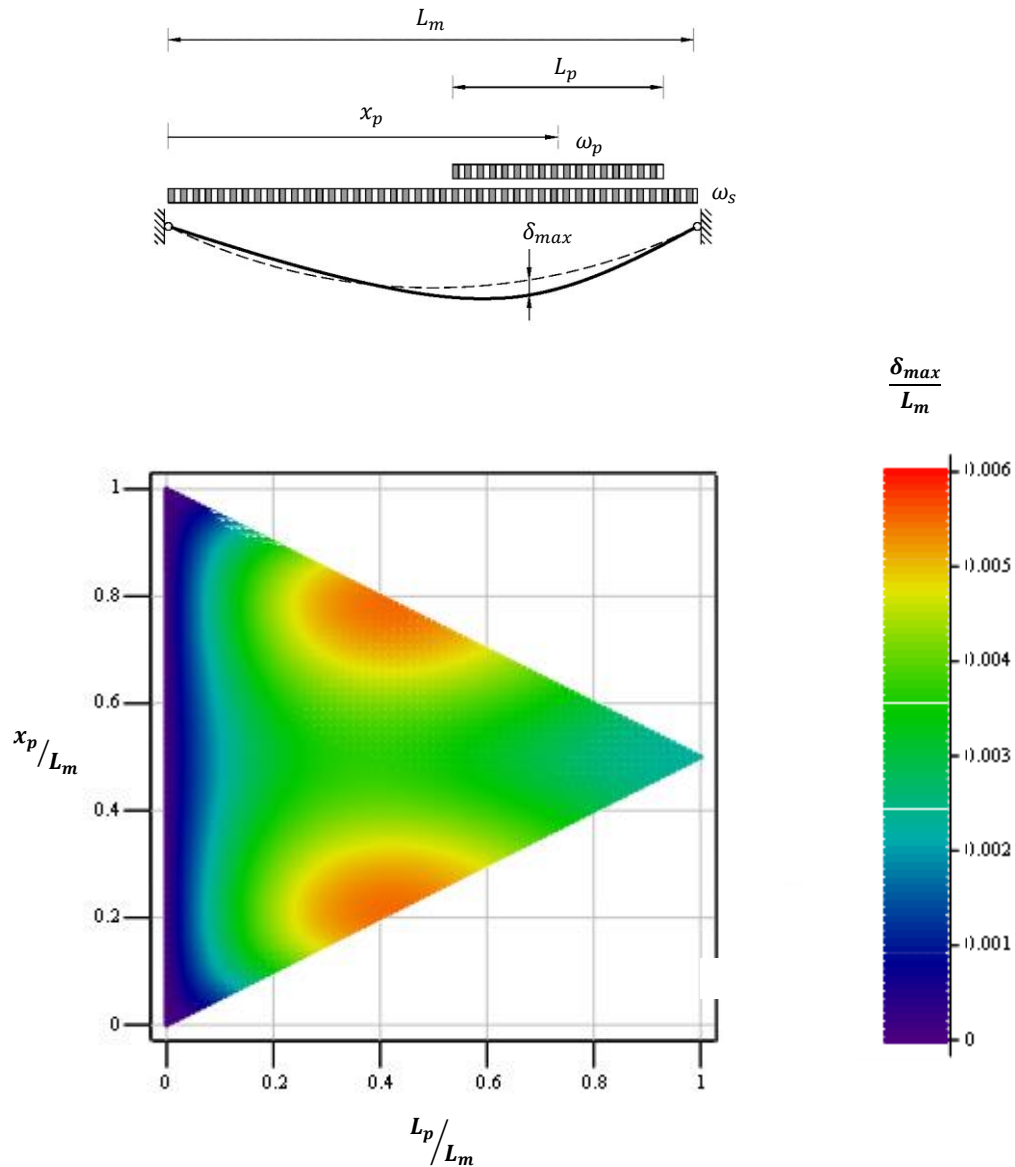
Figure 3.21: 2D Representation of Figure 3.20
Parameters: L_m = 1000m, γ_c = 0.09MN/m³, E_c = 200GPa, σ_{allow} = 800MPa, ω_p = 0.6·ω_s, S_R = 0.1

3.2.2.2   Strain-free Versus Elastic Deformations

Strain-free deformations were first introduced in Section 3.1.2 in relation to stay cables. Although strain-free and elastic deformations are interrelated, the coupling effect between the two is typically inconsequential when infinitesimal strain theory applies. Therefore, strain-free deformation can often be considered a separate phenomenon and characterized as deformation which would otherwise occur in an inextensible or axially stiff cable. Notwithstanding, due to the geometry of suspension cables and the particular manner in which they are loaded, for certain loading scenarios, the role strain-free deformations play in the deflection of suspension cables is much more pronounced relative to stay cables. To illustrate this point, for each value of deflection recorded in Figure 3.20, Figure 3.22 compares the corresponding deflection in an equivalently loaded suspension cable with infinite axial stiffness. Deflections in the axially stiff cable are denoted as, δ_{sf}.

In comparison to Figure 3.20, the horizontal axes in Figure 3.22 have been reversed for clarity. With this in mind, it can be seen that strain-free deformations represent almost 90% of the overall deflection for the loading scenario causing the peak deflection and, in general, represent a large proportion of the overall deflection when the loaded length is small in comparison to the span length of the cable. This is because in order to maintain equilibrium when only a portion of the span is loaded with live load, the deformed shape of the cable must deviate from its dead load state to reflect the altered configuration of the applied loading, and for this to occur, the cable geometry must change accordingly. Moreover, asymmetric loading causes the cable to drift longitudinally in the direction of the load thus permitting additional vertical displacement due to the geometric straightening of the unloaded portion of cable. In contrast, when the entire span is loaded with live load the overall configuration of the load is the same in comparison to the cable's dead load state even though the total load acting on the cable has changed. Consequently, the deformed state of the cable follows roughly the same general parabolic form as it did prior to the application of live load and strain-free deformations become virtually non-existent. At the same time, elastic deformation is proportional to the stress in the cable which increases with increasing loaded length and is greatest when the load is positioned symmetrically.

In connection with the observations made in Section 3.2.2.1, the values in Figure 3.22 do not vary greatly with changes in span length and with small variations in material cable parameters. Interestingly, the values are also virtually unaffected by practical changes in the unfactored live load ratio (assuming the cable area is updated accordingly). However, this is not to say that the absolute amount of deformation (and absolute amount of strain free deformation) will remain unaffected when the unfactored live load ratio is altered.
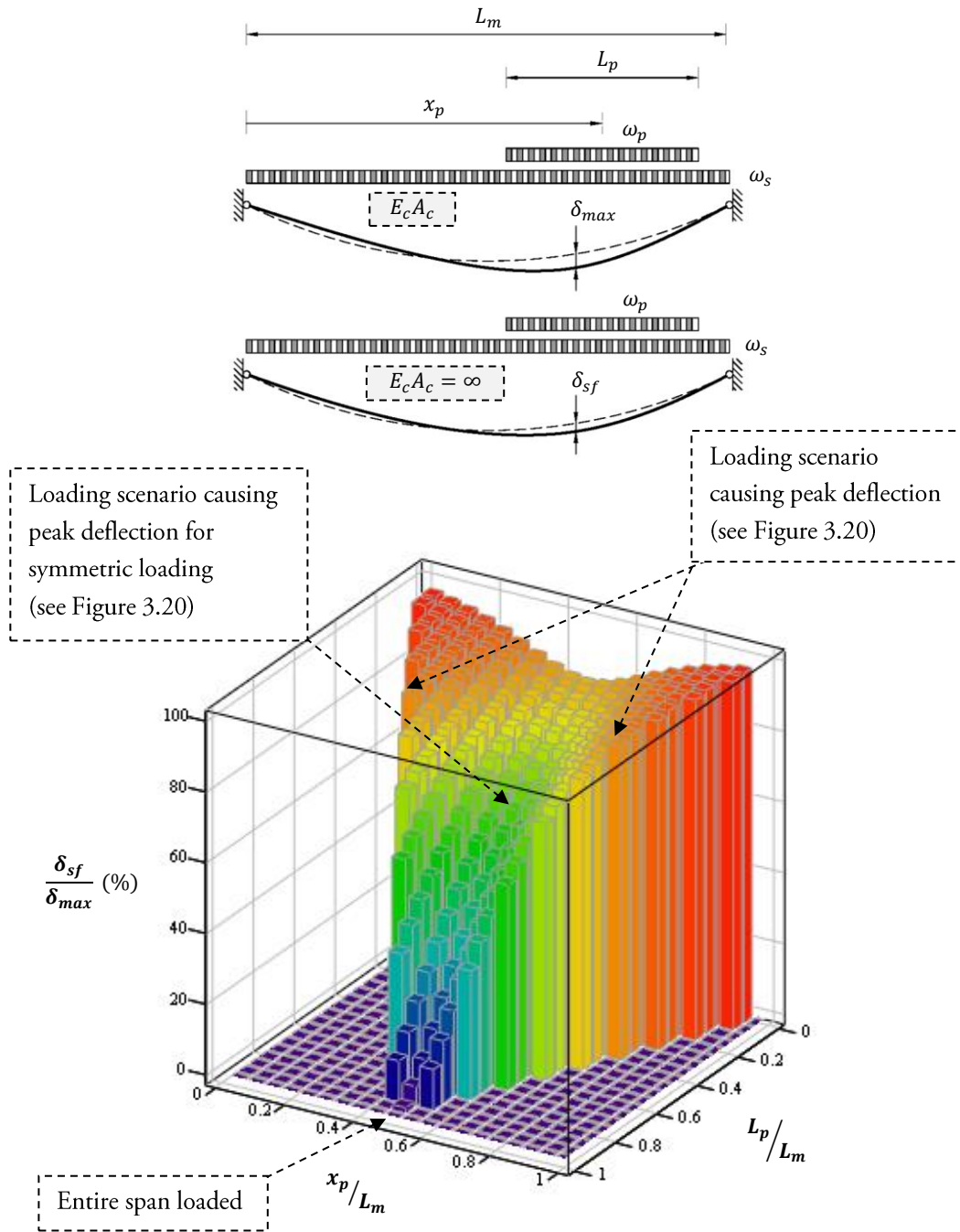
Figure 3.22: Strain-free Deformations in Fully-Laden Suspension Cable under Live Load
Parameters: L_m = 1000m, γ_c = 0.09MN/m³, E_c = 200GPa, σ_{allow} = 800MPa, ω_p = 0.6·ω_s, S_R = 0.1

3.2.2.3   The Stabilizing Effect of Dead Load

Analogous to the amplifying effect large axial compressive forces have on the deflection of slender columns (often referred to in literature as 'the p-delta effect'), the presence of large axial tensile forces causes a reverse 'tension stiffening' effect to occur in suspension cables. Thus the higher the dead load tension is in the cable and the greater the deflection, the higher is the tendency for the cable to restore its dead load shape when acted upon by live load. This is clearly demonstrated in Figure 3.23 which shows the stabilizing effect dead load can have on live load deflections when the dead load of the superstructure is increased by a factor of 2.0. It should be noted that in both cases in Figure 3.23 the area of the cable is kept constant in order to provide a fair comparison though increasing the dead load of the cable has a similar stabilizing effect.

By comparing the relative deflections of the two cables when the loaded length approaches the span length of the cables, it can be seen from Figure 3.23 that deflections arising predominately as a result of elastic deformations are not greatly impacted. This is because, provided displacements are relatively small, increasing the dead load tension in the cable does not significantly alter the magnitude of added stress in the cable due to live load and, therefore, the difference in the total strain of the two cables is marginal. On the other hand, deflections in cases involving a relatively greater degree of strain-free deformations are substantially reduced.

Being cognizant of the stabilizing effect of dead load is very important from a theoretical standpoint during design. For example, if the dead load of the bridge is conservatively increased during analysis through means of a fictitious load factor then the stiffness of the cable system will also be artificially increased which will in turn result in an under-estimation of the global demands on the superstructure. As another consideration, designing a suspension bridge to be extremely lightweight in order to minimize structural quantities can, if not properly detailed, result in a bridge which is exceedingly flexible; the consequences of which could impact both the static and aerodynamic performance of the bridge.

Increasing dead load for the sole purpose of increasing stiffness is also not an efficient or practical measure considering the added material costs which will be incurred, not to mention the ramifications with regards to seismic demands. Rather, a similar stiffening effect may be alternatively achieved by providing an external means of restraint which limits strain-free deformations in the cable. For example, if the superstructure is restrained longitudinally (as opposed to using a floating system) then providing a rigid connection between the suspension cables and superstructure at mid-span prevents the cable from drifting longitudinally, and as a result, live load deflections induced from asymmetric loading can be significantly reduced.
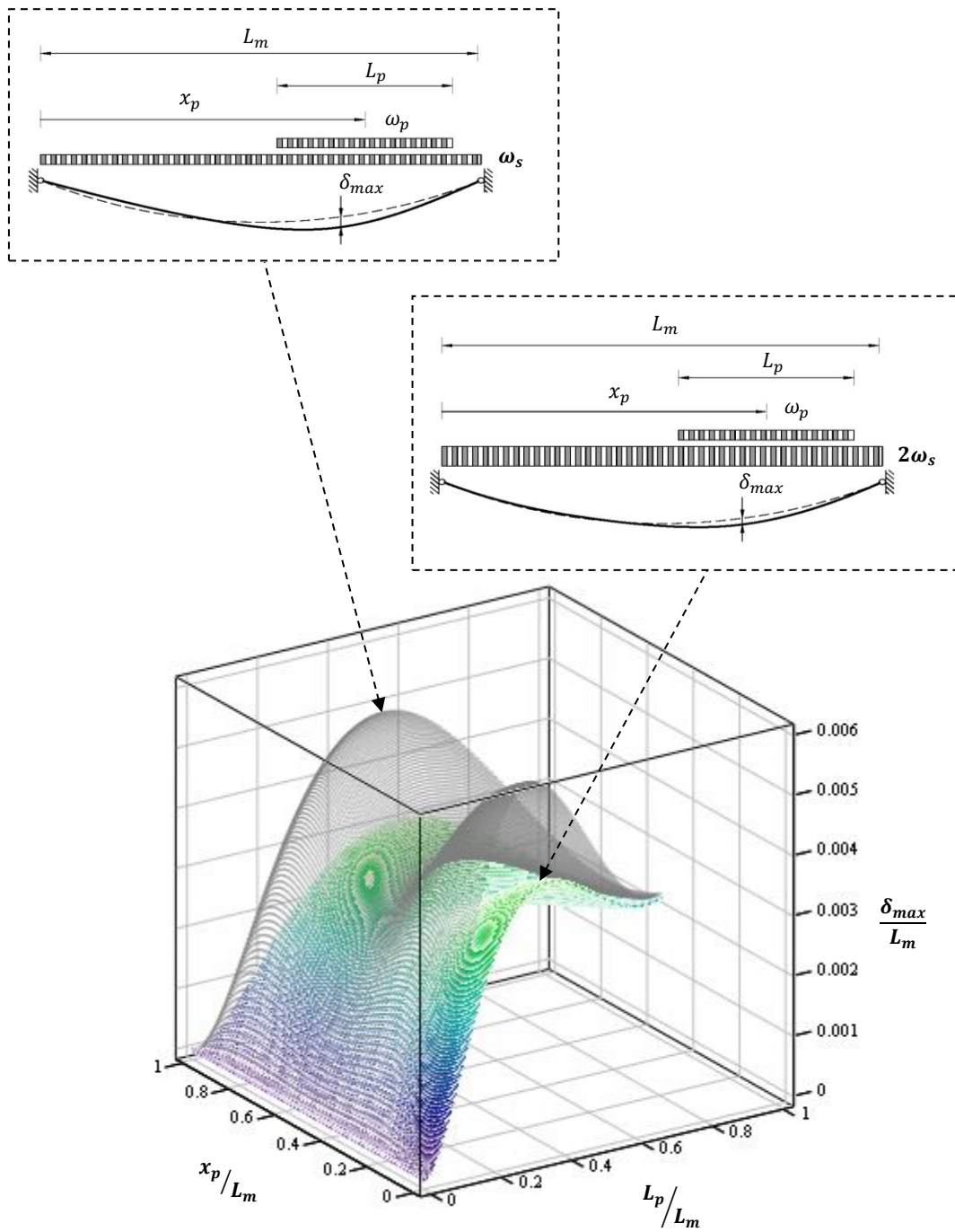
Figure 3.23: Stabilizing Effect of Dead Load on the Deflection of Fully-Laden Suspension Cables
Parameters: L_m = 1000m, γ_c = 0.09MN/m³, E_c = 200GPa, σ_{allow} = 800MPa, ω_p = 0.6·ω_s, S_R = 0.1

As an added note, prior to theoretical advancements in the field of bridge aerodynamics and the adoption of streamlined sections, centrally placed rigid cable connections were used extensively in the decades following 1940 due to their added function in impeding the aerodynamically unstable asymmetric torsional mode of vibration which ultimately led to the notorious collapse of the first Tacoma Narrows Bridge[1]. In this respect, it is not a requirement that the superstructure be longitudinally restrained since asymmetric torsion motion has the propensity in a suspension bridge with two vertical planes of cables to cause each cable to drift longitudinally in opposite directions. When the cables are fixed to the superstructure such movement is inhibited by the deck which acts as a large diaphragm.

Other measures which have been used in the past to vertically stiffen fully-laden suspension bridges include:

- Providing supplementary stays above and/or below deck (examples include the Thousand Islands Bridge, the Deer Isle Bridge, and the Beauharnois Bridge).

  In contrast to hybrid cable bridges wherein the stays and suspension cables act in unison, the stays in this case are of limited number and are only designed to augment the response of the bridge to certain loading scenarios. As such, above deck supplementary stays are typically attached from the towers to either the suspension cables or the stiffening girder near the quarter points of the span where the flexibility is greatest.

  Attaching to the suspension cables introduces localized bending forces in the cables thereby limiting the magnitude of the forces which can be applied. Moreover, unless the superstructure is continuous and is supported in a manner which allows it to act as a rigid strut, unbalanced horizontal forces in the stays must be resisted by the tower legs. Consequently, the strays will not be greatly effective unless an adequately stiff tower section is provided. When the stays are attached to the superstructure a similar problem exists in that unless straight backstays are present (i.e. the side spans of the bridge are not suspended), unbalanced horizontal forces must be resisted by the stiffening girder/truss and/or the towers.

---

[1] *Due to concerns over aerodynamic stability, prior to the opening of the first Tacoma Narrows Bridge, a connection was established at mid-span between the suspension cables and superstructure via a set of inclined cable ties. However, the cable ties were not adequately designed, and as a result, the connection failed under high amplitude cyclic loading. Torsional motion which had previously been non-existent started to develop almost immediately following the failure and approximately one hour later a significant portion of the bridge collapsed.* (Ammann, et al., 1941)

The Thousand Islands Bridge shown in Figure 3.24 exemplifies both types of above deck supplementary stays. Generally, below deck supplementary stays are not desirable as they act to decrease the available clearance envelope for vehicular/navigational traffic running underneath the bridge.

Figure 3.24: The Thousand Islands Bridge (1938)
[CC BY-SA 3.0 (http://creativecommons.org/licenses/by-sa/3.0)], via Wikimedia Commons

▪ Installing a system of diagonal hangers (for more information see Section 5.1.2); and

▪ Increasing the depth of the stiffening girders or trusses.

Unlike an unstiffened cable, the superstructure has a natural proclivity for resisting asymmetric loading. In fully-laden suspension bridges, the superstructure and the suspension cables form a competing system wherein loads are distributed between the two according to their relative stiffness. In simplest terms, the system may be idealized as that shown in Figure 3.25 (note: in this idealization, the elastic elongation of the hangers is neglected).
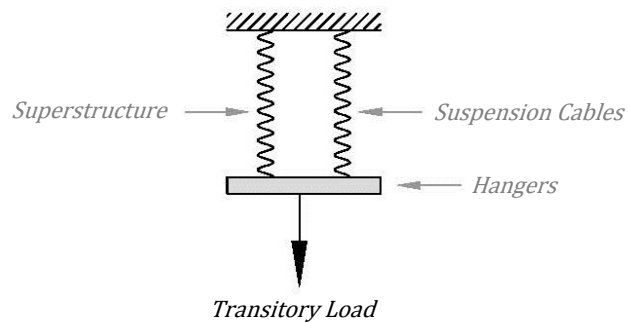
Figure 3.25: Idealization of Superstructure-Cable System

From Figure 3.25 it is clear that the superstructure will take on less force as its stiffness (i.e. its depth) is decreased, and vice versa. Therefore, assuming no strict deflection criterion

must be met, the superstructure can theoretically be designed with negligible stiffness. This same conclusion was mathematically proven in the late 19th century with the introduction of the deflection theory.

In contrast to its predecessors, the deflection theory accounted for the change in shape of the cable under transitory loads and its effect on stress distribution, and thus provided an entirely new basis for the static design of suspension bridges (Buonopane & Billington, 1993). However, it was only after the failure of the first Tacoma Narrows Bridge in 1940 that the engineering profession as a whole grasped the need to account for not just the static behaviour of the bridge but also the dynamic behaviour, and also the importance of providing a superstructure with ample measures of vertical, torsional, and lateral stiffness.

The question as to how much stiffness is required is still being investigated and depends greatly on the details of the design concept along with the static and dynamic characteristics of the applied loading. Figure 3.26 shows the proportions of some major earth-anchored suspension bridges built from 1940 onwards (the first Tacoma Narrows Bridge is also included in the figure for reference). It should be noted though that bridges with exceedingly large ratios generally contain additional features to aid in their aerodynamic performance such as streamlined sections, central stabilizers, air gaps, and/or guide vanes.

As the moments in the stiffening girder/truss are a function of its stiffness, it is also important to recognize from Figure 3.25 that contrary to simple beam bridges, the depth of the stiffening girder/truss should not be increased for the sole purpose of reducing cross-sectional stresses in the girder/truss. The vertical stiffness in a girder/truss increases with the square of the depth; therefore, a notable increase in depth will trigger an iterative cycle which will result in the need for the superstructure to become progressively deeper. In contrast, the vertical stiffness in a girder/truss is approximately proportional to the cross sectional area of its components and, therefore, a more efficient solution can be obtained by simply increasing the area of the overstress components.
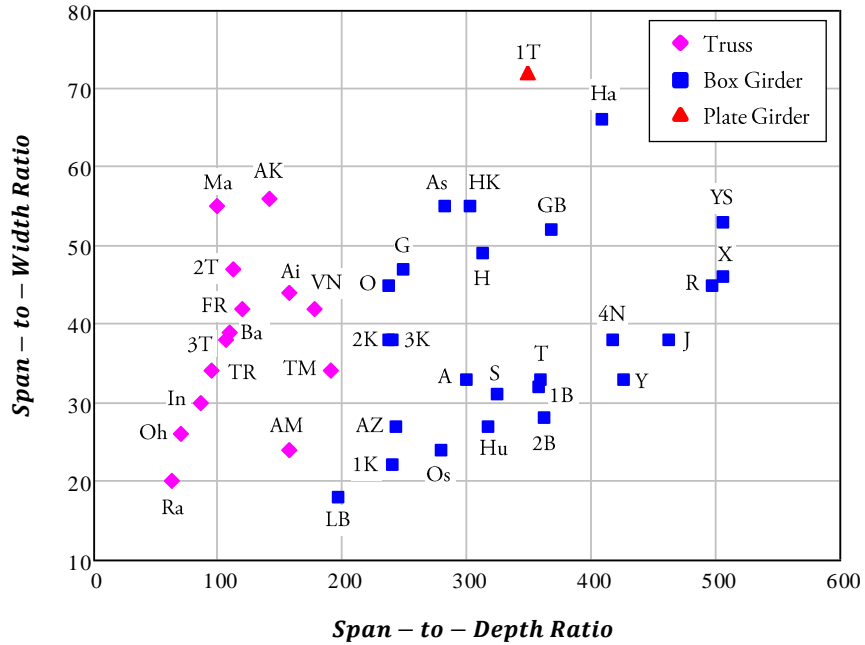
Figure 3.26: Superstructure Proportions for Major EA Suspension Bridges
*Data compiled from a multitude of sources

Legend (Alphabetical): AM – A. Murray MacKay (1970); Ai – Aizhai (2012); AK – Akashi-Kaikyo (1998); A – Akinada (1999); AZ – A. Zampa (2003); As – Askoy (2013); Ba – Baling (2009); 1B – First Bosphorus (1973); 2B – Second Bosphorus (1988); FR – Forth Road (1964); 4N – Fourth Nanjing Yangtze (2012); G – Gjemnessund (1992); GB – Great Belt East (1998); Ha – Hardanger (2013); HK – Hoga Kusten (1997); Hu – Huangpu (2008); H – Humber (1981); In – Innoshima (1983); J – Jiangyin (1999); 1K – First Kurushima (1999); 2K – Second Kurushima (1999); 3K – Third Kurushima (1999); LB – Little Belt (1970); Ma – Mackinac (1957); Oh – Ohnaruto (1984); Os – Ohshima (1988); O – Osteroy (1997); Ra – Rainbow (1993); R – Runyang (2005); S – Severn (1966); 1T – First Tacoma Narrows (1940); 2T – Second Tacoma Narrows (1950); 3T – Third Tacoma Narrows (2007); TR – Tagus River (1966); T – Taizhou (2012); TM – Tsing Ma (1997); VN – Verrazano-Narrows (1964); X – Xihoumen (2009); Y – Yangluo (2007); YS – Yi Sun-shin (2012)

3.2.2.4 Scale Effects

This section examines how the values of maximum deflection, recorded in Figure 3.20, vary with span length when the unfactored live load ratio is held constant. However, instead of studying a multitude of different loading scenarios as was done previously, the effect of span length is instead considered more generally in relation to strain-free and elastic deformations. Accordingly, based on prior observations, only three core loading scenarios are examined: one wherein the maximum deflection is characterized almost entirely by elastic deformations, one wherein the maximum deflection is characterized near evenly by elastic and strain-free deformations, and one wherein the maximum deflection is characterized primarily by strain-free deformations. Respectively, these loading scenarios are as follows:

❖ **Loading Scenario 1 (LS1):** The entire span is loaded with live load.

❖ **Loading Scenario 2 (LS2):** Forty percent of the span is loaded with live load and the load is positioned symmetrically with respect to the centre of the span (this loading scenario is very near to that which causes the peak deflection for symmetric loading – Figure 3.20).

❖ **Loading Scenario 3 (LS3):** Forty percent of the span is loaded with live load and the load is positioned asymmetrically at the far end of the span (this loading scenario is very near to that which causes the peak deflection – see Figure 3.20).

Figure 3.27 shows that for each of the loading scenarios, as the span length is increased, the ratio of maximum deflection-to-span length actually decreases near linearly in scale. This may at first seem counterintuitive; however, the negative trend in the graph can be explained by re-examining Figure 3.19. Based on the cable sizing criteria specified at the beginning of Section 3.2.2, the relationship between the cable area and span length is nonlinear on account that as the span length is increased, an increasingly higher percentage of the cable's load carrying capacity has to be reserved for supporting its own self-weight. As a result, the relative increase in cable area affects the magnitude of elastic deformations (characterized via Loading Scenario 1), and the corresponding relative increase in cable dead load aids in stabilizing the cable against strain-free deformations (characterized via Loading Scenario 3).

As the slope of Loading Scenario 3 is greater than that of Loading Scenario 1, it can also be concluded from Figure 3.27 that scale effects have a greater influence on strain-free deformations relative to elastic deformations. Also, as expected and confirmed by the slope of Loading Scenario 2, the influence that span length has on any given loading scenario may be gauged with respect to the relative contribution strain-free and elastic deformations have on the maximum deflection in the cable.
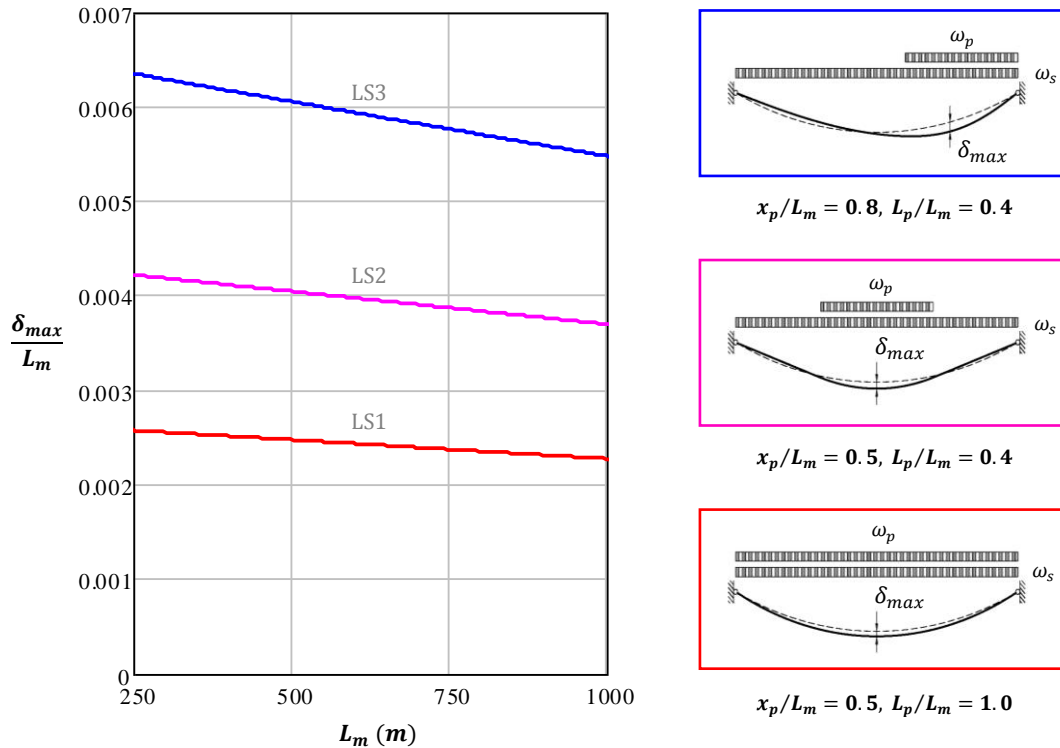
Figure 3.27: Scale Effects on the Deflection of Fully-Laden Suspension Cables
Parameters: γ_c = 0.09MN/m³, E_c = 200GPa, σ_{allow} = 800MPa, ω_p = 0.6·ω_s, S_R = 0.1

3.2.2.5   The Relationship between Load and Deformation

The effects of different loading scenarios were examined in previous sections, and in order to remain consistent, the magnitude of the live load has thus far been assumed constant. Still, it was demonstrated that when the magnitude of the dead load is increased, an added 'tension stiffening' effect is created which acts to mitigate deflections induced from strain-free deformations. As this 'tension stiffening' effect acts relative to the total magnitude of tensile forces within the cable, an added degree of stiffness is also exhibited when the reverse situation is encountered – the magnitude of the live load is increased whilst the magnitude of the dead load is kept constant. As such, similar to stay cables, the presence of strain-free deformations in suspension cables causes nonlinearity in the relationship between load and deflection. As the magnitude of live load acting on a suspension cable may vary significantly over time, this section examines the effects of nonlinearity in fully-laden suspension cables, particularly at the extremes when the magnitude of live load is factored well beyond its standard operating level.

Using the same core loading scenarios presented in Section 3.2.2.4, the corresponding maximum deflections in a cable with a 1000 metre span were computed for live load factors ranging from, α_p = 0 to 2.0. The solid lines in Figure 3.28 represent the result plots, and for comparison, a series of linearly varying dashed lines have also been drawn tangent to the result plots at, $\alpha_p \approx 0$.
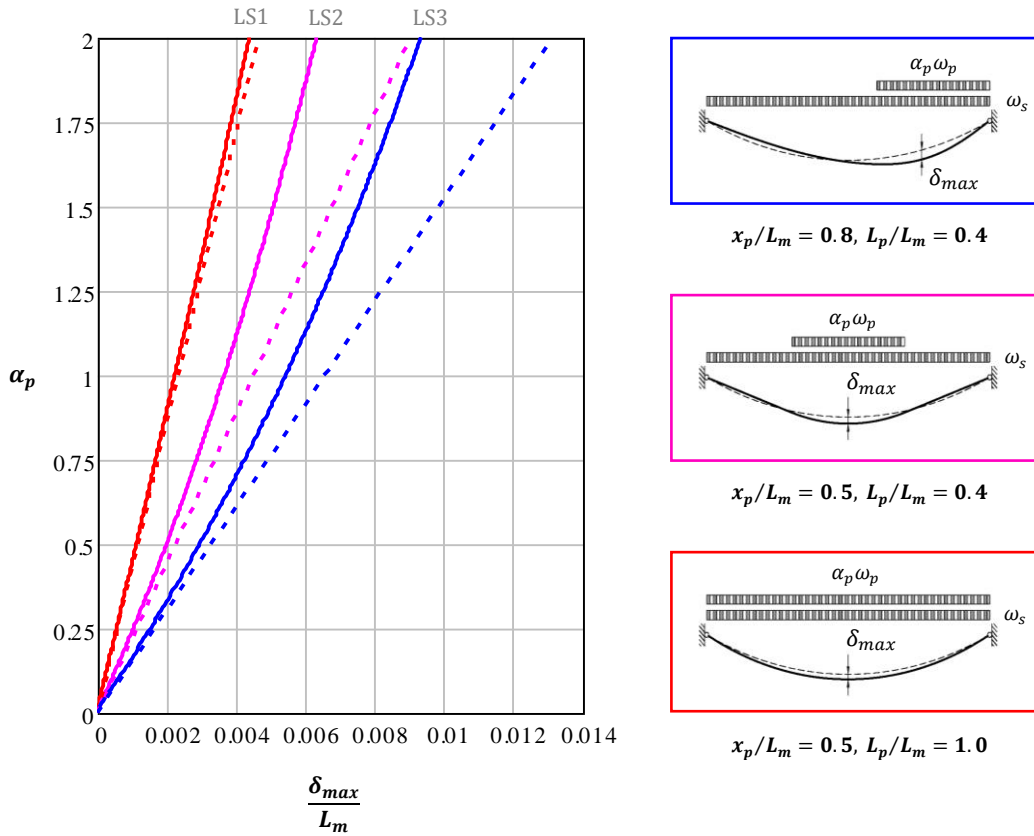
Figure 3.28: Nonlinearity in the Deflection of Fully-Laden Suspension Cables
Parameters: L_m = 1000m, γ_c = 0.09MN/m³, E_c = 200GPa, σ_{allow} = 800MPa, S_R = 0.1, ω_p = 0.6·ω_s

Comparing the dashed and the solid lines, Figure 3.28 shows that when strain-free deformations are present (i.e. Loading Scenarios 2 & 3), even at service level loads (i.e. $\alpha_p = 1$) the effects of nonlinearity are considerable. On the other hand, as expected, Figure 3.28 confirms that nonlinear effects are relatively minor under service loads for loading scenarios producing little to no strain-free deformations (i.e. Loading Scenario 1); however, the same statement is not necessarily valid for higher magnitudes of live load, which are characteristic of extreme loading events. In such cases, as the magnitude of the live load increases, elastic deformations start to cause noteworthy changes in the

shape of the cable profile which in turn affects the internal forces within the cable. The resulting nonlinear behaviour is, therefore, caused by a different, albeit interrelated source of nonlinearity commonly referred to as the 'large displacement effect'. As the tension stiffening effect and the large displacement effect both derive from geometric changes in the cable profile, the two are often grouped together in literature under a broader classification as geometric nonlinearities.

It is also of note that due to the effect of strain-free deformations, the loading scenarios causing the peak asymmetric and symmetric deflections can be expected to vary slightly depending on the load factor applied. As a general guideline, it was observed in these studies that as the live load factor increases, the loaded length causing the peak loading scenario decreases, whereas, the opposite occurs when the live load factor decreases. In most cases though, this variation is so slight that it is of minor practical relevance. As an example, from Figure 3.20 the peak loading scenario for a load factor of 1.0 was recorded when the loaded length covered 42% of the span. For a load factor of 2.0, the loaded length causing the peak loading scenario decreased to only 40% of the span length.

As nonlinear systems preclude the use of superposition and on that account, also the use of a first order influence analysis, analyzing a suspension cable under all possible loading scenarios and load factors whilst precisely capturing nonlinear effects is highly onerous. This may however be circumvented in a similar manner to stay cables by using a linear approximation which essentially produces results equivalent to the dashed lines in Figure 3.28. Such an approximation may be contrived by using the stiffness of the suspension cable in its dead load state for any and all additional loading (more on this in Section 3.2.2.8). In essence, determining deflections in this manner is in many ways analogous to using the tangent stiffness method for stay cables. The error associated with using this second order linearized approach is illustrated in Figure 3.29, where $\delta_{max}{}^{SO}$ is used to denote the approximate maximum deflection obtained using the second order approach.

Figure 3.29 clearly shows that Loading Scenario 2 produces an even greater degree of nonlinearity in comparison to Loading Scenario 3. This is because, as mentioned previously, nonlinear effects are not only affected by the relative contribution that strain-free deformations have on total deflections but also by the magnitude of added live load tension imparted to the cable; the latter being greater when the load is placed symmetrically about the centerline of the cable span. In addition, due to scale effects which were covered in Section 3.2.2.4, Figure 3.29 also shows that nonlinear effects are reduced in a nearly linear trend as the span length of the cable is increased.
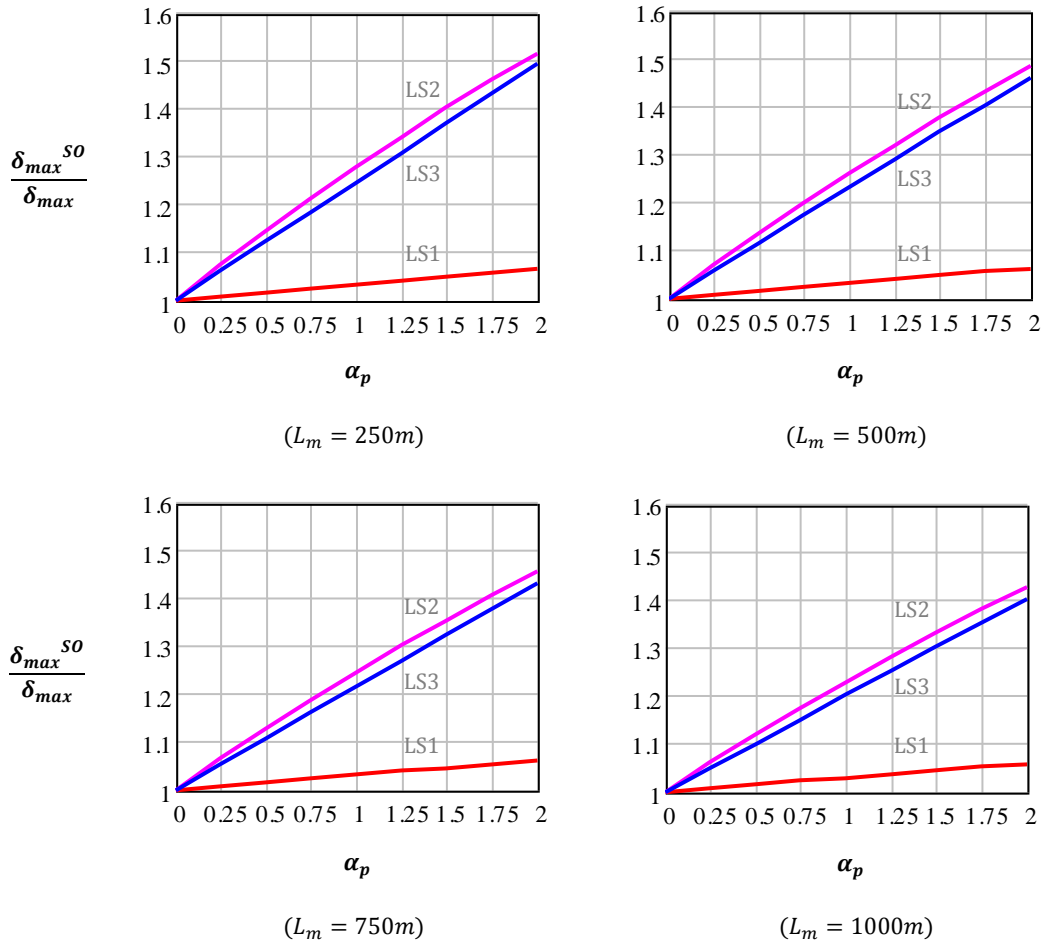
Figure 3.29: Nonlinear Effects in Fully-Laden Suspension Cables with Increasing Live Load Intensity
Parameters: $\gamma_c = 0.09 \text{MN/m}^3$, $E_c = 200 \text{GPa}$, $\sigma_{allow} = 800 \text{MPa}$, $S_R = 0.1$, $\omega_p = 0.6 \cdot \omega_s$

3.2.2.6 Changes in the Unfactored Live Load Ratio

The unfactored live load ratio may markedly decrease if concrete is used in the place of steel for the superstructure or deck. For instance, a typical live load ratio for an all concrete bridge carrying vehicular traffic is 0.2, which is three times lower than the value assumed for a conventional bridge composed of steel. As indicated by the study presented in Section 3.2.2.3, variations in live load ratio affect the absolute amount of elastic and strain-free deformations. However, in any case, similar response characteristics will be exhibited because the amount of elastic/strain-free deformation, relative to the total amount of deformation, remains virtually unaffected. Therefore, rather than reiterating many of the graphs already presented, using the results from previous studies, a general

method will be presented here which allows for the prediction of the response of a cable whose unfactored live load ratio differs from that previously assumed.

Based on fundamental material mechanics, it stands to reason that the amount of elastic deformation in a cable depends on the live load cable force-to-cable area ratio, which in this case, can also be expressed as the ratio of live load-to-cable self-weight, $\omega_p : \omega_c$. Based on prior observations it also stands to reason that the amount of strain-free deformation depends on the ratio of live load-to-total cable load, $\omega_p : (\omega_c + \omega_s + \omega_p)$. Hence, the greater these ratios, the greater the respective deformation will be.

Examining first the relative amount of elastic deformation, from Equation (3.67), the self-weight of the cable can be described by the following relationship,

$$\omega_c = \omega_s \left(1 + \omega_R\right) \cdot K \tag{3.68}$$

where, ω_R represents the unfactored live load ratio $(\omega_p : \omega_s)$, and given a fixed set of material and geometric parameters, K represents a non-dimensional constant whose magnitude is given by,

$$K = \frac{\xi \sqrt{1 + 16\, S_R{}^2}}{1 - \xi \sqrt{1 + 16\, S_R{}^2}} \qquad \text{where,} \qquad \xi = \frac{\gamma_c\, L_m}{8\, \sigma_{allow}\, S_R}$$

Inverting and multiplying both sides by, ω_p ,then gives,

$$\frac{\omega_p}{\omega_c} = \frac{\omega_R}{(1 + \omega_R) \cdot K} \tag{3.69}$$

The amount of deflection arising from elastic deformation in two cables with equal geometric and material parameters, but different unfactored live load ratios, should thus be approximately related via the expression,

$$\frac{\delta_{e_2}}{\delta_{e_1}} \cong \left(\frac{\omega_{R2}}{1 + \omega_{R2}}\right)\left(\frac{1 + \omega_{R1}}{\omega_{R1}}\right) \tag{3.70}$$

where, δ_{e_1} and δ_{e_2} are used to represent the elastic deformation in cables 1 and 2, respectively. Similarly, with use of Equation (3.68), the ratio of live load-to-total cable load may be written as,

$$\frac{\omega_p}{\omega_c + \omega_s + \omega_p} = \frac{\omega_R}{(1 + \omega_R)(K + 1)} \tag{3.71}$$

and the relative amount of deflection arising from strain-free deformation in the two cables should be approximately related, again, via the expression,

$$\frac{\delta_{sf_2}}{\delta_{sf_1}} \cong \left(\frac{\omega_{R2}}{1 + \omega_{R2}}\right)\left(\frac{1 + \omega_{R1}}{\omega_{R1}}\right) \tag{3.72}$$

This leads to the conclusion that when the unfactored live load ratio is varied, the amount of strain-free deformation changes at a similar rate to the amount of elastic deformation (it should be noted that this is not apparent in Figure 3.23 because, in that case, the cable area was kept constant in order to clearly illustrate the stabilizing effect of dead load). Since the total deflection of the two cables is related by,

$$\frac{\delta_{max_2}}{\delta_{max_1}} = \frac{\delta_{sf_2} + \delta_{e_2}}{\delta_{sf_1} + \delta_{e_1}} \tag{3.73}$$

substituting in Equations (3.70) and (3.72) gives,

$$\frac{\delta_{max_2}}{\delta_{max_1}} \cong \frac{\delta_{sf_2}}{\delta_{sf_1}} \cong \frac{\delta_{e_2}}{\delta_{e_1}} \cong \left(\frac{\omega_{R2}}{1 + \omega_{R2}}\right)\left(\frac{1 + \omega_{R1}}{\omega_{R1}}\right) \tag{3.74}$$

This helps explain why the amount of elastic/strain free deformation, relative to the total amount of deformation, remains constant with changes in the unfactored live load ratio. Clearly though, the problem is more complex because the precise value of the ratio ($\delta_{max} : \delta_{sf}$) will also depend on the loading scenario. The loading scenario in turn is characterised by the loaded position (x_p) and the loaded length (L_p) of the applied live load. Nevertheless, when carrying out this study it was found that Equation (3.74) can be utilized to provide a reasonable approximation of the change in the peak deflection. For validation, Figure 3.30 compares the results from nonlinear numerical computations (given by the dashed lines) to the values computed from Equation (3.74) (given as the solid lines) for Loading Scenario 3 ($x_p = 0.5 \cdot L_m$, $L_p = 0.4 \cdot L_m$).

A series of additional nonlinear numerical computations were also carried out in order to study the applicability of Equation (3.74) to other loading scenarios. Generally, it was found that the accuracy of Equation (3.74) improved further when the loaded length was increased to values greater than 40% of the span length (for symmetric and asymmetric loading). Conversely, the accuracy of Equation (3.74) fell sharply when the loaded length was decreased to values lower than 40% of the span length. In any case, Equation (3.74) should only be used for preliminary design purposes in order to obtain a rough estimate in regard to how changes in the unfactored live load ratio may impact the amount of deflection exhibit by a given cable.

(Relative Elastic Deformation)   (Relative Strain-free Deformation)
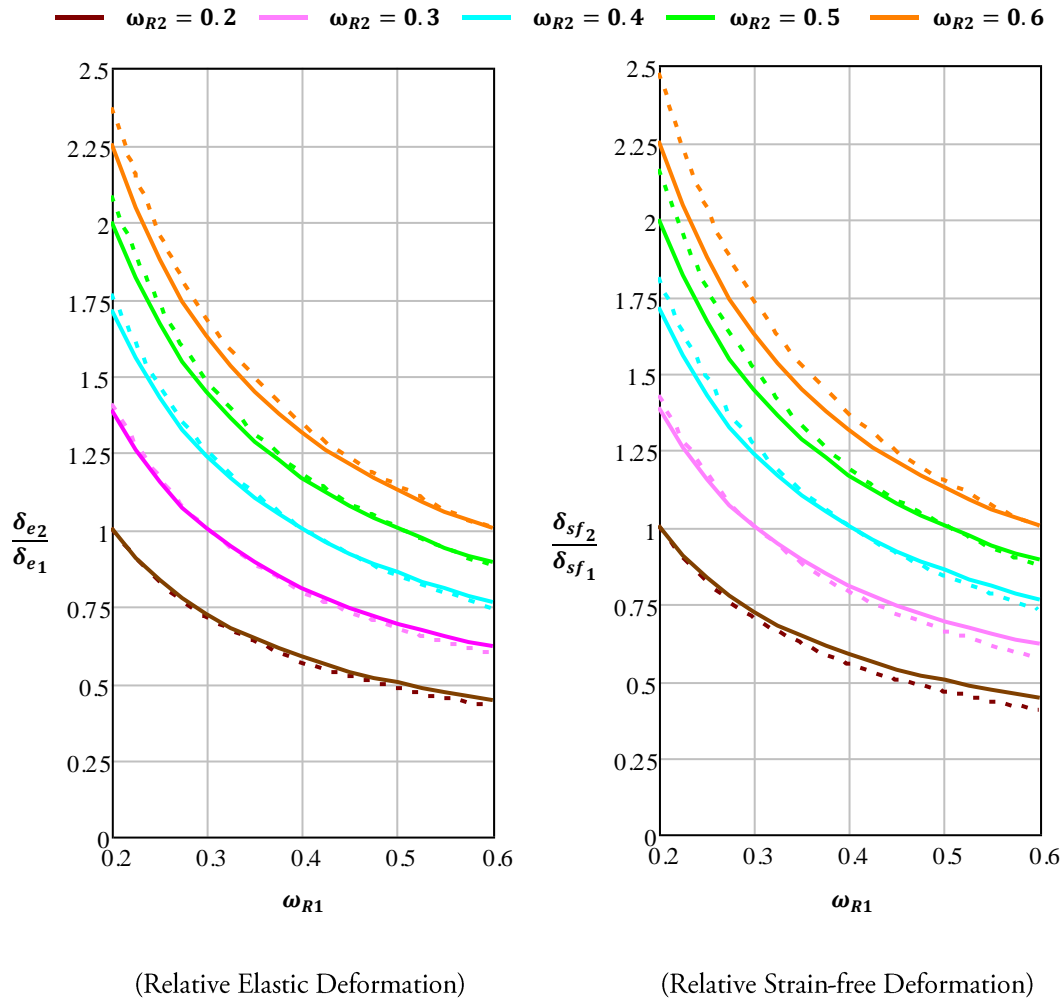
Figure 3.30: Relative Amount of Elastic and Strain-Free Deformations with Varying Load Ratio
Parameters: $L_m = 1000$m, $\gamma_c = 0.09$MN/m^3, $E_c = 200$GPa, $\sigma_{allow} = 800$MPa, $S_R = 0.1$

As an additional consideration, as deformations decrease with decreasing live load ratio, when comparing the response of two different cables subjected to the same loading scenario, it can be expected that nonlinear effects will be less significant in the cable possessing the smaller live load ratio. This is confirmed in Figure 3.31 which gives a measure of the nonlinearity in terms of the unfactored live load ratio (linear deformations are computed in the same manner as in Figure 3.29 – using the second order approach with $\alpha_p = 1$ in all cases).

$$\frac{\delta_{max}^{\ so}}{\delta_{max}}$$

LS2

LS3

LS1

$(L_m = 250m)$

LS2

LS3

LS1

$(L_m = 1000m)$
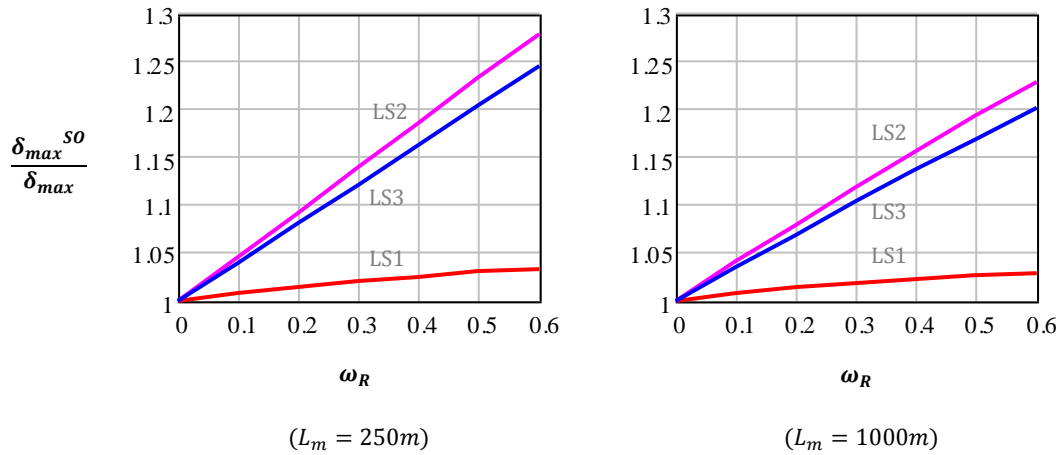
Figure 3.31: Nonlinear Effects in Fully-Laden Suspension Cables as a Function of Live Load Ratio
Parameters: γ_c = 0.09MN/m³, E_c = 200GPa, σ_{allow} = 800MPa, S_R = 0.1

3.2.2.7 Changes in Sag Ratio

It can be easily construed from the derivations in Section 3.2.1 that when a cable is fully loaded along its span, the horizontal force in the cable is approximately inversely proportional to the cable sag. Accordingly, forces in the cable will increase at an increasing rate when the cable sag is decreased, and vice versa. Consequently, varying the cable sag can have a profound effect on the absolute and relative amount of elastic and strain-free deformations. This is illustrated in Figure 3.32 which shows how the maximum deformation for the three previously assigned loading scenarios changes when the sag ratio is varied. It should be noted that for each change in cable sag, the area of the cable is updated accordingly using the cable sizing criterion specified at the beginning of Section 3.2.2.

Evidently, as the sag ratio is reduced, there is a considerable reduction in deflection for Loading Scenarios 2 & 3. This can be attributed to the effect that the relative increase in dead load has on stabilizing the cable against strain-free deformations. Conversely, deflections are shown to increase with decreasing sag when the entire span is loaded (Loading Scenario 1). This may at first seem illogical based on the fact that the ratio of the maximum live load cable force-to-cable area will decrease with decreasing sag as the cable area is increased to compensate for the increased tensile forces. In fact though, even for a span length of 1000 metres the effect of the increased cable area is minor and, therefore, the amount of elastic deformation remains fairly uniform with changes in cable sag. The cause for the resulting increase in deflection can thus be entirely attributed to the geometry of the cable. This can be more clearly illustrated through the following example.
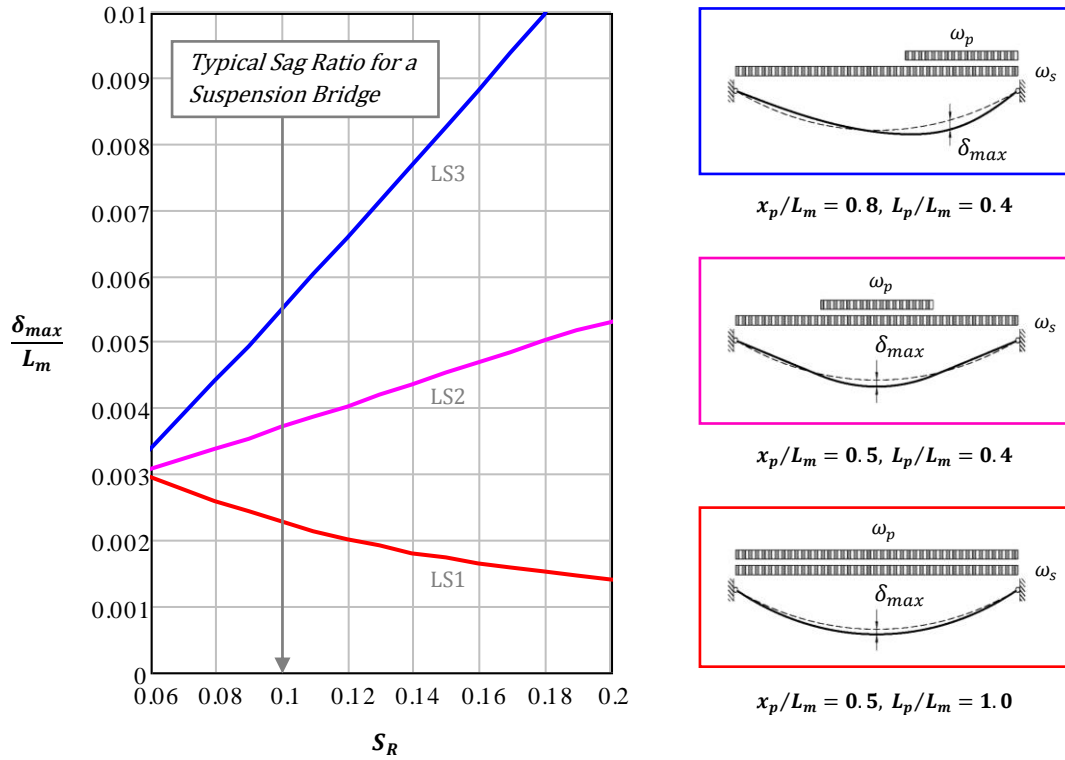
Figure 3.32: Sag Effects on the Deflection of Fully-Laden Suspension Cables
Parameters: L_m = 1000m, γ_c = 0.09MN/m³, E_c = 200GPa, σ_{allow} = 800MPa, $\omega_p = 0.6 \cdot \omega_s$

Shown in Figure 3.33 are two cables with equal chord length; however, one cable has a sag ratio of 0.1, whereas, the other has a sag ratio of 0.05. When both cables are then subjected to an equal amount of elongation corresponding to approximately 3.25% of their chord length, their deformed positions are given by the dashed lines in the figure. Clearly, as a result of their respective geometry, for both cables to have the same amount of elastic elongation, the cable with the smaller sag must have a notably greater deflection at mid span. As further validation, this observation can also be easily proven using mathematics. Similar to stay cables, the stressed length of a suspension cable can be approximated using a Maclaurin series expansion as follows (Steinman, 1922),

$$C_{approx} = L_m \left[1 + \frac{8}{3}\left(\frac{f}{L_m}\right)^2 - \frac{32}{5}\left(\frac{f}{L_m}\right)^4 + \cdots \right] \qquad (3.75)$$

It will be sufficiently accurate in this context to use only the first three terms of the series, and upon partial differentiation with respect to the cable sag, f, the following relationship is obtained,

$$\delta f = \left[\frac{15}{16 \, S_R \left(5 - 24 S_R{}^2 \right)} \right] \delta C_{approx} \tag{3.76}$$

Thus, in order for the cable to retain its parabolic form when the change in length of the cable, δC, is held constant, the change in sag, δf (in this case the mid span deflection) must increase when the sag ratio is decreased.
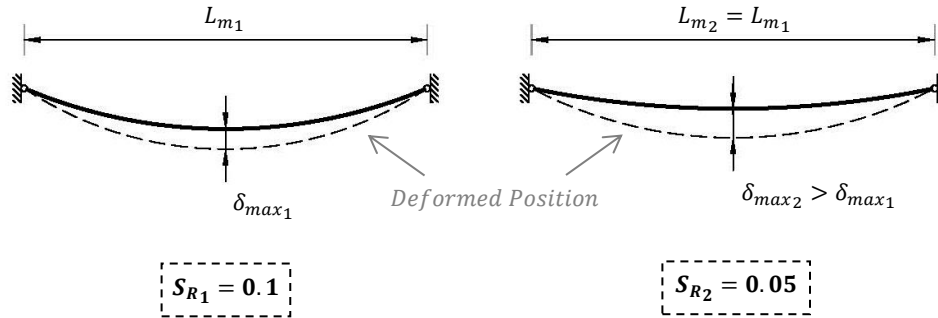
$\Delta_{e_1} = \Delta_{e_2} = 0.0325 \cdot L_{m_1}$ (Note: The amount of elastic elongation is the same in both cables)

Figure 3.33: Deflection of Two Cables with Equal Elastic Deformation and Non Equal Sag

Returning once more to Figure 3.32, it could be contended that the stiffness of suspension bridges could be markedly improved if the sag ratio were decreased below the conventional value of 0.1. However, this argument can be decisively cast aside once economics are considered as a reduction in sag ratio leads to unreasonably large sections for the cables and anchorages: two major bridge components that typically constitute a significant portion of the overall cost. On the other hand, although an increase in sag ratio generally leads to a more economical bridge even with the tower costs considered (Gimsing & Georgakis, 2012), historically, to do so would be at the sacrifice of stiffness.

3.2.2.8   The Effect of Self Anchorage

In previous sections the focus has been on studying the behaviour of a single cable acting in isolation, and since the horizontal cable force has been restrained by fixed end nodes, the cables examined thus far can be considered as earth-anchored systems. When the superstructure is used to restrain the horizontal cable force the system becomes self-anchored. This causes an alteration in the behaviour of the system as a result of the additional nonlinear p-delta effects generated by the compressive force in the superstructure. Therefore, when studying the mechanics of self-anchored systems, the cable can no longer be considered in isolation since the superstructure now forms an integral part of the primary gravity load path, and as a consequence, the analysis becomes much more complex.

To simplify matters, it has been theorized that the analysis of self-anchored suspension bridges can be carried out using a relatively straightforward linear method of analysis, often referred to in literature as 'The elastic theory' (Ochsendorf & Billington, 1999). The basis for this supposition stems from the argument that if the elongation of the hangers is assumed negligible, then both the superstructure and cable will have equal vertical displacement at any point along the bridge, and under this condition, any nonlinear effects arising from the horizontal tensile force in the cable should be equally offset by a reverse effect generated from the horizontal compressive force in the superstructure. Although this argument appears logical, it is flawed in the sense that if the superstructure and cable are isolated and considered as separate entities, then the maximum deflection in each of the two entities will be governed by different loading scenarios. For a simple beam subjected to a compressive force at its ends, the governing loading scenario will occur when the entire span is loaded. Conversely, it has already been established that, for an isolated cable, the governing loading scenario occurs when roughly half of the span is loaded and the load is positioned asymmetric to the centre of the span. Thus, when the two systems are integrated, it is amiss to expect that the nonlinear effects arising in each respective system will entirely counteract one another.

To accurately account for the different nonlinear effects, the finite element (FE) analysis program, LARSA 4D BRIDGE (LARSA, Inc., 2011), was used to study how the basic two-dimensional behaviour of a self-anchored system differs from that of an earth anchored system. To that end, two systems, each with a main span of 250 metres, were analyzed (Figure 3.34). Cable and superstructure members were modelled using truss and beam elements, respectively, and the area for all cable members was determined based on an allowable stress of 800 MPa. The superstructure in the earth-anchored system is restrained vertically at both ends by roller supports which allow for longitudinal translation and in-plane rotation. The superstructure in the self-anchored system is restrained in a similar manner except that one of the supports is changed to a pin support in order to stabilize the model against rigid body motion in the longitudinal bridge direction. Although the articulation scheme for the self-anchored system is somewhat impractical given that hinges have been placed in the superstructure at tower locations, this type of arrangement was purposefully chosen in order to simplify the analysis and minimize the number of parameters involved. As a result, the influence of tower stiffness and side span length is excluded from the analysis, and at the same time, a fair comparison is provided between the earth-anchored and self-anchored systems.

Loading for the two systems consists of a uniformly distributed dead load of 125kN/m, and a uniformly distributed live load of 75kN/m. This level of loading equates to an unfactored live load ratio of 0.6. The position and length of the uniformly distributed live load was considered variable in order to account for all possible loading scenarios. To reduce computational effort, the most extreme loading scenario was determined using what will henceforth be referred to as 'a second order influence

analysis'.

(Self-Anchored System)

(Earth-Anchored System)
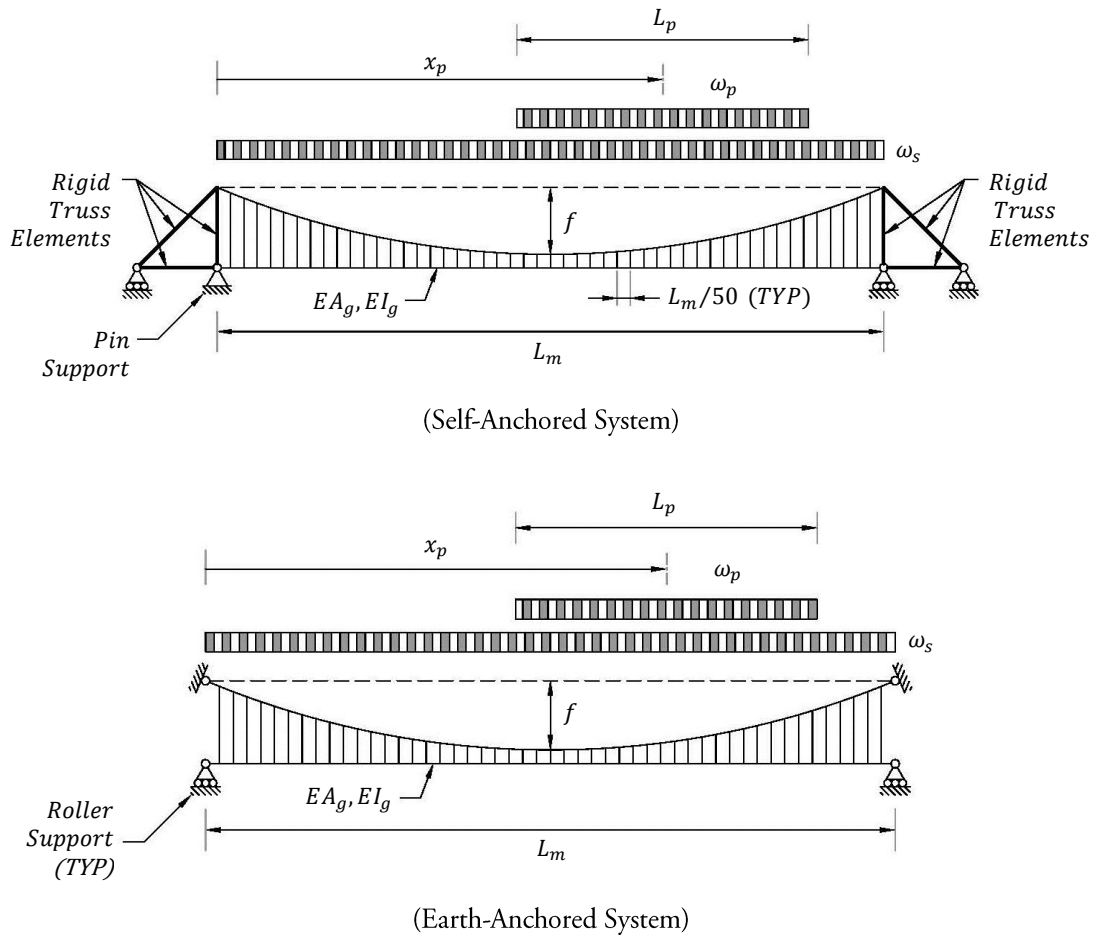
Figure 3.34: Description of Systems Studied in Finite Element Analysis
Parameters: L_m = 250m, EA_g = 200000MN, EI_g = Variable, f = Variable, ω_p = 75 kN/m, ω_s = ω_p/0.6

In the second order influence analysis, nonlinear effects were taken into account by using a tangent stiffness approach which in essence formulates the dead load axial forces into the equations of equilibrium. The magnitudes of the dead load axial forces are then considered constant under the application of live load. In computational terms, this can be achieved by modifying the ordinary stiffness matrix of the structure through the addition of what is commonly referred to as a 'geometric stiffness matrix' or 'stress-stiffening matrix' (Ghali, et al., 2003; Ross, 1998). LARSA 4D BRIDGE is able to perform this modification automatically through use of a built-in 'Staged Construction Analysis' feature. Accordingly, in both the earth-anchored and self-anchored systems, members subject to axial force were first stressed to obtain approximately zero deformation under dead load at all nodal locations (using the cable shape algorithm presented in Section 3.2.1.1 resulted in a

maximum nodal deflection of 1.9 millimetres). These 'prestress' values were then used to form the basis of the geometric stiffness matrix. Thus, only local moments are present in the superstructure under dead load and, for the self-anchored system, the superstructure is axially cambered. Since the dead load axial forces are assumed to remain constant under the application of live load, this second order method does not require iteration and influence coefficients can be linearly scaled to obtain an approximation of actual demands. From these demands, the most extreme loading scenario was identified and a full nonlinear analysis was run using the most extreme loading scenario as the input load case. The entire modelling procedure is described in detail in Figure 3.35.

Step 1: Compute Cable Geometry using Algorithm Presented in Section 3.2.1.1

Step 2: Input Node / Member Geometry into FE Model

Step 3: Apply Dead Load Forces to Model

Step 4: Assign Fictitious Member Properties (*set all members to be axially rigid with negligible bending stiffness*)

Step 5: Run Nonlinear Analysis with Dead Load Forces

Step 6: Verify that Nodal Displacements are Approximately Equal to Zero (*this will only occur if the inputted cable geometry is accurate*)

Step 7: Apply 'Prestress' Forces to Model using the Axial Force Results from Step 5 (*update stiffness matrix using axial force results*)

Step 8: Reassign Member Properties to their Desired/Genuine Values

Step 9: Run Second Order Influence Analysis

Step 10: Identify Peak Loading Scenarios using the Results from Step 9

Step 11: Run Nonlinear Analyses with Peak Loading Scenarios Applied to Model (*include dead load camber and forces in nonlinear analyses*)

Figure 3.35: FE Modelling Procedure
*Shaded boxes describe second order influence analysis procedure

Shown in Figure 3.36 are the peak deflection and moment demands for the superstructure as a function of its bending stiffness. The deflections are in the direction of gravity, and the moment demands are associated with a 'sagging' deflection. The numbers above each plot indicate the length and the position of the corresponding governing loading scenario (refer to Figure 3.34). In most cases, the sag ratio did not greatly affect the governing loading scenario; therefore, only one set of

values is given in the figure. These values represent the governing loading scenarios for a sag ratio of 0.15.

Many observations can be made with respect to Figure 3.36. In regards to the earth-anchored system, it can be seen that when the bending stiffness of the superstructure exceeds a certain threshold, deflections start to decrease with increasing sag. This can be explained by examining the value of the loaded length, L_p, giving rise to the governing loading scenario. When the value of L_p approaches L_m, it is an indication that elastic deformations are starting to govern the response of the system as a result of the effect that the superstructure stiffness has on mitigating strain-free deformations. As a consequence, deflections start to decrease with increasing sag due to the phenomenon explained in Section 3.2.2.7 (Figure 3.33). For the same reason, beyond the threshold the superstructure stiffness has little effect on the magnitude of the maximum deflection. Similar trends are observed when examining the magnitude of the peak bending moment in the superstructure, although even when the flexural stiffness of the superstructure exceeds the threshold, the moment demands will continue to rise, albeit at a lesser rate. This is because the superstructure must continually act to resist strain-free deformations. This is reflected in the governing loading scenarios for the moment demands which remain asymmetric for all the stiffness values examined.

For the self-anchored system, Figure 3.36 shows that the governing loading scenarios are nearly equal to those observed for the earth-anchored system, yet for all values of flexural stiffness, values of deflection and moments decrease with increasing sag. As such, it seems generally advantageous to utilize a greater sag ratio in self-anchored suspension bridges. Further, a self-anchored system with a sag ratio of 0.2 is shown to exhibit a similar degree of system stiffness in comparison to an earth-anchored system with a conventional sag ratio of 0.1 so long as the flexural stiffness of the superstructure is made slightly larger in the self-anchored system. Such an increase in stiffness generally does not pose any significant drawbacks, considering that added flexural stiffness is often prescribed regardless in order to eliminate any possible risk of buckling.

Figure 3.36 also shows that when the flexural stiffness of the superstructure is relatively large, a similar degree of system stiffness is exhibited with both the earth-anchored and self-anchored systems regardless of the sag ratio. This implies that the superstructure becomes nearly fully effective in preventing nonlinear effects from occurring. This is confirmed in Figure 3.37 which compares the results from the second order influence analysis to the results from the full nonlinear analysis. The parametric results obtained from the second order influence analysis are denoted with the superscript 'SO'. Note that, as expected, for small values of flexural stiffness, the nonlinearity in the deflections of the earth-anchored system is nearly equal to the value reported in Figure 3.29 for an isolated, unstiffened cable. For the self-anchored system, nonlinearity will decrease with decreasing sag due to

the p-delta effects in the superstructure which counteract the tension stiffening effect of the cable. Nevertheless, despite the p-delta effects, the second order influence analysis, in general, produces a conservative estimate of the superstructure demands.
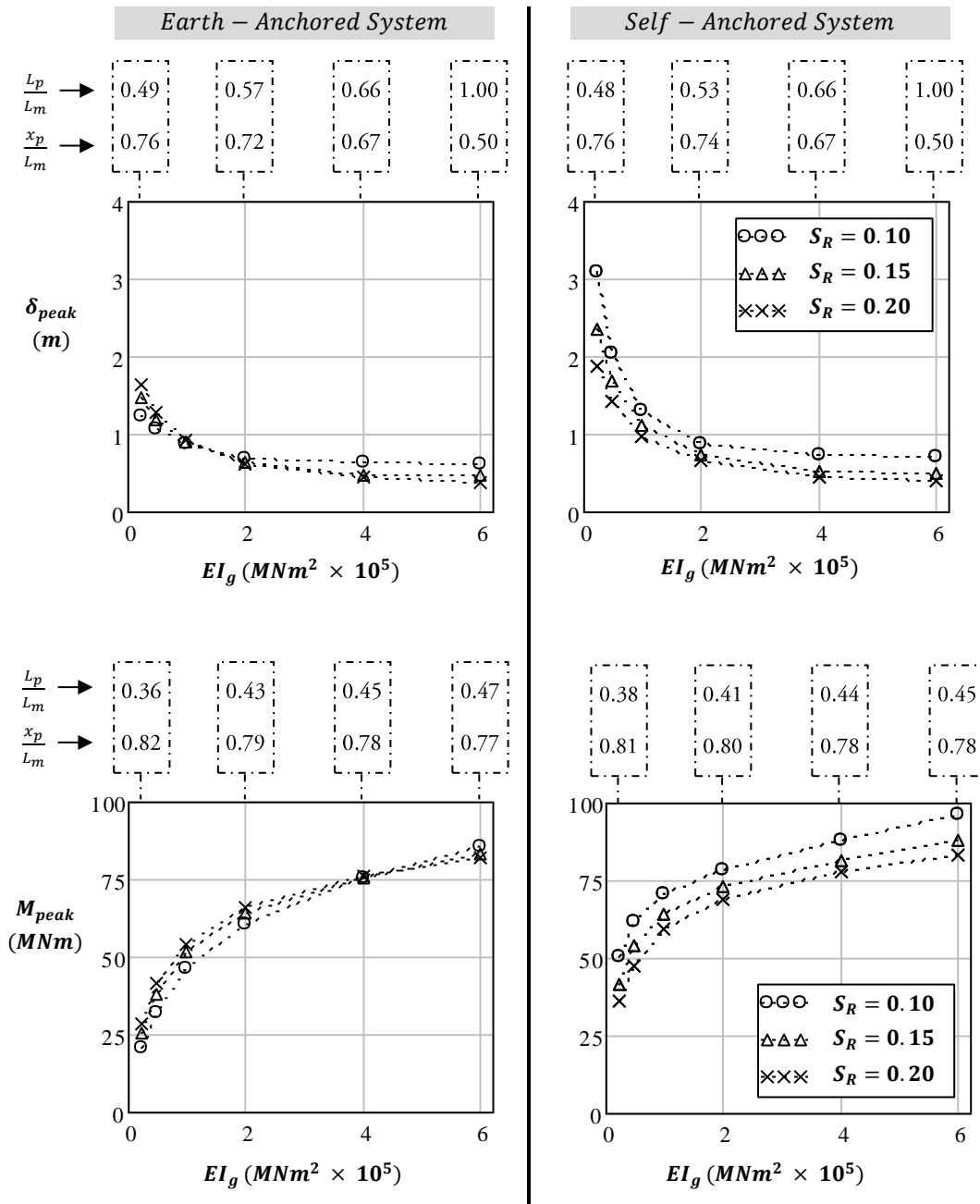
Figure 3.36: Deflections and Moments as a Function of Superstructure Bending Stiffness
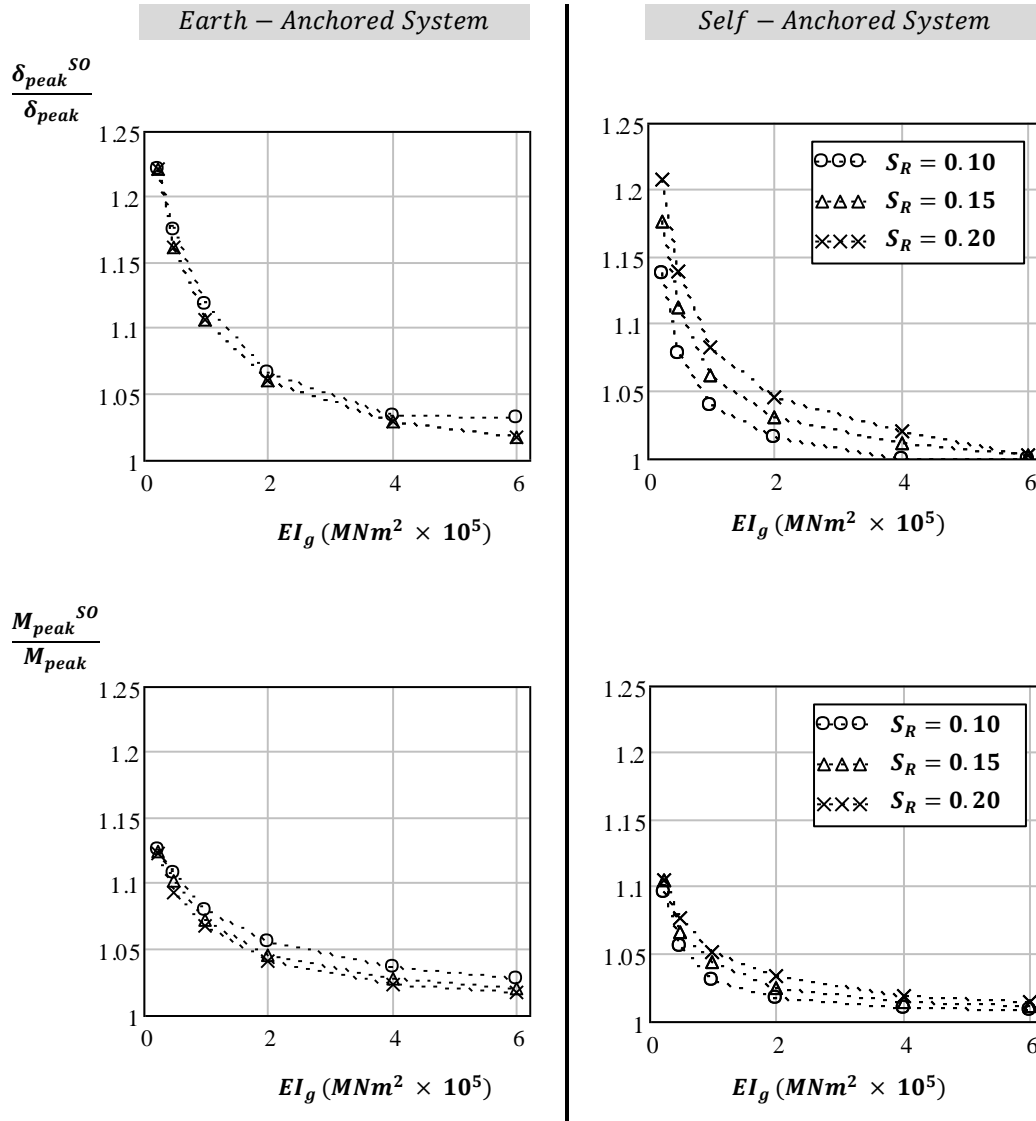
Figure 3.37: Nonlinearity due to Live Load as a Function of Superstructure Bending Stiffness

Based on the current state of practice it seems as though many bridge engineers are already aware of many of the observations made above in regards to self-anchored suspension bridges. Many recently constructed self-anchored suspension bridges such as the WanXin Bridge (China), the Konohana Bridge (Japan), and the Yeoungjong Grand Bridge (Korea) have sag ratios in the range of 0.15 to 0.2. These bridges also possess a relatively high degree of flexural stiffness characterized by span-to-depth

ratios in the range of 25 to 100 (see Figure 3.26 for typical ratios used in earth-anchored suspension bridges). (Goolen, 2006; Zhang, et al., 2006) For such high values of flexural stiffness, nonlinear effects will be minor as noted in literature on the subject (Ochsendorf & Billington, 1999; Romeijn, et al., 2008). However, it is important to recognize that the reduction in nonlinearity cannot be entirely attributed to the counteracting effect of the p-delta effects in the superstructure, but rather the majority of the reduction stems from the flexural stiffness of the superstructure.

One of the most distinguishing behavioural traits observed in the self-anchored system was the reduction in deflections and moments with increasing sag ratio. Interestingly though, upon closer examination, there is not one, but two primary reasons why the relationship between deflection and sag ratio differs dramatically in the case of self-anchored suspension bridges.

1. The first can be attributed to the relationship between the sag ratio and the horizontal force in the superstructure – a lower sag ratio results in a greater horizontal force, giving rise to greater p-delta effects, which in turn amplify deflections.

2. The second is less intuitive and relates to the articulation scheme shown in Figure 3.34, and more specifically, to the pinned support which was compulsorily added to the self-anchored system. In conjunction with the axial stiffness of the superstructure, this support becomes actively engaged in restraining longitudinal movement resulting from strain-free deformations in the cable. Moreover, a bending stiff superstructure is not a precondition. Thus, even in earth-anchored systems, by pinning one of the supports, the stiffness of the entire system can be markedly improved, particularly when the sag ratio is increased beyond the conventional value of 0.1. This is made evident in Figure 3.38.

The upper left plot in Figure 3.38 depicts the relationship between the maximum downward deflection and the sag ratio when the flexural stiffness of the superstructure is held constant at a relatively flexible value of 0.25e5MNm². The axial stiffness of the superstructure is also held constant at a value of 2e5MN. Likewise, the lower left plot depicts the relationship between the maximum superstructure bending moment and the sag ratio. In the upper right plot, the effect that the axial stiffness of the superstructure has on the values of maximum deflection is presented for a sag ratio of 0.2. In all plots, to provide a fair comparison, all other parameters relating to the span length and the loading remain unchanged from the values specified in Figure 3.34.
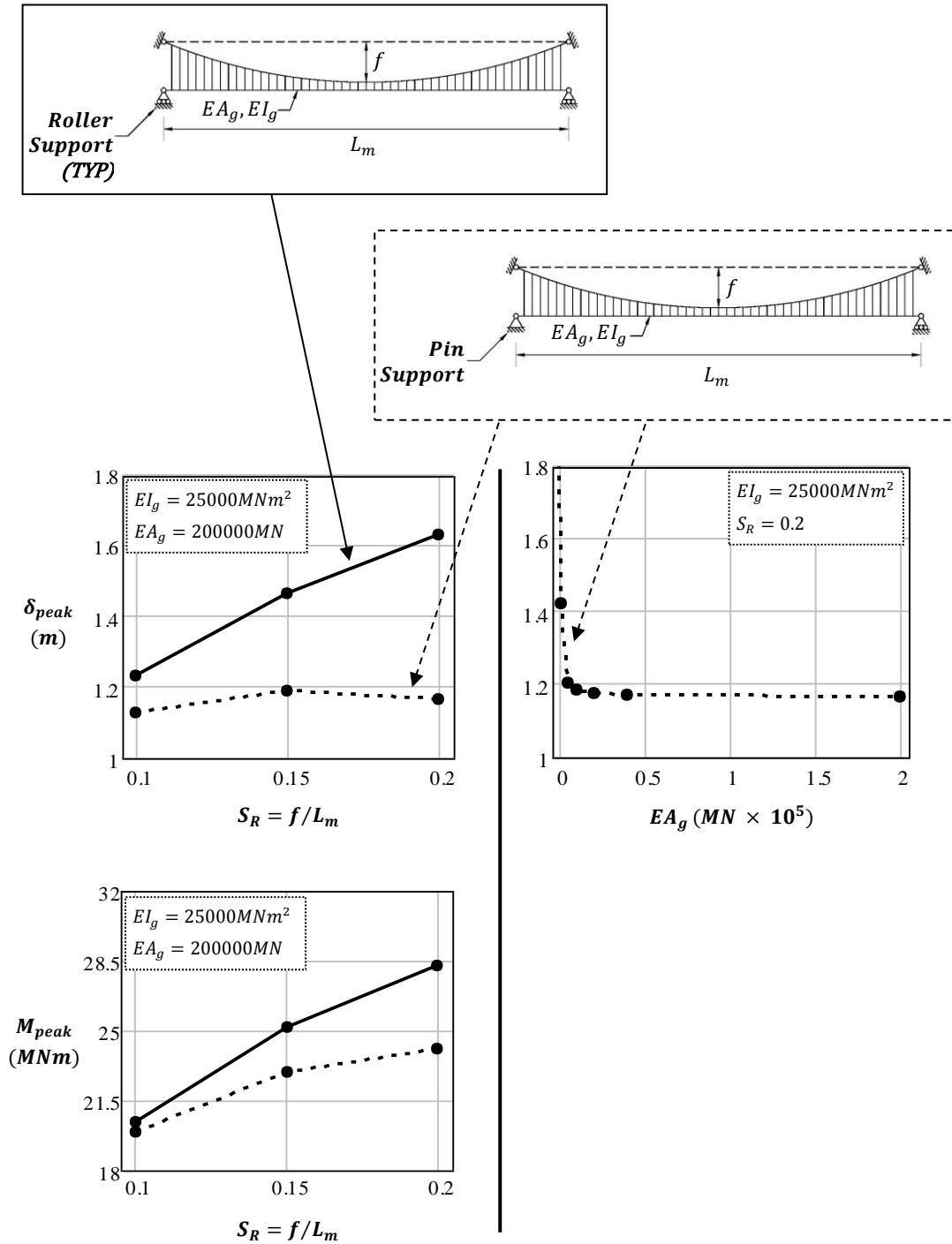
Figure 3.38: A Comparison of Demands in two Earth-Anchored Systems with Different Articulation Schemes (Flexible Superstructure)

Parameters: L_m = 250m, ω_p = 75 kN/m, ω_s = ω_p/0.6

The upper left plot in Figure 3.38 shows that when axial restraint is provided to the superstructure, deflection demands do not vary greatly when the sag ratio is increased. Furthermore, it is evident from the upper right plot that the level of axial restraint provided by the superstructure approaches an asymptote at a very minute value of axial stiffness. As a result, the minimum thickness criteria specified in design codes for the various cross-sectional components (both those consisting of concrete and of steel) ensures that the pinned support is always engaged. From the lower left plot, it can be seen that the moment demands in the superstructure are also similarly affected by the added restraint, albeit, to a much lesser extent. Clearly, the influence of the axial restraint becomes greater as the sag ratio is increased.

In conjunction with the above statements, it is important to mention once again that the flexural stiffness of the superstructure can also be utilized to mitigate strain-free deformations (vertical and longitudinal). This point was first discussed in Section 3.2.2.3, and is partially reflected in Figure 3.36. Thus, when the flexural stiffness of the superstructure is designed to be relatively large, the addition of a longitudinal restraint in the form of a pinned support becomes superfluous. For confirmation, Figure 3.39 shows the relative demands for the two, earth-anchored, articulation schemes shown in Figure 3.38. The demands for the longitudinally restrained system are denoted using the subscript 'R'. For comparison, results are shown for a relatively flexible, and a relatively stiff superstructure. In regard to the latter, it can be seen that the longitudinal restraint has only a minor effect on the demands.
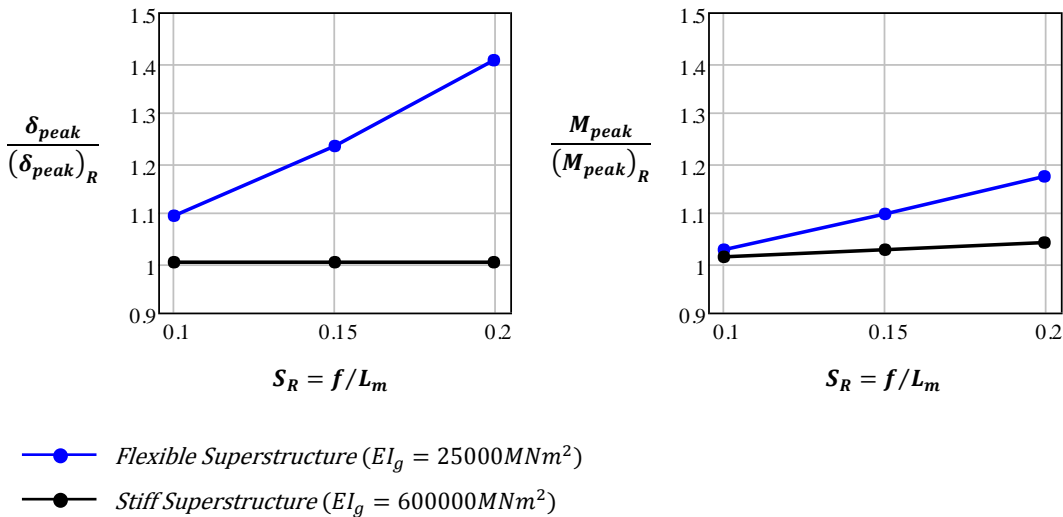
Figure 3.39: Relative Demands in two Earth-Anchored Systems with Different Articulations
Parameters: L_m = 250m, ω_p = 75 kN/m, ω_s = ω_p/0.6, EA_g = 200000 MN
*Refer to Figure 3.38

Despite the influence the flexural stiffness of the superstructure has on mitigating strain-free deformations it will be generally more economical to design a relatively flexible, streamlined, superstructure. The only exception is in cases where a multi-deck bridge is desired. This is because, for the case of a relatively stiff superstructure, a great amount of added material is required to compensate for the increased moment demands (refer to Figure 3.36). Nevertheless, the results presented above suggest that, even when the superstructure is designed to be relatively flexible, the conventional sag ratio used in earth-anchored suspension bridges could be increased without significant detriment to the global stiffness of the system so long as a pinned support is included in the articulation scheme.

Traditional methods of suspension bridge analysis, including the deflection theory, assume that the hangers remain vertical under bridge deformation and that all cable nodes translate along fixed verticals (West & Robinson, 1967). Hence, in the traditional methods of analysis, the axial stiffness of the superstructure is not considered when deriving the equations of equilibrium. Historically, suspension bridges were constructed with expansion joints at both towers (Gimsing & Georgakis, 2012), and these joints would not have been capable of providing any notable axial restraint. The assumptions made in traditional methods of analysis would have been appropriate under these circumstances. Recently though, the trend has been towards minimizing the number of structural joints because joints are not only costly to construct and maintain, they also provide weak points within the structure. As such, many modern suspension bridges are constructed with a continuous superstructure, and in those cases, a pinned support is frequently provided at one of the tower locations (Gimsing & Georgakis, 2012). Even so, based on traditional methods of analysis, engineers have been trained to believe that any increase in sag adversely affects the global stiffness of the bridge to a significant degree. Consequently, since the development of more sophisticated means of analysis, it does not appear that the optimum sag ratio of suspension bridges has ever been fully re-examined.

The main advantage to be gained from increasing the sag ratio would be significant savings in material for the suspension cables, anchorages, and foundations. As a result, suspension bridges with heightened sag ratios could theoretically become more competitive for both small and medium spans. This is, of course, barring any potential issues related to tower buckling, construction demands, and aerodynamic stability. The latter issue can generally be ruled out because by increasing the sag ratio, the cable area becomes smaller, and consequently, there is less mass concentrated at the extremities of the superstructure (assuming two planes of cables). This in turn has the beneficial effect of increasing the separation between the first vertical and first torsional mode of vibration. Studies which have examined the effect that the sag ratio has on aerodynamic stability have thus found that the critical flutter wind speed increases with increasing sag ratio (Zhang & Sun, 2004; Hauge & Petersen, 1999). Nevertheless, it is clear that more research is required in this area; however, since the focus of this

thesis is on hybrid cable bridges, this topic will not be discussed further.

Shifting focus back to the effect of self-anchorage, considering the influence of the pinned support, the true effect of self-anchoring the suspension cable can only be observed when comparing the demand envelopes for a horizontally restrained earth-anchored and a horizontally restrained self-anchored system (Figure 3.40). The demand envelopes were obtained using the results from the second order influence analysis and are thus an approximation of the actual demands. Nevertheless, rather than examining only the peak demands, the demand envelopes provide a good indication of how the demands vary along the length of the superstructure.

With the exception of near mid-span, it can be seen from Figure 3.40 that the amplification of the deflection demands produced by the self-anchoring force is close to uniform along the span length. In contrast, the amplification in the moment demands is more variable. Clearly, the amount of amplification decreases significantly as the sag ratio is increased. However, it is important to note that the amount of amplification will also decrease as the bending stiffness of the superstructure increases. This is because, similar to strain-free deformations, the flexural stiffness of the superstructure is also effective at mitigating deformations resulting from p-delta effects. Therefore, if the bending stiffness of the superstructure is increased enough, the difference between the demands in the earth-anchored and self-anchored systems will become negligible.
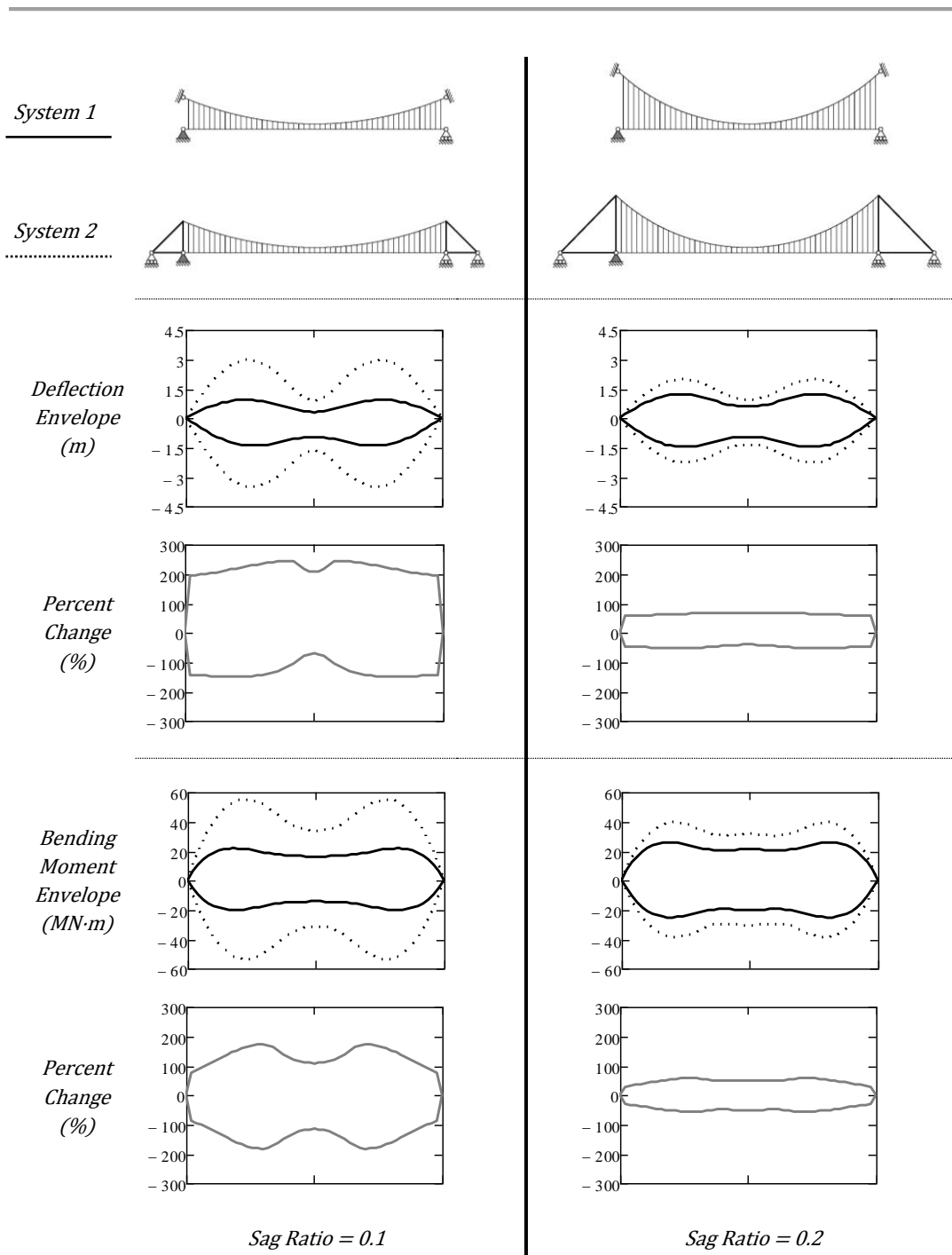
Figure 3.40: Comparison of Earth-Anchored and Self-Anchored Demand Envelopes
Parameters: L_m = 250m, EI_g = 0.25ᴇ5MNm², ω_p = 75 kN/m, ω_s = ω_p/0.6

3.3   End of Chapter Summary

At the beginning of the chapter two sets of equations were presented for the geometric profile of a stay cable under dead load: one set based on a catenary profile and the other based on a parabolic profile. The catenary based equations correctly account for the way self-weight is distributed along the stay cable and thereby provide a near exact solution; however, their formulation is relatively complex. In contrast, the parabolic based equations approximate the cable profile by assuming that the self-weight is distributed along the cable chord. Notwithstanding, their formulation is relatively more simple and, through comparison, it was shown that the parabolic equations provide sufficient accuracy for most practical applications.

When live load is applied, the stress-strain relationship of a general stay cable was shown to consist of linear and nonlinear components. The secant and tangent moduli were introduced as methods to capture the nonlinear effects in a linear analysis. Although the secant modulus is the more accurate of the two methods, it still requires iteration during analysis. In comparison, the tangent modulus method is easy to implement although its accuracy decreases when the cable span is increased and/or the initial cable stress is decreased. The effect of cable inclination on the amount of deformation was also studied and it was found that the least amount of deformation occurs when the cable is inclined at 45 degrees to the horizon.

Following the section on stay cables, fully-laden suspension cables were discussed. Due to the combined loading from the self-weight of the cable and superstructure, their geometric profile presents as an amalgamation of a catenary and a parabola. An iterative method which correctly captures the dead load profile was presented in addition to an approximate, non-iterative, parabolic formulation. The error between the two approaches was discussed in detail.

While studying the deformation characteristics of fully-laden suspension cables, it was observed that the greatest deflection occurs when live load is positioned near the quarter points of the span. This is a result of strain-free deformation in the cable which accompanies the deformation from elastic strain. Through further study, strain-free deformations were shown to be highly impacted by the magnitude of tension in the cable. Thus, when the dead load forces acting on a fully-laden suspension cable are increased the tension stiffening effect which is created acts to stabilize the cable. Elastic deformations were also found to decrease with added dead load as a result of the requisite increase in cable area. On that basis, a simple equation was derived which can be used to estimate the change in peak deflection when the unfactored live load ratio is varied. In a separate study, the peak deflection in a fully-laden suspension cable was shown to substantially increase as the sag ratio increases. This is because, with increasing cable sag, the cable becomes more prone to strain-free deformations.

Another consequence of the tension stiffening effect is that the load-deformation relationship of a fully-laden suspension cable is nonlinear. Nevertheless, it was shown that nonlinear effects can be conservatively accounted for in a live load analysis using a tangent stiffness approach based on the stiffness of the system in its dead load state. When applied to a bridge structure, this approach was labelled a 'second order influence analysis'. Clearly, the error in using such an approach diminishes as the unfactored live load ratio decreases.

Finite element analysis was utilized to study the behaviour of a self-anchored fully-laden cable. Naturally, the flexural stiffness of the superstructure was included in the analysis. When studying the effect of the superstructure stiffness, it was found that increasing the superstructure stiffness resulted in a nonlinear reduction in the peak deflection. Nonlinear effects were similarly reduced. However, as a trade-off, moment demands in the superstructure increase. Despite the above comments, a threshold was observed, beyond which, nonlinear effects become negligible. In addition, the flexural stiffness of the superstructure ceases to have any notable effect on the peak deflection. In contrast, moment demands in the superstructure continue to rise, albeit at a lesser, and near linear rate.

In comparison to an earth-anchored suspension bridge, the most distinguishing trait observed for the self-anchored system analyzed was the effect of the sag ratio. In contrast to previous observations made while studying a single isolated cable, for the self-anchored system, deflections were found to decrease with increasing sag ratio. This was attributed to the de-stabilizing effect created from the anchoring of the cable force, and to the longitudinal restraint provided to the superstructure during the analysis. In regards to the latter, the longitudinal restraint proved extremely effective at mitigating strain-free deformations. However, the influence of the longitudinal restraint diminished as the flexural stiffness of the superstructure was increased. After re-examining the behaviour of an earth-anchored fully-laden cable with longitudinal restraint the only, true, effect which was observed to result from self-anchoring the cable force was that it caused demands to be amplified along the length of the superstructure; the general characteristics of the demands envelopes were essentially unchanged.

Chapter 4

BASIC BEHAVIOUR OF

HYBRID CABLE BRIDGES

The study of basic cable behaviour is extended in this chapter to include partially-laden suspension cables given that they are a principal component of discontinuous hybrid cable bridges. Accordingly, the first half of this chapter follows the same format introduced in Chapter 3. Near exact and approximate methods to determine the geometric form of a partially-laden suspension cable are presented. Thereafter, the deformation characteristics of a single, isolated, partially-laden suspension cable are examined.

Embodied in a partially-laden suspension cable is a fully-laden suspension cable whose ends are supported by stay cables. Therefore, even prior to examination certain inferences can be made regarding its behaviour. It has already been observed in Chapter 3 that the basic behaviour of a fully-laden suspension cable differs once the effects of self-anchorage are included. For that reason, a partially-laden suspension cable can be expected to exhibit similar changes in behaviour.

Since the focus of this thesis relates to self-anchored cables, it would not be pertinent to emulate all of the content provided in Chapter 3. Furthermore, given that a self-anchored partially-laden suspension cable is but one of many components which work in concert in a self-anchored hybrid cable bridge, it would be trivial to study the behaviour of a self-anchored partially-laden suspension cable without due respect to the other components. Therefore, the latter half of this chapter focuses solely on studying the fundamental behavioural traits of self-anchored hybrid cable bridges through means of a simple model. This includes a parametric examination into the general response characteristics of self-anchored hybrid cable bridges and how those characteristics are affected by nonlinear, scale, and loading effects.

4.1 Partially-Laden Suspension Cables

4.1.1 Geometric Form

Gravity loads on partially-laden suspension cables do not differ from those acting upon fully-laden suspension cables. As such, similar means and methods can be used to determine their geometric form. This section describes how the concepts introduced in Section 3.2.1.1 may be adapted to obtain the exact shape of a partially-laden suspension cable considering the catenary effect. In addition, equations which can be used to determine the approximate cable shape assuming a parabolic form are derived. As in the case of fully-laden suspension cables, it is assumed that all hanger forces are vertical and the cable is symmetric with respect to the centre of its span.

4.1.1.1 Terminology

Prior to proceeding, two fundamental parameters which will be used extensively in this chapter must first be defined. Idealizing a partially-laden suspension cable as being comprised of a series of stayed and suspended regions, these two additional parameters are shown in Figure 4.1, and include,

- The distance between end hangers / the length of the suspended region, L_h; and
- The sag of the suspended region, f_h.

Also shown in the figure is cable span, L_m, and the sag of the cable, f. For simplicity, and to further differentiate between the sag of the cable, f, and the sag of the suspended region, f_h, from hereon, the former will be referred to as 'the global sag' and the latter as 'the local sag'. Accordingly, the ratio of the local cable sag-to-suspended length (f_h:L_h) will be referred to as 'the local sag ratio'.
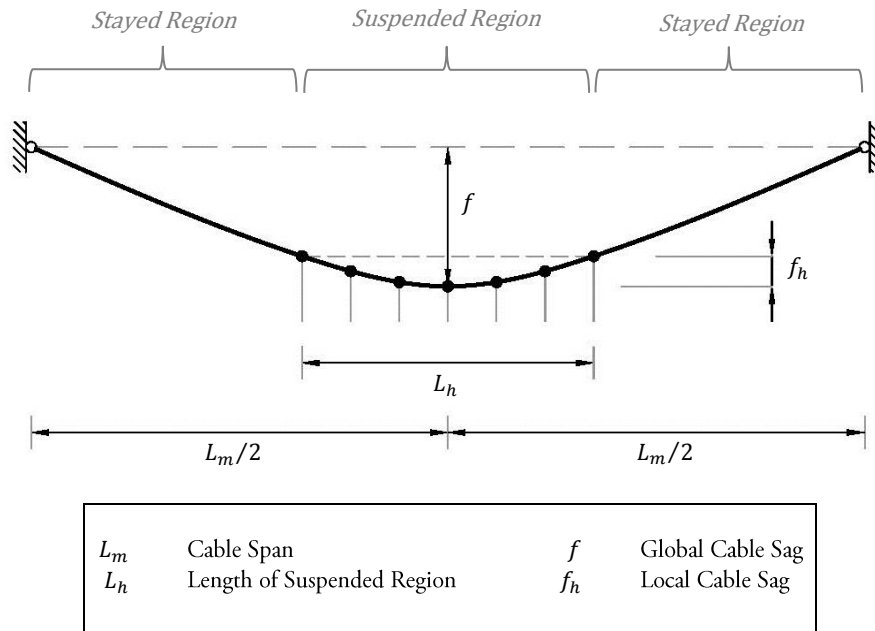
Figure 4.1: Additional Parameters for Partially Laden Suspension Cable

4.1.1.2   Dead Load Geometry Considering Catenary Effect

The local curve of the stayed regions in a partially-laden suspension cable, along with the local segments in the suspended region, take the same catenary form as the local cable segments in a fully-laden suspension cable. Hence the same exact procedure outlined for fully-laden suspension cables in Section 3.2.1.1 may be applied for partially-laden suspension cables so long as the placement of nodes is modified to reflect the altered position of the hangers (see Figure 4.2). However, to improve the speed of convergence it is recommended that the initial guess value for the horizontal cable force be updated to reflect the approximate horizontal cable force in a partially laden cable (the parabolic formulation for the horizontal cable force in a partially laden cable is given in Section 4.1.1.3). In addition, similar adjustments may be made to the procedure presented in Appendix A for special cases wherein three-dimensions are required to describe the shape of the cable curve.

Free Body Diagram of Segment i
†Same as in fully-laden suspension cable
†Similar for Segment n, except $\Delta x_n = (L_m - L_h)/2$

$N_{1...n}$	Nodal Numbering Scheme	L_h	Length of Suspended Region
$S_{1...n}$	Segment Numbering Scheme	T_{max}	Max Cable Tension
Fh_i	Hanger Force Acting at Node i	H	Horizontal Component of the Cable Tension
ω_c	Self-Weight of Suspension Cable	$\{x_i, y_i\}$	Local Coordinates of Segment i
f	Global Cable Sag	Δx_i	Projected Length of Segment i
L_m	Cable Span	Δy_i	Projected Rise of Segment i

Figure 4.2: Modified Reference Diagram for Segmented Catenary Solution
†Refer to Figure 3.14 in Section 3.2.1.1

4.1.1.3   Dead Load Geometry Using Parabolic Approximation

For fully-laden suspension cables the parabolic approximation was derived by considering the self-weight of the suspension cable to act along the cable's projected length, although the accuracy of such an approximation rapidly decreases with increasing values of cable sag. A similar approach is,

therefore, only appropriate for partially-laden suspension cables when the global sag, f, is roughly less than 0.15 times the span of the cable. For all other cases, rather than considering the self-weight of the cable to act along the projected length of the cable, the precision of the parabolic solution may be notably increased, often by a factor greater than 10, by instead considering the self-weight of the cable to act along the line A-B-C-D shown in Figure 4.3.
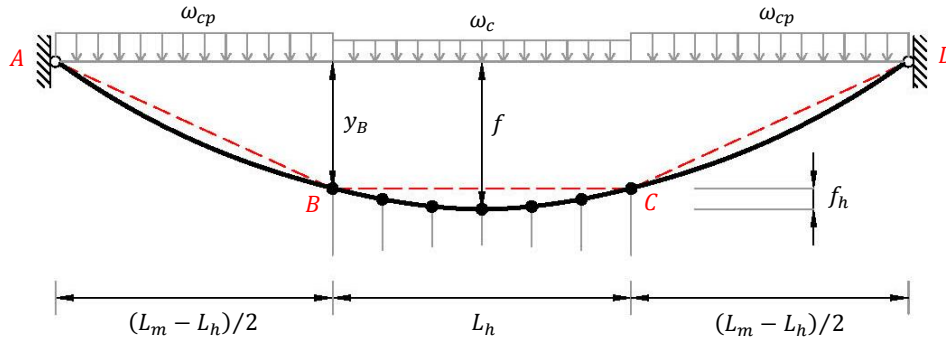
Figure 4.3: Self-Weight Idealization in Parabolic Approximation for Partially Laden Cables
*Note: the sag of the cable in stayed regions has been enlarged for clarity

Thus, the stayed regions are treated similar to stay cables and the projected self-weight of the cable in those regions, denoted as ω_{cp}, is adjusted according to the inclination of cable chords A-B and C-D. Using the equation presented in the section on stay cables (Section 3.1.1.2),

$$\omega_{cp} = \omega_c\sqrt{1 + \Omega^2} \qquad\qquad bis\ (3.17)$$

where, in this case, Ω, represents the rise-to-span ratio of the stayed regions,

$$\Omega = \frac{2\,y_B}{L_m - L_h} \qquad\qquad (4.1)$$

Once the self-weight has been established, the ordinates of the cable can be obtained using the same procedure outlined in Section 3.2.1.2 for fully-laden suspension cables. Though, because the projected self-weight of the cable is now discontinuous, separate functions are required for the stayed and suspended regions. Additionally, in the stayed regions the cable ordinates may be defined over a continuous domain; however, due to the discrete nature of the hanger forces, similar to fully-laden suspensions cables, the cable ordinates in the suspended region must be defined by way of a piecewise function.

Using Figure 4.4 as a reference, from sectional moment equilibrium, the cable ordinates using the parabolic approximation may thereby be expressed as,

For $0 \leq x < (L_m - L_h)/2$

$$y(x) = \frac{1}{H}\left[\frac{\omega_{cp}x^2}{2} - V_s x\right] \tag{4.2}$$

For $(L_m - L_h)/2 \leq x \leq (L_m + L_h)/2$

$$y(x)|_{S_m} = \frac{1}{H}\left[\sum_{j=1}^{m-1} Fh_j\left(x - \sum_{i=1}^{j}\lambda_i\right) + \frac{\omega_{cp}\lambda_1}{2}(2x - \lambda_1) + \frac{\omega_c}{2}(x - \lambda_1)^2 - V_s x\right] \tag{4.3}$$

For $(L_m + L_h)/2 \leq x < L_m$

$$y(x) = \frac{1}{H}\left[\frac{\omega_{cp}}{2}(2\lambda_1 + L_h - x)^2 - V_s x\right] \tag{4.4}$$

where x and y are measured with respect to a global coordinate system placed at the upper left end node of the cable and all parameters including the hanger forces are given as positive values. The vertical component of the cable tension at the supports is derived from global force equilibrium,

$$V_s = \frac{1}{2}\sum_{i=1}^{N_{hangers}} Fh_i + \omega_{cp}\lambda_1 + \frac{\omega_c L_h}{2} \tag{4.5}$$

and an expression relating the cable sag to the horizontal force in the cable is derived from sectional moment equilibrium about mid-span of the cable,

$$H = \frac{1}{f}\left[V_s\frac{L_m}{2} - \frac{\omega_{cp}\lambda_1}{2}(L_m - \lambda_1) - \frac{\omega_c L_h^2}{8} - \sum_{j=1}^{N^*} Fh_j\left(\frac{L_m}{2} - \sum_{i=1}^{j}\lambda_i\right)\right] \tag{4.6}$$

Or alternatively, if the local sag of the cable is known,

$$H = \frac{1}{f_h}\left[(V_s - \omega_{cp}\lambda_1)\frac{L_h}{2} - \frac{\omega_c L_h^2}{8} - \sum_{j=1}^{N^*} Fh_j\left(\frac{L_m}{2} - \sum_{i=1}^{j}\lambda_i\right)\right] \tag{4.7}$$

where,

$$N^* = \begin{cases} \dfrac{N_{hangers}-1}{2}, & \text{if there is a hanger at mid-span} \\[3mm] \dfrac{N_{hangers}}{2}, & \text{if there is no hanger at mid-span} \end{cases} \tag{4.8}$$
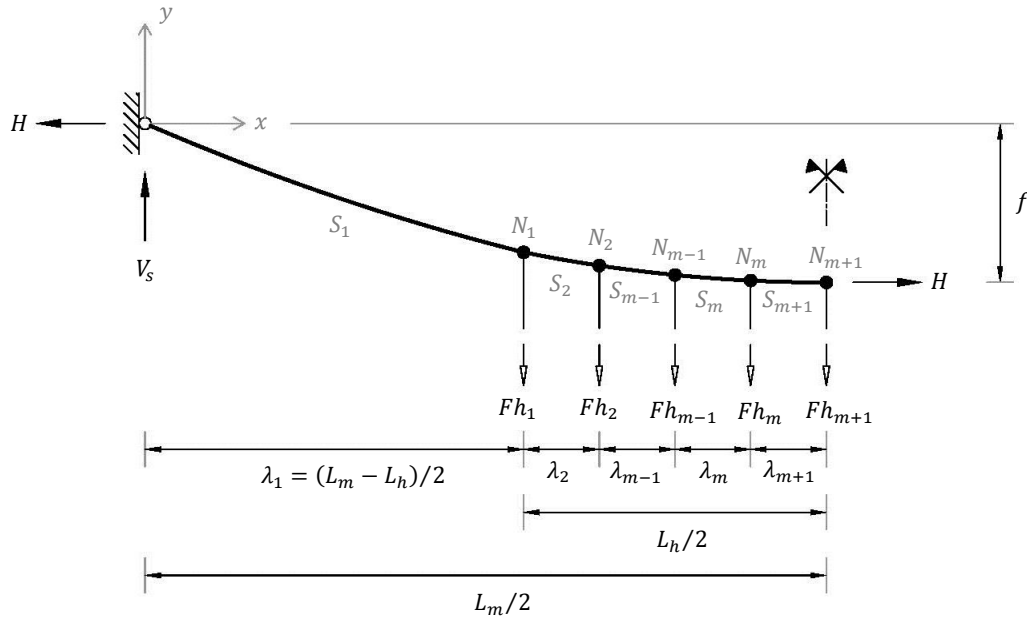
$N_{1...}$	Nodal Numbering Scheme	L_m	Cable Span
$S_{1...}$	Segment Numbering Scheme	L_h	Length of Suspended Region
$N_{hangers}$	‖Number of Hangers	H	Horizontal Component of the Cable Tension
ω_c	‖Self-Weight of Suspension Cable	V_s	Vertical End Component of the Cable Tension
f	Global Cable Sag	λ_m	Relative Spacing of Hanger at Node m
f_h	‖Local Cable Sag	Fh_m	Hanger Force Acting at Node m

‖Not Shown for Clarity

Figure 4.4: Reference Diagram of Partially-Laden Suspension Cable for Parabolic Approximation

As in the case of fully-laden suspension cables, the above equations may be simplified to reduce the computational effort involved in circumstances wherein,

- The cross-sectional area of the superstructure is kept constant along the span supported by the hangers;

- Hangers are designed to have equal spacing, and;

- The weight of the hangers and hanger assemblies may be neglected relative to the combined weight of the suspension cable and superstructure, or alternatively, the weight of the hangers is considered as a uniform load and is included within the overall cable weight, ω_c.

However, in contrast to fully-laden cables, it may not always be assumed that each hanger carries an equal distribution of the superstructure weight. The specific nature of the simplified solution for partially-laden cables will depend upon the tributary length of the superstructure supported by the hangers near the ends of the suspended region. This in turn depends upon the cable stressing/construction sequence adopted in addition to the separation distance between the outermost stay cable and hanger, denoted by the vector, d_0, in Figure 4.5.
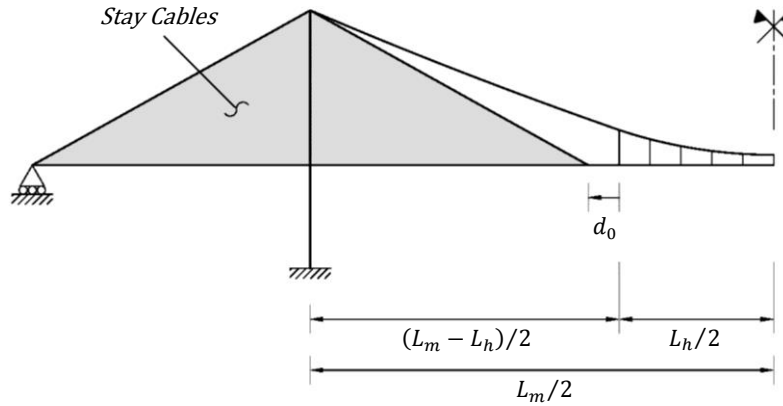
Figure 4.5: Partial Elevation View Depicting Separation Distance

Mathematically, the simplest case occurs when no separation is provided ($d_0 = 0$) and the outermost stay cable and hanger are stressed so that each takes an equal distribution of the superstructure weight. Under these conditions, denoting, λ, as the hanger spacing, and, ω_s, as the uniformly distributed weight of the superstructure, Equations (4.2) to (4.8) reduce to the much simpler form,

$$H = \begin{cases} \dfrac{\omega_{cp}(L_m - L_h)^2 + L_h(2L_m - L_h)(\omega_c + \omega_s)}{8f}, & \text{if there is a hanger at mid-span} \\[4mm] \dfrac{\omega_{cp}(L_m - L_h)^2 + L_h(2L_m - L_h)(\omega_c + \omega_s) - \omega_s\lambda^2}{8f}, & \text{if there is no hanger at mid-span} \end{cases} \tag{4.9}$$

or in terms of local sag,

$$H = \begin{cases} \dfrac{(\omega_c + \omega_s)L_h^2}{8f_h}, & \text{if there is a hanger at mid-span} \\[4mm] \dfrac{(\omega_c + \omega_s)L_h^2 - \omega_s\lambda^2}{8f_h}, & \text{if there is no hanger at mid-span} \end{cases} \tag{4.10}$$

and,

$$y(x) = \begin{cases} \dfrac{x[\omega_{cp}(x-L_m)-L_h(\omega_c+\omega_s-\omega_{cp})]}{2H}, & for \ 0 \leq x < (L_m-L_h)/2 \\[2em] \dfrac{[(L_m-L_h)^2(\omega_c+\omega_s-\omega_{cp})+4x(\omega_c+\omega_s)(x-L_m)]}{8H}, & for \ (L_m-L_h)/2 \leq x \leq (L_m+L_h)/2 \\[2em] \dfrac{(x-L_m)[\omega_{cp}(x)+L_h(\omega_c+\omega_s-\omega_{cp})]}{2H}, & for \ (L_m+L_h)/2 \leq x < L_m \end{cases} \qquad (4.11)$$

where, within the domain $(L_m - L_h)/2 \leq x \leq (L_m + L_h)/2$, x is defined only at hanger locations. Simplified formulas for alternate scenarios may be similarly derived from Equations (4.2) to (4.8) though the complexity of the solution markedly increases when overlap is provided between the stay cables and hangers ($d_0 < 0$).

When computing the unstressed length of the cable, a segmental approach will generally provide superior accuracy. Introducing once more the segment/node numbering scheme shown in Figure 4.4, the stressed length and elastic elongation of an individual segment of cable can be approximated as,

$$C_m = \lambda_m \sqrt{1+\Omega_m{}^2}\left[1+\frac{1}{24}\frac{\Psi_{c_m}{}^2}{\left(1+\Omega_m{}^2\right)}\right] \qquad bis \ (3.61)$$

and,

$$\Delta_{e\,m} = \frac{H\lambda_m}{E_c A_c}\left[1+\Omega_m{}^2+\frac{1}{12}\Psi_{c_m}{}^2\left(1+\Omega_m{}^2\right)\right] \qquad bis \ (3.62)$$

wherein, the dimensionless coefficients are given by,

$$\Psi_{c_m} = \frac{\omega_c \lambda_m}{H} \qquad and \qquad \Omega_m = \frac{h_m}{\lambda_m}$$

All that is required now is the projected rise of each cable segment, h_m, which may be expressed as,

$$h_m = y_m - y_{m-1} \qquad bis \ (3.63)$$

where y_m represents the cable ordinates at a given node, m. In computing the above formulas, the cable ordinates can be determined from Equation(s) (4.2) to (4.4)/(4.11), and similarly, the horizontal force in the cable, H, can be determined from Equation (4.6)/(4.9). Thereafter, summing the unstressed lengths of all cable segments yields the total unstressed length of the cable.

$$USL_{Total} = \sum_{m=1}^{N_{hangers}+1} (USL_m) = \sum_{m=1}^{N_{hangers}+1} \left(C_m - \Delta_{e\,m}\right) \qquad \text{bis (4.47)}$$

4.1.1.4 Approximate Method to Compute Projected Self-Weight of Cable

Substituting Equation (4.1) into Equation (3.17) gives the expression for the projected self-weight of the cable in the stayed regions as,

$$\omega_{cp} = \omega_c \sqrt{1 + \left(\frac{2\,y_B}{L_m - L_h}\right)^2} \qquad (4.12)$$

where,

$$y_B = y\left(x = \frac{L_m - L_h}{2}\right)$$

Still, an issue arises when attempting to compute, ω_{cp}, in that from Equations (4.11) & (4.12), y_B is in itself a function of ω_{cp}. Consequently, as a result of the radical, the root of Equation (4.12) cannot be easily evaluated algebraically. A much simpler expression can however be obtained without introducing any appreciable error by using ω_c in place of ω_{cp} to approximate y_B. As an example, using Equations (4.9) & (4.11) for the ordinates of the cable and neglecting the configuration of the hangers results in the following approximate expression for ω_{cp},

$$\omega_{cp} \cong \omega_c \sqrt{1 + 4f^2 \left[\frac{\omega_c(L_m + L_h) + 2\omega_s L_h}{\omega_c L_m{}^2 + \omega_s L_h(2L_m - L_h)}\right]^2} \qquad (4.13)$$

4.1.1.5 The Relationship between Global Sag and Local Sag

Referring to Figure 4.1, the relationship between the local and the global sag of the cable can be expressed as,

$$f_h = f - y_B \qquad (4.14)$$

By neglecting the configuration of the hangers and by using Equations (4.9) & (4.11) to obtain, y_B, Equation (4.14) may be expanded into the following approximate function which relates the global sag ratio of the cable to the local sag ratio of the suspended region,

$$\frac{f_h}{L_h} \cong L_R \left(\frac{f}{L_m}\right) \left[\frac{\omega_c + \omega_s}{\omega_{cp}(1 - L_R)^2 + L_R(\omega_c + \omega_s)(2 - L_R)}\right] \qquad (4.15)$$

where the parameter, L_R, is defined as the ratio between the length of the suspended region and the span of the cable, which from here on will be referred to as the suspension ratio,

$$L_R = \frac{L_h}{L_m}$$

In this manner, an approximate relationship between the global and local sag of the cable can be expressed independent of the span of the cable.

Several plots are presented in Figure 4.6 in order to better illustrate how the various parameters in Equation (4.15) affect the local sag ratio of the cable. From these plots it is clear that when the global sag ratio is fixed,

> ➢ Increasing the suspension ratio has the effect of increasing the local sag ratio of the cable;

> ➢ Increasing the dead load ratio (ω_c: ω_s) has the effect of decreasing the local sag ratio of the cable, and;

> ➢ The effect that the self-weight of the cable has on the local sag ratio of the cable diminishes as the suspension ratio increases.
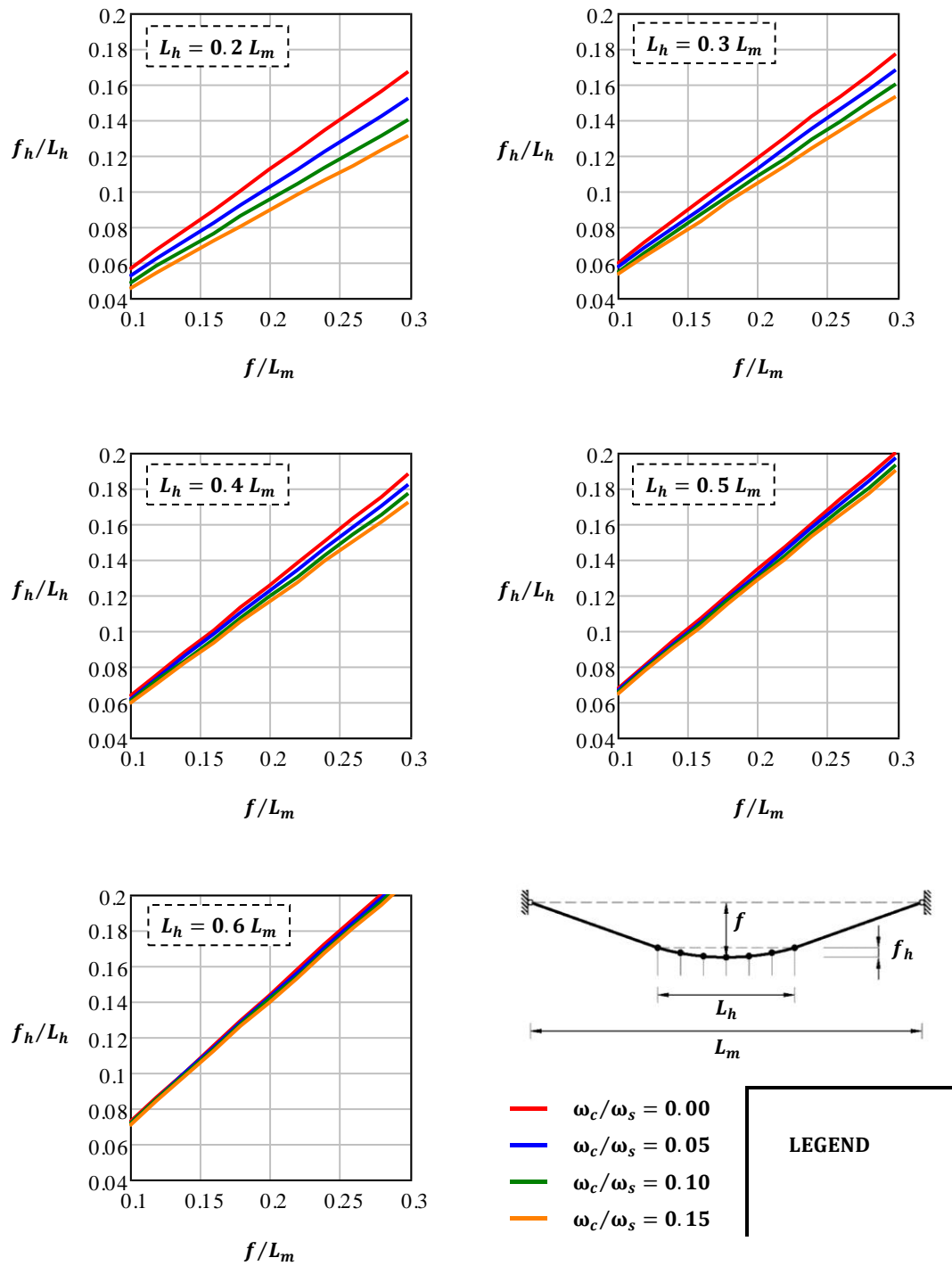
Figure 4.6: The Relationship Between Global and Local Sag

4.1.1.6   Examining the Error in the Parabolic Approximation

In accordance with Sections 3.1.1.3 and 3.2.1.3, this section evaluates the accuracy of the parabolic approximation in computing the ordinates and unstressed length of a partially-laden cable. As follows, Figure 4.7 plots the maximum absolute deviation between the ordinates obtained using the catenary solution (denoted by y_c), and those obtained using Equation (4.11) (denoted y_p) for a range of dead load ratios. For reference, the case of a fully-laden cable is also included (shown by the dashed lines). All values of, x, in the stayed regions of the cable are considered, though for the suspended region, only the values of, x, corresponding to hanger nodes are considered. This is because, as mentioned previously, the continuous form of the parabolic approximation is generally not valid in the suspended region of the cable at intermediate points between hangers. For clarity and due to the gross difference in values, the vertical scales in Figure 4.7 have been adjusted for each global sag ratio examined.

Figure 4.7 shows that for equal global sag and equal dead load ratio ($\omega_c : \omega_s$), the parabolic approximation is more accurate in computing the ordinates for a partially-laden cable in comparison to a fully-laden cable. This is not surprising considering that the error produced from the parabolic approximation is normally much lower for stay cables than it is for suspension cables (see Figures 3.4 and 3.16). Nonetheless, the accuracy of the parabolic solution markedly decreases for larger sag ratios, and therefore, the parabolic approximation may not provide the required accuracy in computing the ordinates for partially-laden cables with a relatively large sag, suspension, and/or dead load ratio. Further, in general, the accuracy of the parabolic approximation decreases as the suspension ratio increases; however, this statement is not always valid when the dead load ratio is high. Figure 4.7 shows that when the suspension ratio equals to 0.2, the error in ordinates rapidly increases after a certain threshold value of the dead load ratio is reached. The cause for this disjunction can be explained as follows.

The maximum error plotted in Figure 4.7 is a function of the error produced from the stayed regions and the error produced from the suspended region. When the dead load ratio is small, the sag in the stayed regions is also small, and as a result, the error produced from the suspended region always governs. However, as the dead load ratio increases, the sag of the cable in the stayed regions becomes more pronounced, and as shown in Figure 3.4, this has the effect of significantly increasing the error in those regions. After a certain threshold value is reached, the error in the stayed regions starts to govern, and this consequently causes a dramatic change in the slope of the error plot. The reason why this change of slope is only observed for a suspension ratio of 0.2 in Figure 4.7 is because the error produced in the stayed region is also a function of the length of the stayed region, and thus the error is smaller in cables with larger suspension ratios. As a result, the change in slope occurs outside of the domain given in Figure 4.7 for cables with large suspension ratios.
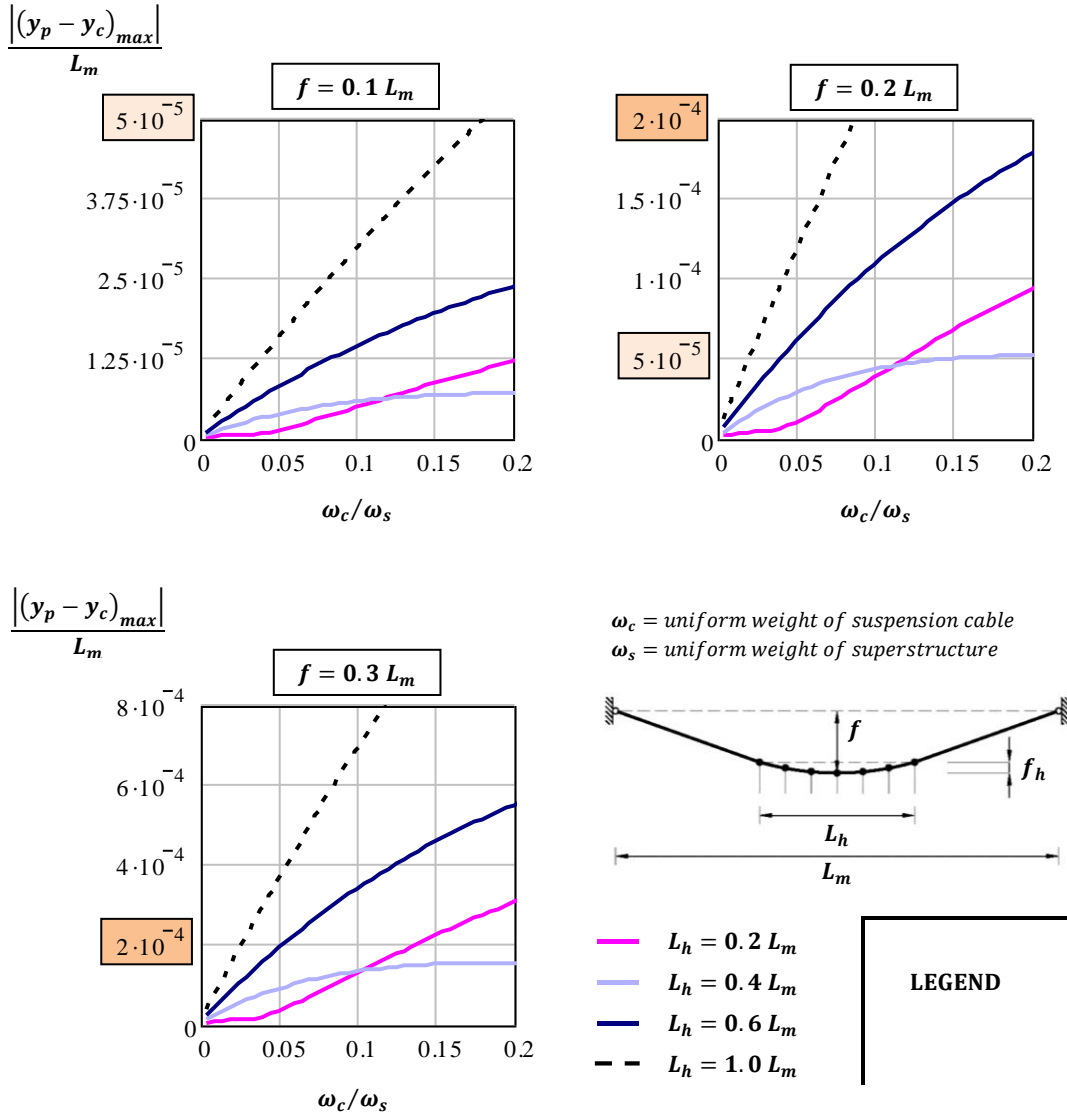
Figure 4.7: Error Produced using Simplified Parabolic Approximation versus Dead Load Ratio

In fact, the specific threshold value that correlates to a sudden increase in error is only of minor practical importance given that cables with small suspension ratios should produce relatively small dead load ratios ($\omega_c : \omega_s$) when the cables are properly proportioned. This is reflected in Figure 4.8 which plots the error in ordinates as a function of the span length assuming an unfactored live load ratio of 0.6 and an allowable cable stress of 800MPa. Under these conditions, although the plot for a suspension ratio of 0.2 exhibits a slight change in slope at a span of 500 metres when the global sag

ratio equals 0.1 and at roughly 800 metres when the global sag ratio equals 0.2, in all cases, the magnitude of the error is trivial.

$$\frac{\left|(y_p - y_c)_{max}\right|}{L_m}$$
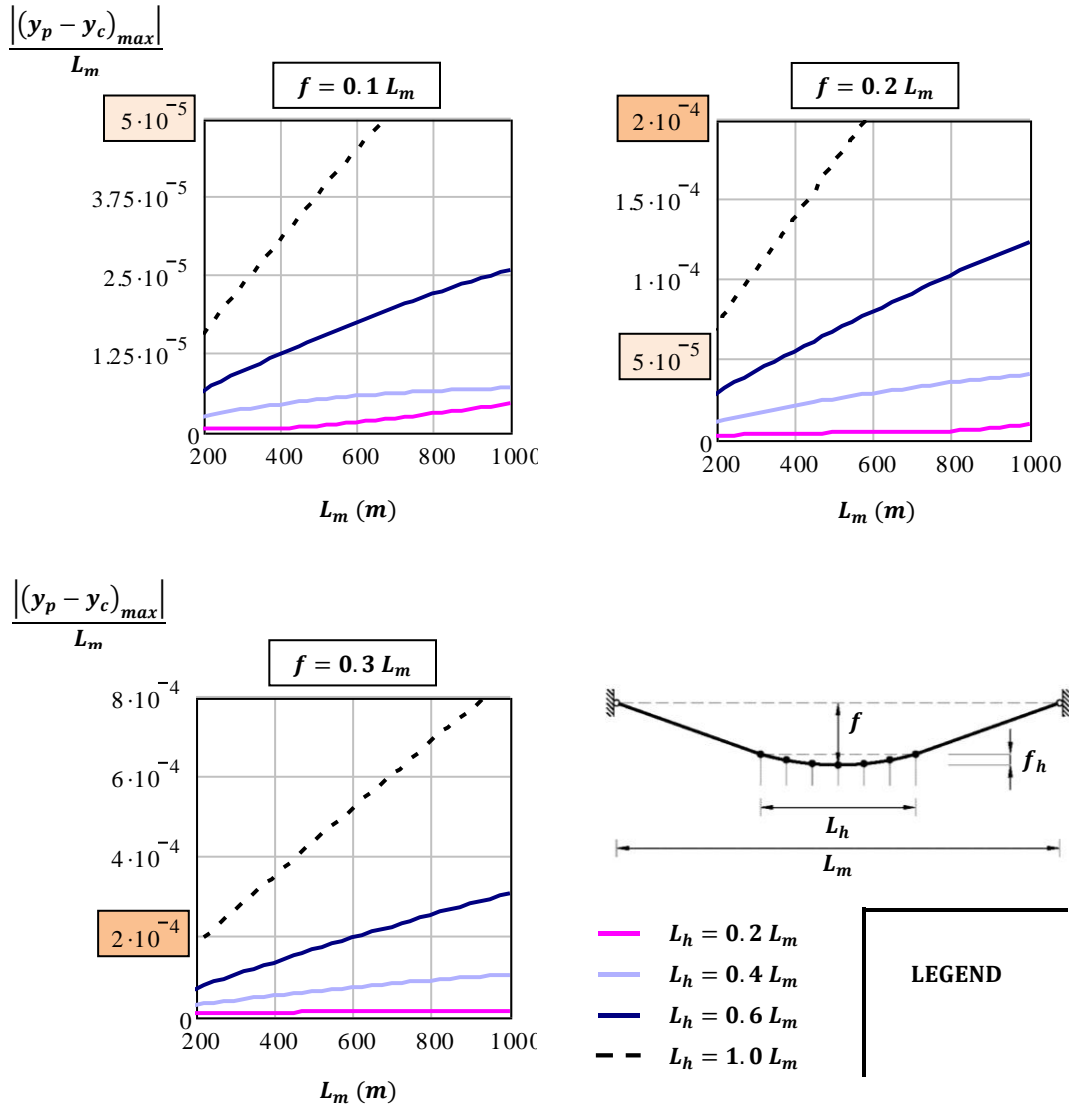
Figure 4.8: Error Produced using Simplified Parabolic Approximation versus Span Length
Parameters: γ_c = 0.09MN/m³, σ_{allow} = 800MPa, ω_p = 0.6·ω_s

Using the same assumptions to size the cable, the error with respect to the unstressed length is plotted in Figure 4.9 as a function of the span length. In computing the error, the hanger spacing was set constant at 5% of the span length. Similar to fully-laden cables, because a segmental approach is

being utilized for the parabolic solution, the error does not change significantly when a different hanger spacing is assumed. However, the error values reported in Figure 4.8 and Figure 4.9 will change somewhat for different unfactored live load ratios (ω_p : ω_s). A comprehensive list of tabulated values is provided in Tables 4.1 and 4.2.
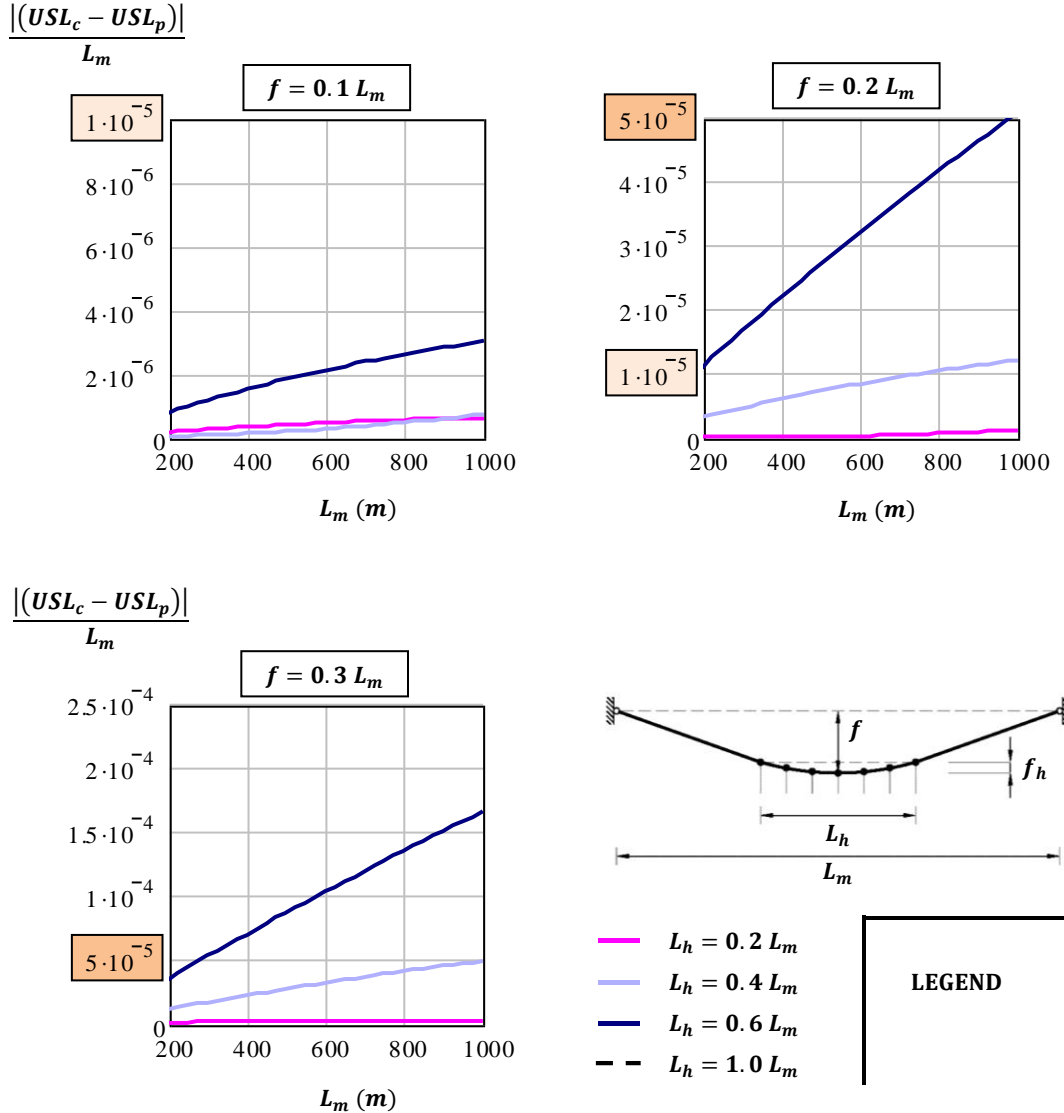
Figure 4.9: Error in USL using Simplified Parabolic Approximation
Parameters: γ_c = 0.09MN/m³, σ_{allow} = 800MPa, ω_p = 0.6·ω_s, E_c = 200GPa, λ = 0.05·L_m

Table 4.1: Error in Ordinates Produced using Simplified Parabolic Approximation (x10^{-5})*

$\dfrac{f}{L_m}$	$\dfrac{L_h}{L_m}$	$\dfrac{\omega_p}{\omega_s}$	L_m (m)				
			200	400	600	800	1000
		0.2	0.02	0.03	0.09	0.18	0.30
	0.2	0.4	0.03	0.04	0.13	0.25	0.39
		0.6	0.03	0.06	0.17	0.31	0.48
		0.2	0.18	0.31	0.42	0.51	0.58
0.1	0.4	0.4	0.20	0.35	0.47	0.56	0.62
		0.6	0.23	0.38	0.50	0.59	0.64
		0.2	0.49	0.94	1.36	1.75	2.10
	0.6	0.4	0.56	1.07	1.54	1.96	2.34
		0.6	0.64	1.20	1.71	2.15	2.54
		0.2	0.13	0.19	0.20	0.28	0.54
	0.2	0.4	0.14	0.20	0.21	0.43	0.79
		0.6	0.15	0.20	0.26	0.61	1.06
		0.2	0.79	1.47	2.05	2.54	3.00
0.2	0.4	0.4	0.91	1.67	2.29	2.83	3.32
		0.6	1.02	1.86	2.51	3.10	3.59
		0.2	2.11	4.12	6.04	7.88	9.63
	0.6	0.4	2.44	4.74	6.92	8.97	10.90
		0.6	2.77	5.36	7.76	10.00	12.09
		0.2	0.32	0.52	0.62	0.61	0.75
	0.2	0.4	0.36	0.56	0.63	0.64	1.19
		0.6	0.40	0.59	0.62	0.88	1.71
		0.2	1.92	3.63	5.13	6.45	7.57
0.3	0.4	0.4	2.21	4.14	5.79	7.18	8.46
		0.6	2.50	4.62	6.39	7.87	9.27
		0.2	5.12	10.05	14.78	19.34	23.72
	0.6	0.4	5.94	11.60	16.99	22.11	26.98
		0.6	6.76	13.12	19.12	24.77	30.08

*Error values are in the form: $\left|\left(y_p - y_c\right)_{max}\right|/L_m$

*Parameters: γ_c = 0.09MN/m³, σ_{allow} = 800MPa

Table 4.2: Error in Unstressed Length Produced using Simplified Parabolic Approximation (x10^{-5})*

$\dfrac{f}{L_m}$	$\dfrac{L_h}{L_m}$	$\dfrac{\omega_p}{\omega_s}$	L_m (m)				
			200	400	600	800	1000
0.1	0.2	0.2	0.02	0.04	0.05	0.06	0.07
		0.4	0.02	0.04	0.05	0.06	0.06
		0.6	0.02	0.03	0.05	0.06	0.06
	0.4	0.2	0.02	0.04	0.06	0.08	0.10
		0.4	0.01	0.02	0.04	0.06	0.09
		0.6	0.00	0.01	0.03	0.05	0.07
	0.6	0.2	0.04	0.07	0.10	0.13	0.15
		0.4	0.06	0.11	0.16	0.20	0.23
		0.6	0.08	0.15	0.21	0.26	0.30
0.2	0.2	0.2	0.01	0.02	0.05	0.07	0.11
		0.4	0.00	0.01	0.03	0.07	0.11
		0.6	0.01	0.00	0.02	0.06	0.12
	0.4	0.2	0.21	0.40	0.57	0.72	0.85
		0.4	0.26	0.50	0.71	0.89	1.04
		0.6	0.32	0.60	0.84	1.04	1.21
	0.6	0.2	0.79	1.56	2.31	3.04	3.74
		0.4	0.96	1.88	2.77	3.62	4.43
		0.6	1.12	2.19	3.21	4.17	5.08
0.3	0.2	0.2	0.07	0.11	0.14	0.15	0.14
		0.4	0.09	0.16	0.20	0.21	0.19
		0.6	0.12	0.20	0.25	0.25	0.22
	0.4	0.2	0.82	1.59	2.33	3.02	3.66
		0.4	0.99	1.92	2.79	3.59	4.32
		0.6	1.16	2.24	3.23	4.12	4.93
	0.6	0.2	2.60	5.14	7.64	10.07	12.46
		0.4	3.09	6.09	9.01	11.84	14.58
		0.6	3.58	7.03	10.35	13.55	16.62

*Error values are in the form: $\left|\left(USL_c - USL_p\right)_{max}\right|/L_m$

*Parameters: γ_c = 0.09MN/m³, σ_{allow} = 800MPa, E_c= 200GPa, λ = 0.05·L_m

4.1.2 Deformation Characteristics

This section focuses on the response of partially-laden suspension cables to vehicular loading. Analogous to Section 3.2.2, in carrying out the computations in this section, the following simplifications are made to limit the number of parameters involved:

- The weight of the hangers and hanger assemblies is neglected relative to the combined weight of the suspension cable, ω_c, and superstructure, ω_s.

- In the suspended region dead loads are considered to act uniformly along the projected length of the cable. Unless otherwise noted, the dead load of the cable in the stayed regions is assumed to act along the cable chord.

- The effects of concentrated wheel loads are neglected and live load is idealized as a uniformly distributed load with magnitude, ω_p.

- Based on standard cable types applied in bridge engineering, an effective unit weight of 0.09MN/m^3, and a modulus of elasticity of 200GPa are assumed

In addition to these simplifications, to reduce the number of computations, a simple and convenient non-iterative expression is derived in Section 4.1.2.1. This expression is used to determine an appropriate size for the partially-laden suspension cable area, given a specific set of design parameters.

4.1.2.1 Cable Sizing

Several additional assumptions are required to determine an approximate cable sizing equation for a partially-laden suspension cable. These assumptions are stated as follows:

- Nonlinear behaviour is ignored. (The governing loading scenario for the maximum tension in the cable occurs when the entire span is loaded. In practical cases, under this loading scenario, nonlinear effects do not have a significant effect on the internal cable forces.)

- The influence of the superstructure bending stiffness is ignored. It follows that the influence of the adjoining array of stay cables is also ignored.

- The parabolic approximation may be accurately applied. In addition, as a modification to the parabolic approximation included in Section 4.1.1.3, the self-weight of the cable is assumed to act over the projected length of the entire cable. (This assumption slightly underestimates the maximum cable force; however, this is offset by the conservative nature of the previous assumption.)

- ▪ The area required for the partially-laden suspension cable is independent of the area required for the anchor cables.

With these assumptions in mind, the maximum tension in the cable can be expressed as a function of the horizontal force in the cable and the slope of the cable curve at one of the supports,

$$T_{max} = H \sqrt{1 + \left(\frac{dy}{dx}\bigg|_{x=0}\right)^2} \qquad (4.16)$$

Adopting an allowable stress design approach then gives the required area of the cable as,

$$A_{c\_req} = \frac{T_{max}}{\sigma_{allow}} = \frac{H}{\sigma_{allow}} \sqrt{1 + \left(\frac{dy}{dx}\bigg|_{x=0}\right)^2} \qquad (4.17)$$

From here on, it is more convenient to work in terms of the cable weight rather than the cable area. Accordingly, substituting the self-weight of the cable in place of A_{c_req} yields,

$$\omega_c = \frac{\gamma_c H}{\sigma_{allow}} \sqrt{1 + \left(\frac{dy}{dx}\bigg|_{x=0}\right)^2} \qquad (4.18)$$

Thereafter, using Equations (4.9) & (4.11), the slope of the cable curve at the supports can be expanded to obtain the following expression,

$$\omega_c = \frac{\gamma_c L_m[\omega_c + \omega_s L_R(2 - L_R)]}{8\, S_R \sigma_{allow}} \sqrt{1 + 16{S_R}^2 \left(\frac{\omega_c + \omega_s L_R}{\omega_c - \omega_s {L_R}^2 + 2\omega_s L_R}\right)^2} \qquad (4.19)$$

where, as defined previously, the parameter, S_R, represents the global cable sag-to-span length ratio ($f{:}L_m$), and L_R is the suspension ratio ($L_h{:}L_m$). To arrive at an expression which does not require iteration, ω_c must be isolated. Unfortunately, the presence of the radical makes the solution highly complex. Note that this problem does not arise for fully-laden suspension cables because when $L_R = 1$ the parabolic slope of the cable curve can be expressed independent of the self-weight of the cable. Nonetheless, since ω_c is assumed to act uniformly over the entire projected length of the partially-laden cable, it is reasonable to also assume that the effect ω_c has on the slope of the cable curve at the supports is minor. With this added assumption, Equation (4.19) becomes,

$$\omega_c = \frac{\gamma_c L_m [\omega_c + \omega_s L_R (2 - L_R)]}{8\, S_R \sigma_{allow}} \sqrt{1 + 16 \left(\frac{S_R}{2 - L_R} \right)^2} \qquad (4.20)$$

As an additional consideration, Equation (4.20) was derived using the dead load cable forces; however, the governing loading scenario for the cable area occurs when the entire span is loaded with dead, and live load. Therefore, ω_s in Equation (4.20) needs to be replaced by $(\omega_s + \omega_p)$, and once ω_c is isolated, the final expression can be written as,

$$\omega_c = \frac{(\omega_s + \omega_p)\, \xi\, L_R\, (2 - L_R) \sqrt{1 + 16 \left(\frac{S_R}{2 - L_R} \right)^2}}{1 - \xi \sqrt{1 + 16 \left(\frac{S_R}{2 - L_R} \right)^2}} \qquad (4.21)$$

where, as in the case of fully-laden suspension cables, the dimensionless parameter, ξ, is defined by,

$$\xi = \frac{\gamma_c\, L_m}{8\, \sigma_{allow}\, S_R}$$

Note that, for $L_R = 1$, Equation (4.21) reduces to the same equation presented in Section 3.2.2 for fully-laden cables. For other values of L_R, Figure 4.10 shows how the self-weight varies with increasing span length. Although the values in Figure 4.10 are based on the assumption that the self-weight of the cable acts along the projected length of the entire cable, and further, that the self-weight of the cable does not notably affect the slope of the cable at the supports, through investigation it was found that for $S_R \leq 0.3$ and $L_m \leq 1000$ metres, the error introduced as a result of these assumptions is at most 2.5%.

Suspension Ratio = 0.2

$$\frac{\omega_c}{\omega_s + \omega_p}$$

$L_m \ (m)$

Suspension Ratio = 0.4

$$\frac{\omega_c}{\omega_s + \omega_p}$$

$L_m \ (m)$

Suspension Ratio = 0.6

$$\frac{\omega_c}{\omega_s + \omega_p}$$

$L_m \ (m)$

$S_R = 0.1$ .... $S_R = 0.2$ —— $S_R = 0.3$
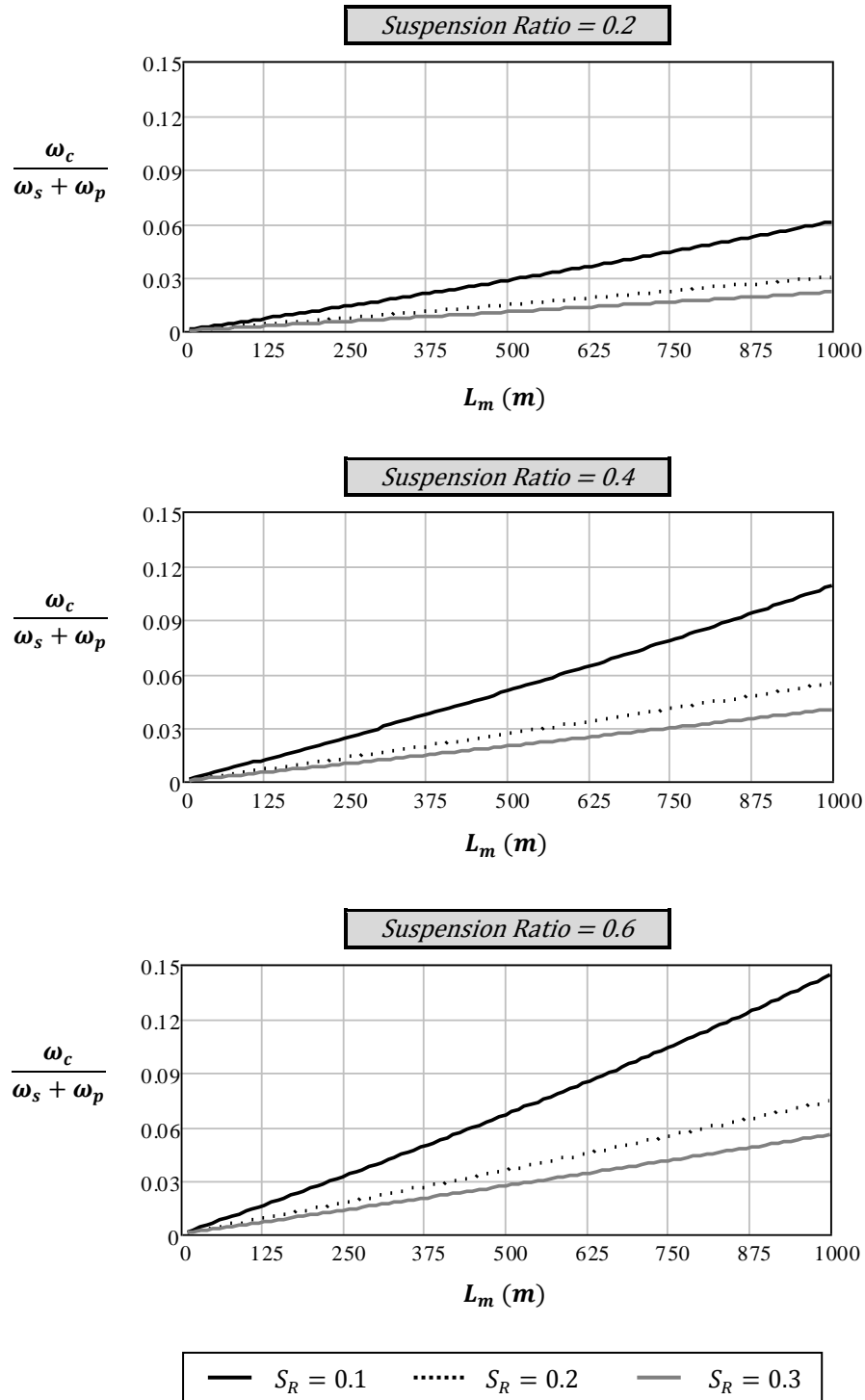
Figure 4.10: Variation of Cable Weight with Span Length in Partially-Laden Suspension Cables
Parameters: $\gamma_c = 0.09$MN/m^3, $\sigma_{allow} = 800$MPa

4.1.2.2 General Response

The general response of an isolated partially-laden cable will be studied using the same methodology presented in Section 3.2.2.1. Accordingly, assuming a live load ratio equal to 0.6, the deflection of a 1000 metre span partially-laden cable was computed numerically for a variety of loading scenarios. Suspension ratios of 0.2 and 0.6 were considered. A fully-laden cable (suspension ratio of 1.0) is also included for comparison. In each case, the cable area is updated using Equation (4.21), and for consistency, the local sag ratio (f_h:L_h) is kept constant at a value of 0.1. The results for each suspension ratio are displayed in Figure 4.11 (note: the plot for the fully-laden cable is the same as Figure 3.20).

Similar to the fully-laden cable, it was observed that the location of the maximum vertical deflection along the span of the partially-laden cables falls, in most cases, within close proximity to the centre of the applied live load. For the loading scenario when the entire suspended span is loaded with live load it can be seen that cables with equal local sag ratio but different suspension ratios yield a similar maximum deflection. Through investigation, it turns out that the same is also true for partially-laden cables with larger local sag ratios. Nonetheless, for other loading scenarios, the maximum deflection is shown, in some cases, to notably vary with changes in suspension ratio. To understand why this is the case, it is important to investigate further the effect that the stayed regions have on the response of a partially-laden cable.

To isolate the effects of the stayed regions, Figure 4.12 compares the deformation response of the partially-laden cables in Figure 4.11 with the deformation response of fully-laden cables that have equivalent properties to the suspended regions of the partially-laden cables. For each loading scenario, the comparison is made by subtracting the maximum deflection in the fully-laden cable, denoted by $(\delta_{max})_{FL}$, from the maximum deflection in the partially-laden cable, denoted by $(\delta_{max})_{PL}$. The result is then normalized with respect to peak deflection (i.e. the maximum deflection considering all loading scenarios) in the fully-laden cable $(\delta_{peak})_{FL}$. For clarity, the vertical scales of the plots are adjusted based on the ordinates.

From Figure 4.12, regardless of the suspension ratio or the loading scenario, the largest difference in deflection occurs when the load is positioned asymmetrically. It can also be seen that for longer loaded lengths the stayed region has a substantial effect on the amount of deflection and that effect increases as the suspension ratio decreases. Again, this is not unexpected because the stayed regions can be idealized by a pair of springs whose stiffness can be broken down into: (1) an elastic component, k_E, which controls the amount of deformation in the stayed region due to strain, and (2) a nonlinear geometric component, k_G, which controls the amount of strain-free deformation in the stayed region (see Figure 4.13).

Suspension Ratio = 1.0

L_p

x_p

ω_p

ω_s

$0.1 \cdot L_h$

$L_h = 1.0 \cdot L_m$

$\dfrac{\delta_{max}}{L_m}$

x_p/L_h

L_p/L_h

Suspension Ratio = 0.6

L_p

x_p

ω_p

ω_s

$0.1 \cdot L_h$

$L_h = 0.6 \cdot L_m$

$\dfrac{\delta_{max}}{L_m}$

x_p/L_h

L_p/L_h

Suspension Ratio = 0.2

L_p

x_p

ω_p

ω_s

$0.1 \cdot L_h$

$L_h = 0.2 \cdot L_m$

$\dfrac{\delta_{max}}{L_m}$

x_p/L_h

L_p/L_h
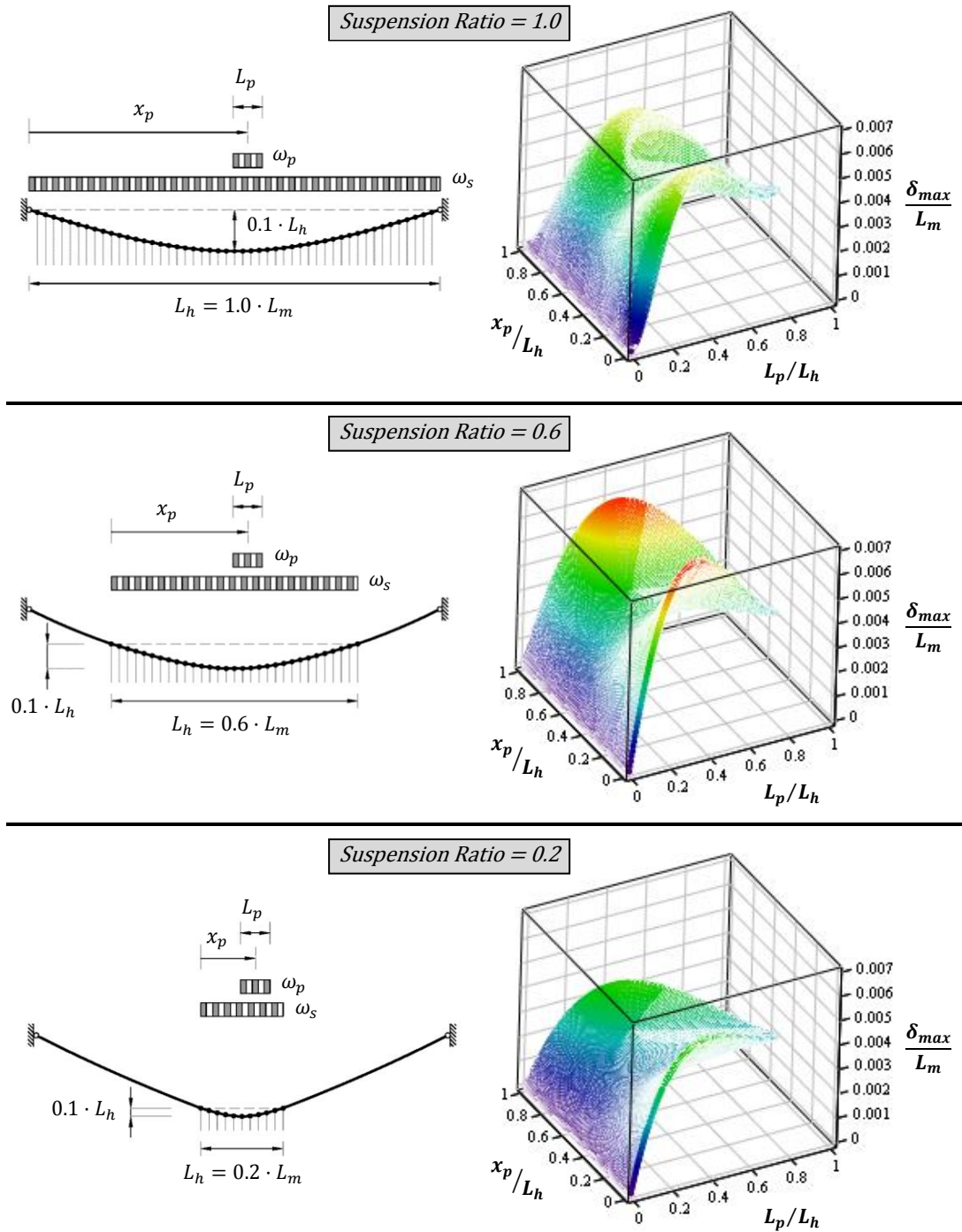
Figure 4.11: Max Deflection under Live Load for Different Partially-Laden Cables with Equal Local Sag Ratio

Parameters: L_m = 1000m, γ_c = 0.09MN/m³, E_c = 200GPa, σ_{allow} = 800MPa, ω_p = 0.6·ω_s
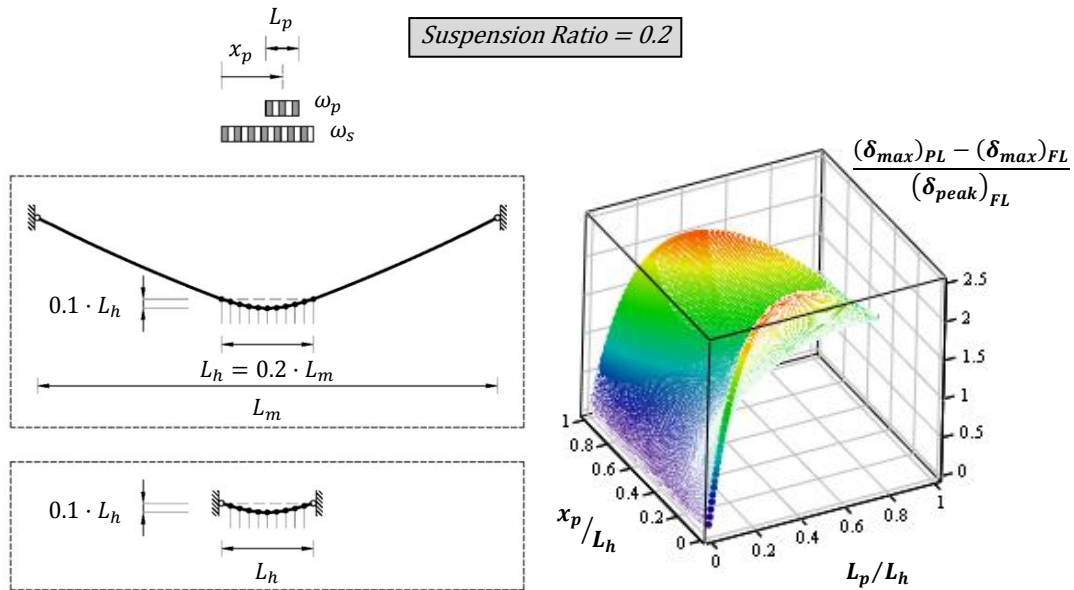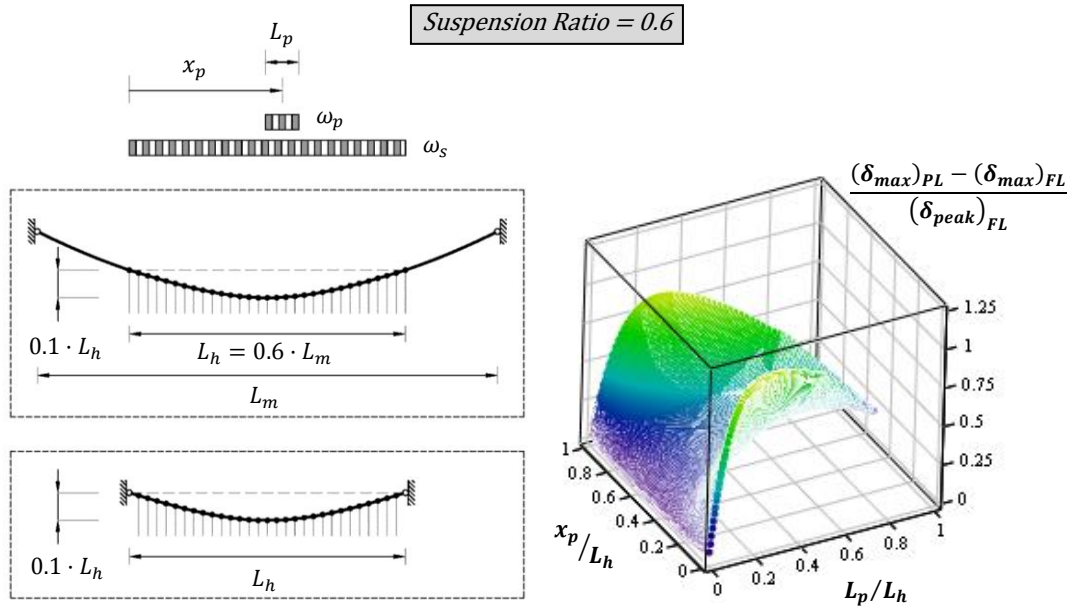
Figure 4.12: Isolated Effect of Stayed Region for Different Partially-Laden Cables with Equal Local Sag Ratio

Parameters: L_m = 1000m, γ_c = 0.09MN/m³, E_c = 200GPa, σ_{allow} = 800MPa, ω_p = 0.6·ω_s

The elastic component is proportional to the area of the cable and inversely proportional to the length of the stayed region. As the suspension ratio decreases, the area of the cable gets smaller (refer to Figure 4.10), and the length of the stayed region gets longer. Thus, decreasing the suspension ratio lowers the elastic stiffness of the stayed region which in turn increases deflections. It should be recognized though that the decrease in the elastic stiffness due to the decrease in cable area is more or less offset by the consequent decrease in the cable force at the stayed region (when the local sag ratio is constant the force in the cable at the stayed region will be approximately proportional to the suspended length – refer to Equation (4.10)). Therefore, the length of the stayed region is the primary factor contributing to the decrease in elastic stiffness. Similarly, the geometric stiffness also decreases when the length of the stayed region increases, which again increases deflections (refer to Section 3.1.2).
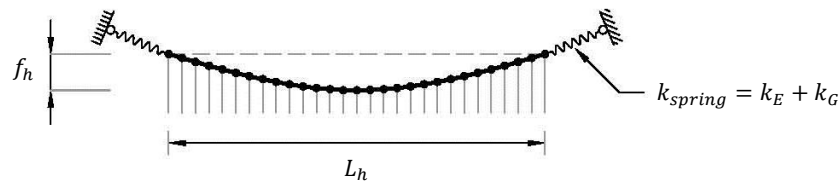
Figure 4.13: Idealization of a Partially-Laden Cable

For symmetric loading scenarios, as the local sag ratio increases, the values reported in Figure 4.12 do not change considerably. So long as the cables are properly sized, the chord stress in the stayed regions does not significantly change with reasonable increases in local sag. Since the projected length of the stayed regions remains constant with changes in the local sag, neither the geometric nor the elastic stiffness of the stayed regions is notably affected. Conversely, the greatest amount of variance occurs from asymmetric loading scenarios because as the local sag ratio increases the stayed regions become less effective at resisting sidesway.

Despite the above observations, it should not be construed that a partially-laden cable will always exhibit larger deflections in comparison to a fully-laden cable. When comparing the deflection of fully-laden and partially-laden cables it is more appropriate to fix the global sag ratio as oppose to the local sag ratio because it is the former which controls the proportions of other bridge components such as the tower height. Accordingly, when the global sag ratio and main span length are set constant, the peak deflection in a partially-laden cable will vary with the suspension ratio as shown in Figure 4.14. Under these conditions, it is clear that for any global sag ratio, the peak deflection increases with increasing suspension ratio and is greatest in the case of a fully-laden cable (suspension ratio of 1.0).
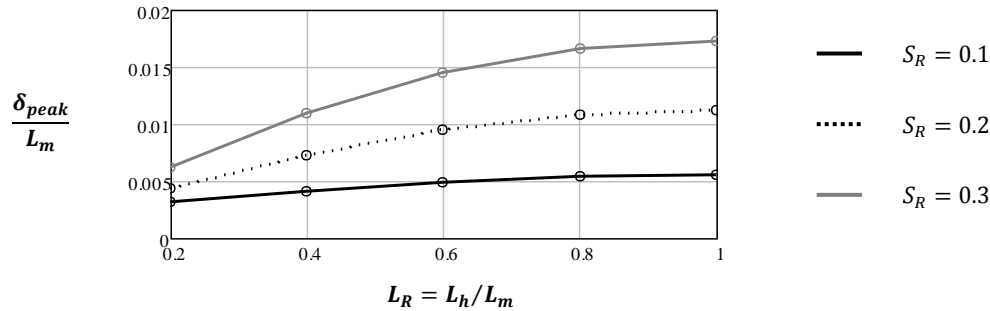
Figure 4.14: Maximum Deflection as a Function of the Suspension Ratio
Parameters: L_m = 1000m, γ_c = 0.09MN/m³, E_c = 200GPa, σ_{allow} = 800MPa, ω_p = 0.6·ω_s

The trends displayed in Figure 4.14 can primarily be attributed to scale effects. In Section 3.2.2.4, it was demonstrated that for fully-laden cables deflections increase with increasing suspended span. Moreover, a negative trend was observed when the maximum deflection was normalized with respect to the span length (refer to Figure 3.27). When Figure 4.14 is re-plotted with the ordinates normalized according to the suspended span length, L_h, a similar trend occurs (see Figure 4.15). However, it should be recognized that there are other factors which contribute to the response. Specifically, when the global sag ratio is fixed, the local sag ratio will increase with increasing suspension ratio, and this has the effect of increasing strain-free deformations. Additionally, there is the effect of the stayed region.
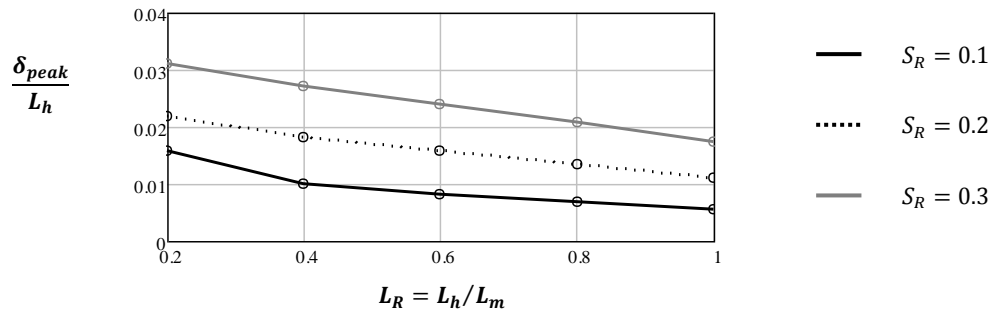
Figure 4.15: Maximum Deflection Normalized According to Suspended Span
Parameters: L_m = 1000m, γ_c = 0.09MN/m³, E_c = 200GPa, σ_{allow} = 800MPa, ω_p = 0.6·ω_s

As a final remark, the general observations made above considering a live load ratio of 0.6 and a span length of 1000 metres are also valid for lesser live load ratios and span lengths.

4.2   Self-Anchored Discontinuous Hybrid Cable Bridges

4.2.1   Fundamental Deformation Characteristics

Partially-laden suspension cables were studied in the previous section in order to better understand their behaviour. However, it can be expected that the behaviour of a partially-laden cable will be affected when the cable is employed in conjunction with other structural components, such as in a bridge. This is particularly true for self-anchored bridges. As such, this section studies what effect cable, superstructure, and loading parameters have on the fundamental system behaviour of a self-anchored discontinuous hybrid cable bridge. This is achieved through means of a simple finite element model which is illustrated in Figure 4.16. As in Section 4.1.2, the effects of concentrated wheel loads are neglected and live load is idealized as a uniformly distributed load. A number of rigid truss elements are used together with a fan type configuration for the stay cables to further simplify the model and to remove the influence of the side-span length and tower bending stiffness.

Figure 4.16: Description of Finite Element Model

Akin to Section 3.2.2.8, the model was analyzed using the finite element program LARSA 4D BRIDGE. In the program, superstructure members are modelled using beam elements and all ground supports are free to translate in the longitudinal direction with the exception of one pin support which is required to stabilize the model against rigid body motion. Tower heights are controlled by the global sag of the partially-laden cable in addition to the offset of the cable at mid-span. The latter is fixed at $L_m/500$. Each stay cable and hanger is modelled as a single truss element with a material unit weight and elastic modulus of 0.09 MN/m^3 and 200 GPa, respectively. The connection points of the stay cables and hangers are uniformly spaced along the span length of the bridge, and the area for each stay cable and hanger is determined based on an allowable chord stress of 800 MPa.

Nonlinear sag effects in the stay cables are taken into account using the tangent modulus approach outlined in Section 3.1.2.1. Based on the results in Section 3.1.2.1, the stay cables nearest to the hangers are subject to the greatest nonlinear effects. In addition, the amount of nonlinearity in those stay cables will increase when the span length is increased and/or the suspension ratio is decreased. Under an extreme scenario when the span length is 1000 metres, the suspension ratio is 0.2, and the live load ratio is 0.6, there will be roughly an 8% maximum difference between the tangent and secant moduli for the stay cables nearest to the hangers. The consequent error in the global demands will be smaller still as a result of the superstructure's bending stiffness. As such, this level of accuracy is considered sufficient given the level of detail included in the finite element model.

To capture sag effects in the stayed regions of the partially-laden cable, the cable is modelled using a series of truss elements, each with a projected length of $L_m/100$ (one half of the hanger spacing). As with the other cable elements, the truss elements are modelled using a material unit weight and elastic modulus of 0.09 MN/m^3 and 200 GPa, respectively. Moreover, Equation (4.21) is utilized to determine the area for the partially-laden cable assuming an allowable stress of 800 MPa. The modulus of elasticity of the truss elements for the partially-laden cable is not adjusted because at the specified level of discretization the sag measured from node-to-node of the truss elements is negligible.

For the loading, the magnitude of the live load applied to the model is considered constant at 75 kN/m, whereas the magnitude of the uniform dead load applied to the superstructure is determined from the value specified for the unfactored live load ratio. Following the same procedure outlined in Figure 3.35 (steps 1 to 9), prior to the application of live load, all elements are initially stressed (axially) to achieve approximately zero nodal deflection under dead load. A second order influence analysis is then carried out to capture all possible loading scenarios.

4.2.1.1 General Response

Currently, there are only three self-anchored cable bridges in the world built with spans in excess of 1000 metres. All are cable-stayed bridges. When studying the basic deformation characteristics of a discontinuous self-anchored hybrid cable bridge it is, therefore, appropriate to start with an extreme span of 1000 metres, and then subsequently study how scaling the main span affects the behaviour. Accordingly, for a 1000 metre span, Figure 4.17 shows the envelopes of the superstructure demands obtained from the second order influence analysis considering an unfactored live load ratio of 0.6. The envelopes are generated assuming a relatively small superstructure flexural stiffness of 1.25E6 MNm^2. Moreover, envelopes are compared for different suspension ratios and multiple values of the global sag ratio, $(S_R = f/L_m)$. The convention for the sign of the demand values is such that a negative deflection is in the direction of gravity, a positive moment causes a 'sagging' deflection, and a negative

axial force causes compression. Although not a great deal is meant to be gained from the specific values of the ordinates as their magnitude depends on the flexural stiffness of the superstructure and the magnitude of the applied loading, several observations can be made regarding the relative magnitude and shape of the plots.

In the suspended region, the demand envelopes possess similar characteristics to those observed for suspension bridges. Specifically, the demands are typically greatest near the quarter points of the suspended region and the peak demands are, in most cases, generated from asymmetrical loading. The only exceptions occur when the suspension ratio and/or the sag ratio are small.

When the suspension ratio is small, the superstructure does not have to span as far between the stayed regions of the bridge which are, by comparison, much stiffer in relation to the suspended region. As a result, the superstructure becomes more effective at limiting strain-free deformations in the partially-laden suspension cable and the peak negative deflection occurs at mid-span from primarily elastic deformation. Evidence of the effectiveness of the superstructure in limiting strain-free deformations is provided in the moment demand envelopes which still show peaks at the quarter points of the suspended span. Decreasing the sag ratio in addition to the suspension ratio serves to further increase the relative amount of deflection due to elastic deformation.

In contrast to other types of cable supported bridges, one unique characteristic of the demand envelopes in Figure 4.17 is the presence of moment cusps near the stay cable-hanger junction. However, the presence of such cusps is not surprising given the dramatic change in stiffness at the junction. The moment cusps will become more diffuse as the bending stiffness of the superstructure is increased, because with increased bending stiffness the superstructure becomes more effective at distributing load across the junction.
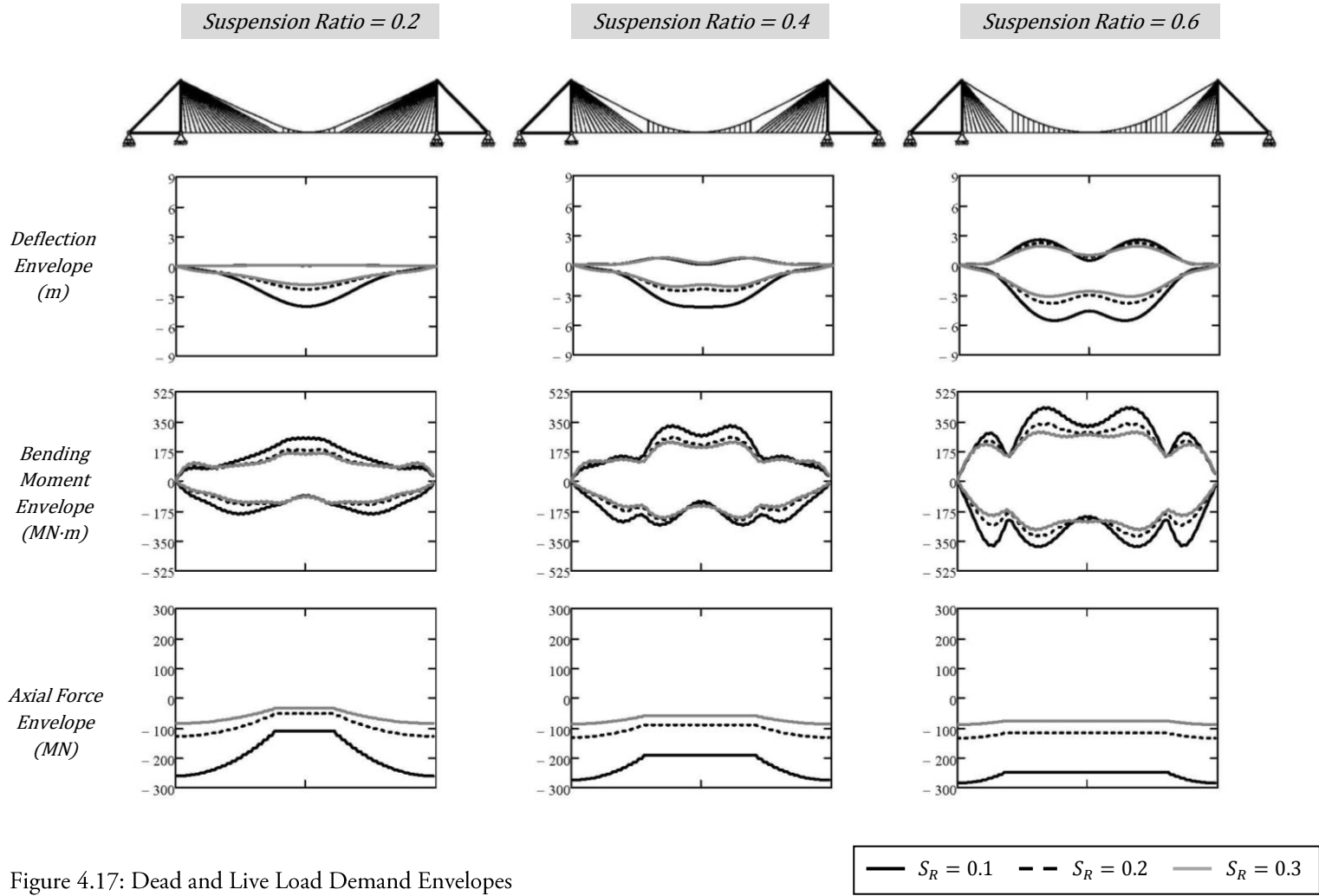
Figure 4.17: Dead and Live Load Demand Envelopes
Parameters: L_m = 1000m, EI_g = 1.25E6MN·m², EA_g = 2.4E5MN, ω_p = 75kN/m, ω_s = ω_p/0.6

4.2.1.2 The Influence of the Sag and Suspension Ratios on Peak Demands

The plots in the previous section provide a good indication of how demands vary along the length of the bridge. However, the plots were generated using the results from a second order influence analysis and, thus, contain some measure of error (more detail provided in Section 4.2.1.4). In addition, the interrelationship between the parameters and demand values is not clearly illustrated. This section, therefore, examines the precise influence the sag and suspension ratios have on the peak demand values.

To fully account for nonlinear effects, for each of the peak demands in Figure 4.17 the corresponding loading scenario was first identified from the second order influence analysis. Then, akin to the procedure outlined in Figure 3.35 (steps 10 to 11), a full nonlinear analysis was run. The results are shown in Figure 4.18. On the right, the peak demands are plotted as a function of the global sag ratio whereas on the left the peak demands are plotted as a function of the suspension ratio.

Similar to prior observations made while studying the effects of self-anchorage in suspension bridges, regardless of the suspension ratio, demands are shown to decrease nonlinearly with increasing sag ratio. Once more, this can be attributed to the combined influence of the axial restraint provided by the pinned support and the destabilizing effect of the self-anchoring compression force. From the left side of Figure 4.18, it is clear that deflections increase when the suspension ratio is increased, which is consistent with the observations made in Section 4.1.2.2. However, because the bending stiffness of the superstructure is now accounted for and the partially-laden cable is self-anchored, the rate of change in the peak deflection increases with increasing suspension ratio, whereas, the rate of change in the superstructure moment demands is nearly constant.
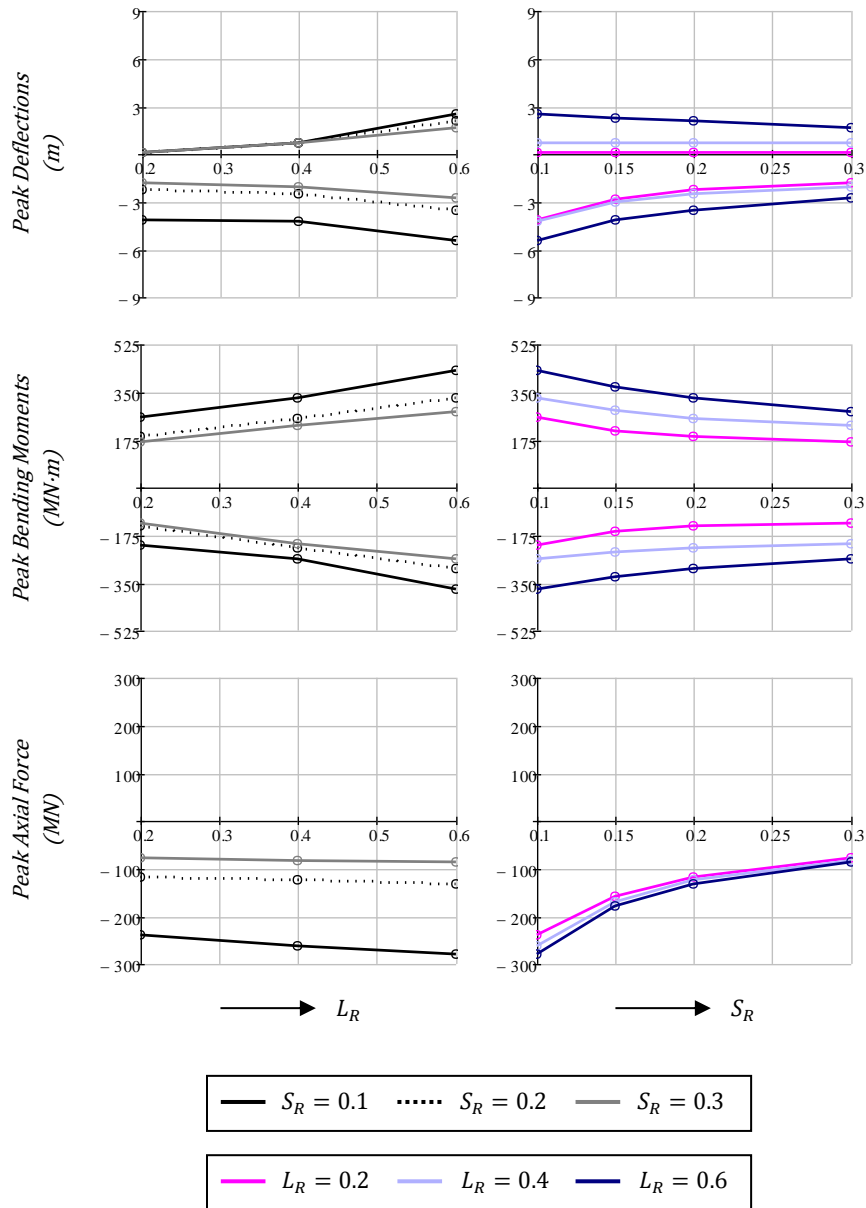
Figure 4.18: Peak Demands as a Function of Suspension Ratio (Left) and Sag Ratio (Right)
Parameters: L_m = 1000m, EI_g = 1.25E6MN·m², EA_g = 2.4E5MN, ω_p = 75kN/m, $\omega_s = \omega_p/0.6$

In regard to the peak axial demands, it can be seen that the value of the suspension ratio does not greatly impact the peak axial force in the superstructure. This can be explained from Figure 4.19 which shows an idealized free-body diagram of the system from which the value of the peak axial force can be approximated. In the figure, the bridge has been 'cut' at the side span face of the tower.

Furthermore, on the main span side, the suspension cable has been 'cut' at the tower, and the superstructure has been 'cut' at the end of the stayed region. The shear force and bending moment in the superstructure have been neglected because the governing loading scenario for the maximum axial force in the superstructure occurs when the entire span is loaded with live load, and under this loading scenario, the cable system carries the majority of the load.
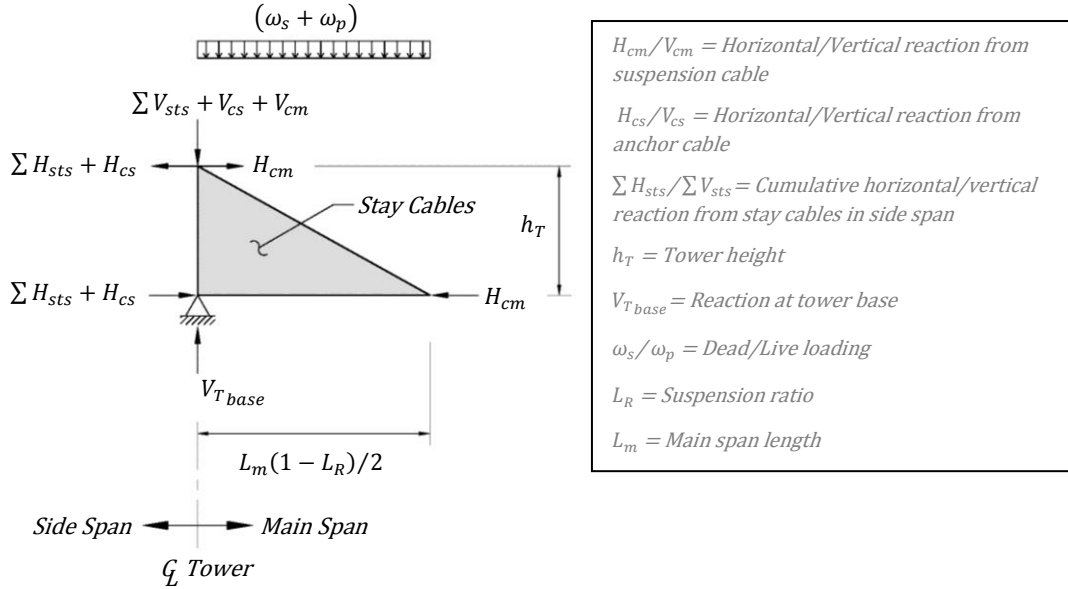
Figure 4.19: Idealized Free-Body Diagram of Hybrid System under Full Live Loading

Summing moments about the base of the tower gives the following expression for the total horizontal reaction at the tower, which also represents the peak axial force in the superstructure,

$$F_{peak} \cong \sum H_{sts} + H_{cs} = \frac{(\omega_s + \omega_p)[L_m(1 - L_R)]^2}{8\,h_T} + H_{cm} \qquad (4.22)$$

Equation (4.9) can be then be substituted in for H_{cm}; however, due to the approximate nature of the expression it is appropriate to make further simplifications by assuming that the weight of the suspension cable is uniform along its span ($\omega_{cp} \approx \omega_c$), and the tower height is roughly equal to the global sag of the suspension cable ($h_T \approx f$). Thereafter, Equation (4.22) becomes,

$$F_{peak} \cong \frac{(\gamma_{cm}A_{cm} + \omega_s + \omega_p)L_m}{8\,S_R} \qquad (4.23)$$

where γ_{cm} represents the unit weight and A_{cm} represents the area of the suspension cable. From

Equation (4.23) it becomes clear why the maximum axial force recorded is not shown to vary markedly with changes in suspension ratio – the only effect the suspension ratio has on the maximum axial force derives from the weight of the suspension cable. On the other hand, as shown in Figure 4.17, the suspension ratio does have a considerable impact on the axial force at mid-span (refer to Equation (4.10)).

4.2.1.3 The Influence of Girder Stiffness

Similar to self-anchored suspension bridges, the bending stiffness of the superstructure/girder(s) can be expected to have a notable effect on the response of self-anchored hybrid cable bridges. To study the effect, the peak demand values are plotted in Figure 4.20 as a function of the superstructure stiffness. The peak axial force demands are left out because they are, as previously mentioned, virtually unaffected.
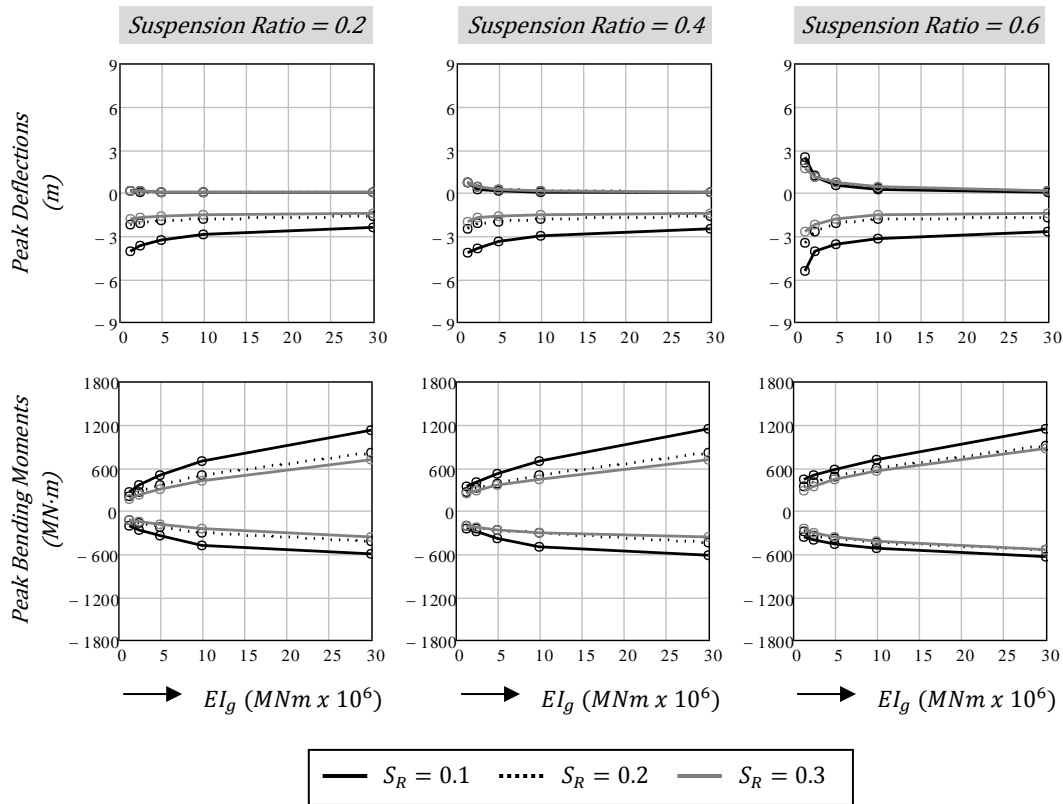
Figure 4.20: Peak Demands as a Function of Superstructure Stiffness
Parameters: L_m = 1000m, EA_g = 2.4E5MN, ω_p = 75kN/m, ω_s = ω_p/0.6

Figure 4.20 shows trends similar to those observed for self-anchored suspension bridges. Initially, deflections are reduced when the stiffness of the superstructure is increased while, at the same time, moment demands are intensified. Thereafter, beyond a certain stiffness threshold, the peak deflection remains nearly constant whereas moment demands continue to increase at a near linear rate. In regard to the effect the superstructure bending stiffness has on the influence of the sag ratio and the suspension ratio, with the exception of the positive deflection demands, the global sag ratio has only a minor effect on the rate of change in the demands. In addition, after the aforementioned stiffness threshold has been reached, the suspension ratio has little influence on the peak deflection.

4.2.1.4 Nonlinear Effects Due to Live Load

Thus far, the peak demand values have been reported from the results of nonlinear analyses which employed loading scenarios identified from a second order influence analysis. Identifying the governing loading scenarios is an arduous process, particularly when results are desired at multiple points of interest on the structure. In practice, a great deal of time and effort can be saved by instead employing the second order influence based results. However, the second order influence based results neglect nonlinear effects stemming from the application of live load. It is, therefore, of interest to study the amount of error which can be expected from the second order influence based results.

Undoubtedly, the degree of nonlinearity generated from the application of live load will vary depending on a number of factors including the applied loading scenario and the demand value/location of interest. Investigating all possible cases would be impractical given the number of variables involved. Thus, the intent here is not to provide an all-encompassing list of error values to be used in design, but rather to give designers an indication of the magnitude of error which may be present in the peak demands. Accordingly, the peak demands generated from the nonlinear and second order influence analyses are compared in Figure 4.21. For simplicity, the peak positive deflection demands have been omitted because they are, for all practical purposes, inconsequential. Using the same convention already established demands from the second order influence analysis are denoted with the superscript 'SO'.

In many cases, the data in Figure 4.21 follows clear trends. In general, the error in the second order influence analysis decreases with increasing superstructure bending stiffness, and with decreasing sag ratio. The only gross exceptions occur for the cases when the suspension ratio equals 0.4 and 0.6, and the global sag ratio equals 0.1. In those instances, there is a jump in the error for the peak negative moment because as the superstructure stiffness increases, the location of the peak negative moment transitions from the quarter point of the suspended region to near the stay cable-hanger junction. Therefore, apart from the aforementioned inconsistencies, the data in Figure 4.21 is in line with the

previous observations made in regard to self-anchored suspension bridges. However, there is one significant distinction. Due to the presence of the stayed regions, when the sag ratio is relatively small, the second order influence analysis in some cases underestimates the peak demands. This is particularly true when the suspension ratio is also small and there is less of a tension stiffening effect from the suspension cable. Therefore, for self-anchored hybrid cable bridges, a second order influence analysis cannot always be relied upon to produce conservative estimates of the superstructure demands.
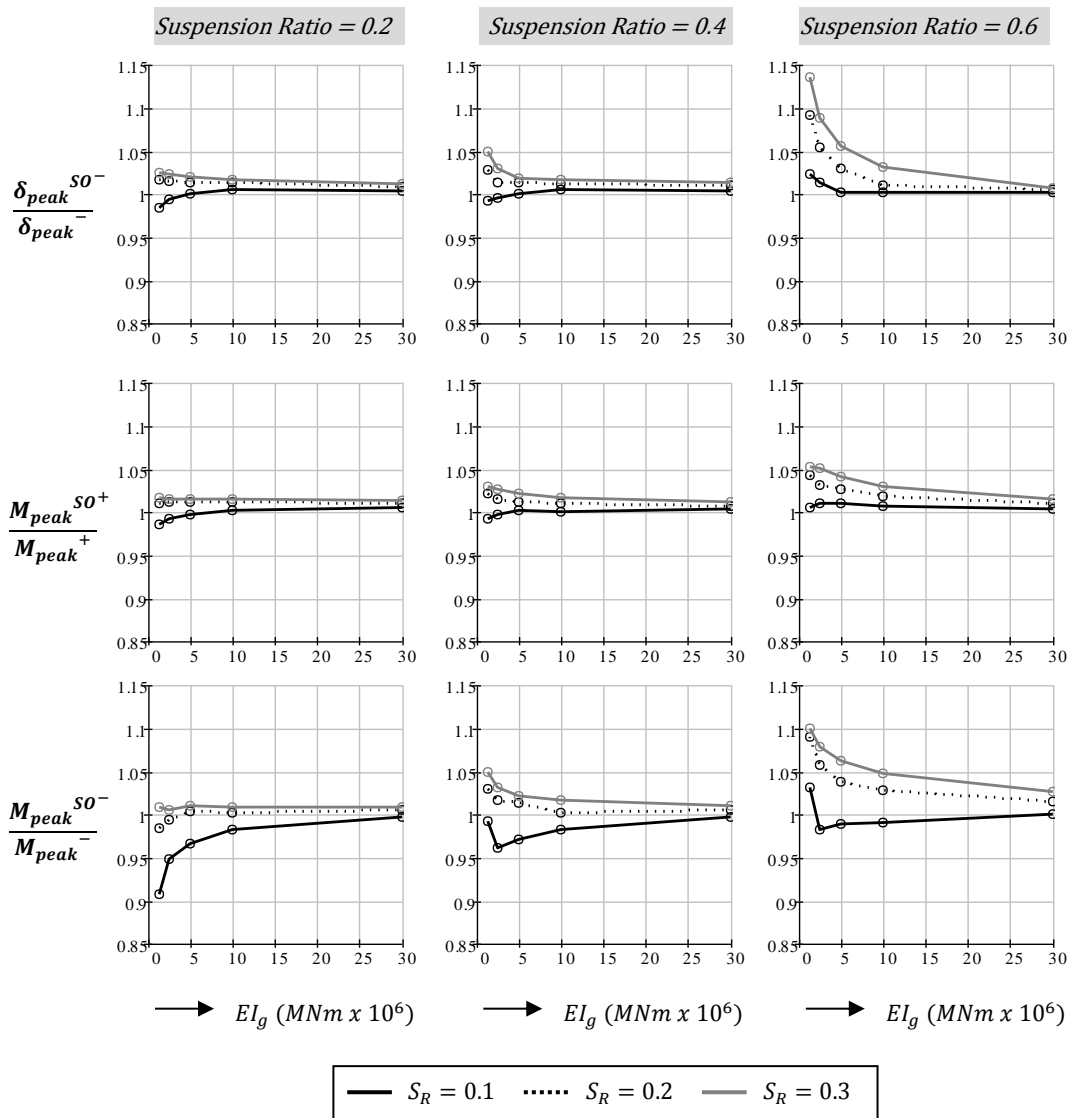
Figure 4.21: Nonlinearity due to Live Load
Parameters: L_m = 1000m, EA_g = 2.4E5MN, ω_p = 75kN/m, ω_s = ω_p/0.6

4.2.1.5   The Influence of the Anchor Cables

Previous sections have excluded the influence of the anchor cables so that the influence of other structural components could be more easily assessed. However, this is not meant to imply that the influence of the anchor cables is immaterial. On the contrary, anchor cables have a pivotal role in the overall function of a self-anchored hybrid cable bridge. Accordingly, this section first explains the function and importance of anchor cables and then examines their influence on the behaviour of self-anchored discontinuous hybrid cable bridges.

Essentially, in a self-anchored hybrid cable bridge, each tower acts as a fulcrum. Whenever load is distributed unevenly about the centerline of the towers, anchor cables act as a counterpoise. More often than not, anchor cables are designed to resist not only unbalanced live loading, but also unbalanced dead loading. Consequently, the failure of an anchor cable can result in significant damage to and/or collapse of the structure.

Another important consideration is that, during service, elastic and strain-free deformations in the anchor cable cause the towers to displace longitudinally. As the top of the towers displace longitudinally, the geometry of the structure changes. This in turn can have significant ramifications to the demands placed on the bridge.

The mechanics of how longitudinal tower deflections affect the behaviour of suspension bridges is highly complex. Nevertheless, the importance of anchor cables can be easily demonstrated by examining their effect on the mid-span deflection of cable-stayed bridges. Shown in Figure 4.22 is one half of a three-span symmetrical cable-stayed bridge, subject to live loading in the main span. Consistent with previous models, the influence of the tower and side span flexural stiffness is excluded. Also, only half of the bridge is included on account of symmetry and, for clarity, all of the stay cables are hidden with the exception of the outermost forestay and anchor cable.

In Figure 4.22, the mid-span vertical deflection is broken down into two components. Neglecting the bending stiffness of the superstructure, from Section 3.1.2.2, the deflection at mid-span caused by the deformation of the forestay is,

$$\delta_{v1} = \frac{\sigma_{c-f}}{E_{eff-f}}\left(\frac{1}{sin\theta_{c-f}}\frac{1}{cos\theta_{c-f}}\right)\frac{L_m}{2} \tag{4.24}$$

This can be regarded as the deflection which would occur if the anchor cables were axially rigid. Similarly, the horizontal deflection at the top of the towers due to the deformation of the anchor cable is,

$$\delta_h = \frac{\sigma_{c-a}}{E_{eff-a}}\left(\frac{1}{cos\theta_{c-a}}\frac{1}{sin\theta_{c-a}}\right)h_T \tag{4.25}$$

and, using simple geometry, the rotation of the towers results in a mid-span deflection equal to,

$$\delta_{v2} = \frac{\sigma_{c-a}}{E_{eff-a}} \left(\frac{1}{cos\theta_{c-a}} \frac{1}{sin\theta_{c-a}} \right) \frac{L_m}{2} \qquad (4.26)$$

where σ_{c-f}/E_{eff-f} and σ_{c-a}/E_{eff-a} are the chord stress / effective stiffness of the forestay and anchor cable, respectively. If the areas of the two cables are determined based on allowable stress then the chord stress in the two cables will be given by (Gimsing & Georgakis, 2012),

$$\sigma_{c-f} = \left(\frac{\omega_R}{1 + \omega_R} \right) \sigma_{allow} \qquad (4.27)$$

and

$$\sigma_{c-a} = \left(\frac{\omega_R}{1 + \omega_R - 4L_{SR}^{2}} \right) \sigma_{allow} \qquad (4.28)$$

where ω_R is the unfactored live load ratio ($\omega_p : \omega_s$) and L_{SR} is the side-to-main span length ratio ($L_s : L_m$). In contrast to models in previous sections where the side spans stays were excluded, Equation (4.28) represents the chord stress in the anchor cable under the actual condition where the side span stays are actively engaged in supporting the side span superstructure dead load.
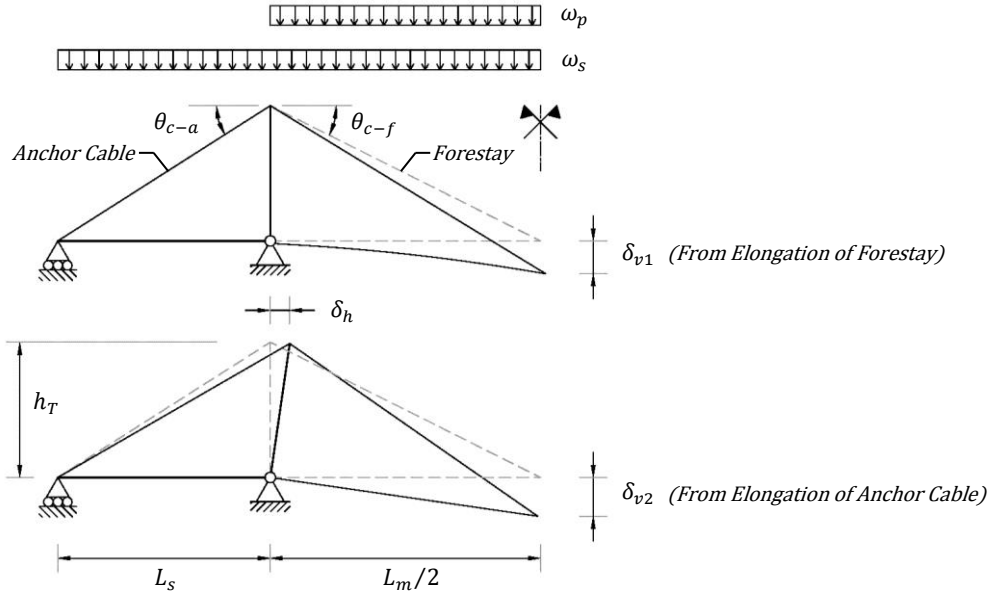
Figure 4.22: Mid-Span Deflection Components in a Cable-Stayed Bridge

Using Equations (4.27) and (4.28), if it is further assumed that the difference in the effective elastic modulus of the two cables is negligible, the amplification of the mid-span deflection caused by the

elastic deformation of the anchor cable can be written as,

$$\frac{\delta_{v1} + \delta_{v2}}{\delta_{v1}} = 1 + \left(\frac{1 + \omega_R}{1 + \omega_R - 4L_{SR}^2}\right)\left(\frac{\sin\theta_{c-f}}{\sin\theta_{c-a}}\frac{\cos\theta_{c-f}}{\cos\theta_{c-a}}\right) \qquad (4.29)$$

Substituting in the appropriate values for θ_{c-f} and θ_{c-a} then gives,

$$\frac{\delta_{v1} + \delta_{v2}}{\delta_{v1}} = 1 + \left(\frac{1 + \omega_R}{1 + \omega_R - 4L_{SR}^2}\right)\left(\frac{2}{L_{SR}}\right)\left(\frac{h_{TR} + L_{SR}^2}{4h_{TR}^2 + 1}\right) \qquad (4.30)$$

where h_{TR} is the tower height-to-span ratio ($h_T : L_m$). Note that for hybrid cable bridges, the tower height-to-span ratio will be roughly equal to the global sag ratio.

Equation (4.30) is plotted in Figure 4.23 as a function of the side-to-main span ratio (left) and the tower height-to-span ratio (right). For the typical range of values, it can be seen that the elastic elongation of the anchor cable amplifies the mid-span deflection by more than a factor of 2. Furthermore, the amount of amplification is greatly dependent on the side-to-main span ratio, but only moderately dependent on the tower height-to-span ratio.
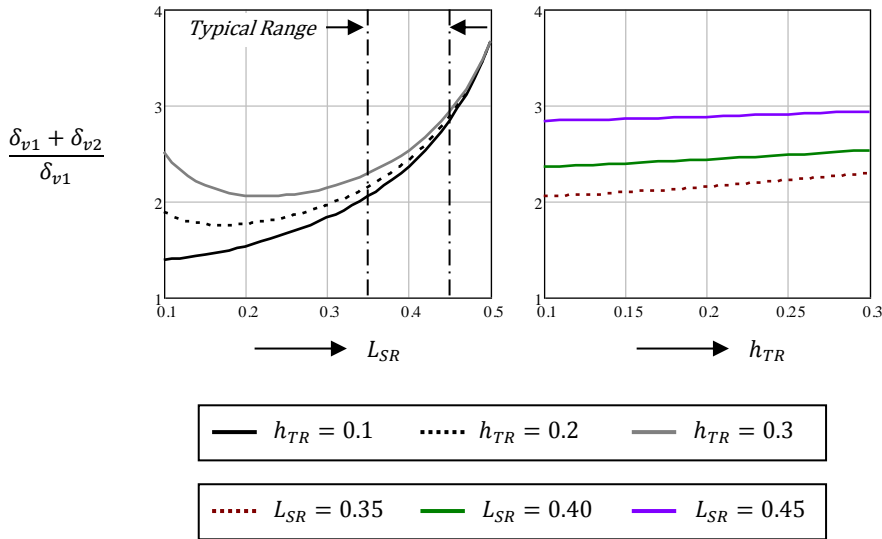
Figure 4.23: Amplification of Mid-Span Deflection in Cable-Stayed Bridge
Parameters: $\omega_R = 0.6$

It may also be observed from the left side of Figure 4.23 that the least amount of amplification does not occur for the case when the side span length equals the tower height (i.e. when the anchor cable is

inclined at 45 degrees – refer to Section 3.1.2.2). This is because, as the side-to-main ratio increases, there is less unbalanced dead load and the live load chord stress in the anchor cable therefore, becomes greater. Additionally, the dead load stress in the cable decreases. This in turn increases sag effects in the anchor cable. If the difference in the effective elastic modulus of the outermost forestay and anchor cable is taken into account, the amplification will increase much more dramatically as the side-to-main span ratio increases beyond a value of 0.4, particularly for long spanning bridges.

It has already been shown that in a discontinuous hybrid cable bridge, strain-free deformations in the suspension cable are greatest under partial main span loading, particularly when the load is positioned asymmetric to the center of the span. In contrast, the anchor cable will exhibit the greatest amount of axial deformation when the entire main span is loaded because that is the loading scenario which produces the maximum horizontal force at the top of the towers. Therefore, given the strong influence of the anchor cable, for key loading scenarios, its inclusion will undoubtedly change the relative amount of strain-free deformation.

Figure 4.24 shows the revised demand envelopes (from a second order influence analysis) when the elastic stiffness of the anchor cable is included in the analysis. The projected length of the anchor cable (i.e. the side span length) is set equal to 35% of the main span length. Due to the simplistic nature of the model, sag effects in the anchor cable were approximated using the tangent modulus approach. Also, although the influence of the side span flexural stiffness and side span stays are excluded in the model, the anchor cables are sized so that under full main span loading the chord stress in the anchor cable adheres to Equation (4.28).

From Figure 4.24 it can be seen that when the elastic stiffness of the anchor cable is taken into account, the absolute peak deflection now occurs at mid-span for all practical values of sag ratio, up to a suspension ratio of 0.4. Moreover, those peak values of deflection occur when the entire main span is loaded. Thus, strain-free deformations no longer control the peak deflection in these cases. To gain a true sense of the influence of the anchor cable, Figure 4.25 compares the values of absolute peak deflection to those given in Figure 4.17. $|\delta_e|_{peak}$ denotes the absolute peak deflection when the elastic stiffness of the anchor cable is included and $|\delta_r|_{peak}$ denotes the absolute peak deflection when the anchor cable is axially rigid.

When the suspension ratio is small, it can be seen from Figure 4.25 that the influence of the anchor cable follows closely the relationship established by Equation (4.30). However, the amount of amplification notably decreases as the suspension ratio increases. As a consequence, the absolute peak deflection now shows little variance amongst the suspension ratios examined. This can be clearly seen in Figure 4.26 which shows the trends in the revised peak demand values.

Suspension Ratio = 0.2   Suspension Ratio = 0.4   Suspension Ratio = 0.6

Deflection
Envelope
(m)

Bending
Moment
Envelope
(MN·m)

Axial Force
Envelope
(MN)
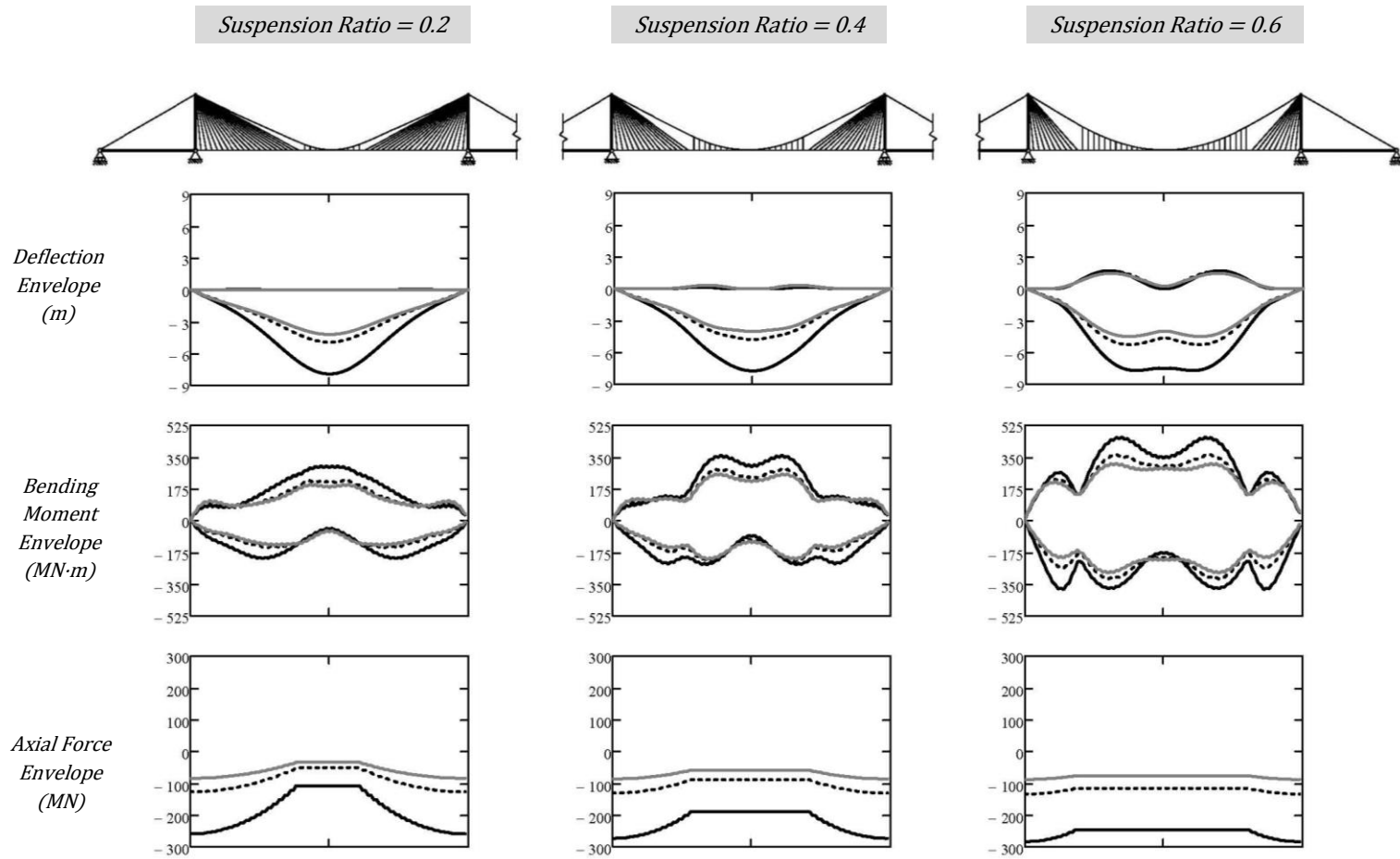
Figure 4.24: Dead and Live Load Demand Envelopes (Including Anchor Cable)

Parameters: L_m = 1000m, L_{SR} = 0.35, EI_g = 1.25E6MN·m², EA_g = 2.4E5MN, ω_p = 75kN/m, ω_s = ω_p/0.6

$S_R = 0.1$ $S_R = 0.2$ $S_R = 0.3$
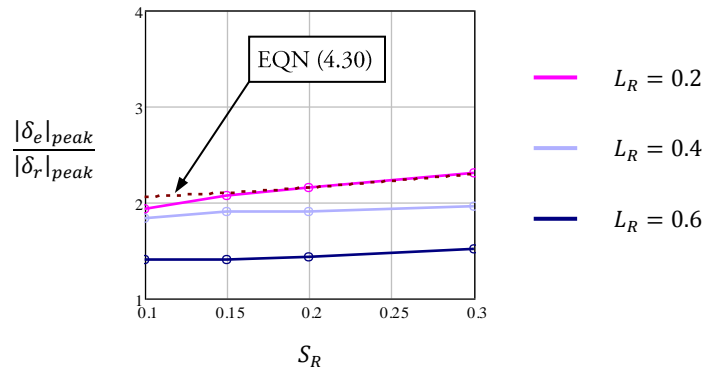
Figure 4.25: Amplification of Absolute Peak Deflection
Parameters: L_m = 1000m, L_{SR} = 0.35, EI_g = 1.25E6MN·m², EA_g = 2.4E5MN, ω_p = 75kN/m, ω_s = ω_p/0.6
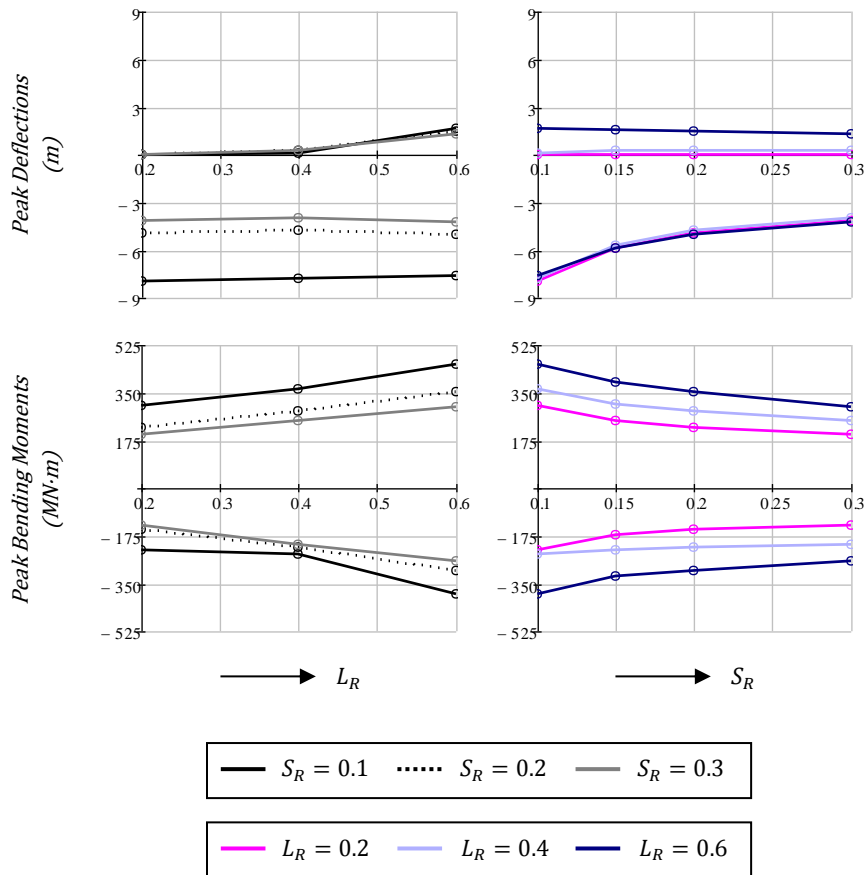
Figure 4.26: Peak Demands (Including Anchor Cable) as a Function of Suspension Ratio (Left) and Sag Ratio (Right)
Parameters: L_m = 1000m, L_{SR} = 0.35, EI_g = 1.25E6MN·m², EA_g = 2.4E5MN, ω_p = 75kN/m, ω_s = ω_p/0.6

In contrast to the deflection demands, the inclusion of the elastic stiffness of the anchor cable results in only slight changes to the superstructure moment demands. However, the same cannot be said when the flexural stiffness of the superstructure is increased. As the flexural stiffness of the superstructure increases the resistance provided by the superstructure starts to compete with the axial stiffness of the anchor cable. Consequently, positive moment demands in the superstructure increase. This is made evident when comparing Figure 4.27 to Figure 4.20. Conversely, the peak negative moment demands show little change. This is because the peak negative moment demands occur at the stay cable-hanger junction and the stiffness at the junction is largely controlled by the adjoining array of stay cables. In all cases, including the elastic stiffness of the anchor cable decreases the relative amount of strain-free deformation. As a result, the trends in Figure 4.27 show less nonlinearity in comparison to Figure 4.20. It may also be inferred that nonlinear effects due to live load will be, in general, less than the values reported in Figure 4.21.
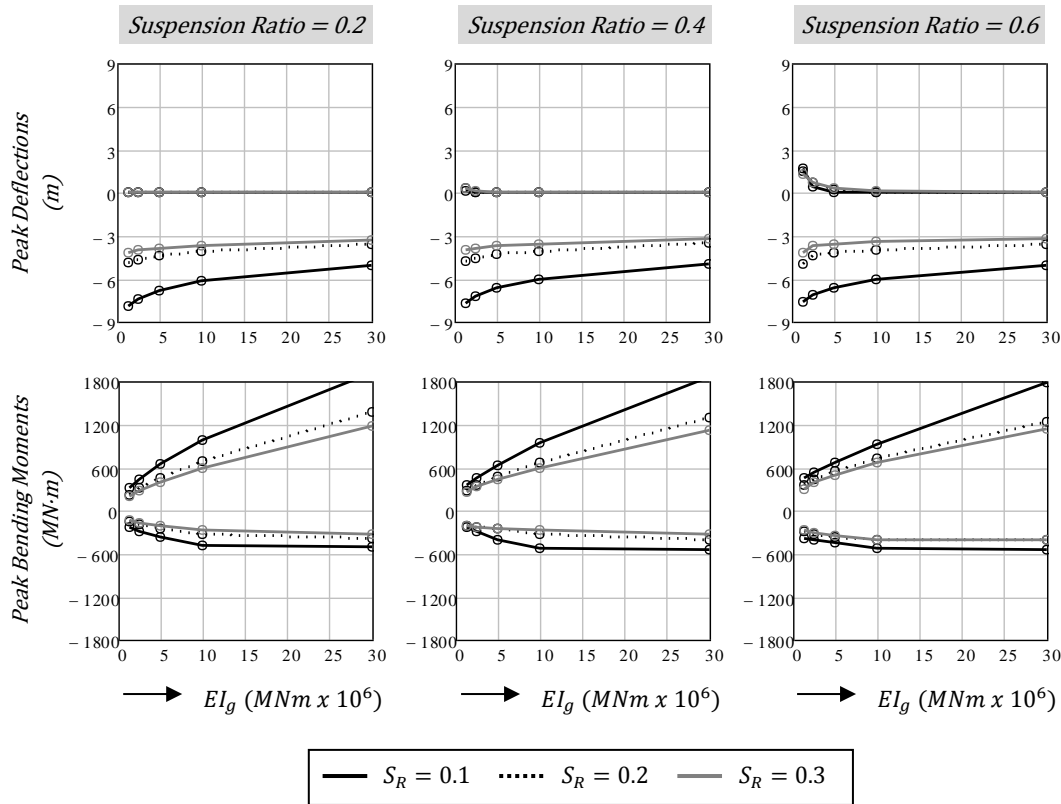
Figure 4.27: Peak Demands (Including Anchor Cable) as a Function of Superstructure Stiffness
Parameters: L_m = 1000m, L_{SR} = 0.35, EA_g = 2.4E5MN, ω_p = 75kN/m, ω_s = ω_p/0.6

As a final note, because infinitesimal strain theory is still applicable, the superstructure axial force

demands are essentially unaffected. As such, they are not included in Figure 4.26. Also, due to the importance of the anchor cable, all further studies in this chapter will include its influence. However, for simplicity, the influence of the side span and tower stiffness will remain excluded.

4.2.1.6 Scale Effects

This section studies how the behaviour of a self-anchored discontinuous hybrid cable bridge changes with span length. As the span length decreases, the global stiffness of the superstructure naturally increases. Consequently, relative to the span length, smaller deflections and larger moments can be expected in the superstructure. However, from a design perspective, it is desirable that the global stiffness of the superstructure remains uniform. That way, no premium is paid in regard to moment demands.

For conventional cable bridges, the increase in the global stiffness of the superstructure is typically compensated by decreasing the depth of the superstructure. This, in turn, decreases the moment of inertia of the superstructure section. Generally, the depth is varied in proportion to the span length,

$$d \propto L_m \qquad (4.31)$$

On that account, the span-to-depth ratio of the superstructure becomes an important parameter during conceptual design.

When the superstructure is isolated, it can be considered to act in the same manner as a girder bridge. For a simply supported girder bridge loaded with live load, the peak deflection is given by (Leet & Uang, 2005),

$$\delta_{peak} = \frac{5\omega_p L_m^{\,4}}{384EI_g} \qquad (4.32)$$

From the above equation, for the global stiffness (i.e. the deflection-to-span ratio) to be constant, the moment of inertia of the girder must be proportional to the third power of the span length (note: the same relationship also exists for multi-span continuous girders),

$$I_g \propto L_m^{\,3} \qquad (4.33)$$

Figure 4.28 shows how the peak deflection-to-span ratio varies when the flexural stiffness of the superstructure in a self-anchored hybrid bridge is scaled according to Equation (4.33). As in previous sections, for the reference case (1000 metre span), the flexural stiffness was set equal to a relatively small value of 1.25×10^6 MNm^2.

The results indicate that Equation (4.33) can also be used to achieve a uniform deflection-to-span ratio in self-anchored hybrid cable bridges. Through further investigation it was found that the same can be said regardless of whether the flexural stiffness of the reference superstructure is relatively flexible or stiff. Therefore, given that a uniform level of global stiffness has been satisfied, it is now of interest to determine how the other demand parameters vary.
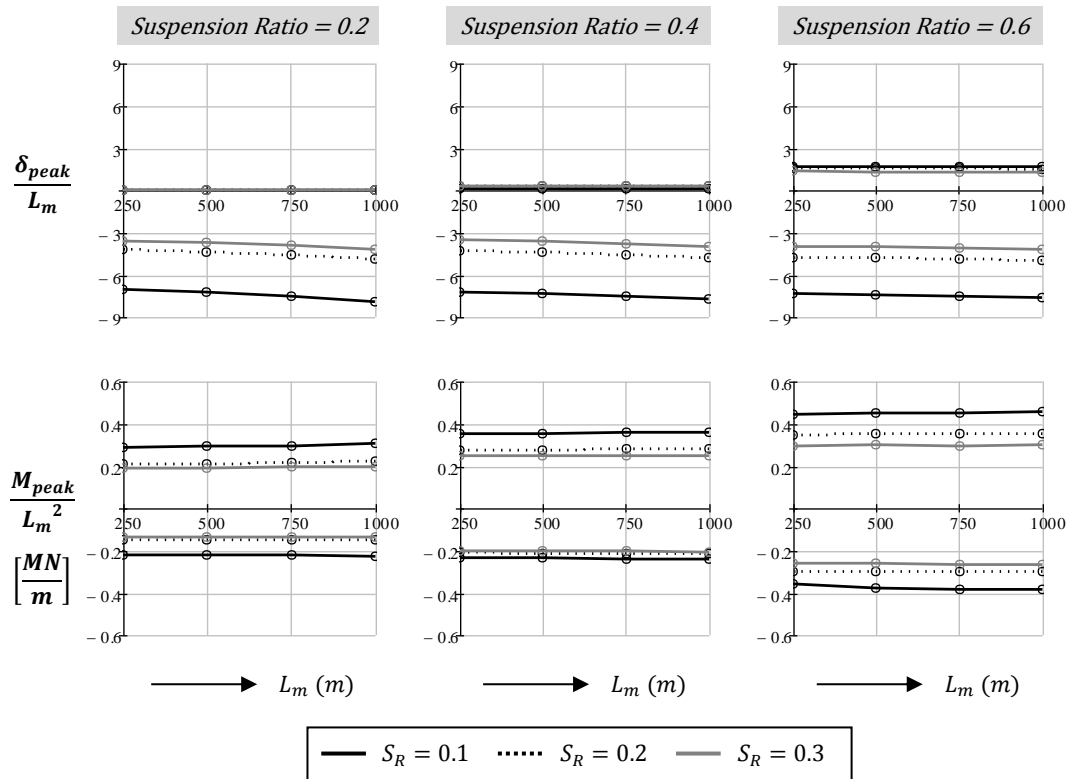
Figure 4.28: Peak Demands as a Function of Span Length (x10^{-3})
Parameters: $EI_g = 0.00125 \cdot L_m^3$ MN/m, $EA_g = 2.4\text{E}5$MN, $\omega_p = 75$kN/m, $\omega_s = \omega_p/0.6$

When the moment of inertia of the superstructure is scaled, not a great deal can be gained by studying the magnitude of the peak bending moment values. Rather, it is the resulting stresses in the superstructure which are of real interest. Nevertheless, the variation in the stresses can be obtained from the moment demands.

Assuming that plane sections remain plane, the material of the superstructure is homogenous, and the material of the superstructure remains linearly elastic, the peak live load bending stresses at the extreme fibres of the cross-section can be obtained from the well-known flexure formula,

$$\left(\sigma_{b,LL}\right)_{peak} = \frac{M_{peak}c}{I_g} \qquad (4.34)$$

where, c, is the distance from the neutral axis of the superstructure to the extreme fibre of the cross-section. The parameter, c, can be expressed as a relative amount of the superstructure depth, d,

$$c = kd \qquad (4.35)$$

where, k, is a constant with a value less than 1.0. Therefore, if, d, is considered to be proportional to L_m and, I_g is considered to be proportional to $L_m{}^3$, it then follows that the bending stresses in the superstructure will be proportional to,

$$\left(\sigma_{b,LL}\right)_{peak} \propto \frac{M_{peak}}{L_m{}^2} \qquad (4.36)$$

When the right side of Equation (4.36) is plotted (see Figure 4.28 – units in meganewton per metre), it becomes evident that, in general, if $d \propto L_m$, and $I_g \propto L_m{}^3$, then the live load bending stresses in the superstructure will remain constant regardless of the span length.

Although the peak live load axial forces are not shown in Figure 4.28, their values can be easily estimated from Equation (4.23). Accordingly, the peak live load axial stress in the superstructure will be approximately equal to,

$$\left(\sigma_{a,LL}\right)_{peak} \cong \frac{\omega_p L_m}{8\, S_R A_g} \qquad (4.37)$$

where A_g is the cross-sectional area of the superstructure. The area of a typical superstructure section can be related to, I_g, and, d, in general terms only after certain approximations are made. As an example, a typical cross-section of a conventional steel box girder is shown at the top in Figure 4.29. For all intents and purposes, the transverse stiffeners can be ignored as they do not contribute to the longitudinal bending stiffness of the section. In addition, the depth of the section is generally much smaller than its width and so the contribution of the webs can be neglected. If the slope of the bottom plate is also neglected, then the section can be idealized as consisting of only a top and bottom plate, offset from one another by a distance, d (see bottom of Figure 4.29). Note that in such an idealization, the area of the longitudinal stiffeners would be included in the area of the plates. By further assuming that the total area is equally distributed between the top and bottom plate, the moment of inertia for the idealized section can be approximately equated to,

$$I_g \cong \frac{A_g d^2}{4} \qquad (4.38)$$

Therefore, if $d \propto L_m$, and $I_g \propto L_m{}^3$, then, it must also follow that,

$$A_g \propto L_m \qquad (4.39)$$

This relationship can also be shown to exist for all other types of conventional cross-sections, regardless of whether or not the cross-sectional area is equally distributed around the flanges. Combining Equation (4.39) with (4.37) leads to the conclusion that, in general, if $d \propto L_m$, and $I_g \propto L_m{}^3$, then the live load axial stresses in the superstructure will also remain constant regardless of the span length.
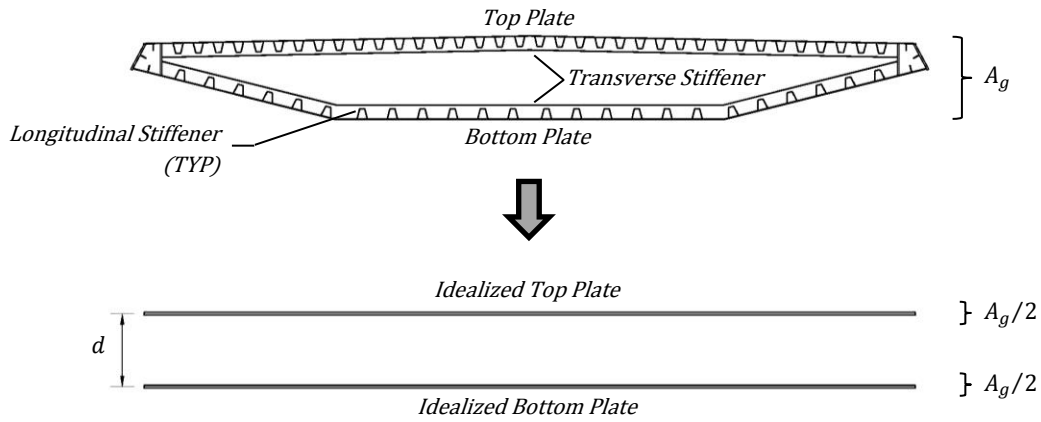
Figure 4.29: Typical (Top) and Idealized (Bottom) Section of a Steel Box Girder

Based on the above results, scaling the superstructure's properties by way of Equations (4.31) and (4.33) yields consistent live load demands, which is a highly favourable design outcome. However, an issue does arise when the dead load demands are also considered. Dead load moments in the superstructure will typically be minor; however, the peak dead load axial stress in the superstructure will be approximately equal to (refer to Equation (4.23)),

$$\left(\sigma_{a,DL}\right)_{peak} \cong \frac{(\gamma_{cm}A_{cm} + \omega_s)L_m}{8\,S_R A_g} \qquad (4.40)$$

In many cases, the stress caused by the self-weight of the suspension cable will be small in comparison to that caused by the self-weight of the superstructure. If the contribution from the self-weight of the suspension cable is neglected, then Equation (4.40) reduces to,

$$\left(\sigma_{a,DL}\right)_{peak} \cong \frac{(\gamma_s A_g \alpha_{sdl})L_m}{8\,S_R A_g} \qquad (4.41)$$

where α_{sdl} is a factor which is included to account for any superimposed dead load and/or miscellaneous components. A_g can be eliminated from Equation (4.41) and, thereafter, it can be seen that the dead load axial stress in the superstructure will always be proportional to the span length, regardless of how the superstructure properties are scaled. Thus, when scaling from a long span to a shorter span, the superstructure will acquire a certain amount of reserved strength as the dead load axial stress decreases. In contrast, when scaling from a short span to a longer span, the stress capacity of the superstructure will be exceeded. Because the dead load axial stress will inevitably change in proportion to the span length, the only way to offset the change in dead load stress is to reduce the live load stresses when scaling upwards, or alternatively, increase the live load stresses when scaling downwards (in order to save on material costs). This can be achieved in one of two ways: (1) increase/decrease the depth of the section, or (2) increase/decrease the area of the section.

For a given moment, increasing the depth of the section will increase the lever arm upon which the moment acts. Consequently, bending stresses will be reduced. However, the moment of inertia of the section is approximately proportional to the square of the section depth (Equation (4.38)); therefore, increasing the depth of the section will notably affect the flexural stiffness of the superstructure. This will in turn attract higher moments which will negate some or all of the beneficial effect created by the added lever arm. In addition, increasing the depth of the section does little to reduce live load axial stresses. In contrast, increasing the area of the section will not as greatly affect the flexural stiffness of the superstructure and will also result in reduced live load axial stresses. On that basis, it can be inferred that increasing/decreasing the area of the section is more favourable in comparison to increasing/decreasing the depth of the section.

An additional aspect to consider which was not accounted for in this section is the effect that the change in superstructure area has on live load demands. In order to isolate certain scaling effects, the magnitude of the superstructure dead load was kept constant when the span length was varied. In reality, as discussed above, there will be some variation in the cross-sectional area of the superstructure and, thereby also, in its dead load. The resulting change to the axial stiffness of the superstructure will typically only have a minor impact on demands; however, the same cannot be said of the change in the superstructure dead load. Changing the superstructure dead load will alter the influence of nonlinear effects and will also affect the required area / the axial stiffness of the cables. This is not only relevant for changes in span length but also for changes in the superstructure material. Thus, further investigation is warranted to determine the effects resulting from dead load changes.

4.2.1.7 Dead Load Effects

Thus far, a value of 0.6 has been assumed for the live load ratio ($\omega_R = \omega_p / \omega_s$). However, the use of

different superstructure materials will alter the live load ratio. For the case of when the suspension ratio equals 0.4, the global sag ratio equals 0.2, and the main span length equals 500 metres, Figure 4.30 shows the variation in the live load deflection and moment envelopes for several live load ratios assuming a relatively flexible superstructure stiffness of EI_g = 0.156E6 MN·m². In each case, the magnitude of the applied live load was kept constant while the magnitude of the superstructure area/dead load was varied. In all cases, the resulting changes to the live load axial forces in the superstructure are negligible. As such, the axial force envelope has been omitted from the figure.
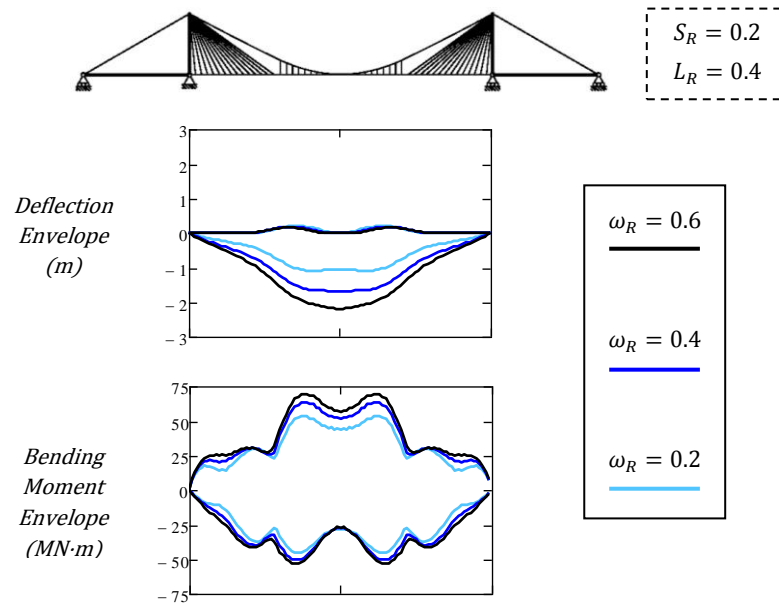
Figure 4.30: Live Load Demand Envelopes as a Function of the Live Load Ratio
Parameters: L_m = 500m, L_{SR} = 0.35, S_R = 0.2, L_R = 0.4, EI_g = 0.156E6MN·m², EA_g = Variable, ω_p = 75kN/m

As can be seen from Figure 4.30, increasing the superstructure dead load has the effect of reducing demands across the entire length of the bridge. Some locations clearly show more of a reduction than others. At first this may seem counterintuitive given that the increase in the superstructure dead load will cause a greater axial force in the superstructure, which in turn causes greater destabilization effects to occur, particularly in the stayed regions of the bridge. However, the detrimental effects created by the increased axial forces are outweighed by the stiffening effects created from the added cable area which is required to support the increased superstructure dead load. The only exceptions which were noted relate to the positive displacement demands which are generally of little practical concern. In addition, for the case when the global sag ratio equals 0.1, similar patterns were observed except at the stay cable-hanger junction where increased dead load caused a notable amplification of the moment demands at the junction.

In Chapter 3 (Section 3.2.2.6), the rate of change in the peak negative deflection demands for a suspension cable subject to a load change were approximated via the following equation,

$$\frac{\delta_{peak_2}}{\delta_{peak_1}} \cong \frac{\left(\dfrac{\omega_{R2}}{1+\omega_{R2}}\right)}{\left(\dfrac{\omega_{R1}}{1+\omega_{R1}}\right)} \qquad\qquad bis\ (3.74)$$

where the subscript '1' is used to represent the cable in its initial loading state and the subscript '2' is used to represent the cable after its loading has been modified. Interestingly, this is the same relationship which would be derived for a cable-stayed bridge with an axially rigid anchor cable (refer to Equations (4.24) and (4.27)). When taking into account the influence of the anchor cable, given that the stress of the anchor cable depends on the side-to-main span ratio, an additional term must be included in the numerator and denominator so that Equation (3.74) becomes (refer to Equation (4.28)),

$$\frac{\delta_{peak_2}}{\delta_{peak_1}} \cong \frac{\left(\dfrac{\omega_{R2}}{1+\omega_{R2}}\right)+\left(\dfrac{\omega_{R2}}{1+\omega_{R2}-4L_{SR}^{2}}\right)K_r}{\left(\dfrac{\omega_{R1}}{1+\omega_{R1}}\right)+\left(\dfrac{\omega_{R1}}{1+\omega_{R1}-4L_{SR}^{2}}\right)K_r} \qquad (4.42)$$

where K_r is a ratio that describes the relative contribution of the anchor cable. For a pure cable-stayed bridge, using Equations (4.24) and (4.26), K_r can be easily derived as,

$$K_r = \left(\frac{2}{L_{SR}}\right)\left(\frac{h_{TR}+L_{SR}^{2}}{4h_{TR}^{2}+1}\right) \qquad (4.43)$$

Note that as the side-to-main ratio approaches zero, Equation (4.42) converges to Equation (3.74).

The actual rate of change in the peak demands from the finite element analyses are plotted in Figure 4.31. To express the rate of change in the demands, the values are normalized with respect to the results for a live load ratio of 0.6. With the exception of the inconsistencies previously mentioned for the peak negative moment demands when the sag ratio equals 0.1, similar trends exist for the other values of suspension and sag ratio examined in the preceding sections.

As can be seen from Figure 4.31, the rate of change in the peak negative deflection demands follows closely the relationship established by Equation (4.42). In regard to the other demand values, it is apparent that the peak moment demands are less affected by the live load ratio. Nevertheless, when the span length is scaled, the effect that the live load ratio has on moment demands will work favourably to offset the accompanying change in dead load axial stresses (refer to previous section). As a final note, similar to the case of earth-anchored fully-laden suspension bridges, nonlinear effects due

to live load will typically decrease when the live load ratio is reduced.
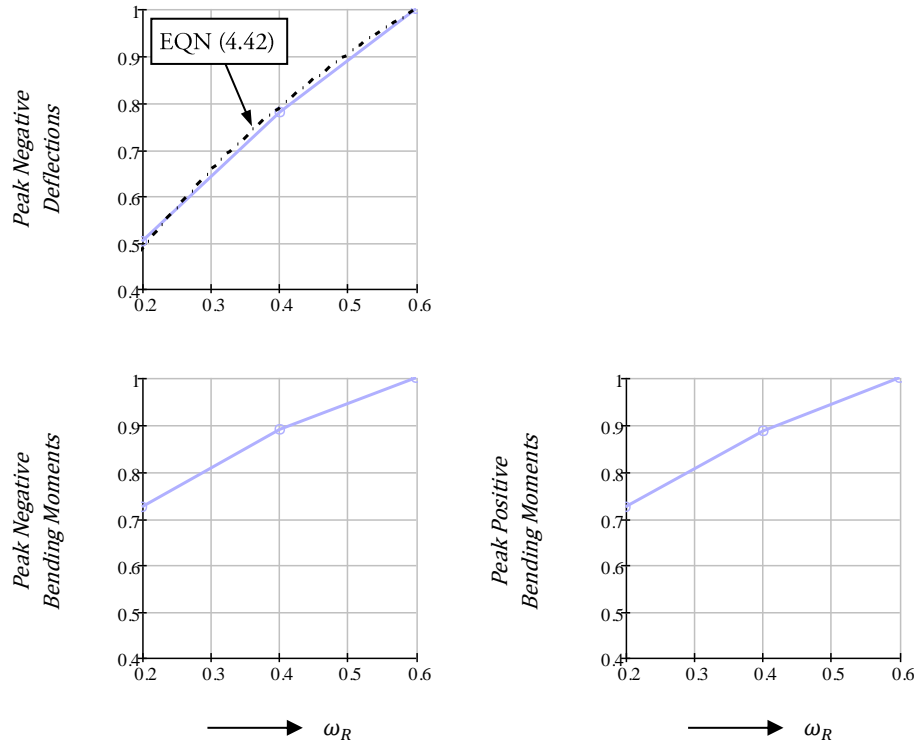
Figure 4.31: Rate of Change in Live Load Peak Demand Values as a Function of Live Load Ratio

Parameters: L_m = 500m, L_{SR} = 0.35, S_R = 0.2, L_R = 0.4, EI_g = 0.156E6MN·m², EA_g = Variable, ω_p = 75kN/m

4.3   End of Chapter Summary

The general study of cable behaviour was extended in this chapter to include partially-laden suspension cables and it was demonstrated that the geometric form of a partially-laden suspension cable can be obtained using the methods presented in Chapter 3 for fully-laden suspension cables. In addition, the difference between assuming a catenary profile versus a parabolic profile for the geometric form was discussed at length. When the deformation characteristics of an isolated partially-laden cable were studied it was found that when the local sag ratio is fixed and the entire suspended region is loaded with live load, the suspension ratio has little bearing on the maximum deflection. Nevertheless, the value of the suspension ratio impacts all other loading scenarios. When the global sag ratio is fixed, it was generally found that the peak deflection in a partially-laden cable will increase as the suspension ratio is increased. This is primarily a result of the scale effects which occur when the

suspended region of the cable is increased.

The fundamental characteristics of self-anchored discontinuous hybrid cable bridges were studied using a simple finite element model. Three different suspension and sag ratios were considered. For simplicity, the influence of the anchor cable was initially excluded, as was the influence of the flexural stiffness of the towers and side spans. The results are also predicated on there being some measure of horizontal restraint provided to the superstructure.

The demand envelopes generated from the finite element analysis showed similar attributes to self-anchored suspension bridges. The peak demands typically occurred at the quarter points of the suspended span and decreased nonlinearly in magnitude when the global sag ratio was increased. Notwithstanding, the influence of the global sag ratio diminished considerably beyond a sag ratio of 0.2.

Unique to discontinuous hybrid cable bridges, moment cusps (positive and negative) were observed in the superstructure near the stay cable-hanger junction. Compared to when the partially-laden cable was isolated, the suspension ratio was observed to have a similar influence on the peak deflection demands: larger suspension ratios yielded larger demands. However, contrary to the previous statement, the rate of change in the peak deflection was found to increase with increasing suspension ratio. Peak moment demands in the superstructure were also observed to increase at a near linear rate, whereas, the axial force demands in the superstructure were found to be virtually unaffected.

With increasing superstructure flexural stiffness, peak deflections decreased nonlinearly, while peak moments increased nonlinearly. Nevertheless, beyond a certain threshold, peak deflections remained nearly constant and became less dependent on the suspension ratio. In addition, the change in the peak moment demands became nearly linear. In all cases, the sag ratio was found to have only a minor effect on the rate of change in the demands.

When investigating nonlinear effects due to the application of live load, for sag ratios greater than 0.2, accounting for the nonlinear effects typically resulted in a reduction of all the demand values considered. Moreover, the degree of nonlinearity generally increased with increasing suspension ratio and with increasing sag ratio. In contrast, for lesser sag ratios, it was demonstrated that nonlinear effects can in some cases produce an amplification of the demands. Thus, for lesser sag ratios, a linearized live load analysis cannot be relied upon to produce a conservative estimate of the demands.

The anchor cable was shown to have a considerable effect on the deformation of cable bridges. When including the influence of the anchor cable, deflection demands were significantly amplified. The

amount of amplification in the peak deflection demands increased with decreasing suspension ratio. As a result, similar peak deflection demands were recorded for all of the suspension ratios examined. For suspension ratios less than or equal to 0.4, the absolute peak deflection demand was governed by full main span loading. In comparison to the deflection demands, the superstructure moment demands were much less affected by the inclusion of the anchor cable stiffness. However, the influence of the anchor cable on positive superstructure moment demands increased with increasing superstructure flexural stiffness. Negative superstructure moment demands were only slightly impacted and little to no change was observed in superstructure axial force demands. Lastly, only a slight reduction in live load nonlinearity was recorded.

In order to generalize the results for various span lengths, the effect of the main span length on the demand values was studied. It was found that live load demands remained approximately constant when the depth of the superstructure is scaled in proportion to the span length and the flexural stiffness of the superstructure is scaled in proportion to the cube of the span length. However, when scaling on that basis, dead load axial stresses in the superstructure will change in proportion to the span length. Designing for the change in dead load stresses necessitates modification of the area/properties of the superstructure. Additionally, the cable area must also be modified to accommodate the change in superstructure dead load. When the superstructure dead load is increased the added stiffening effect resulting from the increased cable area acts to reduce demands. The opposite is true when the area of the superstructure is decreased. Thus, this acts favourably to offset the change in dead load stresses when scaling the main span. In addition, it can be inferred that heavier superstructures, such as those composed of concrete, will be subject to comparatively lower demands. Naturally, the amount of nonlinearity generated by the application of live load will also decrease as the ratio of live load-to-superstructure dead load decreases.

Chapter 5

OPTIMUM PROPORTIONS

The optimum proportions of cable-stayed and suspension bridges have long been established. The optimum proportions are commonly expressed in terms of a number of ratios which are frequently employed during conceptual design. The two most important design ratios for conventional cable bridges include the tower height-to-span ratio and the side-to-main span length ratio. This chapter examines the optimum values of these ratios with respect to self-anchored discontinuous hybrid cable bridges. Specific to discontinuous hybrid cable bridges, the optimum suspension ratio is also studied.

The optimum design ratios depend upon the cable arrangement employed. Therefore, the first section in this chapter focuses on investigating the optimum cable arrangement. The other requisite for evaluating the optimum design ratios is the determination of expressions which can be used to estimate the volumetric quantities for major bridge components such as the cables, towers, and superstructure. These expressions are derived in the second section of this chapter and are later used to evaluate the optimum design ratios from a cost perspective. Notwithstanding, in the process, other factors relating to structural efficiency and aesthetics are also considered. In addition, the overall economic attributes of self-anchored discontinuous hybrid bridges are discussed.

In a generalized study of this nature, a number of simplifications are necessary because different bridges are subject to unique loading, market, and site conditions. Therefore, the intent is not to produce precise optimum values for the design ratios; this can only be achieved through rigorous case specific optimization studies. Instead, the intent is to provide a range of optimal values for each design ratio to be used during conceptual design. It is then expected that engineering judgment be employed to determine the appropriate value for each design ratio given the specific nature of the bridge project; nevertheless, guidance is provided to aid designers in making that determination.

5.1   Cable Arrangement

An array of cables may be configured into numerous different longitudinal arrangements; however, from a practical standpoint the choices are limited as there are only a few options which are advantageous from both a form, and function perspective. This section discusses the positive and negative attributes of the more conventional stay cable and hanger arrangements which have used throughout history.

5.1.1   Stay Cables

Traditionally, stay cables have been arranged in a harp, or a fan type of arrangement. Each is pictured in Figure 5.1 below.

(Harp Arrangement)
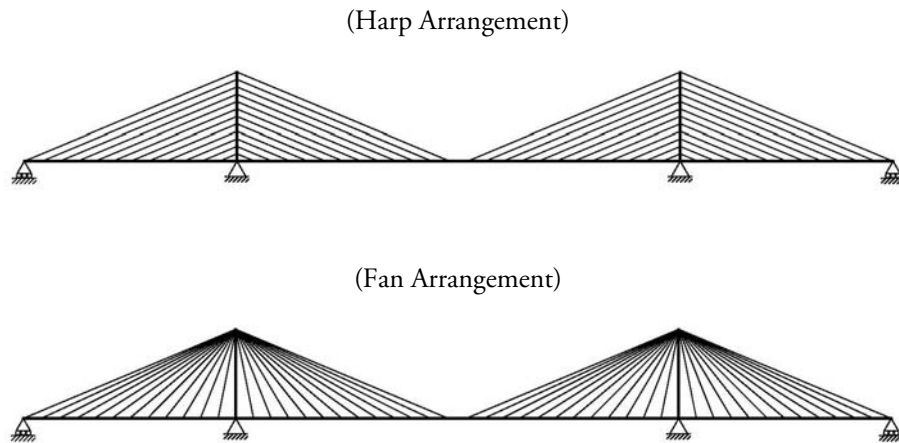
(Fan Arrangement)

Figure 5.1: Traditional Longitudinal Arrangements for Stay Cables

The selection of the longitudinal cable arrangement is a subject which has been extensively discussed in literature by a number of different authors (Podolny & Scalzi, 1976; Leonhardt & Zellner, 1980; Troitsky, 1988; Gimsing & Georgakis, 2012; Svensson, 2012). The following sections summarize the key aspects of arrangement selection.

5.1.1.1   Cost

For stay cables symmetrically arranged about the centre-line of the towers, the following formulas obtained from Podolny & Scalzi (1976) provide an estimate of the cable steel quantity in a conventional cable-stayed bridge,

$$Q_{Fan} \cong \frac{\rho_{st}}{\sigma_{st}}(\omega_s + \omega_p)L_m^2\left[2\left(\frac{h_T}{L_m}\right) + \frac{1}{6}\left(\frac{L_m}{h_T}\right)\right] \qquad (5.1)$$

$$Q_{Harp} \cong \frac{\rho_{st}}{\sigma_{st}}(\omega_s + \omega_p)L_m^2\left[\left(\frac{h_T}{L_m}\right) + \frac{1}{4}\left(\frac{L_m}{h_T}\right)\right] \qquad (5.2)$$

ρ_{st} and σ_{st} are the density and design stress of the stay cable material; ω_s and ω_p are the magnitude of the uniformly distributed dead and live load; L_m is the main span length; and h_T is the tower height above deck. A plot of these equations is provided in Figure 5.2 as a function of the tower height-to-span ratio ($h_T : L_m$).
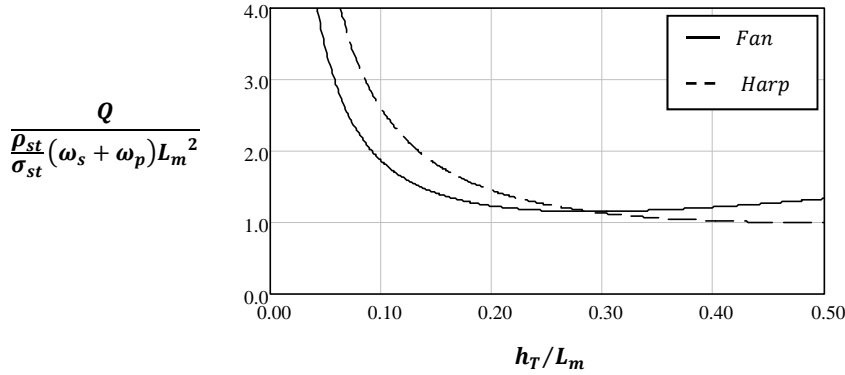
Figure 5.2: Variation of Stay Cable Quantity in Harp and Fan Arrangements

Since cost is directly related to the quantity of cable steel, the fan arrangement clearly yields the lowest cost for most practical cases; the harp arrangement being only advantageous from a cost perspective when the tower height-to-span ratio exceeds a value of approximately 0.3. Moreover, because Equation (5.1) and Equation (5.2) have the same coefficients the above result is independent of the specified loading, cable material, and span length.

5.1.1.2 Structural Efficiency

The structural efficiency of a structure is often measured in terms of its strength-to-weight ratio or stiffness-to-weight ratio. In both respects the fan arrangement is more efficient. This is because in a harp arrangement, the bending stiffness of the towers and/or the superstructure needs to be activated in order for the bridge to remain stable when live loads are positioned asymmetrically with respect to the center-line of the towers. This is demonstrated in Figure 5.3 wherein hinges have been placed at all cable anchorage locations in order to inhibit the bending ability of the towers and superstructure.

From the figure it can clearly be observed that the harp arrangement is unstable under the applied loading scenario. Consequently, more material is required in the superstructure or towers to provide the necessary stability. For the same reason, unless additional anchor piers are provided in the side spans, the dead load distribution of moments in the superstructure cannot be as greatly optimized when utilizing the harp arrangement. In addition, there is less flexibility in configuring the side-to-main span ratio.
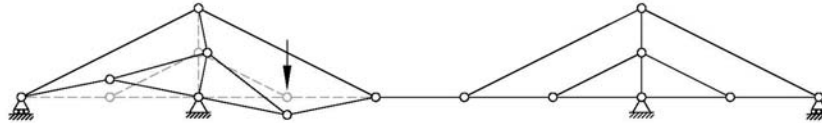
Figure 5.3: Unstable Model of a Harp Arrangement
Figure adapted from (Schüller, 1998)

In contrast, in a fan arrangement there is a direct load path between the main span cables and the anchorage cables and thus stability can still be obtained even when the superstructure and towers are devoid of bending stiffness. This characteristic has led some authors to conclude that the fan arrangement is advantageous from not only a static, but also an aerodynamic perspective (Gimsing & Georgakis, 2012). However, there is a trade-off. Because the anchor cables stabilize unbalanced loading in the main span, and in the side span, they are subject to a greater stress range during service. Consequently, the side span length must be restricted, or alternatively, the area of the anchor cable must be increased to avoid any possibility of fatigue (more information is provided in Section 5.3.2). It should be noted though that the same fatigue concerns exist in a harp arrangement if used in conjunction with relatively stiff towers.

5.1.1.3 Aesthetics

Aesthetics is one aspect where the harp arrangement triumphs. When multiple planes of cables are used and the bridge is viewed at a skewed angle, a fan arrangement gives rise to the optical effect of cables crossing each other which can be displeasing to the viewer depending on the angle of observation. However, the effect does become less pronounced with increasing span length. In contrast, this phenomenon does not occur when a harp arrangement is used because in a harp arrangement all cables have the same inclination.

5.1.1.4 Additional Considerations

Due to the relatively low inclination of the stays in a harp arrangement, inclined cable planes are not possible as their use would interfere with vehicular clearance requirements. Consequently, a harp

arrangement cannot be used in conjunction with A-frame, diamond shaped, modified-diamond shaped, or inverted Y-shaped towers whenever multiple cable planes are desired. In addition to affecting the tower layout, this also affects the foundation design and the amount of torsional stiffness which can be achieved by the cable system alone.

In regard to construction, the first cable tower anchorage point in a harp arrangement is located much closer to the deck in comparison to in a fan arrangement. As a result, by using a harp arrangement, cantilever construction can theoretically commence at an earlier date and then subsequently proceed in unison with the construction of the towers.

5.1.1.5 Concluding Remarks

Considering all of the above aspects, cost and structural efficiency are generally the most heavily weighted, and in regard to these aspects, the fan arrangement is undoubtedly superior. This finding is reflected in the current state of design: upon surveying the one hundred longest spanning cable-stayed bridges, less than five percent possess what can be classified as harp arrangements. On these grounds, the harp configuration will not be considered in deriving the optimum proportions for a self-anchored discontinuous hybrid cable bridge.

Despite the advantages of the fan arrangement, in modern cable bridges fan arrangements are impractical because there is not enough anchorage space at each tower to allow for the axes of all adjoining cables to converge at a common point. This has led to the adoption of what is commonly referred to as the 'semi-fan' configuration which is picture in Figure 5.4. The only difference relative to the fan configuration is that the anchorage zone at the towers is extended downwards.

Figure 5.4: The Semi-Fan Arrangement

5.1.2 Hangers

In addition to the conventional vertical arrangement of hangers, a diagonal arrangement of hangers (Figure 5.5) has also been employed. Notwithstanding, the diagonal arrangement has only been applied in three vehicular bridges: the Severn Bridge (1966), the Bosporus Bridge (1973), and the Humber Bridge (1981). All three were designed by the same engineering firm, each serving as a model for the latter. (Kawada, 2010)

(Vertical Arrangement)

(Diagonal Arrangement)
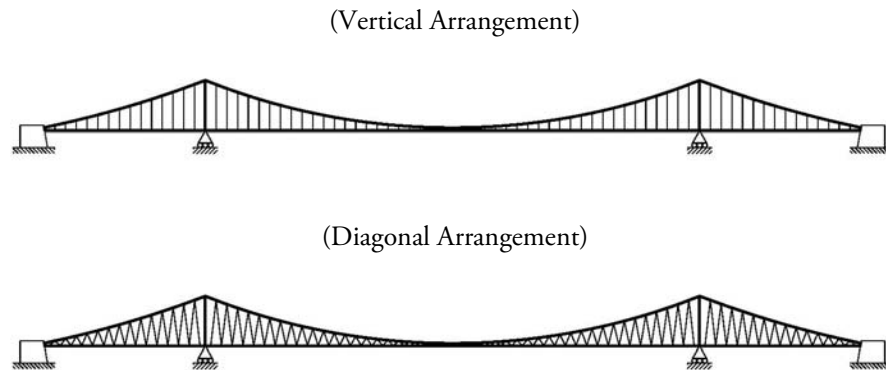
Figure 5.5: Types of Longitudinal Arrangements for Hangers

The primary advantage of diagonal hangers is that they form a truss-like structure between the suspension cables and the superstructure which significantly suppresses strain-free deformations. Consequently, the stiffness of the cable system, and thus the bridge as a whole, is greatly increased. Nevertheless, diagonal hangers were first employed in the Severn Bridge for a different reason, as explained below.

The suppression of strain-free deformations from live, wind, and other forms of loading causes a cyclic variation of forces in the hangers. Prior to the Severn Bridge, heavy space trusses were used exclusively in suspension bridges due to ongoing concerns regarding aerodynamic stability following the Tacoma Narrows Disaster in 1940. The Severn Bridge was the first bridge to use to a lightweight, streamlined box girder for the superstructure. Because of its reduced gravity stiffness, attention was directed towards enhancing structural damping. (Kawada, 2010) This was achieved by using diagonal hangers in conjunction with helical cables. The helical cables have a unique hysteresis which is activated by the cyclic variation of wind forces in the hangers.

Unfortunately, it was not until near the opening of the Humber Bridge, that severe structural problems started to emerge with the hangers in the Severn Bridge. There were many contributing factors. Poor penetration of the hanger socketing material was observed, in addition to a lack of axial and angular alignment along the hanger pin centre axes (Flint & Smith, 1992). It also became evident that live load demands had reached levels close to three times the original design estimate (Bradley, 2010). Nevertheless, ironically, the foremost cause of the problems can be linked to the rationale behind the employment of the diagonal arrangement. Although advantageous from a structural damping perspective, the cyclic variation of forces in the hangers from live load severely reduced their fatigue life. Moreover, the slackening of the hangers made them particularly susceptible to wind-induced vibration which further exacerbated their fatigue. Prior to the Severn Bridge, wind-

induced vibration of hangers had never been observed. (Kawada, 2010)

When studies were undertaken to replace the hanger system, it was found that by using a vertical arrangement the combined bending and axial stress range in the hangers could be reduced by roughly 50% at mid-span, and 85% at the quarter span. However, replacing the original hangers with a vertical arrangement would have required repositioning of the hanger clamps or, alternatively, the installation of new deck attachment stools. Furthermore, the deck and tower would have had to be substantially strengthened. For these reasons, the diagonal arrangement was retained. (Flint & Smith, 1992) Notwithstanding, following the Humber Bridge, the diagonal arrangement was completely abandoned in vehicular bridges.

The reasons that led to the abandonment of the diagonal arrangement in suspension bridges are no less valid in regard to hybrid cable bridges. Consequently, the diagonal arrangement will not be considered when deriving the optimum proportions for a self-anchored discontinuous hybrid cable bridge.

5.2 Derivation of Bridge Quantities

As previously mentioned, the accurate calculation of quantities required in principal bridge components is an exceedingly complex task. Numerous assumptions are required in order to generalize and simplify the calculations. In addition, extreme caution must be exercised in differentiating parameters which are arbitrary from those which have a prominent effect. Bearing this in mind, the estimation approach utilized in Gimsing & Georgakis (2012) for conventional cable bridges is adapted herein for the hybrid system.

Inherent in the adopted approach are several general assumptions:

1. The governing loading scenarios for the principal bridge components are assumed to occur when either the entire bridge, or the entire main span, is loaded with dead and live load. Under these loading scenarios the majority of the applied load is transferred through the cable system and, on that account, the bending stiffness of the superstructure can be neglected. This assumption is particularly valid in modern cable bridges where the superstructure is often of slender construction. It allows principal bridge components to be considered isolated from the rest of the bridge when deriving their internal forces which greatly simplifies the calculations involved.

2. Secondary forms of loading (i.e. wind, temperature, earthquake, etc…) are not directly

considered as their effects are site specific. Still, the impacts of secondary loads are indirectly considered in the assigned design stress of the principal components.

3. The quantity of cable steel in a single array of cables is approximated by assuming that the cables act as a continuous membrane. This assumption derives from the fact that in modern cable bridges the spacing of cables along the superstructure is relatively small in comparison to the span length of the bridge.

4. Out-of-plane effects are not directly considered in the derivation of quantities. Accordingly, only two dimensions are considered.

In addition, since the overall goal is to determine the optimum proportions of the hybrid system, it is appropriate to neglect the difference between the tower height above deck and the global sag of the suspension cable. A large difference between these two parameters only serves to reduce the efficiency of the system. Furthermore, to simplify some of the expressions, it is sufficiently accurate in this context to assume that the self-weight of the suspension cable acts uniformly along its projected length.

5.2.1 Stay Cable Quantity

When determining the area required for each stay cable it is appropriate to assume that each cable is effectively anchored at its respective tower connection point since the governing loading scenario producing the maximum tension will occur when live load is balanced on both sides of the tower. In this regard, Figure 5.6 shows an idealized array of stay cables. h_T is the height of the towers above deck; b is the height above deck of the first tower connection; and a is the length of the array.
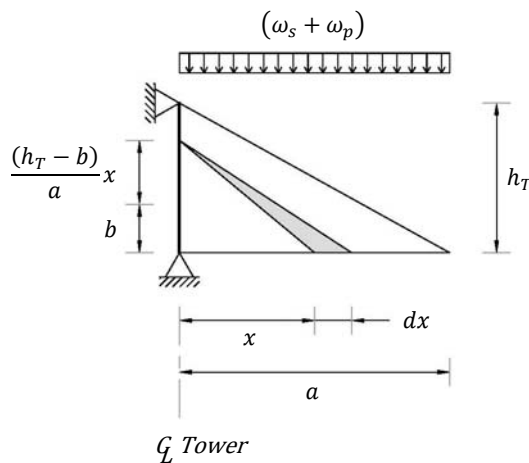
Figure 5.6: Idealized Array of Stay Cables

The shaded area in Figure 5.6 is meant to represent an infinitesimal segment of the array. The tension in the infinitesimal segment due to uniformly distributed dead and live load ($\omega_s + \omega_p$) acting over a tributary length of dx, is given by the following expression:

$$dT = (\omega_s + \omega_p)\frac{\sqrt{\left[\left(\frac{h_T - b}{a}\right)x + b\right]^2 + x^2}}{\left[\left(\frac{h_T - b}{a}\right)x + b\right]}dx + \frac{1}{2}\frac{dT}{\sigma_{st}}\gamma_{st}\sqrt{\left[\left(\frac{h_T - b}{a}\right)x + b\right]^2 + x^2} \tag{5.3}$$

where σ_{st} and γ_{st} are the design stress and unit weight of the stay cable material. The first term in Equation (5.3) is due to the applied loading, whereas the second term is due to self-weight. If dT is isolated, the following equation is obtained,

$$dT = \frac{(\omega_s + \omega_p)\sqrt{\left[\left(\frac{h_T - b}{a}\right)x + b\right]^2 + x^2}}{\left[\left(\frac{h_T - b}{a}\right)x + b\right]\left[1 - \frac{1}{2}\frac{\gamma_{st}}{\sigma_{st}}\sqrt{\left[\left(\frac{h_T - b}{a}\right)x + b\right]^2 + x^2}\right]}dx \tag{5.4}$$

The quantity of cable steel in the infinitesimal segment, dQ, will then be given by the density of the stay cable material, ρ_{st}, multiplied by the cable area required, multiplied by the length of the segment:

$$dQ = \rho_{st}\frac{dT}{\sigma_{st}}\sqrt{\left[\left(\frac{h_T - b}{a}\right)x + b\right]^2 + x^2} \tag{5.5}$$

When Equation (5.4) is substituted in for dT, the quantity becomes,

$$dQ = (\omega_s + \omega_p)\frac{\rho_{st}}{\sigma_{st}}\frac{\left[\left(\frac{h_T - b}{a}\right)x + b\right]^2 + x^2}{\left[\left(\frac{h_T - b}{a}\right)x + b\right]\left[1 - \frac{1}{2}\frac{\gamma_{st}}{\sigma_{st}}\sqrt{\left[\left(\frac{h_T - b}{a}\right)x + b\right]^2 + x^2}\right]}dx \tag{5.6}$$

Thereupon, the total quantity of cable steel in the array can be obtained by integrating dQ over the length of the array,

$$Q = (\omega_s + \omega_p)\frac{\rho_{st}}{\sigma_{st}}\int_0^a \frac{\left[\left(\frac{h_T - b}{a}\right)x + b\right]^2 + x^2}{\left[\left(\frac{h_T - b}{a}\right)x + b\right]\left[1 - \frac{1}{2}\frac{\gamma_{st}}{\sigma_{st}}\sqrt{\left[\left(\frac{h_T - b}{a}\right)x + b\right]^2 + x^2}\right]}dx \tag{5.7}$$

Figure 5.7 plots the quantity of cable steel in a single array of cables for a fan arrangement ($b = h_T$). The quantity for a semi-fan arrangement is also included assuming that the tower anchorages for the cables are distributed over the top quarter of the tower ($b = 3/4h_T$). In accordance with the remarks in Section 5.1.1, the harp arrangement is not considered.

As can be seen from the Figure 5.7, there is little difference in quantity between the two, particularly in the range of tower height-to-span ratios commonly employed for cable-stayed bridges. Furthermore, for conventional cable types, the plots do not greatly depend on the unit weight and design stress of the cable material.

$$\frac{Q}{\frac{\rho_{st}}{\sigma_{st}}(\omega_s + \omega_p)a^2}$$
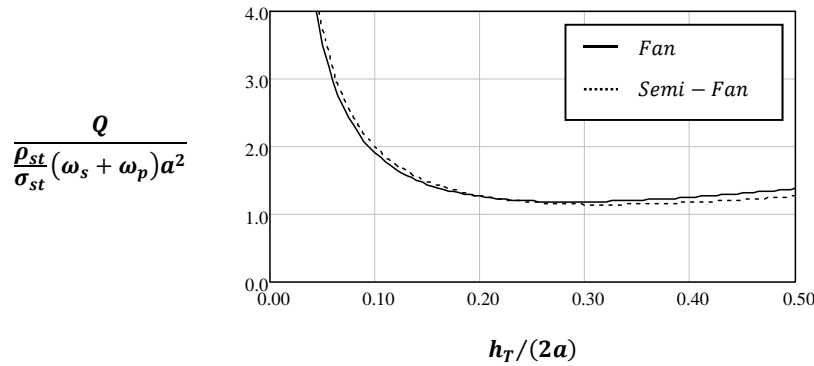
Figure 5.7: Variation of Stay Cable Quantity in Fan and Semi-Fan Arrangements
Parameters: a = 500m, σ_{allow} = 800MPa, γ_{stay} = 0.09MN/m³

Since the quantity for a fan arrangement is mathematically more convenient, its formulation will be used in place of the formulation for a semi-fan arrangement. Still, even for the fan arrangement the symbolical evaluation of Equation (5.7) produces a highly complex expression. However, a simple approximate expression can be obtained by neglecting the contribution from the self-weight of the cables. This is equivalent to setting γ_{stay} equal to zero, at which point, the expression becomes,

$$Q_{approx} = \frac{\rho_{st}}{\sigma_{st}}a^2(\omega_s + \omega_p)\left(\frac{a}{3h_T}\right)\left[1 + 3\left(\frac{h_T}{a}\right)^2\right] \tag{5.8}$$

Note that if a is replaced by $L_m/2$ and the whole expression is multiplied by 4, then Equation (5.1) is obtained. Also, the error produced by neglecting the self-weight of the cable is plotted in Figure 5.8 for various lengths of cable arrays. Even for long spanning arrays, it can be seen that the error is marginal.
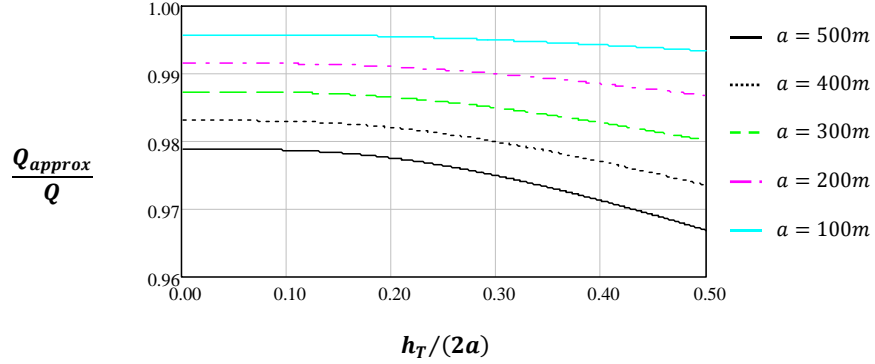
Figure 5.8: The Influence of Self-Weight on Cable Steel Quantity in a Fan Arrangement
Parameters: σ_{st} = 800MPa, γ_{st} = 0.09MN/m³

The final step to arrive at an expression for the total quantity of stay cable steel in a discontinuous hybrid cable bridge involves summing the contributions from the stay cable arrays in the main span and side spans. Denoting L_R as the suspension ratio, h_{TR} as the tower height-to-main span ratio, L_{SR} as the side-to-main span length ratio, and L_m as the main span length, the final expression may be written as,

$$Q_{st} = \frac{\rho_{st}}{\sigma_{st}} L_m{}^2 (\omega_s + \omega_p) \left[\frac{(1-L_R)^3}{12 h_{TR}} + (1-L_R) h_{TR} + \frac{2}{3} \frac{L_{SR}{}^3}{h_{TR}} + 2 h_{TR} L_{SR} \right] \qquad (5.9)$$

5.2.2   Suspension Cable Quantity

In deriving the suspension cable quantity, it is assumed that the cable area required for the suspension cable is independent to the cable area required for the anchor cables. Accordingly, an expression for the area of the suspension cable has already been derived. From Equation (4.21), the required area is,

$$A_{cm} = \frac{1}{\gamma_{cm}} \frac{(\omega_s + \omega_p)\, \xi\, L_R\, (2-L_R) \sqrt{1 + 16 \left(\frac{h_{TR}}{2-L_R} \right)^2}}{1 - \xi \sqrt{1 + 16 \left(\frac{h_{TR}}{2-L_R} \right)^2}} \qquad (5.10)$$

where as before,

$$\xi = \frac{\gamma_{cm}\, L_m}{8\, \sigma_{cm} h_{TR}}$$

Using Equation (5.10), the quantity of cable steel can then be expressed as,

$$Q = \rho_{cm} A_{cm} \left[2L_{cm\_1} + L_{cm\_2} \right] \tag{5.11}$$

where ρ_{cm} and A_{cm} are the density and area of the cable material. In addition, L_{cm_1} is the length of the cable in the stayed region (the value is multiplied by two because there are two stayed regions) and L_{cm_2} is the length of the cable in the suspended region. There will be a negligible difference in the total cable quantity if the elastic elongation of the cable is ignored. In view of that, the stressed length can be used in place of the unstressed length when computing L_{cm_1} and L_{cm_2}. The expression for the cable quantity then becomes,

$$Q = \rho_{cm} A_{cm} \left[2 \int_0^{\frac{L_m(1-L_R)}{2}} \sqrt{1 + \left(\frac{dy(x)}{dx}\right)^2} \, dx + \int_{\frac{L_m(1-L_R)}{2}}^{\frac{L_m(1+L_R)}{2}} \sqrt{1 + \left(\frac{dy(x)}{dx}\right)^2} \, dx \right] \tag{5.12}$$

The ordinates of the cable curve, represented by $y(x)$, can be approximated by Equation (4.11); however, additional simplifications must still be made in order to arrive at a straightforward solution. For the stayed region, it can be assumed that the sag of the cable in the stayed region is small relative to the length of the stayed region so that the length can be approximated as,

$$L_{cm\_1\_approx} = \sqrt{\left(\frac{L_m(1-L_R)}{2}\right)^2 + y_B{}^2} \tag{5.13}$$

where y_B is the vertical distance from the tower anchorage point to the start of the suspended region (Figure 4.3). If it is further assumed that the weight of the cable has a negligible effect on y_B, then after substitution of Equations (4.9) and (4.11), Equation (5.13) reduces to,

$$L_{cm\_1\_approx} = \frac{L_m(1-L_R)}{2} \sqrt{1 + h_{TR}{}^2 \left(\frac{4}{2-L_R}\right)^2} \tag{5.14}$$

For the length of the cable in the suspended region, a Maclaurin series expansion can be used to eliminate the radical in the expression for the stressed length. The integral then becomes,

$$L_{cm\_2\_approx} = \int_{\frac{L_m(1-L_R)}{2}}^{\frac{L_m(1+L_R)}{2}} \left[1 + \frac{1}{2} \left(\frac{dy(x)}{dx}\right)^2 \right] dx \tag{5.15}$$

Thereafter, neglecting the effect of the weight of the cable and substituting in Equation (4.11) yields,

$$L_{cm\_2\_approx} = L_m L_R \left[1 + \frac{8}{3} h_{TR}^2 \left(\frac{1}{2 - L_R} \right)^2 \right] \tag{5.16}$$

The final expression for the approximate quantity can then be obtained by substituting Equations (5.14) and (5.16) into Equation (5.11),

$$Q_{approx} = \rho_{cm} A_{cm} L_m \left[(1 - L_R) \sqrt{1 + \left(\frac{4 h_{TR}}{2 - L_R} \right)^2} + L_R \left[1 + \frac{8}{3} \left(\frac{h_{TR}}{2 - L_R} \right)^2 \right] \right] \tag{5.17}$$

To provide an indication of the error in the approximate expression for the stressed length, Figure 5.9 compares the approximate quantity obtained from Equation (5.17) to the quantity obtained from Equation (5.12).
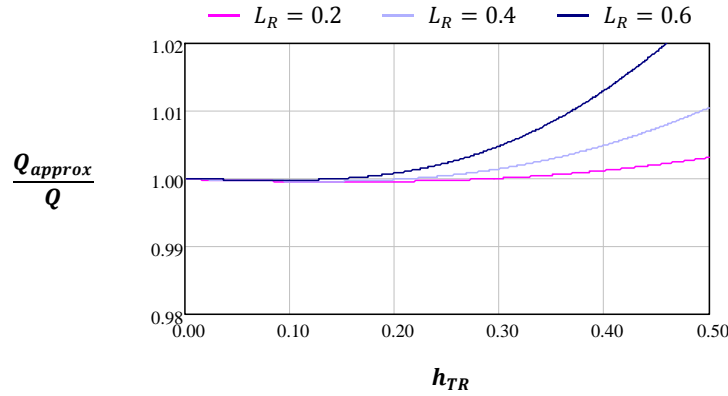
Figure 5.9: Error in Approximate Suspension Cable Quantity
Parameters: L_m = 1000m, σ_{cm} = 800MPa, γ_{cm} = 0.09MN/m³

Clearly, as the suspension ratio increases, the self-weight of the cable becomes more dominant and, consequently, the error increases. Nevertheless, for all practical cases Equation (5.17) provides sufficient accuracy for the purposes of this study. Therefore, upon substitution of the cable area, the approximate formula for the suspension cable can be given as,

$$Q_{cm} = \frac{1}{g} L_m (\omega_s + \omega_p) \frac{L_R (2 - L_R) \xi \eta}{1 - \xi \eta} \left[(1 - L_R) \eta + L_R \frac{(\eta^2 + 5)}{6} \right] \tag{5.18}$$

where g is the standard acceleration due to gravity, and the additional dimensionless parameter, η, is defined as,

$$\eta = \sqrt{1 + 16\left(\frac{h_{TR}}{2 - L_R}\right)^2}$$

5.2.3 Anchor Cable Quantity

Anchor cables serve to balance loads positioned asymmetric to the centerline of the towers (refer to Section 4.2.1.5). The maximum force in the anchor cables will, therefore, occur when only the main span is loaded with live load. In accordance with Section 5.1.1, when deriving the required area for the anchor cables it will be assumed that the stay cables are arranged in a semi-fan configuration. Furthermore, it will also be assumed that the anchorage zone at the towers is relatively small and any unbalanced loading taken by the stay cables transfers directly to the anchor cables. These assumptions are reflected in the free body diagram shown in Figure 5.10.
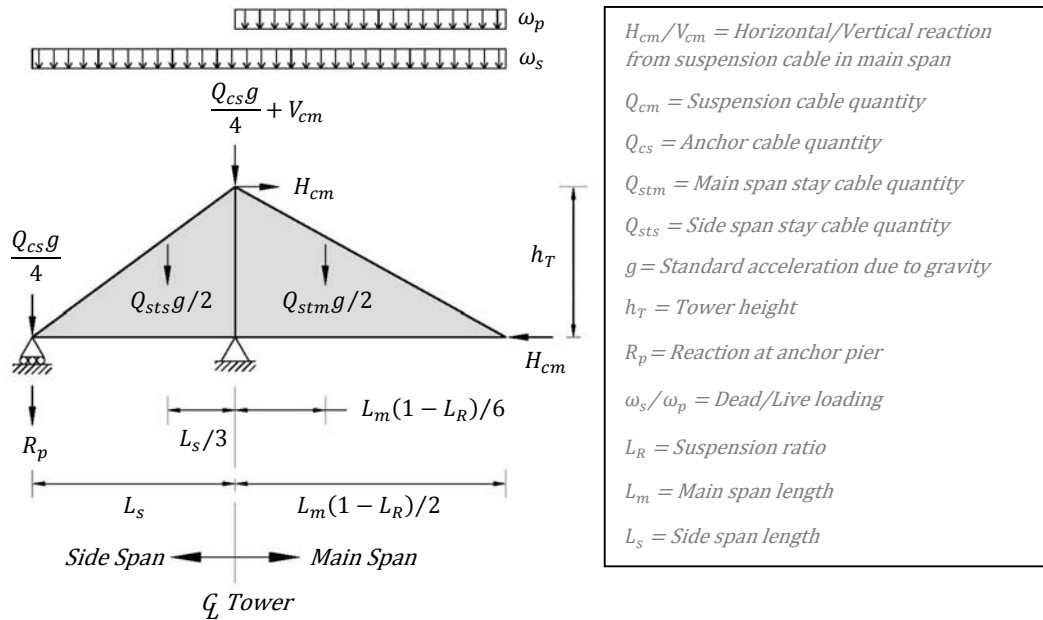
Figure 5.10: Idealized Free-Body Diagram for Maximum Anchor Pier Reaction

In Figure 5.10, it is important to note that the superstructure has been 'cut' at the end of the stayed region, and the suspension cable has been 'cut' at the tower. Furthermore, for simplicity, for each array of stay cables, the centre of gravity for the overall stay cable weight is assumed to be consistent with that of a pure triangle. This is not entirely accurate because in a semi-fan arrangement the weight of the stay cables is not uniformly distributed throughout the array. Nevertheless, in practical cases the distance from the tower to the centre of gravity of a stay cable array will vary from 0.28 to 0.35 times the length of the array (Gimsing & Georgakis, 2012). It is, therefore, sufficient to fix the

distance at 1/3 times the length of the array, particularly given that the weight of the stay cables is minor in comparison to the weight of the applied loading.

In accordance with the above assumptions, the reaction at the anchor pier can be obtained by taking moments about the base of the tower,

$$
\begin{aligned}
R_p = {} & \frac{(\omega_s + \omega_p)L_m(1 - L_R)^2}{8L_{SR}} + H_{cm}\frac{h_{TR}}{L_{SR}} + \frac{Q_{stm}g}{12L_{SR}}(1 - L_R) - \frac{Q_{sts}g}{6} \\
& - \frac{1}{2}\omega_s L_m L_{SR} - \frac{Q_{cs}g}{4}
\end{aligned}
\tag{5.19}
$$

Vertical equilibrium at the anchor pier then gives the vertical component of the anchor cable chord tension,

$$
V_{cs} = \frac{(\omega_s + \omega_p)L_m(1 - L_R)^2}{8L_{SR}} + H_{cm}\frac{h_{TR}}{L_{SR}} + \frac{Q_{stm}g}{12L_{SR}}(1 - L_R) - \frac{Q_{sts}g}{6} - \frac{1}{2}\omega_s L_m L_{SR}
\tag{5.20}
$$

Equation (4.9) can be substituted in for H_{cm} (during the substitution ω_s must be replaced by $\omega_s + \omega_p$ to account for the applied live loading), and an expression for the tensile chord force in the anchor cable can then be found by combining the vertical and horizontal components of the tensile chord force,

$$
\begin{aligned}
T_{cs} = {} & \frac{1}{24L_{SR}}\big[3L_m(\omega_s + \omega_p) + 3Q_{cm}g + 2Q_{stm}g(1 - L_R) - 4Q_{sts}g(L_{SR}) \\
& - 12L_m L_{SR}{}^2\omega_s\big]\frac{\sqrt{L_{SR}{}^2 + h_{TR}{}^2}}{h_{TR}}
\end{aligned}
\tag{5.21}
$$

It then follows that the total quantity of cable steel in both anchor cables is,

$$
Q_{cs} = 2\rho_{cs}\frac{T_{cs}}{\sigma_{cs}}L_m\sqrt{L_{SR}{}^2 + h_{TR}{}^2}
\tag{5.22}
$$

where ρ_{cs} and σ_{cs} are the density and design stress of the anchor cable material. When expanded, Equation (5.22) becomes,

$$
\begin{aligned}
Q_{cs} = {} & \frac{1}{12}\frac{\rho_{cs}}{\sigma_{cs}}L_m\big[3L_m(\omega_s + \omega_p) + 3Q_{cm}g + 2Q_{stm}g(1 - L_R) - 4Q_{sts}g(L_{SR}) \\
& - 12L_m L_{SR}{}^2\omega_s\big]\left(\frac{L_{SR}}{h_{TR}} + \frac{h_{TR}}{L_{SR}}\right)
\end{aligned}
\tag{5.23}
$$

where from Equation (5.9),

$$Q_{stm} = \frac{\rho_{st}}{\sigma_{st}} L_m{}^2 (\omega_s + \omega_p)(1 - L_R) h_{TR} \left[\frac{(1 - L_R)^2}{12 h_{TR}{}^2} + 1 \right] \qquad (5.24)$$

and,

$$Q_{sts} = \frac{\rho_{st}}{\sigma_{st}} L_m{}^2 (\omega_s + \omega_p) h_{TR} L_{SR} \left[\frac{2}{3} \left(\frac{L_{SR}}{h_{TR}} \right)^2 + 2 \right] \qquad (5.25)$$

Note from Equation (5.23) that the contribution from Q_{stm} and Q_{sts} amount to zero when the stay cables are symmetrically arranged about the centre of the towers (i.e. when $L_{SR} = (1 - L_R)/2$). Also, their contribution will be negligible when the length of the side span is less than the length of the stay cable array in the main span. This has mainly to do with the side span length. When the side span length is short, the anchorage force markedly increases due to the shortened lever arm. Consequently, the contribution from the stay cable weight becomes of little importance.

As a final note, it is important to acknowledge that, for simplicity, the anchor cable quantity was derived based on the chord force in the anchor cable. The maximum force in the anchor cable, which occurs near the tower, is somewhat larger. In this respect, Equation (5.23) underestimates the quantity required. Nevertheless, for efficiently designed anchor cables, the difference between the chord force and the maximum cable force is minor (Podolny & Scalzi, 1976).

5.2.4 Hanger Quantity

Figure 5.11 shows a reference diagram for the derivation of the hanger quantity. Similar to when estimating the quantity for the stay cables, the hanger area required for self-weight can be neglected. The error introduced as a result will be even less than in an array of stay cables due to the relatively shorter length and vertical inclination of the hangers.
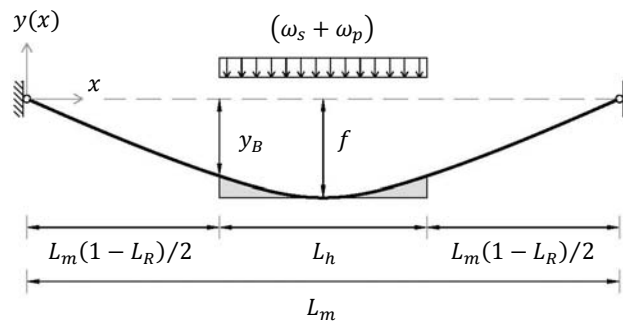
Figure 5.11: Diagram for Hanger Steel Quantity

In contrast to the derivation of the stay cable quantity, rather than integrating the quantity of cable steel in an infinitesimal segment of the hanger array, the solution can be obtained using a simpler approach. The total quantity in the hanger array can be obtained by multiplying together the density of the hanger material, the total hanger area required to carry the applied loads, and the average length of the hangers,

$$Q = \rho_h (A_{h\_total})(L_{h\_avg}) \tag{5.26}$$

When expanded, the expression becomes,

$$Q = \rho_h \frac{(\omega_s + \omega_p)L_h}{\sigma_h} \left(\frac{h_T - y_B}{3} \right) \tag{5.27}$$

where σ_h is the design stress of the hangers. Substituting in Equations (4.9) and (4.11) then gives,

$$Q = \frac{1}{3} \frac{\rho_h}{\sigma_h} L_m{}^2 (\omega_s + \omega_p) h_{TR} L_R{}^3 \left[\frac{\omega_s + \left(\frac{Q_{cm}g}{L_m} \right)}{\omega_s L_R (2 - L_R) + \left(\frac{Q_{cm}g}{L_m} \right)} \right] \tag{5.28}$$

However, a simpler expression can be obtained by neglecting the contribution from the self-weight of the suspension cable,

$$Q_{approx} = \frac{1}{3} \frac{\rho_h}{\sigma_h} L_m{}^2 (\omega_s + \omega_p) h_{TR} L_R{}^2 \left(\frac{1}{2 - L_R} \right) \tag{5.29}$$

Figure 5.12 shows a comparison of the quantities obtained from Equations (5.28) and (5.29) for an extreme main span length of 1000 metres. Although the error can be exorbitant when the tower height-to-span ratio is small it is important to recognize that, in those instances, the hanger quantity contributes very little to the overall cable steel quantity. This is demonstrated in Figure 5.13 where the hanger quantity is defined by Q_h (the design stress and unit weight of each cable type is set to 800MPa and 0.09MN/m³, respectively). Accordingly, the error introduced as a result of the use of Equation (5.29) will ultimately be insignificant.
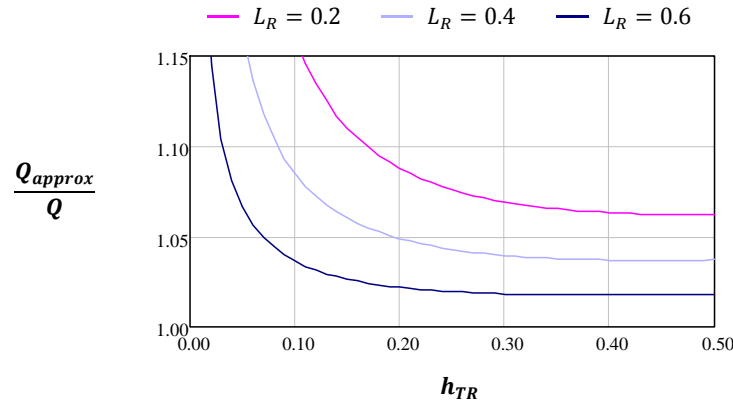
Figure 5.12: Error in Approximate Hanger Cable Quantity
Parameters: L_m = 1000m, σ_{cm} = 800MPa, γ_{cm} = 0.09MN/m³, ω_R = 0.6
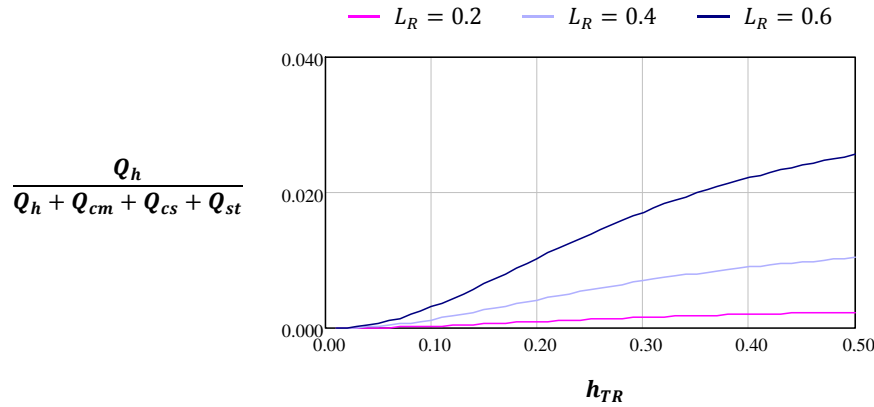
Figure 5.13: Hanger Cable Quantity in Relation to Total Cable Steel Quantity
Parameters: L_m = 1000m, ω_R = 0.6

5.2.5 Tower Quantity

The derivation of the tower quantity is particularly challenging. The required quantity strongly depends on both in-plane, and out-of-plane loading. For the in-plane loading, the towers must be capable of sustaining considerable axial and bending demands; each governed by different loading scenarios. Furthermore, the magnitude of the bending demands will depend on the geometry of the tower section as well as the articulation scheme for the superstructure; two parameters which are very difficult to generalize. Likewise, for out-of-plane loading, bending demands are no less difficult to quantify in general terms.

To facilitate the computations involved, Gimsing & Georgakis (2012) stipulate that the tower quantity should be based on the cross-sectional area required to support the maximum possible vertical load acting on the tower. This can be justified for in-plane forces because the governing loading scenario for the longitudinal bending demands produces comparatively less axial force in the tower. Therefore, sizing the towers based on the maximum possible vertical load ensures that there is some measure of reserved strength to handle the longitudinal bending demands.

To account for coincidental out-of-plane loading, the design stress of the tower is reduced in proportion to the ratio of the out-of-plane bending and the in-plane axial demands. Thus, the design stress is in essence considered variable along the height of the towers. Nonetheless, it is sufficient in this context to assign an average value for the design stress. For efficiently designed towers, Gimsing & Georgakis (2012) cite that a reduction in design stress of anywhere from 20% to 40% is appropriate. Accordingly, a reduction of 30% will be assumed herein.

Although reducing the design stress of the tower by a fixed percentage to account for out-of-plane loading may appear crude, it must be remembered that a precise estimate of the tower quantity is not the primary concern. Rather, the optimum proportions are ultimately influenced by the rate of change in the tower quantity. On that account, the use of a simplistic approach is justified. Nevertheless, the impact of varying the design stress of the tower / the reduction coefficient will be examined in Section 5.3.1.

Conveniently, the free body diagram given in Figure 5.10 can be re-purposed to derive the maximum possible vertical load on the towers. The only change that needs to be considered is that in this case, the governing load scenario occurs when live load covers the entire bridge. Bearing this in mind, taking moments about the anchor piers results in the following expression for the axial force acting on the tower,

$$N_v = \frac{Q_{stm}g}{2}\left(1 + \frac{1 - L_R}{6L_{SR}}\right) + \frac{Q_{sts}g}{3} + V_{cm} + H_{cm}\left(\frac{h_{TR}}{L_{SR}}\right) + (\omega_s + \omega_p)\frac{L_m L_{SR}}{2}$$
$$+ (\omega_s + \omega_p)\frac{(1 - L_R)L_m}{2}\left(1 + \frac{1 - L_R}{4L_{SR}}\right) + \frac{Q_{cs}g}{4}$$

(5.30)

Substituting in the horizontal and vertical components of the suspension cable force then gives,

$$N_v = \frac{1}{24L_{SR}}\Big[3L_m(\omega_s + \omega_p)(2L_{SR} + 1)^2 + 2Q_{stm}g(6L_{SR} - L_R + 1) + 8Q_{sts}g(L_{SR})$$
$$+ 3Q_{cm}g(4L_{SR} + 1) + 6Q_{cs}g(L_{SR})\Big]$$

(5.31)

However, to obtain the total vertical force acting on each tower, the vertical force from the cable

system must be added to the vertical force from self-weight,

$$V_T = N_v + W_t(z) \tag{5.32}$$

The self-weight of the tower varies along its height and, consequently, the self-weight is a function of the distance from the tower top, denoted by the letter, z. The area required in each tower can be obtained as,

$$A_t = \frac{N_v + W_t(z)}{\beta_t \sigma_t} \tag{5.33}$$

where σ_t is the design stress of the tower and β_t is the reduction coefficient to account for the effect of out-of-plane loading ($\beta_t = 0.7$). Notwithstanding, the self-weight of the tower is also a function of the tower area,

$$W_t(z) = A_t \gamma_t z \tag{5.34}$$

where γ_t is the unit weight of the tower material. Substituting Equation (5.34) into Equation (5.33) results in,

$$A_t = \frac{N_v}{\beta_t \sigma_t - \gamma_t z} \tag{5.35}$$

Accordingly, the total quantity of material required in both towers can be calculated as,

$$Q_t = 2\rho_t N_v \int_0^{h_T + h_B} \left(\frac{1}{\beta_t \sigma_t - \gamma_t z} \right) dz \tag{5.36}$$

which then simplifies to,

$$Q_t = \frac{2N_v}{g} \ln \left[\frac{1}{1 - \dfrac{(h_T + h_B)\gamma_t}{\beta_t \sigma_t}} \right] \tag{5.37}$$

The only parameter left to assign is h_B which represents the height of the towers below deck. This is again a difficult parameter to generalize. Typically, it is desirable that the tower height below deck be made as short as possible in order to minimize costs. Nonetheless, the majority of cable bridges are constructed over large waterways and a clearance envelope is often required at mid-span so that vessel navigation is not curtailed. Therefore, assuming the following:

- The base of the towers is at water level;
- The vertical profile of the roadway is parabolic;

- The vertical clearance required at mid-span is 50 metres; and
- The vertical slope of the roadway cannot exceed 5%.

Then, the minimum tower height below deck can be calculated as,

$$h_B = 50 \left(1 - \frac{L_m}{4000}\right) \qquad [in\ metres] \tag{5.38}$$

5.2.6 Superstructure Quantity

The superstructure quantity is defined as the quantity of material required to support the roadway. Using the assumed weight of the superstructure, ω_s, an expression for the superstructure quantity can be readily obtained,

$$Q_s = \frac{\omega_s L_m}{g \alpha_{sdl}} (1 + 2L_{SR}) \tag{5.39}$$

However, ω_s has thus far been used to represent the entire dead load acting on the superstructure which consists partly of superimposed dead load. The contribution from superimposed dead load must be removed and, therefore, an additional reduction coefficient, $\alpha_{sdl} \geq 1.0$, has been included for this purpose.

5.2.7 Load Correction

All of the expressions derived in previous sections depend on two main loading parameters: the dead load of the superstructure (ω_s) and the magnitude of the live load (ω_p). In contrast to the magnitude of the live load which can be considered constant, the superstructure dead load will be affected by the values of the other parameters. It is, therefore, necessary to develop an expression that accounts for the variation in the superstructure dead load.

If ω_{so} is used to represent the superstructure dead load of a bridge with known parameters (i.e. a reference bridge), then the variation in the dead load of the superstructure for a bridge with different parameters can be expressed as,

$$\Delta \omega_s = \gamma_s [(A_{sm} - A_{smo}) + (A_{sa} - A_{sao}) + (A_{sb} - A_{sbo})] \tag{5.40}$$

where γ_s is the unit weight of the superstructure material. In addition, A_{sm}/A_{smo} is the area required for miscellaneous transverse support members (i.e. floor beams, diaphragms, etc.), A_{sa}/A_{sao} is the area required for longitudinal axial demands, and A_{sb}/A_{sbo} is the area required for longitudinal bending demands. Accordingly, when the longitudinal bridge proportions are varied $(A_{sm} - A_{smo})$

can be assumed equal to zero, upon which,

$$\Delta\omega_s = \gamma_s[(A_{sa} - A_{sao}) + (A_{sb} - A_{sbo})] \tag{5.41}$$

The area required for longitudinal axial demands can be derived by integrating the axial demands in the superstructure. The governing loading scenario and the corresponding axial forces are shown in Figure 5.14.
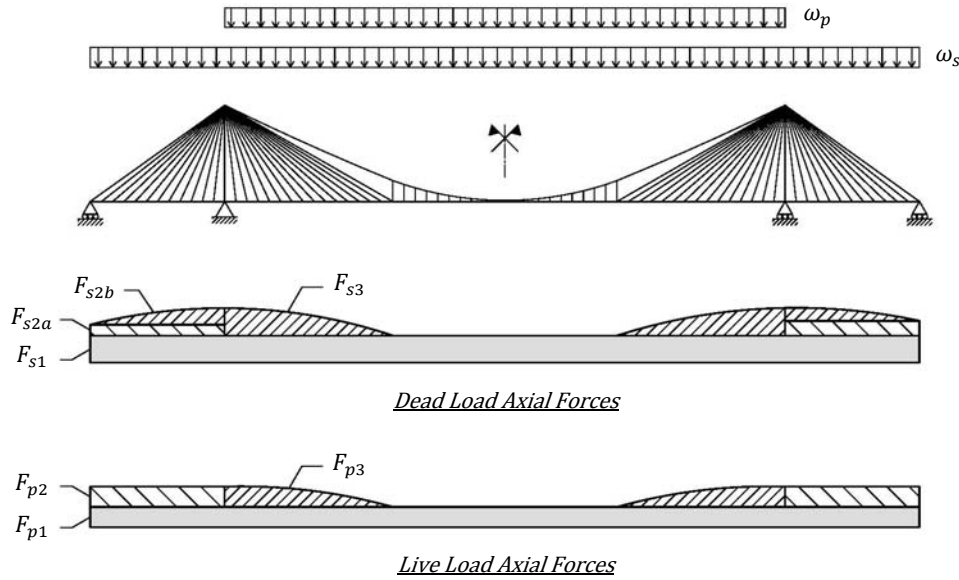
Figure 5.14: Longitudinal Axial Demands in Superstructure

A free body diagram of the pertinent forces has already been depicted in Figure 5.10. From Figure 5.10, it is clear that the superstructure axial force components F_{s1} and F_{p1} are, together, equal to the horizontal force in the suspension cable. Thus,

$$F_{s1} + F_{p1} = H_{cm} \tag{5.42}$$

Substituting in the appropriate expression for H_{cm} then yields,

$$F_{s1} + F_{p1} = \frac{1}{8h_{TR}}\left[Q_{cm}g + (\omega_s + \omega_p)L_R(2 - L_R)\right] \tag{5.43}$$

The uniform axial force components in the side span (F_{s2a} and F_{p2}) are a result of the anchorage force required to equilibrate the unbalanced portion of the dead and live load in the stayed regions of

the bridge. These force components will, therefore, be equal to the horizontal component of the anchorage force or, written another way,

$$F_{s2a} + F_{p2} = \overline{V_{cs}} \frac{L_{SR}}{h_{TR}} \tag{5.44}$$

where $\overline{V_{cs}}$ is the vertical component of the anchorage force. $\overline{V_{cs}}$ can be obtained from Equation (5.20); however, it is important to exclude the horizontal component of the suspension cable force since its contribution has already been accounted for in Equation (5.43). Accordingly,

$$\begin{aligned} F_{s2a} + F_{p2} = \frac{1}{24h_{TR}} \Big[&3\big(\omega_s + \omega_p\big)L_m(1 - L_R)^2 + 2Q_{stm}g(1 - L_R) - 4Q_{sts}gL_{SR} \\ &- 12\omega_s L_m L_{SR}{}^2 \Big] \end{aligned} \tag{5.45}$$

The portion of the side span dead load which is balanced produces a variable axial force in the side span which is represented by F_{s2b}. The magnitude of the axial force can be found by integrating the axial force in a small segment of the side span stay cable array,

$$F_{s2ba} = \int_0^x \frac{\omega_s x}{h_T} dx = \frac{1}{2} \frac{\omega_s x^2}{h_T} \tag{5.46}$$

where the origin for x is situated at the anchor pier. Similarly, the axial force in the main span stayed regions of the bridge due to dead and live load can be expressed as,

$$F_{s3} + F_{p3} = \int_0^x \frac{\big(\omega_s + \omega_p\big)x}{h_T} dx = \frac{1}{2} \frac{\big(\omega_s + \omega_p\big)x^2}{h_T} \tag{5.47}$$

where in this case, the origin for x is situated at the stay cable-hanger junction. Considering each of the axial force components in Figure 5.14, the volume of material required for the axial demands is,

$$\begin{aligned} VOL_{sa} = \frac{1}{\sigma_s} \Bigg[&\big(F_{s1} + F_{p1}\big)L_m(1 + 2L_{SR}) + 2\big(F_{s2a} + F_{p2}\big)(L_{SR}L_m) \\ &+ 2\int_0^{L_{SR}L_m} \big(F_{s2ba}\big)dx + 2\int_0^{\frac{L_m(1-L_R)}{2}} \big(F_{s3} + F_{p3}\big)dx \Bigg] \end{aligned} \tag{5.48}$$

which simplifies to,

$$VOL_{sa} = \frac{L_m}{24h_{TR}\sigma_s}\left[L_m(\omega_s + \omega_p)(1 - L_R{}^3 + 3L_R + 6L_{SR}) - 16L_m L_{SR}{}^3\omega_s \right.$$
$$\left. + 4Q_{stm}gL_{SR}(1 - L_R) - 8Q_{sts}g(L_{SR})^2 + 3Q_{cm}g(2L_{SR} + 1)\right] \tag{5.49}$$

Clearly, the cross sectional area required for the longitudinal axial demands varies along the length of the bridge; however, in this context it will be sufficiently accurate to use the average area required, which can be readily obtained from Equation (5.49),

$$A_{sa} = \frac{VOL_{sa}}{L_m(1 + 2L_{SR})} \tag{5.50}$$

In contrast to the longitudinal axial demands, the change in the longitudinal bending demands is difficult to estimate without employing sophisticated analyses. In addition, the area required for the longitudinal bending demands depends on the depth of the superstructure which is a difficult parameter to generalize. Therefore, for the time being it will be assumed that the change in longitudinal bending demands has zero effect on the superstructure quantity. The validity of this assumption will be revisited later in the chapter. Accordingly, Equation (5.41) becomes,

$$\Delta\omega_s = \gamma_s(A_{as} - A_{sao}) \tag{5.51}$$

and the dead load of the superstructure can be written as,

$$\omega_s = \omega_{so} + \gamma_s(A_{as} - A_{sao}) \tag{5.52}$$

However, because ω_s depends on A_{as}, which is also a function of ω_s, an unavoidable consequence of this approach is that iteration is required to determine the various bridge component quantities. Also, because the superstructure quantity directly depends on ω_s, it is important to make one more modification. Specifically, it is important that the magnitude of the superimposed dead load be made constant and independent of ω_s. This can be achieved by linking the superimposed dead load to the superstructure dead load of the reference bridge. On that account, Equation (5.39) becomes,

$$Q_s = \frac{L_m(1 + 2L_{SR})}{g}[\omega_s - (\alpha_{sdl} - 1)\omega_{so}] \tag{5.53}$$

5.2.8 Summary of Equations

L_m = Main span length	ω_s = Superstructure dead load
L_R = Suspension ratio	ω_{so} = Reference superstructure dead load
L_{SR} = Side-to-main span length ratio	ω_p = Live load
h_{TR} = Tower height-to-span ratio	$\rho_m\,/\gamma_m$ = Density/Unit weight of material 'm'
β_t = Factor for out-of-plane loading on towers	σ_m = Design stress of material 'm'
α_{sdl} = Factor for superimposed dead load	g = Standard acceleration due to gravity

Stay Cable Steel Quantity

Main Span
$$Q_{stm} = \frac{\rho_{st}}{\sigma_{st}} L_m{}^2 (\omega_s + \omega_p)(1 - L_R)h_{TR}\left[\frac{(1-L_R)^2}{12h_{TR}{}^2} + 1\right] \qquad (5.54)$$

Side Span
$$Q_{sts} = \frac{\rho_{st}}{\sigma_{st}} L_m{}^2 (\omega_s + \omega_p)h_{TR}L_{SR}\left[\frac{2}{3}\left(\frac{L_{SR}}{h_{TR}}\right)^2 + 2\right] \qquad (5.55)$$

Suspension Cable Quantity

$$Q_{cm} = \frac{1}{g}L_m(\omega_s + \omega_p)\frac{L_R(2 - L_R)\xi\eta}{1 - \xi\eta}\left[(1 - L_R)\eta + L_R\frac{(\eta^2 + 5)}{6}\right] \qquad (5.56)$$

where,

$$\eta = \sqrt{1 + 16\left(\frac{h_{TR}}{2 - L_R}\right)^2} \qquad \text{and} \qquad \xi = \frac{\gamma_{cm}\,L_m}{8\,\sigma_{cm}h_{TR}}$$

Anchor Cable Quantity

$$Q_{cs} = \frac{1}{12}\frac{\rho_{cs}}{\sigma_{cs}}L_m\big[3L_m(\omega_s + \omega_p) + 3Q_{cm}g + 2Q_{stm}g(1 - L_R) - 4Q_{sts}g(L_{SR})$$
$$- 12L_mL_{SR}{}^2\omega_s\big]\left(\frac{L_{SR}}{h_{TR}} + \frac{h_{TR}}{L_{SR}}\right) \qquad (5.57)$$

Hanger Cable Quantity

$$Q_h = \frac{1}{3}\frac{\rho_h}{\sigma_h}L_m{}^2(\omega_s + \omega_p)h_{TR}L_R{}^2\left(\frac{1}{2 - L_R}\right) \qquad (5.58)$$

Tower Quantity

$$Q_t = \frac{2N_v}{g} \ln \left[\frac{1}{1 - \frac{(h_{TR}L_m + h_B)\gamma_t}{\beta_t \sigma_t}} \right] \tag{5.59}$$

where,

$$N_v = \frac{1}{24L_{SR}} \Big[3L_m(\omega_s + \omega_p)(2L_{SR} + 1)^2 + 2Q_{stm}g(6L_{SR} - L_R + 1) + 8Q_{sts}g(L_{SR})$$
$$+ 3Q_{cm}g(4L_{SR} + 1) + 6Q_{cs}g(L_{SR}) \Big]$$

and,

$$h_B = 50 \left(1 - \frac{L_m}{4000} \right) \qquad [in \; metres]$$

Superstructure Quantity

$$Q_s = \frac{L_m(1 + 2L_{SR})}{g} [\omega_s - (\alpha_{sdl} - 1)\omega_{so}] \tag{5.60}$$

Load Correction Equation

$$\omega_s = \omega_{so} + \gamma_s(A_{sa} - A_{sao}) \tag{5.61}$$

where,

$$A_{sa} = \frac{1}{24h_{TR}\sigma_s(2L_{SR} + 1)} \Big[L_m(\omega_s + \omega_p)\big(1 - L_R{}^3 + 3L_R + 6L_{SR}\big) - 16L_mL_{SR}{}^3\omega_s$$
$$+ 4Q_{stm}gL_{SR}(1 - L_R) - 8Q_{sts}g(L_{SR})^2 + 3Q_{cm}g(2L_{SR} + 1) \Big]$$

and,

A_{sao} is computed using the same expression as A_{sa} with the corresponding parameters for the reference bridge.

5.3 Span Proportions

5.3.1 Tower Height-to-Span Ratio

Based on the quantities given by Equations (5.54) to (5.61), the expected cost of a self-anchored discontinuous hybrid cable bridge, C_H, can be expressed as,

$$C_H = c_{st}(Q_{stm} + Q_{sts}) + c_{cm}(Q_{cm} + Q_{cs}) + c_h Q_h + c_t Q_t + c_s Q_s + c_f Q_f \qquad (5.62)$$

where c_m represents the unit cost of component 'm' and Q_f represents the quantity of the bridge foundations. For simplicity, the anchor cables and the suspension cable are considered as a collective entity and it is assumed both cables share the same material/cost parameters. This is justified given that the anchor cables and suspension cable share a common load path. In regard to the foundation quantity, Q_f was not discussed in Section 5.2 because it is a parameter which cannot be generalized. Many different types of foundations exist and the type chosen will depend on a wide variety of local conditions. Nevertheless, an accurate estimate of the optimum tower height-to-span ratio can still be obtained if it is assumed that the tower height-to-span ratio has a negligible effect on the foundation quantity. This is because the optimum tower height-to-span ratio depends only on the rate of change in the quantities. This is reflected in the mathematical equation which gives the condition upon which the optimum ratio is found,

$$\frac{dC_H}{dh_{TR}} = 0 \qquad (5.63)$$

Neglecting the change in the foundation quantity, Equation (5.63) may also be written as,

$$\frac{d(Q_{stm} + Q_{sts})}{dh_{TR}} + \frac{c_{cm}}{c_{st}}\frac{d(Q_{cm} + Q_{cs})}{dh_{TR}} + \frac{c_h}{c_{st}}\frac{dQ_h}{dh_{TR}} + \frac{c_t}{c_{st}}\frac{dQ_t}{dh_{TR}} + \frac{c_s}{c_{st}}\frac{dQ_s}{dh_{TR}} = 0 \qquad (5.64)$$

whereupon it also becomes clear that the optimal solution does not depend on the specific values assigned for the unit costs – only the ratios of the unit costs affect the solution. This is highly convenient given that specific unit costs may vary greatly from site-to-site whereas the ratios of the unit costs can be more or less generalized.

Although less apparent, the optimal solution will also not depend on the specific values assigned for the live load (ω_p) and superstructure dead load (ω_s). Examining closely the equations for the quantities of the various components, it can be seen that the superstructure dead load can be entirely factored out of Equation (5.64) so that, from a loading perspective, the optimal solution depends only on the live load ratio of the reference bridge, ω_{Ro}, which is defined as,

$$\omega_{Ro} = \frac{\omega_p}{\omega_{so}} \qquad\qquad (5.65)$$

Notwithstanding, the iterative nature and complexity of Equations (5.54) to (5.61) make it necessary to evaluate Equation (5.64) numerically. However, values first need to be assigned to the input parameters.

The assigned values for the material and cost input parameters are given in Table 5.1. The material input parameters are based on engineering experience and reflect current design standards. For simplicity, the material input parameters for the superstructure and towers are defined for all-steel or all-concrete scenarios. In addition, the material input parameters are assumed equal for each of the cable types. The cost input parameters are based on historical unit price information for conventional cable bridge projects. The information was obtained from a comprehensive structure study report compiled by multiple professional engineering firms (Parsons, 2008). The use of the unit cost parameters reflects the current method by which the cost of large infrastructure projects is assessed. Accordingly, the value of the parameters incorporates all costs related to the construction of a particular component. This mainly includes material, fabrication, transportation, erection, and testing costs.

Table 5.1: Material and Cost Input Parameters

Input Parameter	Superstructure		Towers		Cables		
	(Concrete)	(Steel)	(Concrete)	(Steel)	(Stays)	(Suspension & Anchor)	(Hangers)
γ (kN/m³)	24	77	24	77	90	90	90
σ (MPa)	25	250	25	250	800	800	800
β_t	n/a	n/a	0.7	0.7	n/a	n/a	n/a
α_{sdl}	1.1	1.1	n/a	n/a	n/a	n/a	n/a
c/c_{st}	0.1	0.85	0.125	0.6	1.0	0.75	1.0

Also required is the assignment of the input parameters for the reference bridge. For familiarity, the reference bridge is designated as a standard cable-stayed bridge (L_{Ro} = 0). All of the input material and cost parameters for the reference bridge are assigned values consistent with those given in Table 5.1. The only unique input parameters which need to be assigned for the reference bridge are the tower height-to-span ratio (h_{TRo}) and the live load ratio (ω_{Ro}). The tower height-to-span ratio is set at a conventional value for cable-stayed bridges, h_{TRo} = 0.25. The live load ratio depends on the superstructure material and, accordingly, for the all-steel and all-concrete scenarios the live load ratio is assigned values of ω_{Ro} = 0.6 and ω_{Ro} = 0.2, respectively.

Using the assigned input values, Table 5.2 gives the calculated optimum tower height-to-span ratio for a self-anchored discontinuous hybrid cable bridge with a span length of 500 metres. Optimal values are presented considering multiple suspension ratios (L_R) and multiple side-to-main span

length ratios (L_{SR}). For consistency, the span lengths of the reference bridge were set to equal the span lengths defined for the hybrid cable bridge when computing the optimal values.

Table 5.2: Optimal Tower Height-to-Span Ratio for Bridge with 500 metre Main Span

| | | Tower Material | | | | | |
| | | (Concrete) | | | (Steel) | | |
L_{SR} \ L_R		0.2	0.4	0.6	0.2	0.4	0.6
(Concrete)	0.3	0.23	0.24	0.25	0.21	0.23	0.24
	0.4	0.24	0.25	0.26	0.22	0.24	0.25
	0.5	0.24	0.25	0.26	0.22	0.24	0.25
(Steel)	0.3	0.27	0.29	0.30	0.25	0.27	0.28
	0.4	0.29	0.30	0.32	0.27	0.29	0.30
	0.5	0.30	0.31	0.32	0.28	0.29	0.30

(Superstructure Material shown in left margin: Concrete for first three rows, Steel for last three rows)

Parameters: L_m = 500m, $L_{mo} = L_m$, $L_{SRo} = L_{SR}$, h_{TRo} = 0.25, also refer to Table 5.1

Based on Table 5.2, the optimum tower height-to-span ratio,

- Decreases when steel is used in place of concrete for the towers;
- Increases when steel is used in place of concrete for the superstructure;
- Increases with increasing suspension ratio; and
- Increases when the side-to-main span length ratio is increased.

However, in each case, the change to the optimum tower height-to-span ratio is minor. The cause for these trends can be explained by examining the cost function (Equation (5.62)) which is plotted in Figure 5.15 as a function of the tower height-to-span ratio, for a suspension ratio of 0.4 and a side-to-main span ratio of 0.3. For clarity, the cost function is broken down on a component-by-component basis. Moreover, the cost of each component is normalized with respect to the cost of the reference bridge.

From Figure 5.15, it can be seen that when steel is used in place of concrete for the towers, the cost of the towers increases relative to the other components. Consequently, the overall optimum shifts towards the optimum for the tower cost. Similarly, when steel is used in place of concrete for the superstructure, the overall cost becomes largely controlled by the cost of the superstructure. Accordingly, the overall optimum shifts towards the optimum for the superstructure cost. In addition, although not apparent from Figure 5.15, increasing the suspension ratio leads to slight increases in the cost of the superstructure and suspension cable. As a result, the overall optimum increases since the cost of both these components diminishes when the tower height-to-span ratio is

increased. Likewise, as the side-to-main span length increases, the total length of the bridge increases. This again has the effect of increasing the relative contribution of the superstructure cost.
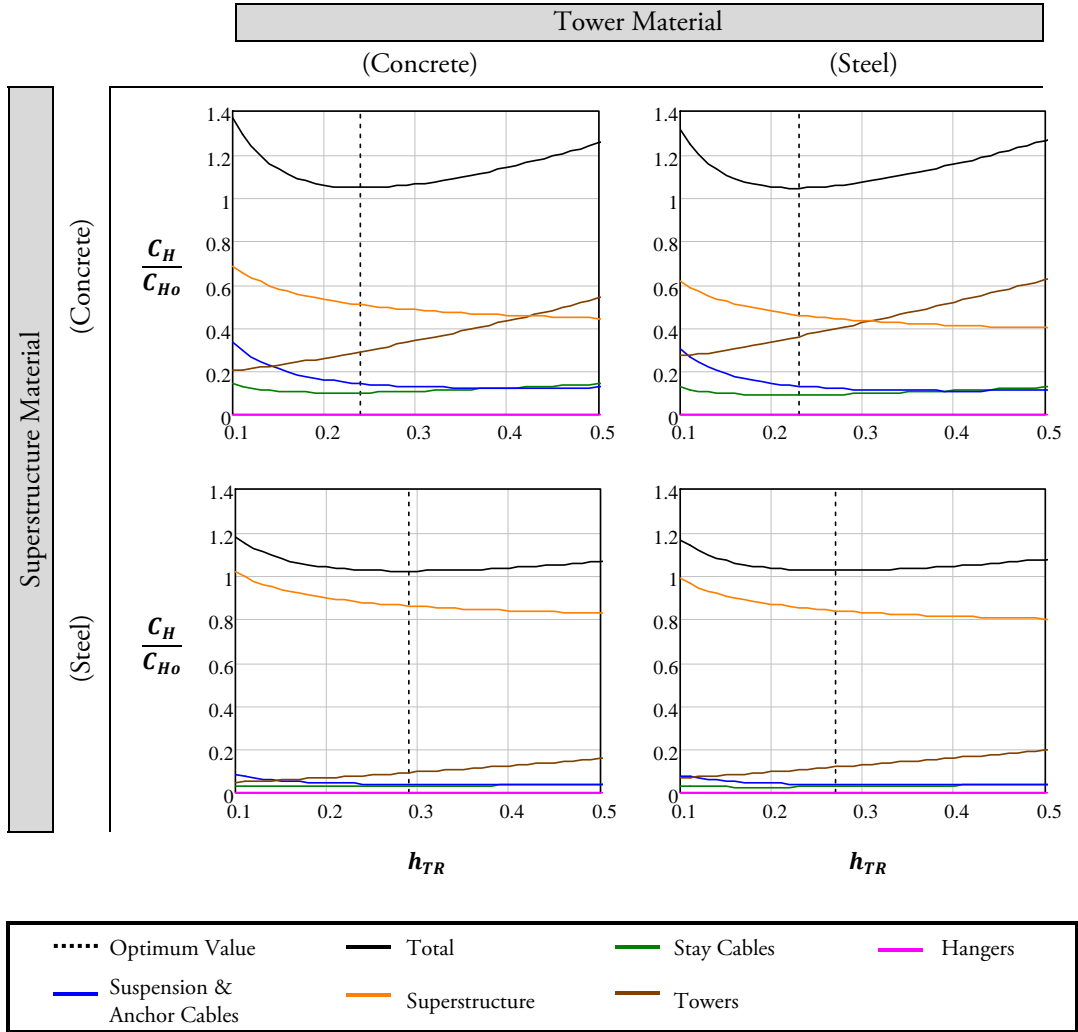
Figure 5.15: Cost Function Normalized with Respect to Cost of Reference Bridge
Parameters: L_m = 500m, L_R = 0.4, L_{SR} = 0.3, L_{mo} = L_m, L_{SRo} = L_{SR}, h_{TRo} = 0.25, also refer to Table 5.1
*Excludes foundation cost

Another important observation from Figure 5.15 is that the hanger cost is inconsequential relative to the cost of the other components. This is also true when the value of the suspension ratio is increased. Thus, the cost of the hangers can be effectively negated in the calculation of the total cost.

It is also of note that the optimum tower height-to-span ratio is fairly impervious to changes in the

main span length. As confirmation, Figure 5.16 shows how the optimum tower height-to-span ratio varies with the main span length for a suspension ratio of 0.4 and a side-to-main span ratio of 0.3. The positive trend occurs because as the span length is increased the cost of the suspension/anchor cable steel and the superstructure become slightly more dominant. The only exception is for the case of a steel superstructure and concrete tower where it is the cost of the tower which becomes more dominant.
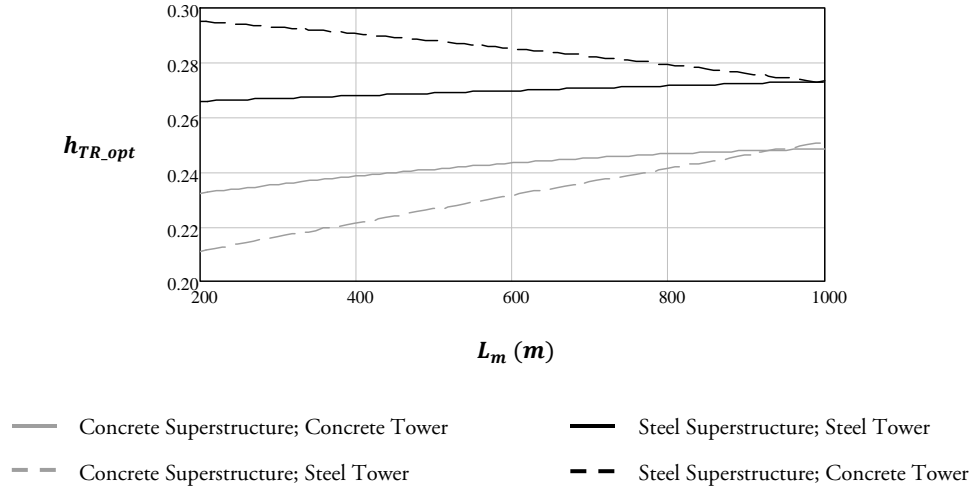
Figure 5.16: Optimum Tower Height-to-Span Ratio versus Main Span Length
Parameters: L_R = 0.4, L_{SR} = 0.3, L_{mo} = L_m, L_{SRo} = L_{SR}, h_{TRo} = 0.25, also refer to Table 5.1

Considering all of the data presented above, the optimum tower height-to-span ratio of self-anchored discontinuous hybrid cable bridges can be specified to be within the range of 0.2 to 0.3. However, it is important to revisit some of the initial assumptions made in the derivation of the optimal range. In regards to the assumed values for the input parameters (Table 5.1), the sensitivity of the optimum tower height-to-span ratio to changes in the assumed values was computed by varying each input parameter independently to within plus or minus twenty percent of its original assumed value. The results are plotted in Figure 5.17. In accordance with Figure 5.16, the results are only marginally dependent on the main span length.

It is not surprising that, based on Figure 5.15, the optimum tower height-to-span ratio is most affected by the design stress and unit cost of the towers and superstructure. Nevertheless, a twenty percent change in the design stress or unit cost of the towers or superstructure returns less than a ten percent change in the optimum tower height-to-span ratio. Comparatively, the sensitivity with respect to all other input parameters is minor. This includes the input parameters for the reference bridge (ω_{Ro}, h_{TRo}), and the input factor which accounts for superimposed dead load (α_{sdl}). The only exception is the design stress and unit cost of the suspension/anchor cable which have a notable

influence when the superstructure is composed of concrete.
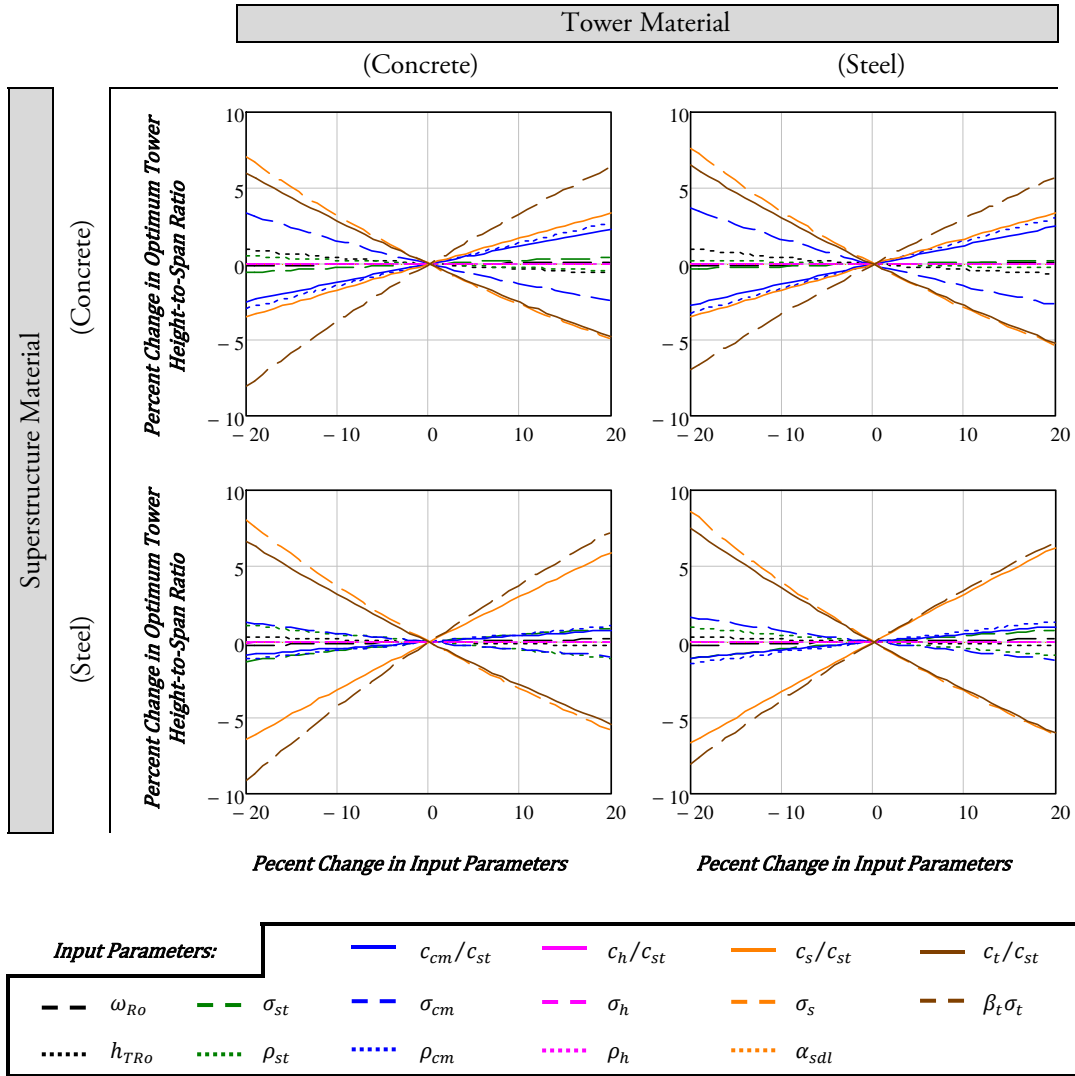
Figure 5.17: Sensitivity of Optimum Tower Height-to-Span Ratio
Parameters: L_m = 500m, L_R = 0.4, L_{SR} = 0.3, L_{mo} = L_m, L_{SRo} = L_{SR}, h_{TRo} = 0.25, also refer to Table 5.1

During the derivation of the optimal range it was also assumed that the rate of change in the superstructure bending moment envelope could be neglected. Although the rate of change in the bending moment envelope is too complex to compute algebraically, this assumption can be justified from the results presented in Chapter 4. Specifically, Figure 4.24 and Figure 4.26 show that the superstructure bending moment envelope is not highly sensitive to the tower height-to-span ratio when the tower height-to-span ratio is varied within the optimal range.

The optimal range was also derived assuming that the tower foundation cost could be neglected. The tower foundation cost is, again, too complex to compute algebraically. However, the vertical force from dead and live load constitutes a large portion of the foundation demands. Therefore, the cost of the foundation can be gauged by examining the magnitude of the vertical force acting on the foundation from dead and live load. This force is given by,

$$N_f = N_v + \frac{1}{2}Q_t g \qquad (5.66)$$

where N_v is the vertical force at the top of the towers from the cable system (Equation (5.31)), and Q_t is the tower quantity. The relationship between N_f and the tower height-to-span ratio is plotted in Figure 5.18. For ease of comparison, the ordinates are normalized with respect to the resulting force when the tower height-to-span ratio equals 0.25.
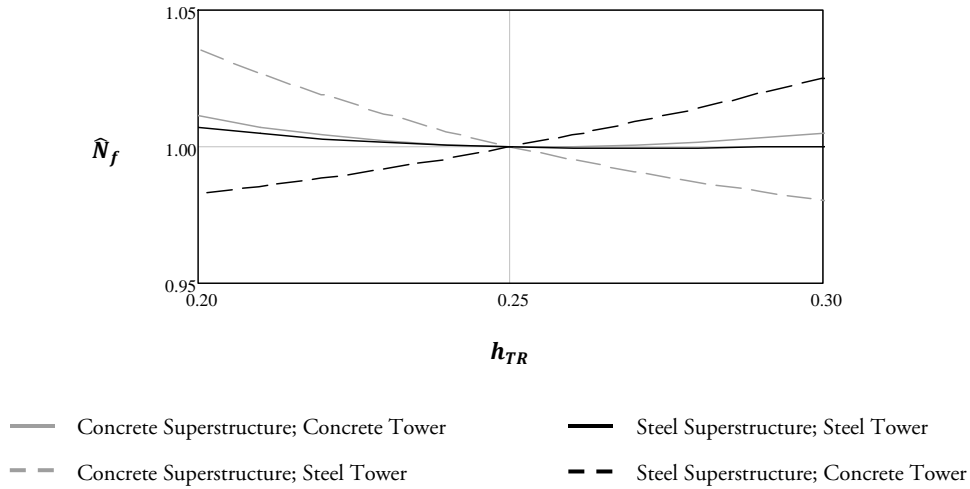
Figure 5.18: Vertical Force at Tower Foundation versus Tower Height-to-Span Ratio
Parameters: L_m = 500m, L_R = 0.4, L_{SR} = 0.3, $L_{mo} = L_m$, $L_{SRo} = L_{SR}$, h_{TRo} = 0.25, also refer to Table 5.1

It can be seen from Figure 5.18 that when the tower height-to-span ratio is varied within the optimal range the vertical force on the foundation varies by less than 5%. Still, the tower foundation cost generally constitutes a large portion of the overall bridge cost. Therefore, for cases when the tower is composed of concrete, it would be prudent to slightly reduce the value of the optimum tower height-to-span ratio reported in Table 5.2. Moreover, there are other justifications for reducing the tower height-to-span ratio. Aesthetically, lofty towers can be overly striking on most landscapes and, structurally, nonlinear effects and tower bending moments will increase with increasing tower height.

Ultimately, for the aforementioned reasons, a tower height-to-span ratio in the range of 0.20-0.25 is

recommended. This is in disagreement with pre-established notions that the optimum tower height-to-span ratio should be computed by achieving consistency between the tower height-to-span ratio of the stayed region and the historically established optimum tower height-to-span ratio for cable-stayed bridges. Or, alternatively, that the optimum tower height-to-span ratio should be computed by achieving consistency between the sag ratio of the suspension cable and the historically established optimum tower height-to-span ratio for self-anchored suspension bridges. However, these notions are flawed in that they violate the basic principle of sub-optimization which states, 'Optimizing each subsystem independently will not in general lead to a system optimum, or more strongly, improvement of a particular subsystem may actually worsen the overall system' (Machol, 1965).

In addition, it is logical that the optimal range for the tower height-to-span ratio should match so closely with the historically established optimal range for cable-stayed bridges. Based on Equations (4.23) and (5.31), the maximum axial force in the superstructure and towers does not depend significantly on the suspension ratio. This becomes clear when the contribution from the weight of the cable steel is neglected. Furthermore, the cost of the cable steel only changes marginally when the suspension ratio is varied. This is because the additional cost of the suspension cable and hanger steel is offset by the discounted cost of the stay cable steel. It could, therefore, be reasoned that the optimum tower height-to-span ratio should remain fairly constant regardless of the suspension ratio and this is what the calculations presented above reflect.

5.3.2   Side-to-Main Span Ratio

The span lengths of a bridge are normally constrained by the site topography and, therefore, the side-to-main span ratio is a parameter which cannot be freely assigned. It is also a parameter which affects many design aspects. For these reasons, attempting to specify a single optimal value for the side-to-main span ratio would be misguided. However, the effects associated with the side-to-main span ratio are more or less independent of the suspension ratio. This will become clear later on in this section. Therefore, an optimal range for the side-to-main span ratio can be determined based on the established optimal range for cable-stayed bridges.

Most authors agree that the optimal side-to-main span ratio for a cable-stayed bridge lies within the range 0.35 to 0.45 (Podolny & Scalzi, 1976; Leonhardt, 1991; Farquhar, 2008). The rationale behind this range is based on a mixture of qualitative and quantitative reasoning. Details discussed below will provide guidance for the selection of the appropriate side-to-main span ratio in discontinuous hybrid cable bridges.

The lower limit for the optimal side-to-main span range is normally governed by the uplift force at the anchor pier and by the tower/tower foundation cost. An uplift force is generated at the anchor

pier when there is an imbalance of loading between the main span and the side spans. Thus, the magnitude of the uplift force increases as the side-to-main span ratio decreases. In addition, the maximum uplift force occurs when only the main span is loaded with live load. Large uplift forces are undesirable because the presence of large tensile forces adversely affects the design of the anchor pier and anchor pier foundation.

If the contribution from the self-weight of the cables is neglected then, from Equation (5.19), the maximum uplift force at the anchor pier can be approximated as,

$$R_p \cong \frac{\omega_s L_m}{8 L_{SR}} \left[1 + \omega_R - 4 L_{SR}^2 \right] \tag{5.67}$$

The relationship between the side-to-main span ratio (L_{SR}) and the uplift force (R_p) is plotted in Figure 5.19. The ordinates of the plot are normalized so that they are independent of the superstructure dead load (ω_s), and the main span length (L_m). In doing so, it is assumed that the main span length is fixed and the effect the side-to-main span ratio has on the superstructure dead load is negligible.
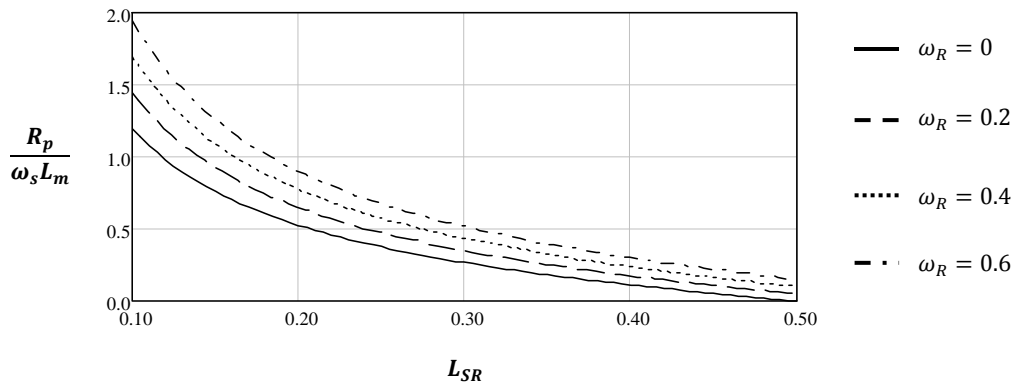
Figure 5.19: Uplift Force at Anchor Pier versus Side-to-Main Span Ratio

As an example, it can be seen from Figure 5.19 that transitioning from a side-to-main span ratio of 0.4 to 0.2 amplifies the uplift force at the anchor pier by more than a factor of 3. From a design perspective, the consequences resulting from decreasing the side-to-main span ratio are perhaps made clearer by considering the magnitude of added dead load required in the side spans to balance the uplift force. Accordingly, denoting ω_{ss} and ω_{sm} as the superstructure dead load in the side and main spans, respectively, Equation (5.67) can be re-written as,

$$R_p \cong \frac{\omega_{sm} L_m}{8 L_{SR}} \left[1 + \omega_{Rm} - 4 L_{SR}^2 \left(\frac{\omega_{ss}}{\omega_{sm}} \right) \right] \qquad (5.68)$$

where ω_{Rm} is the unfactored live load ratio for the main span only ($\omega_{Rm} = \omega_p / \omega_{sm}$). Solving for the superstructure dead load ratio (ω_{ss}/ω_{sm}) when R_p equals zero then gives the balancing condition as,

$$\frac{\omega_{ss}}{\omega_{sm}} \cong \frac{1 + \omega_{Rm}}{4 L_{SR}^2} \qquad (5.69)$$
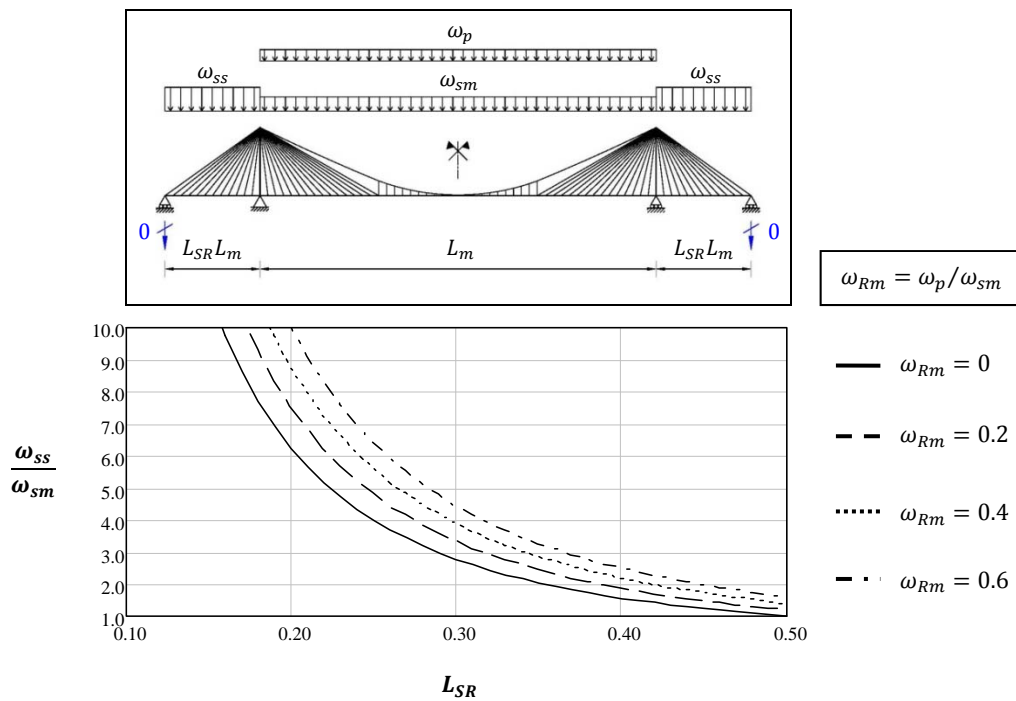
Figure 5.20: Dead Load Ratio Required to Balance Uplift Force at Anchor Pier

For convenience, the balancing condition is plotted in Figure 5.20. Clearly, for a side-to-main span ratio of 0.2 the dead load of the superstructure in the side span is required to be anywhere from 6 to 10 times greater than the dead load in the main span to prevent uplift under service loads. Designing for a variance this large is not practical. Normally, in regards to the superstructure, even if two different materials are judiciously employed to balance the uplift force, a conventional concrete section is only in the order of 4 times heavier than a conventional steel section. Therefore, if uplift forces are to be avoided under service loads without any additional ballast, a lower limit of roughly 0.35 must be imposed on the side-to-main span ratio. However, it should be recognized that this

value is conservative because the influence of the superstructure bending stiffness was ignored in its formation.

The cost of the tower and tower foundation can again be gauged with respect to the total vertical force acting on the foundation (Equation (5.66)). However, for simplicity, it is appropriate here to neglect the contribution from the weight of the cable steel. Accordingly, the expression for the total vertical force at the tower foundation becomes,

$$N_f \cong \frac{L_m}{8L_{SR}}(\omega_s + \omega_p)(2L_{SR} + 1)^2 \Lambda \tag{5.70}$$

where,

$$\Lambda = 1 + ln\left[\frac{1}{1 - \frac{(h_{TR}L_m + h_B)\gamma_t}{\beta_t \sigma_t}}\right]$$

Since all of the parameters can be assumed independent of L_{SR}, it becomes apparent from Equation (5.70) that a simple common relationship exists between the total vertical force at the tower foundation and the side-to-main span ratio. When the relationship is plotted (Figure 5.21), it also becomes apparent that the total vertical force at the tower foundation starts to increase rapidly when the side-to-span ratio falls below 0.40. This is how the cost of the tower and tower foundation factor in to the lower limit of the side-to-main span ratio.
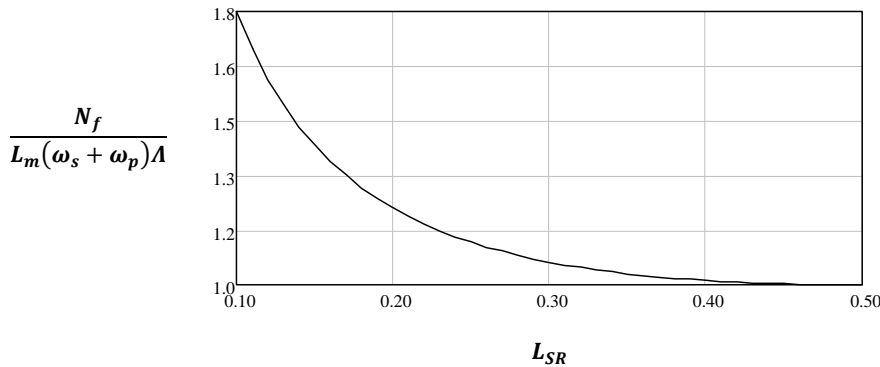
Figure 5.21: Vertical Force at Tower Foundation versus Side-to-Main Span Ratio

At the opposite end of the range, the effective stiffness and the stress range of the anchor cable normally set the upper limit for the side-to-main span ratio. The effective stiffness of the anchor cable controls the longitudinal deflection at the top of the towers. From Chapter 4 (Figure 4.23), it has already been observed that the effective stiffness of the anchor cable is greatest when the side-to-main

span ratio is slightly less than the tower height-to-span ratio. Accordingly, based on this one aspect, the optimum side-to-main span ratio would be within, or slightly below, the range of 0.2 to 0.25. Since this is clearly below the lower limit specified above, the effectiveness of the anchor cable is simply an important design aspect to keep in mind when assigning the side-to-main span ratio. In that respect, the effective stiffness of the anchor cable is greater when the side-to-main span ratio is kept relatively small.

The stress range of the anchor cable is important to consider because of its relation to fatigue. Fatigue can severely reduce the life span of a cable and, therefore, it is important that any concerns of fatigue are abated. This requires that the stress range in the anchor cable be kept within reasonable limits. Live load positioned in the main span increases the stress in the anchor cable and live load positioned in the side spans decreases the stress in the anchor cable. Therefore, the larger the side-to-main span ratio, the larger the stress range will be in the anchor cable.

Historically, fatigue of the anchor cable has been evaluated using the two worst case loading scenarios – full main span lane loading alternating with full side span lane loading. However, the magnitude of the applied live load was reduced given that these loading scenarios are unlikely to occur regularly and fatigue is a phenomenon which in this case is associated with high frequency loading. Furthermore, to simplify the calculations involved the influence of the superstructure bending stiffness was neglected. On this basis, for vehicular bridges employing steel and concrete superstructures, the upper limit for the side-to-main span ratio was computed to be roughly, 0.35 and 0.4, respectively (Leonhardt & Zellner, 1980).

Recent studies on the fatigue of anchor cables have revealed that approaches based on the worst case loading scenarios are overly conservative (Goodyear, 1987). Consequently, many design codes now specify that that the load from a single design truck be used to evaluate fatigue. This type of loading is more consistent with real fatigue loading conditions. When the stiffness of the superstructure is also taken into account, the upper limit for the side-to-main span ratio from a fatigue perspective is likely to be between 0.4 and 0.45 (Farquhar, 2008).

5.3.3 Suspension Ratio

When the tower-to-height ratio is in the range of 0.2 to 0.25, costs will increase moderately with increasing suspension ratio primarily in response to increased superstructure and tower demands (Figure 4.24). As such, it is best to keep the suspension ratio to a minimum. Ultimately, aesthetics will dictate the upper limit of the suspension ratio.

The importance of bridge aesthetics should not be undervalued. Bridges are designed and built to

provide decades of service. An unsightly bridge, even if functional, can become a long-lasting scar on a city landscape resulting in property devaluation and public outcry. In contrast, an aesthetically pleasing bridge can more quickly gain the approval of client groups, approving authorities, and the public in general. Moreover, a well-balanced and pleasing design can often become a local or even national icon. Bridge aesthetics is thereby becoming increasingly more relevant during the bridge procurement process.

There are many different theories regarding the best aesthetic practices. However, for long span bridges, there is one rule which is universal: the emphasis should be on the main span. The longer the main span is relative to the side spans, the longer the main span will appear and this lends to an overall slender appearance for the bridge. For the same reason, a discontinuous hybrid cable bridge will be more aesthetically appealing if the length of the stayed region in the main span is made greater than or equal to the length of the side span. This is demonstrated in Figure 5.22 which shows two discontinuous hybrid cable bridges with the same span lengths and tower heights. In the first case, the suspension ratio is relatively large so that the length of the stayed region in the main span is less than the length of the side span. In the second case, the suspension ratio is set so that the length of the stayed region in the main span is equal to the length of the side span.

Bridge 1

$$L_{SR}L_m \quad > \quad L_m(1 - L_{R1})/2$$

Bridge 2

$$L_{SR}L_m \quad = \quad L_m(1 - L_{R2})/2$$
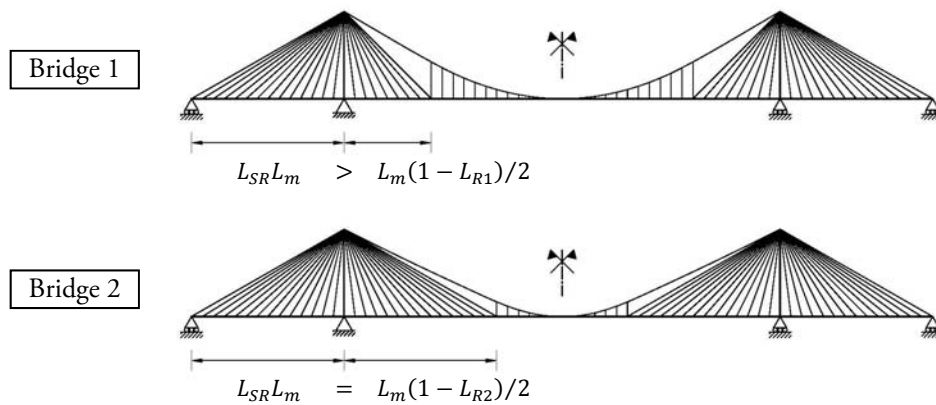
Figure 5.22: The Effect of the Suspension Ratio on Bridge Appearance

Clearly, the second bridge in Figure 5.22 is more appealing. This also has to do with the fact that as the suspension ratio increases, a larger gap manifests between the suspension cable and the outermost stay cable. As a result, the suspension cable and the stay cables appear disjointed. Accordingly, from an aesthetics perspective, in order for the length of the stayed region in the main span to be greater than or equal to the length of the side span, the following condition must be satisfied,

$$L_R \leq 1 - 2L_{SR} \tag{5.71}$$

The optimal range for side-to-main span length ratio established in the previous section was 0.35 to 0.45. Substituting these values into Equation (5.71) yields the following range for the suspension ratio,

$$0.1 \leq L_R \leq 0.3$$

However, designing a hybrid bridge with a suspension ratio of 0.1 would be fruitless. A lower limit of 0.2 is more sensible; although as a consequence, to satisfy Equation (5.71) the upper limit of the side-to-main span ratio would need to be decreased to 0.4. Thereafter, the optimal ranges for the side-to-main span ratio and the suspension ratio become,

$$0.35 \leq L_{SR\_opt} \leq 0.4$$

$$0.2 \leq L_{R\_opt} \leq 0.3$$

If necessary, the upper limit of these ranges could be extended by using a number of cross stays / cross hangers at the stay cable-hanger junction.

When selecting the suspension ratio within the above range, it is also important to take into account the impact the suspension ratio has on construction demands. As previously mentioned, in order to erect a self-anchored discontinuous hybrid cable bridge the superstructure needs to be temporarily supported or, alternatively, the horizontal component of the suspension cable force needs to be temporarily restrained. For long span bridges, the latter option is undoubtedly more efficient.

From Chapter 4 (Equation (4.9)), the horizontal component of the suspension cable force under dead load which must be restrained can be approximately equated to,

$$(H_{cm})_{DL} \cong \frac{L_m \omega_s}{8 S_R} \left[\frac{\omega_{cm}}{\omega_s} + L_R (2 - L_R) \right] \tag{5.72}$$

Equation (5.72) is plotted in Figure 5.23 as a function of the suspension ratio. The ordinates are normalized with respect to the case when the suspension ratio equals 0.2. As a result, the plot is virtually independent of the applied loading, the main span length, and the tower height-to-span ratio.
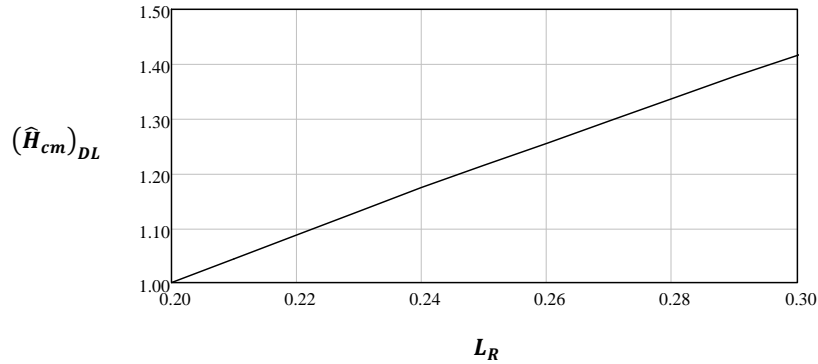
Figure 5.23: Horizontal Component of Suspension Cable Force under Dead Load versus Suspension Ratio

From Figure 5.23, an increase in the suspension ratio from 0.2 to 0.3 results in roughly a 40% increase in the dead load horizontal cable force. Whether or not it is efficient to accommodate this increase depends on the starting value of the horizontal cable force in addition to the choice of the anchorage structure and the geological conditions at the bridge site, all of which are further discussed in Chapter 7.

5.4   Economic Outcome

With the optimum portions established, it is now appropriate to study the expected costs associated with the construction of a self-anchored discontinuous hybrid cable bridge. Similar to the methodology used in Section 5.3.1 to evaluate the optimum sag ratio, it is convenient to examine the expected cost of the hybrid bridge system relative to a conventional cable-stayed bridge. This is because the two bridge systems possess many of the same features and, consequently, the results can be more or less generalized. Accordingly, using Equation (5.62), Figure 5.24 plots the expected cost of a self-anchored discontinuous hybrid cable bridge relative to a conventional cable-stayed bridge with the ordinates expressed in terms of percent change. Sub-plots are also presented for the individual bridge components. All input parameters are assumed equal between the two bridge systems and the comparison is made for the maximum recommended suspension ratio of 0.3. Because the parameters are assumed equal for the two bridge systems the plots are only slightly sensitive to the presumed input parameters (refer to Table 5.1).
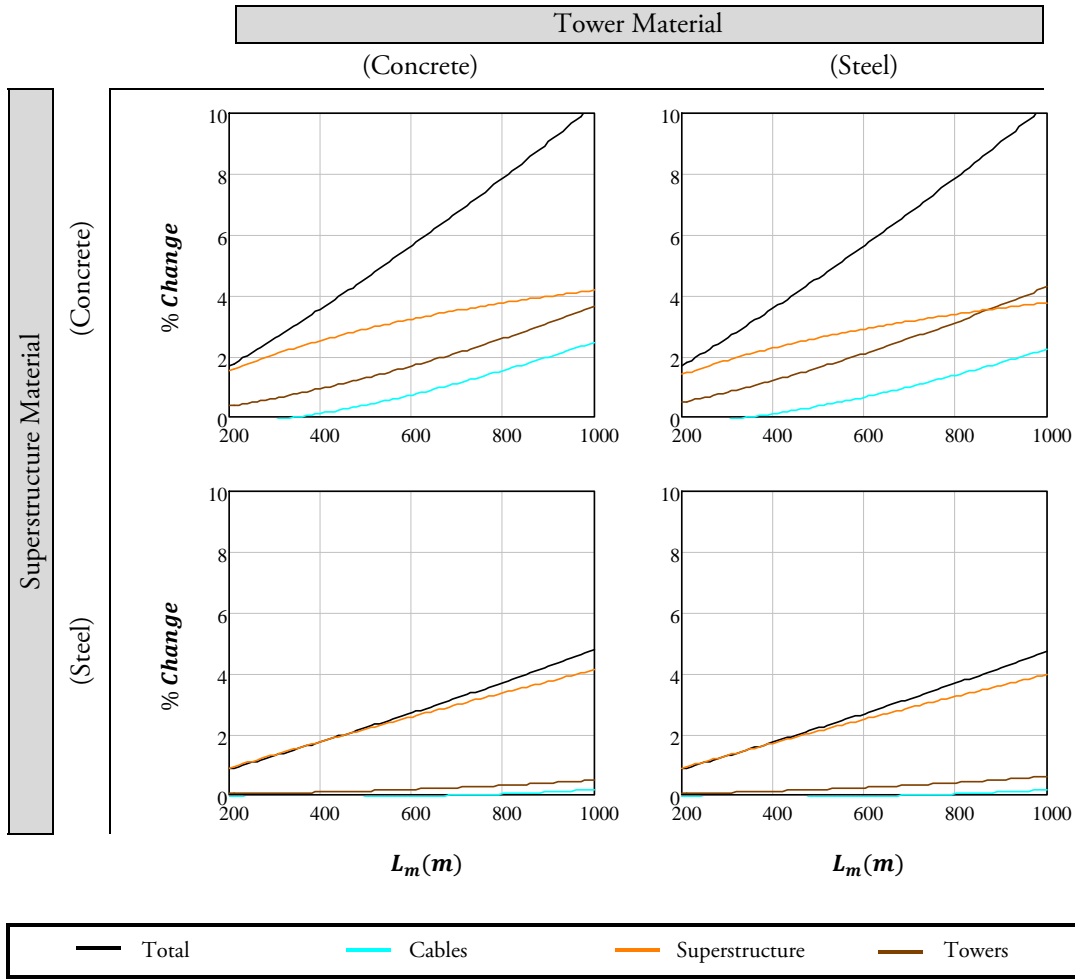
Figure 5.24: Cost versus Span Length in Relation to a Cable-Stayed Bridge

Parameters: h_{TR} = 0.25, L_R = 0.3, L_{SR} = 0.35, L_{mo} = L_m, L_{SRo} = L_{SR}, h_{TRo} = h_{TR}, also refer to Table 5.1

*Difference in foundation cost assumed negligible (refer to Equation (5.70))

Based on Equation (5.62), it can be observed from Figure 5.24 that the total cost of a self-anchored discontinuous hybrid cable bridge is slightly greater than the cost which would be incurred by a conventional cable-stayed bridge. Notwithstanding, considering that it is generally uneconomic to employ concrete superstructures for relatively long spans, the percent change in cost between the two systems can be expected to be less than 5% for any practical span length. This result should not be interpreted to underrate the potential economic advantages of self-anchored discontinuous hybrid cable bridges. There are many factors which are not accounted for in Equation (5.62).

Primarily, in the hybrid system, Equation (5.62) treats the uniform compression force transferred to the superstructure by the suspension cable as a disadvantage because it assumes additional

superstructure material is be required to carry the force. In Figure 5.24, it can be seen that this is actually the major source of the cost discrepancy between the hybrid system and the conventional cable-stayed system. In reality, the compression force can theoretically be exploited as an advantage, ultimately saving costs. For steel superstructures, continual compression is beneficial from a durability standpoint because it reduces the likelihood of fatigue, thereby reducing costs associated with fabrication. For concrete and composite superstructures, continual compression reduces or eliminates the need for longitudinal post tensioning steel. As a result, the thickness, and more importantly the weight, of certain cross-sectional components can be reduced. This in turn generates cost savings as it reduces the load which must be supported by the other major bridge components. Equation (5.62) also neglects the relationship between cost and construction duration, which can have a significant impact on overall costs. This is discussed in more detail in Chapter 7. In consideration of the above, the cost of a self-anchored discontinuous hybrid cable bridge can be expected to be closely comparable to the cost of a conventional cable-stayed bridge. The economic span range of the two bridges should, therefore, also be comparable.

5.5   End of Chapter Summary

The optimum stay cable and hanger arrangements were discussed at the beginning of the chapter. For reasons associated with cost, structural efficiency, and aesthetics, a fan or semi-fan arrangement can be considered optimum for an array of stay cables and a vertical arrangement can be considered optimum for an array of hangers. With respect to the aforementioned optimum cable arrangements, parametric equations were derived giving material estimates for principal components of a generalized self-anchored discontinuous hybrid cable bridge. These equations were then used to study optimum ranges for the span proportions.

Based on convention, the optimum tower height-to-span ratio was studied primarily from a cost perspective. In that regard, the optimum tower height-to-span ratio was shown to be not greatly dependent on the choice of material for the superstructure and/or the towers. Furthermore, the optimum tower height-to-span ratio was shown to be fairly insensitive to changes in the assumed material and cost parameters of the principal components. After qualitatively including the influence of the foundation cost, a tower height-to-span ratio in the range of 0.2 to 0.25 was recommended.

The optimum side-to-main span ratio can be considered independent of the suspension ratio. As such, the historically established optimum side-to-main span ratio for cable-stayed bridges is equally applicable to self-anchored discontinuous hybrid cable bridges. The rationale behind the historically established range of 0.35 to 0.45 was discussed in detail. Nevertheless, when examining the optimum

suspension ratio, due to the correlation between the suspension ratio and the side-to-main span ratio, aesthetics and function dictated that the optimum side-to-main span range should be slightly adjusted. Ultimately, a range of 0.35 to 0.4 was recommended for the side-to-main span ratio and a range of 0.2 to 0.3 was recommended for the suspension ratio. The upper limit of these ranges can be extended if cross stays / cross hangers are employed; however, construction of the suspended region becomes more challenging as the suspension ratio increases.

For the established optimal proportions, the expected cost of a self-anchored discontinuous hybrid cable bridge is closely comparable to a conventional cable-stayed bridge. Additional economies unique to self-anchored discontinuous hybrid cable bridges may also be achieved by exploiting the continual compression force produced by the hybrid cable system. Based on these results it was deduced that the economic span range of a self-anchored discontinuous hybrid cable bridge is similar to that which has been established for conventional cable-stayed bridges.

Chapter 6

DESIGN CONSIDERATIONS

Previous chapters have dealt with the general behaviour of self-anchored discontinuous hybrid cable bridges. However, general studies, by their very nature, preclude any detailed investigations. This is mainly due to the number of design parameters (structural and geometric in this case) which must be considered, a number which significantly increases when also including the potential range of each design parameter. This creates a dilemma because additional studies of a more detailed nature are required for a complete and thorough examination.

The evaluation of the optimum span proportions executed in Chapter 5 drastically reduces the number of geometric design parameters to consider and thus provides a practical foundation upon which a detailed study can be based. Accordingly, to circumvent the aforementioned dilemma, the studies in this chapter are centered on a reference model which employs the optimum proportions identified in Chapter 5. As a result, a relatively large amount of detail can be included in the model while maintaining a certain degree of generality.

For consistency, the base model which has been used thus far for studying the behaviour of self-anchored hybrid cable bridges is utilized once more in this chapter. However, the model is expanded to include certain details which were previously neglected, such as the influence of the flexural stiffness of the side span and towers. Using the expanded model, the effect of different tower-superstructure articulation schemes is investigated. In addition, a conclusive comparison is made between self-anchored discontinuous hybrid cable bridges and conventional cable-stayed bridges. This is followed by a sensitivity study which examines the importance each major structural design parameter has on the behaviour of self-anchored discontinuous hybrid cable bridges. Lastly, the effectiveness of various design components is assessed, specifically, the effectiveness of employing a central suspension cable clamp, cross stays/hangers, and intermediate piers.

6.1 Reference Model

6.1.1 Description of Model

As previously mentioned, the base / reference model used throughout this chapter can be viewed as an extension to the model employed in the latter half of Chapter 4 (refer to Figure 4.16). The amended version of the model used in this chapter is illustrated in Figure 6.1. For simplicity, the model is completely symmetric about mid-span.
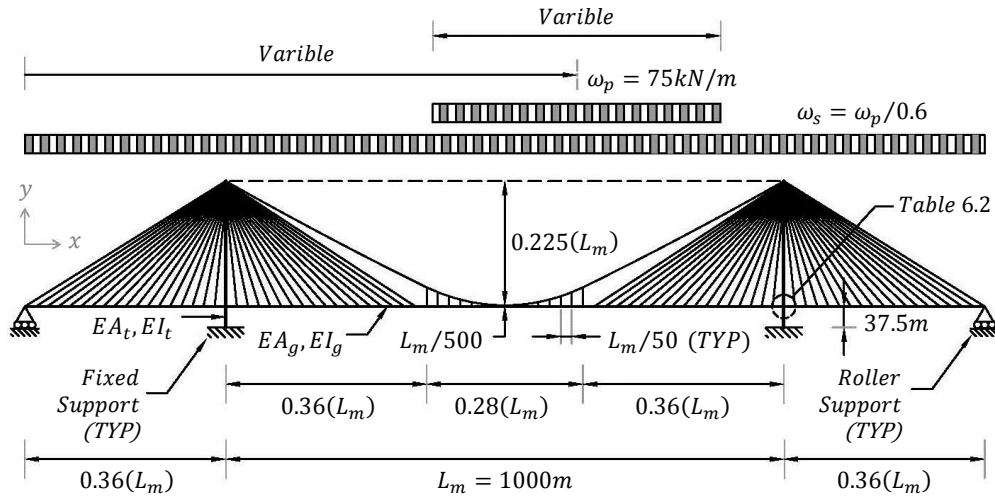
Figure 6.1: Description of Reference Model

In comparison to the model employed in Chapter 4, the amended model includes the influences of the anchor cables, towers, side spans, and side span stay cables. Also, in accordance with Chapter 5, fixed geometric parameters are assigned for the sag (0.225), suspension (0.28), and side-to-main span ratios (0.36). The assumed structural parameters for the superstructure and towers are given in Table 6.1 (structural parameters for the cables are discussed in Section 6.1.1.1). In addition, the tower-superstructure articulation schemes which are considered for the tower-superstructure connection are given in Table 6.2. Demands are computed using a second order influence analysis (refer to Figure 3.35).

Table 6.1: Structural Parameters for Superstructure and Towers

Parameter	Description	Value	Unit
EA_g	Axial Stiffness of Superstructure	2.4×10^5	MN
EI_g	Flexural Stiffness of Superstructure	1.25×10^6	MNm^2
EA_t	Axial Stiffness of Tower	8.0×10^5	MN
EI_t	Flexural Stiffness of Tower	1.0×10^7	MNm^2

Table 6.2: Articulation Schemes Considered for Tower-Superstructure Connection
*Refer to Coordinate System in Figure 6.1

ID	Description	Sub-Model	Linked Degrees of Freedom*		
			Translation (x)	Translation (y)	Rotation (z)
AS1	FIXED		▨	▨	▨
AS2	PINNED		▨	▨	
AS3	ROLLER			▨	

6.1.1.1   Cable Modelling

The suspension cable is modelled in the same meticulous manner as described in Chapter 4, Section 4.2.1. Likewise, each hanger is again modelled as a single truss element. In contrast, the stay cables are now arranged in a semi-fan configuration with a 2 metre spacing at the towers. As in previous chapters, all cables are designed with an allowable peak stress of 800 MPa, a material unit weight of 0.09 MN/m^3, and an elastic modulus of 200 GPa. Furthermore, the area of the anchor cables is assumed to be independent of the area of the suspension cable.

Given the additional detail included in the model, a small study was carried out to determine the most appropriate method for modelling the stay and anchor cables. The following modelling approaches were considered, going from most to least accurate/computationally demanding:

1. Stay and anchor cables modelled as catenaries.
2. Stay cables modelled using tangent modulus approximation; Anchor cables modelled as catenaries.
3. Stay and anchor cables modelled using tangent modulus approximation.

Under full main span loading, Figure 6.2 shows the deflected shape from the three modelling approaches. The relative deflection at mid-span is also recorded in the figure. As shall be later demonstrated in Section 6.1.2, the result, in this case, does not greatly depend on the tower-superstructure articulation scheme.
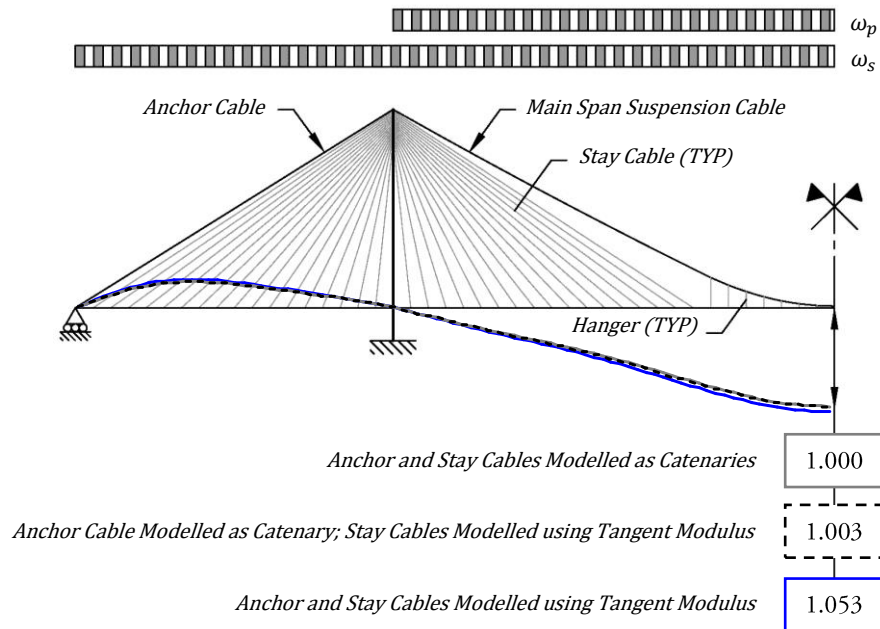
Figure 6.2: The Effect of Different Modelling Approaches for Stay and Anchor Cables
*Refer to Section 6.1.1 for Parameters

From Figure 6.2 it is evident that the modelling approach chosen for the stay cables is of little consequence[1]. However, there is a small but appreciable amount of error which occurs when the anchor cable is modelled using the tangent modulus approximation. This testifies to the relative importance of the anchor cables which was already discussed in Chapter 4, Section 4.2.1.5. Consequently, the second modelling approach specified above was adopted. Thus, the anchor cables are modelled using the same method and discretization as the suspension cable. The stay cables are modelled using the tangent modulus approximation.

6.1.2   Response to Different Tower-Superstructure Articulation Schemes

The superstructure and cable live load demand envelopes for the reference model are illustrated in Figure 6.3. The three tower-superstructure articulation schemes described in Table 6.2 are included in the figure. It should be noted that the tower dead load was not considered in the computation of live load demands. In addition, the sign of the live load demands adheres to the same convention used in previous chapters. For the superstructure, a positive deflection is in the direction opposite gravity. For the towers, a positive deflection is in the direction of the main span. Also, a positive moment is characterized by a 'sagging' deflection and a negative axial force by compression.

---

[1] This statement does not apply when evaluating construction demands.
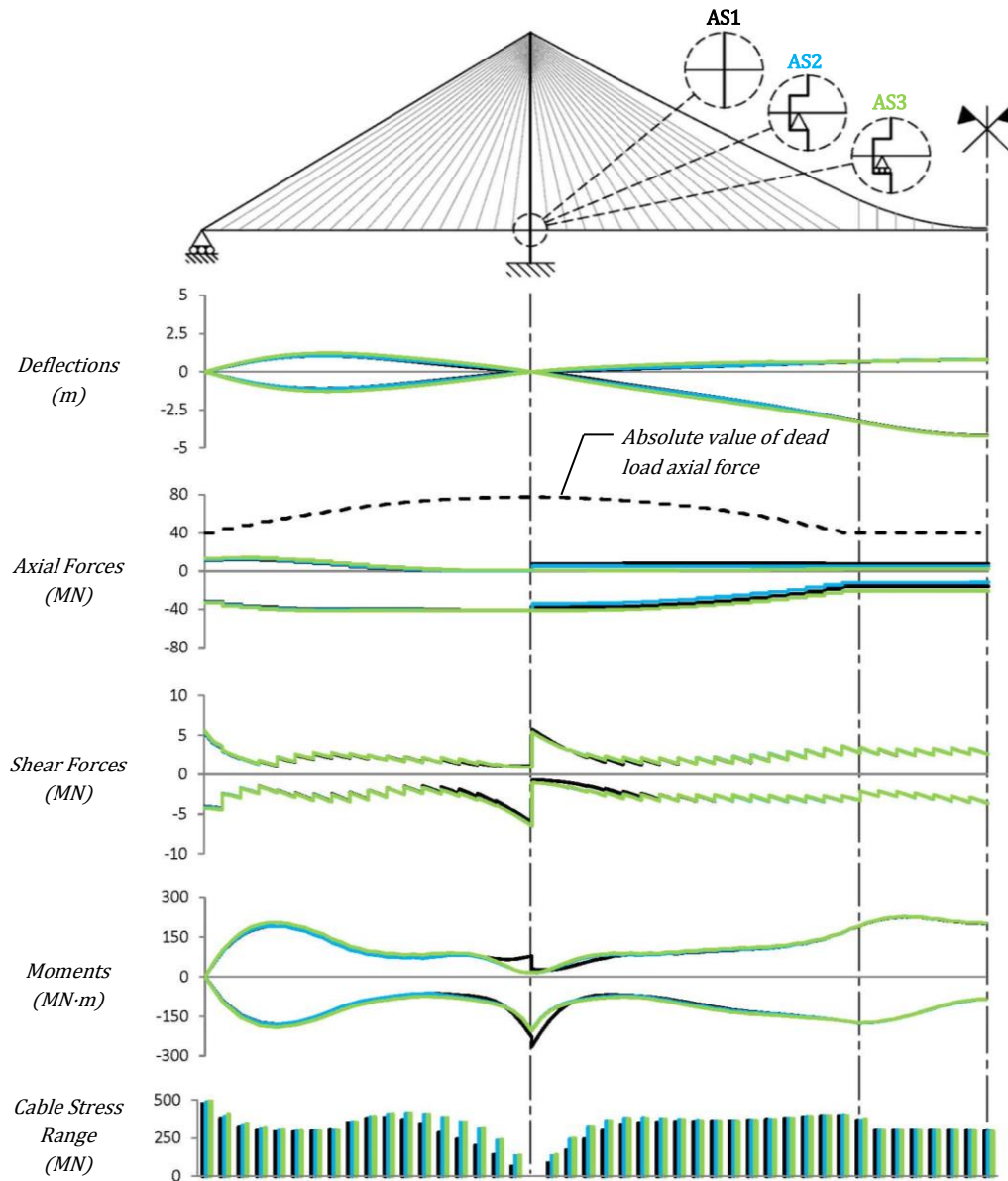
Figure 6.3: Superstructure and Cable Live Load Demand Envelopes

The demands shown in Figure 6.3 generally adhere to the results from previous chapters. Nevertheless, this is the first time cable stress ranges have been recorded. As speculated in the introductory chapters of the thesis, it is the stay cables, not the hangers, which are subject to the greatest stress range. Furthermore, the greatest stress range in the stay cables occurs in the side spans as opposed to near the stay cable-hanger junction. The hangers near the junction are subject to above

average stresses; however, the relative stress range of the outermost hangers is highly dependent on the loaded length of the applied live load. In many design codes, fatigue loading is based on concentrated loads from heavy trucks. Therefore, when evaluating fatigue demands the stress range of the outermost hangers will be substantially less, relative to, the stress range of the stay cables. The same also applies to the stress range of the anchor cables. As an example, Figure 6.4 shows the cable stress range for the three tower-superstructure articulation schemes considered when the bridge is subjected to the fatigue loading scenario (FLS) specified in the 2006 Canadian Highway Bridge Design Code (CHBDC)[1]. For simplicity, the transverse distribution of the load is ignored.
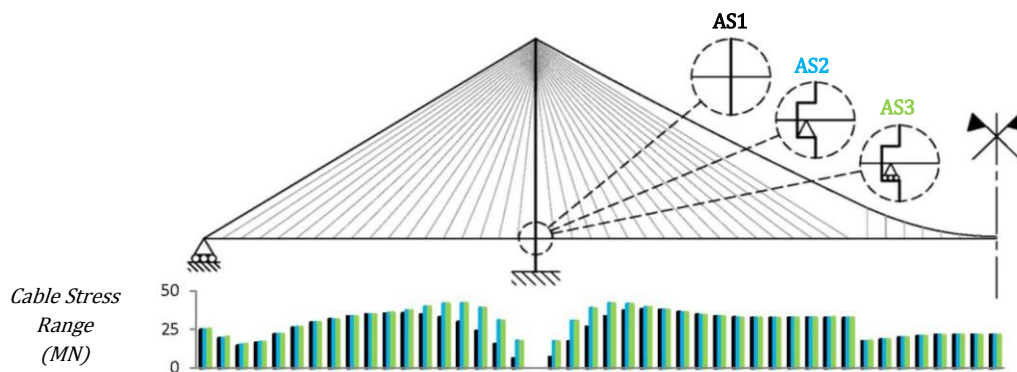
Figure 6.4: Cable Live Load Stress Range Computed using the CHBDC FLS

Interestingly, Figure 6.3 and Figure 6.4 both indicate that the tower-superstructure articulation scheme has only a minor effect on the superstructure and cable demands. The primary differences between the tower-superstructure articulation schemes described in Table 6.2 relate to the level of rotational and axial restraint provided to the superstructure at the towers. Due to the typically large span length of cable bridges and the relatively small flexural stiffness of the towers and superstructure, the level of rotational restraint generally only affects the demands in members that are situated within close proximity to the towers. This is evidenced by the superstructure moment and cable live load demands. In contrast, it has already been observed in previous chapters that the level of axial restraint can have a significant impact on global demands. Nevertheless, the results from Chapter 4 indicate that, within the optimal range specified for the suspension ratio (refer to Chapter 5), the peak vertical deflection is governed primarily by elastic deformation, from live loading positioned symmetrically about mid-span. Demands generated from symmetrically positioned live loading are generally not

---

[1] The CHBDC fatigue loading scenario is based on a single five-axle truck with a total length and weight of 18 metres and 625 kilonewtons (approximately 64 metric tonnes), respectively.

significantly impacted by the amount of longitudinal restraint at the towers[1]. Therefore, the indifference the tower-superstructure articulation scheme has on vertical live load deflections could have been anticipated. Likewise, it is not surprising that the live load axial demands are similarly unaffected. However, since the peak moment demands occur from asymmetrically positioned live loading, one would expect the moment demands to deviate.

The similarity in the moment demands can be essentially attributed to two phenomena:

1. The first relates to scale effects. The flexural stiffness of the superstructure assigned in Table 6.1 is appropriate relative to the 1000 metre main span length. However, relative to the suspended length (280 metres), the flexural stiffness of the superstructure is exceedingly large. This remark is based on the observation in Chapter 4 (Section 4.2.1.6) that the global stiffness of the superstructure is proportional to the cube of its span length. Consequently, since the stayed regions of the bridge do not have the same potential for large strain-free deformations, the superstructure becomes highly effective at mitigating strain-free deformations within the suspended region. This is, in part, why the peak vertical deflection is governed by elastic, as opposed to strain-free deformation. Referring back to Figure 3.39, it also partly explains why the level of axial restraint does not affect the peak moment demands. Naturally, this beneficial scaling effect gradually diminishes as the suspension ratio is increased to values beyond the recommended optimal range specified in Chapter 5.

2. The second relates to the influence of the anchor cables. In a self-anchored system, relative horizontal movement between the superstructure and the top of the towers is limited due to the link provided by the anchor cables. Therefore, even when the superstructure is longitudinally unrestrained at the towers, the superstructure is still longitudinally constrained relative to the end nodes of the suspension cable. Consequently, regardless of the tower-superstructure articulation scheme, a self-anchored system achieves a similar restraining effect compared to an earth-anchored system that has been designed with longitudinal superstructure restraint at the towers.

Although relative horizontal movements between the superstructure and the end nodes of the suspension cable are limited, absolute horizontal movements can still occur. Consequently, even though the amount of longitudinal restraint at the towers only marginally affects vertical deflections and their associated demands, horizontal deflections and their associated demands are greatly affected. As confirmation, the recorded values of longitudinal superstructure deflection at the anchor/end pier,

---

[1] This statement assumes that membrane effects in the superstructure are negligible, which is normally a valid assumption.

for the three tower-superstructure articulation schemes, are given in Table 6.3. Clearly, when longitudinal restraint is removed (AS3), the recorded longitudinal deflection increases by a multiplication factor of nearly 20.

Table 6.3: Absolute Peak Longitudinal Superstructure Deflection at End Pier
*Values are in units of metres

Tower-Superstructure Articulation Scheme		
AS1	AS2	AS3
0.120	0.109	2.18

For AS3, the longitudinal superstructure deflection at the end pier is governed primarily by asymmetric main span loading[1]. It was already noted in Chapter 3 that when a suspension cable is loaded asymmetrically, strain-free deformations in the cable cause the superstructure to drift longitudinally in the direction of the load. Nevertheless, as previously discussed, in a self-anchored discontinuous hybrid cable bridge, the longitudinal superstructure deflection caused by the partially-laden suspension cable is limited by the relatively large effective stiffness of the suspended region and by the restraining effect of the anchor cable. Rather, it is the presence of the stay cables, not the partially-laden cable, which greatly increases the peak longitudinal deflection when the longitudinal superstructure restraint at the towers is removed.

The direct cause of the longitudinal movement can be traced back to the imbalance of forces created at the towers from the semi-fan configuration of the stay cables. When the superstructure is longitudinally restrained at the towers the superstructure can be engaged to counterbalance the forces. With no longitudinal restraint, the resulting moment from the unbalanced forces must be resisted solely by the bending stiffness of the tower legs which must act as long cantilever beams. In that circumstance, the superstructure must horizontally deflect in order to satisfy equilibrium. For the same reason, the tower demands are also affected by the amount of longitudinal superstructure restraint (Figure 6.5). For AS3, the deflection of the towers significantly increases and the tower moment demands become more uniform over the height of the towers. Although, as a trade-off, the shear force demand at the base of the towers is reduced. In general, minimizing the cable anchorage zone at the towers will reduce the longitudinal movement and associated demands.

---

[1] The peak longitudinal superstructure deflection occurs when the asymmetric main span loading is paired with side span loading on the side opposite the main span loading.
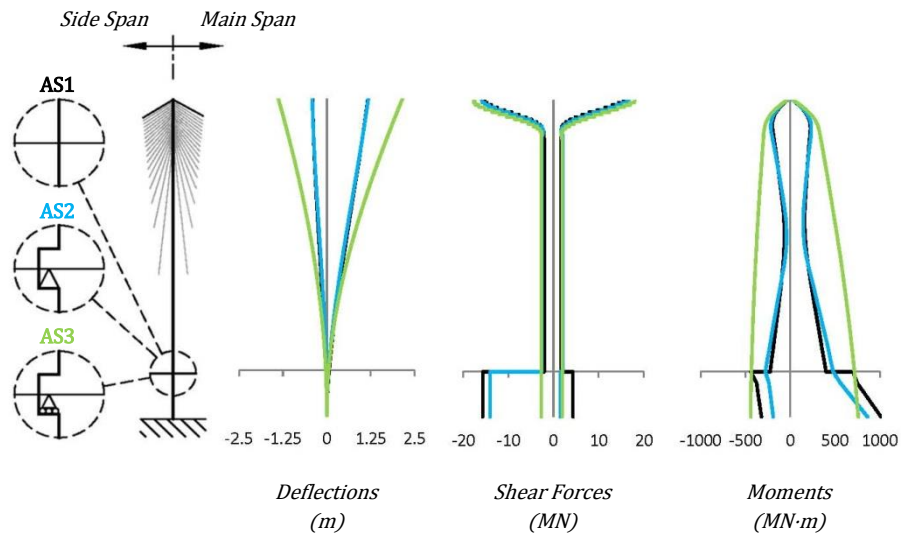
Figure 6.5: Tower Live Load Demand Envelopes

6.1.3   Comparison to Conventional Cable-Stayed Bridge

Derivations made in Chapter 5 clearly reveal the similarity between the predominant force demands for self-anchored hybrid and cable-stayed cable bridges. Nevertheless, this still leaves the question as to how other demands vary. Considering that all of the major bridge components have now been included in the reference model, a conclusive comparison can finally be made between the two bridge types. Accordingly, a model for a conventional cable-stayed bridge was constructed using the same input properties as the reference model. To achieve a consistent dead load state, the suspended portion of the hybrid model was replaced with stay cables in a fan type configuration. Therefore, the cable-system and the section properties of each cable element are the only differences between the two models. The results are shown in Figure 6.6 and Figure 6.7.

The indifference the tower-superstructure articulation scheme has on the superstructure and cable demands is not a unique characteristic of self-anchored hybrid cable bridges. The same level of indifference was also observed in the results for the cable-stayed bridge model. Accordingly, for the superstructure and cable demands, only the results for AS2 are included. Nevertheless, even when considering the tower demands, the overall conclusion is the same regardless of the tower-superstructure articulation scheme. Figure 6.6 and Figure 6.7 prove that self-anchored discontinuous hybrid cable bridges (when constructed with the optimum proportions outlined in Chapter 5) and conventional cable-stayed bridges are, in general, subject to very similar demands. However, it is important to note that in reality there will be somewhat higher local moments (from dead and live

loads) in a cable-stayed bridge due to the added imbalance of forces at the towers when all of the stay cables are arranged in a semi-fan configuration. This is a result of the stayed regions in the main span being longer than the stayed regions in the side spans. Notwithstanding, since live load induced cable fatigue is normally not an issue in cable-stayed bridges it can, therefore, be inferred that live load induced cable fatigue should not be a concern in self-anchored discontinuous hybrid cable bridges. Although not shown, temperature loading also yielded very similar demands between the two systems confirming once more that the operating demands for the two bridge systems are highly comparable.
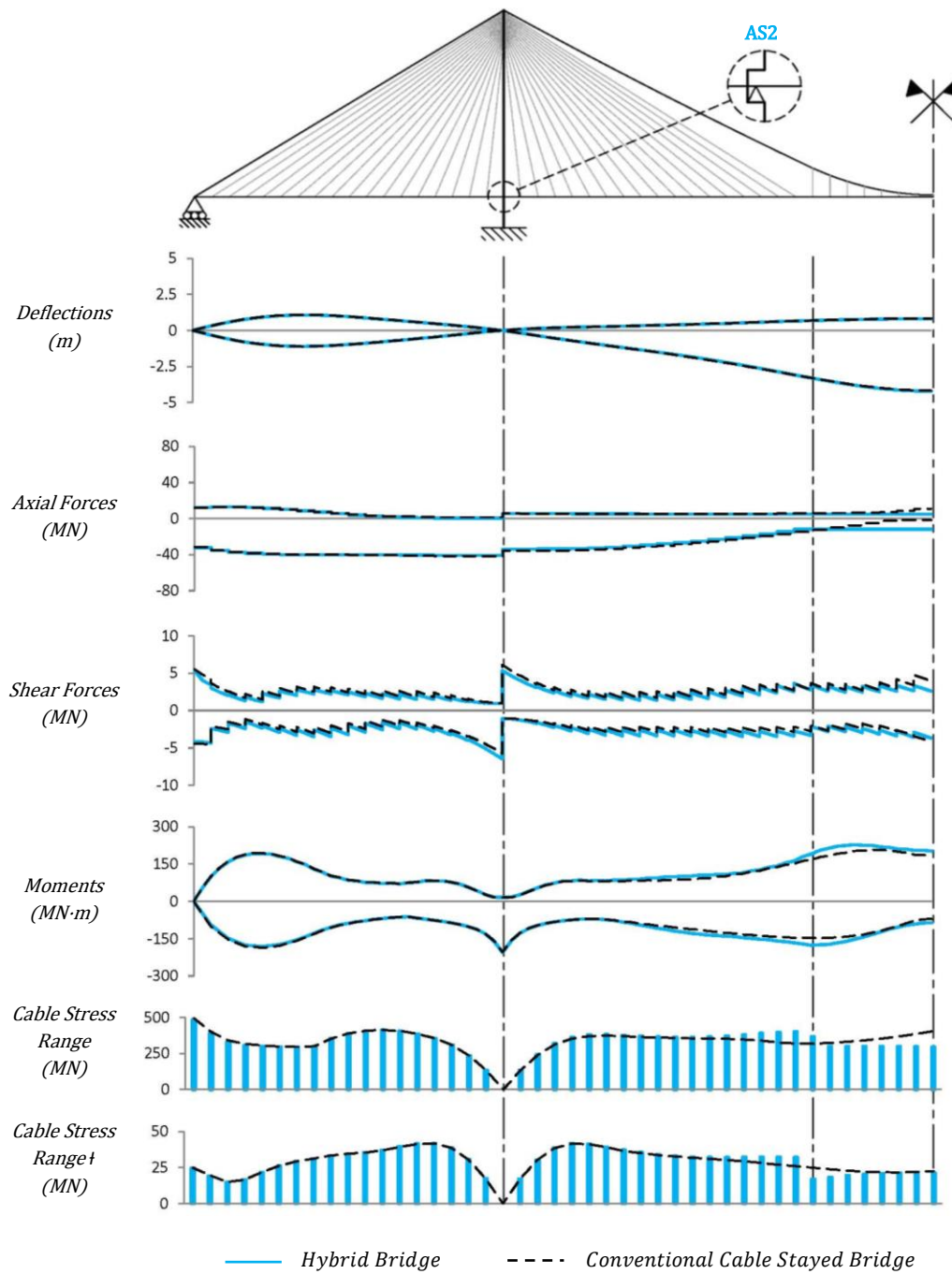
Figure 6.6: Comparison of Superstructure and Cable Live Load Demands
*Similar for AS1 and AS3
‡ Computed using the CHBDC FLS
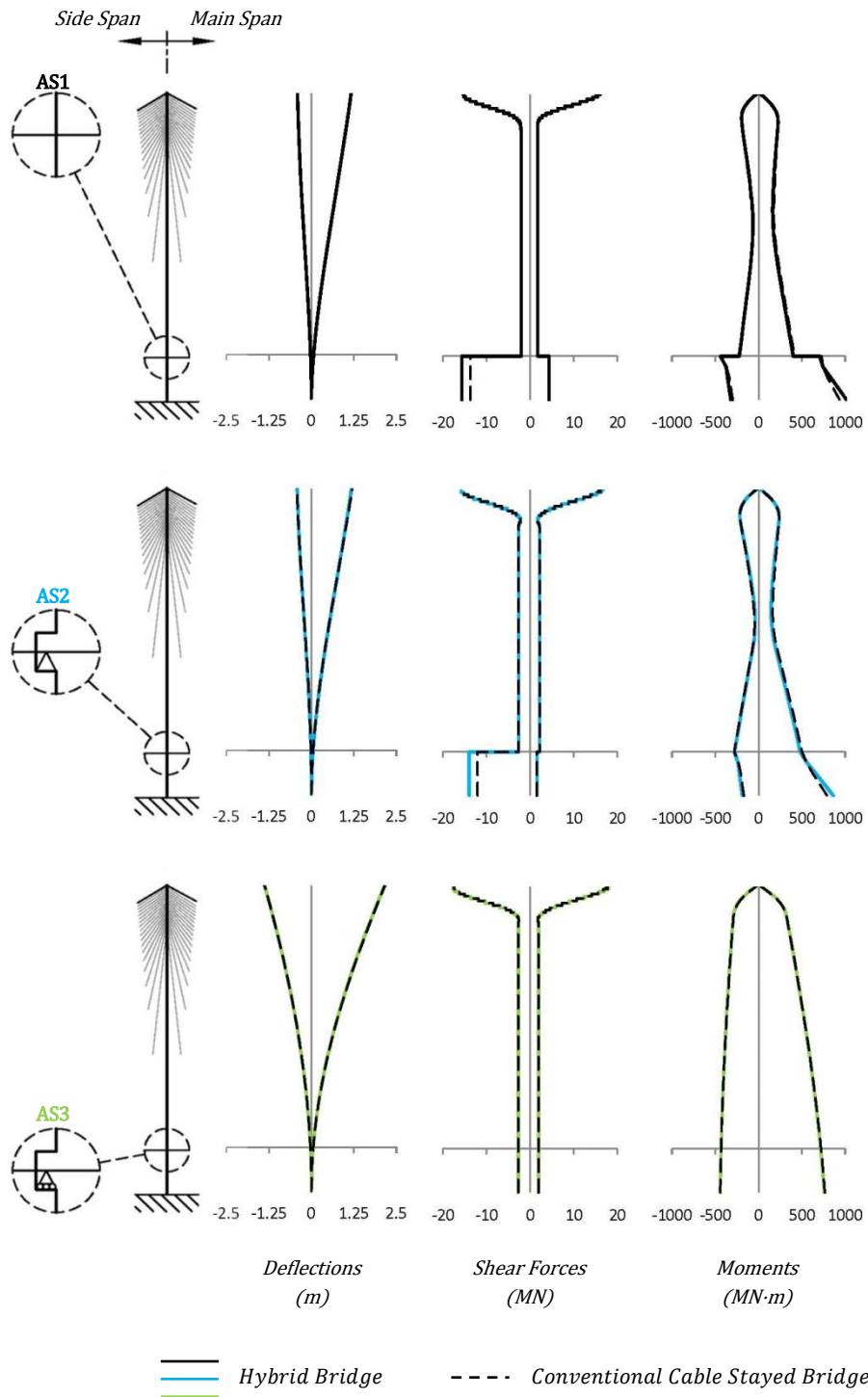
Figure 6.7: Comparison of Tower Live Load Demands

6.1.4 Nonlinear Effects Due to Live Load

The results presented thus far were obtained from a second order influence analysis. As in previous chapters, in order to assess the accuracy of the second order influence analysis, the governing loading scenarios for numerous demand parameters were identified. Subsequently, a series of full nonlinear analyses were conducted using the identified loading scenarios.

Table 6.4 compares the results obtained from the second order influence analysis to those obtained from the nonlinear analyses. For each demand parameter, the tabulated value gives the percent change of the second order influence analysis result, relative to, the nonlinear analysis result. In other words, this can be viewed as the percent error in the second order influence analysis results. Positive values, therefore, signify cases where the second order influence analysis produced conservative results.

Table 6.4: Nonlinearity Due to Live Load
(Percent Change Relative to Nonlinear Analysis Result)

		Articulation Scheme		
		1	2	3
Superstructure	Negative Vertical Deflection at Mid-Span	5	6	5
	Absolute Maximum Horizontal Deflection at End Pier	-9	-11	6
	Maximum Negative Axial Force at Tower	0	0	0
	Absolute Maximum Shear at Tower	-1	5	3
	Absolute Maximum Shear at End Pier	-9	-9	-10
	Peak Negative Moment in Main Span	4	5	3
	Peak Positive Moment in Main Span	4	4	2
	Maximum Negative Moment at Tower	5	0	0
	Peak Negative Moment in Side Span	1	1	2
	Peak Positive Moment in Side Span	0	0	0
Towers	Positive Horizontal Deflection at Top of Tower	5	5	-6
	Negative Horizontal Deflection at Top of Tower	-4	-5	5
	Negative Axial Force at Base of Tower	0	0	0
	Absolute Maximum Shear at Top of Tower	-3	-3	-5
	Absolute Maximum Shear at Base of Tower	-18	-20	9
	Negative Moment at Base of Tower	3	6	6
	Positive Moment at Base of Tower	-11	-13	-7
Cables	Peak Tension in Main Span Suspension Cable	0	0	-1
	Peak Tension in Anchor Cable	-2	-2	-1
	Peak Tension in Main Span Stay Cables	1	1	1
	Peak Tension in Side Span Stay Cables	3	3	3
	Peak Tension in Hangers	0	0	0

In Chapter 4, only a few selective demand parameters were investigated and, in those cases, a second order influence analysis generally produced conservative results when the span proportions were configured within the optimal range specified in Chapter 5. From Table 6.4 it is clear that when

considering many different types of demands, at various locations on the structure, a second order influence analysis does not always produce conservative results. Consequently, during final design, a second order influence analysis should not be wholly relied upon. Nevertheless, for many of the demand parameters, the error is similar for the three tower-superstructure articulation schemes and, with the gross exception of the shear force demand at the base of the tower, the majority of the error values are within acceptable margins.

Even though there are a few error values in Table 6.4 above that which would normally be considered acceptable for final design, the continued use of the second order influence analysis results in the context of this chapter can be justified. This because the main interest in this chapter is to study the relative change in the demands when input parameters are altered or, alternatively, when additional design components are added. Since the demands will be studied relative to their original values, the error should remain somewhat consistent. As a result, when considering the relative change in a demand parameter the error should be significantly lower than the corresponding value in Table 6.4. Therefore, although the values generated from a second order influence analysis are approximate, to reduce the exorbitant amount of computational effort which would otherwise be required, the second order influence analysis results will be used exclusively for the remainder of the chapter.

6.1.5 Sensitivity of Response to Structural Design Parameters

In configuring the reference model several assumptions were made with regard to the input structural parameters, specifically, the input member stiffnesses. The intent of this section is to gauge the relative importance of the stiffness parameters and to determine the extent to which they affect various demand parameters. For the superstructure and towers, it is their flexural stiffnesses (EI_g,EI_t) which are assessed. Typically, when varied within a practical range, the axial stiffness of those members has little effect. Conversely, for the suspension and anchor cables, it is their axial stiffness (EA_c) which is assessed and the effect their bending stiffness has on global demands can be neglected. Changes to the axial stiffness of the stay cables and hangers are not considered because, generally, their precise stiffnesses are of relatively less consequence (refer to Section 6.1.1.1). Also, the ratio of the elastic modulus to design stress of conventional stay / hanger cable types is similar (Gimsing, 1996). Consequently, the axial stiffness of a stay / hanger cable is not a parameter which is typically varied greatly during design.

For each stiffness parameter considered, its importance is assessed by incrementally varying its original value to within +/- 20%, each time recording the resulting change in the demands on the structure. Every time a stiffness parameter is varied all other input parameters are kept constant. The only exception is the area of each cable which is recalculated based on the modified demands. The results for all three tower-superstructure articulation schemes are recorded in Table 6.5. For each demand

parameter listed, the tabulated value gives the percent change in the demand parameter, relative to, its original value. For convenience the original value is also included in the table. Positive values signify cases where the demands were amplified, whereas, negative values reflect cases where the demands were reduced.

Consistent with previous sections, the results for AS1 and AS2 are similar. Therefore, within the range considered, when the input stiffness parameters are altered, the amount of rotational restraint provided to the superstructure at the towers remains trivial. With further regard to AS1 and AS2, based on Chapter 4 it is not surprising that increasing the flexural stiffness of the superstructure increases the force demands on the superstructure. Notwithstanding, there are some benefits which include:

- A reduction in the horizontal superstructure deflection;

- A reduction in the positive moment and shear force demands at the base of the towers; and

- A reduction in the stress range of the cables when subjected to concentrated loads.

Similarly, increasing the flexural stiffness of the towers increases the force demands on the towers. However, unlike the superstructure, there are no great benefits associated with increasing the flexural stiffness of the towers. Therefore, the flexural stiffness of the towers should be made as small as stability permits in order to minimize costs. In contrast, there are only benefits to be gained when increasing the axial stiffness of the suspension and anchor cables. For the superstructure, these include a reduction in the vertical deflection and in the peak negative side span moment. For the towers, the horizontal deflection is reduced, as is the negative moment at the base of the towers.

Many of the same conclusions made for AS1 and AS2 also apply to AS3 although, there are some distinct differences. For AS3, increasing the superstructure stiffness does not yield any substantial benefits, whereas, increasing the flexural stiffness of the towers is now highly beneficial. By increasing the flexural stiffness of the towers horizontal deflections are significantly reduced. Moreover, tower demands are not significantly adversely affected. Rather, the negative moment at the base of the towers is reduced. The shear force demand at the base of the towers is an exception; however, the tower shear force demands are originally relatively small for AS3.

Clearly, the relative importance of each stiffness parameter depends on the tower-superstructure articulation scheme, in addition to the demand parameter of interest. Of the stiffness parameters examined, all had a notable impact on certain superstructure and tower demand parameters. Nevertheless, the cable demands were fairly impervious to changes in the stiffness parameters (excluding the CHBDC FLS), as were the superstructure and tower axial force demands. In all cases,

the maximum change in the axial force demands was less than 2 percent. This somewhat validates the assumptions made in Chapter 5 that these demand parameters can be approximately determined without considering the relative stiffnesses of the superstructure, towers, and cables. As an additional testament, comparing the average required cable volume obtained from the analyses to the estimated cable volume computed using the equations derived in Chapter 5 yielded an error of less than 2.5%.

Table 6.5a: Sensitivity of Live Load Demand Values to Input Structural Parameters (AS 1)

*Percent Change Relative to Original Demand Value (units: MN,m)

	Demand Parameter	Original Value	EI_g				EI_t				EA_c			
			-20	-10	10	20	-20	-10	10	20	-20	-10	10	20
Superstructure	Negative Vertical Deflection at Mid-Span	-4.18	3	1	-1	-2	1	0	0	-1	17	8	-6	-12
	Absolute Maximum Horizontal Deflection at End Pier	0.120	14	6	-6	-10	5	3	-2	-4	2	1	-1	-2
	Maximum Negative Axial Force at Tower	-40.8	1	0	0	0	0	0	0	-1	-1	0	0	1
	Absolute Maximum Shear at Tower	6.08	-6	-3	3	5	0	0	0	0	0	0	0	0
	Absolute Maximum Shear at End Pier	5.40	-6	-3	3	5	0	0	0	0	5	2	-2	-3
	Peak Negative Moment in Main Span	-176	-6	-3	2	5	0	0	0	0	2	1	-1	-1
	Peak Positive Moment in Main Span	227	-7	-4	3	7	0	0	0	0	6	3	-2	-4
	Maximum Negative Moment at Tower	-266	-12	-6	6	11	0	0	0	0	5	2	-2	-4
	Peak Negative Moment in Side Span	-181	-9	-5	4	8	1	0	0	-1	16	7	-6	-11
	Peak Positive Moment in Side Span	192	-9	-4	4	8	0	0	0	0	5	2	-2	-3
Towers	Positive Horizontal Deflection at Top of Tower	1.18	3	1	-1	-2	1	1	-1	-1	14	6	-5	-10
	Negative Horizontal Deflection at Top of Tower	-0.41	5	2	-2	-4	1	1	0	-1	16	7	-6	-11
	Negative Axial Force at Base of Tower	-76.4	0	0	0	0	0	0	0	0	0	0	0	0
	Absolute Maximum Shear at Top of Tower	16.0	4	2	-2	-3	1	1	-1	-1	-5	-2	2	4
	Absolute Maximum Shear at Base of Tower	15.7	9	4	-4	-7	-4	-2	2	3	-6	-3	2	4
	Negative Moment at Base of Tower	-321	-2	-1	1	3	-9	-5	4	9	8	4	-3	-5
	Positive Moment at Base of Tower	1016	7	3	-3	-6	-12	-6	6	11	3	1	-1	-2
Cables	Peak Tension in Main Span Suspension Cable	23.0	1	1	-1	-1	0	0	0	0	-5	-2	2	3
	Peak Tension in Anchor Cable	37.2	2	1	-1	-2	1	0	0	-1	-6	-3	2	4
	Peak Stress Range in Side Span Cables (Inc. Anchor Cable)	475	2	1	-1	-2	1	0	0	0	-3	-1	1	2
	↳ Computed using the CHBDC FLS	35.3	6	3	-2	-5	0	0	0	0	1	0	0	-1
	Peak Stress Range in Main Span Stay Cables	399	5	2	-2	-4	0	0	0	0	1	1	0	0
	↳ Computed using the CHBDC FLS	38.0	7	3	-3	-6	0	0	0	0	1	0	0	-1
	Peak Stress Range in Hangers	367	1	0	0	-1	0	0	0	0	-5	-2	2	3
	↳ Computed using the CHBDC FLS	21.4	7	3	-3	-5	0	0	0	0	-1	-1	1	1
	Total Cable Steel Volume	333	0.7	0.3	-0.3	-0.6	0.1	0.0	-0.1	-0.2	-0.5	-0.3	0.2	0.3

Table 6.5b: Sensitivity of Live Load Demand Values to Input Structural Parameters (AS 2)

*Percent Change Relative to Original Demand Value (units: MN,m)

		Input Structural Parameter											
		EI_g				EI_t				EA_c			
Demand Parameter	Original Value	Percent Change in Input Structural Parameter											
		-20	-10	10	20	-20	-10	10	20	-20	-10	10	20
Superstructure													
Negative Vertical Deflection at Mid-Span	-4.22	3	1	-1	-2	1	0	0	-1	17	8	-6	-12
Absolute Maximum Horizontal Deflection at End Pier	0.109	17	7	-6	-12	4	2	-2	-3	2	1	-1	-1
Maximum Negative Axial Force at Tower	-40.9	1	0	0	0	1	0	0	-1	-1	0	0	1
Absolute Maximum Shear at Tower	6.50	-4	-2	2	3	1	0	0	0	1	0	0	-1
Absolute Maximum Shear at End Pier	5.46	-6	-3	2	5	0	0	0	0	5	2	-2	-3
Peak Negative Moment in Main Span	-176	-5	-3	2	4	0	0	0	0	2	1	-1	-1
Peak Positive Moment in Main Span	228	-7	-4	3	7	0	0	0	0	6	3	-2	-4
Maximum Negative Moment at Tower	-204	-11	-5	5	10	0	0	0	0	0	0	0	0
Peak Negative Moment in Side Span	-181	-9	-4	4	8	1	0	0	-1	16	7	-6	-11
Peak Positive Moment in Side Span	192	-9	-4	4	8	0	0	0	0	6	2	-2	-3
Towers													
Positive Horizontal Deflection at Top of Tower	1.19	3	1	-1	-2	1	1	-1	-1	14	7	-6	-10
Negative Horizontal Deflection at Top of Tower	-0.42	4	2	-2	-3	1	0	0	0	16	7	-6	-11
Negative Axial Force at Base of Tower	-76.6	0	0	0	0	0	0	0	0	0	0	0	0
Absolute Maximum Shear at Top of Tower	16.7	3	1	-1	-2	1	1	-1	-1	-5	-2	2	3
Absolute Maximum Shear at Base of Tower	14.0	13	6	-6	-11	-7	-3	3	5	-5	-3	2	4
Negative Moment at Base of Tower	-188	5	2	-2	-3	-14	-7	7	14	11	5	-4	-7
Positive Moment at Base of Tower	864	10	5	-4	-8	-14	-7	6	13	3	1	-1	-2
Cables													
Peak Tension in Main Span Suspension Cable	23.0	1	1	-1	-1	0	0	0	0	-5	-2	2	3
Peak Tension in Anchor Cable	38.2	2	1	-1	-1	1	0	0	-1	-5	-2	2	4
Peak Stress Range in Side Span Cables (Inc. Anchor Cable)	485	2	1	-1	-1	1	0	0	0	-3	-1	1	2
⮡ Computed using the CHBDC FLS	41.8	7	3	-3	-5	0	0	0	0	0	0	0	0
Peak Stress Range in Main Span Stay Cables	403	4	2	-2	-4	0	0	0	0	1	1	0	-1
⮡ Computed using the CHBDC FLS	41.7	7	3	-3	-5	0	0	0	0	0	0	0	0
Peak Stress Range in Hangers	367	1	0	0	-1	0	0	0	0	-5	-2	2	3
⮡ Computed using the CHBDC FLS	21.4	7	3	-3	-5	0	0	0	0	-1	-1	1	1
Total Cable Steel Volume	336	0.6	0.3	-0.3	-0.5	0.1	0.1	-0.1	-0.1	-0.5	-0.2	0.2	0.3

Table 6.5c: Sensitivity of Live Load Demand Values to Input Structural Parameters (AS 3)
*Percent Change Relative to Original Demand Value (units: MN,m)

			Input Structural Parameter											
		Original Value	EI_g				EI_t				EA_c			
			Percent Change in Input Structural Parameter											
			-20	-10	10	20	-20	-10	10	20	-20	-10	10	20
Superstructure	Negative Vertical Deflection at Mid-Span	-4.22	3	1	-1	-2	1	0	0	-1	16	7	-6	-12
	Absolute Maximum Horizontal Deflection at End Pier	2.18	2	1	-1	-2	32	13	-10	-17	4	2	-1	-3
	Maximum Negative Axial Force at Tower	-41.0	0	0	0	0	0	0	0	0	-1	0	0	1
	Absolute Maximum Shear at Tower	6.51	-4	-2	2	3	1	0	0	-1	1	0	0	-1
	Absolute Maximum Shear at End Pier	5.65	-6	-3	3	5	0	0	0	0	5	2	-2	-3
	Peak Negative Moment in Main Span	-176	-6	-3	2	5	-1	0	0	0	2	1	-1	-1
	Peak Positive Moment in Main Span	229	-7	-4	3	7	0	0	0	0	6	3	-2	-4
	Maximum Negative Moment at Tower	-204	-11	-5	5	10	0	0	0	0	0	0	0	0
	Peak Negative Moment in Side Span	-192	-10	-5	4	8	2	1	-1	-1	16	7	-6	-11
	Peak Positive Moment in Side Span	206	-9	-4	4	8	1	1	0	-1	6	3	-2	-4
Towers	Positive Horizontal Deflection at Top of Tower	2.18	2	1	-1	-2	31	12	-9	-16	4	2	-2	-3
	Negative Horizontal Deflection at Top of Tower	-1.40	2	1	-1	-2	47	19	-14	-24	0	0	0	0
	Negative Axial Force at Base of Tower	-76.4	0	0	0	0	0	0	0	0	0	0	0	0
	Absolute Maximum Shear at Top of Tower	18.1	3	1	-1	-3	0	0	0	0	-4	-2	2	3
	Absolute Maximum Shear at Base of Tower	2.7	2	1	-1	-2	-14	-7	7	14	6	3	-2	-4
	Negative Moment at Base of Tower	-442	2	1	-1	-2	18	7	-4	-7	1	0	0	0
	Positive Moment at Base of Tower	759	3	1	-1	-2	2	0	2	4	6	3	-2	-4
Cables	Peak Tension in Main Span Suspension Cable	23.0	1	1	-1	-1	0	0	0	0	-5	-2	2	3
	Peak Tension in Anchor Cable	39.2	2	1	-1	-2	1	0	0	-1	-5	-2	2	4
	Peak Stress Range in Side Span Cables (Inc. Anchor Cable)	500	2	1	-1	-1	0	0	0	0	-3	-1	1	2
	⮕ Computed using the CHBDC FLS	41.7	7	3	-3	-5	0	0	0	0	0	0	0	0
	Peak Stress Range in Main Span Stay Cables	399	5	2	-2	-4	-1	0	0	0	1	0	-1	-1
	⮕ Computed using the CHBDC FLS	41.4	7	3	-3	-5	0	0	0	0	0	0	0	0
	Peak Stress Range in Hangers	376	1	0	0	-1	1	0	0	0	-4	-2	2	3
	⮕ Computed using the CHBDC FLS	21.4	7	3	-3	-5	0	0	0	0	-1	-1	1	1
	Total Cable Steel Volume	337	0.6	0.3	-0.2	-0.5	0.1	0.0	0.0	-0.1	-0.3	-0.1	0.1	0.3

6.2   Design Components

6.2.1   Central Suspension Cable Clamp

A central suspension cable clamp is a rigid connection provided at mid span between the suspension cable and superstructure. It is designed to inhibit longitudinal movement between the two members. As mentioned in Chapter 3, central suspension cable clamps are occasionally employed in suspension bridges to mitigate static strain free deformations and/or to impede dynamic asymmetric torsional motion. A few examples include the Little Belt Bridge (Denmark), the Lions Gate Bridge (Canada), and the Runyang Yangtze River Bridge (China). A photograph of the central suspension cable clamps used in the Lions Gate Bridge is given in Figure 6.8. There are two cable clamps in the photograph, one on each side of the bridge deck. Their apparent offset is simply a result of the skewed angle from which the photograph was taken. As shown, in the case of the Lions Gate Bridge, the rigid connection is achieved via a king post truss type configuration.
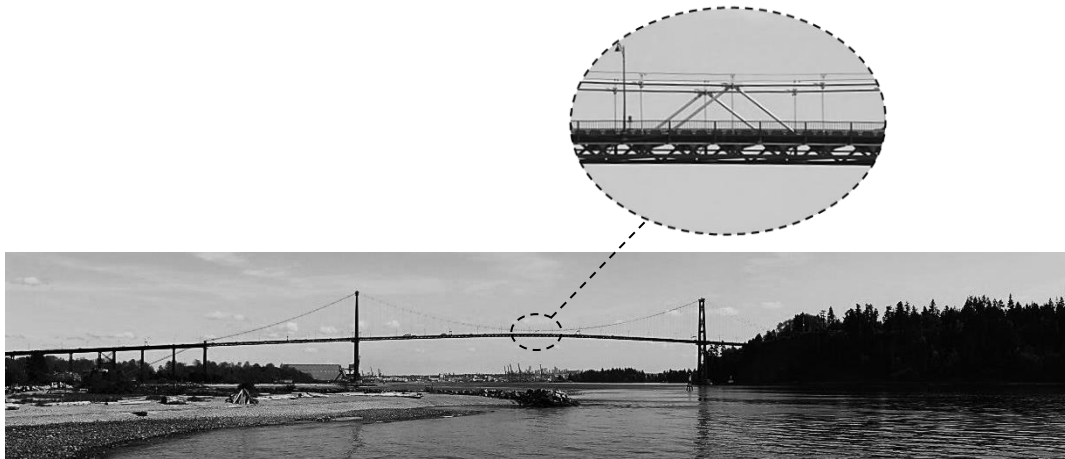
Figure 6.8: Photograph of Lions Gate Bridge (Vancouver, Canada)

Through investigation it was found that for the reference hybrid model, superstructure and tower demands were only marginally impacted by the addition of a central suspension cable clamp. Further details are included in Section 6.2.5. Again, this is because, relative to the span length, the suspended region is not long enough for the central suspension cable clamp to have any appreciable effect. Nevertheless, the central suspension cable clamp does have a slight impact on the live load stress range for cables situated within, or in close proximity to, the suspended region. The results for AS2 are displayed in Figure 6.9.
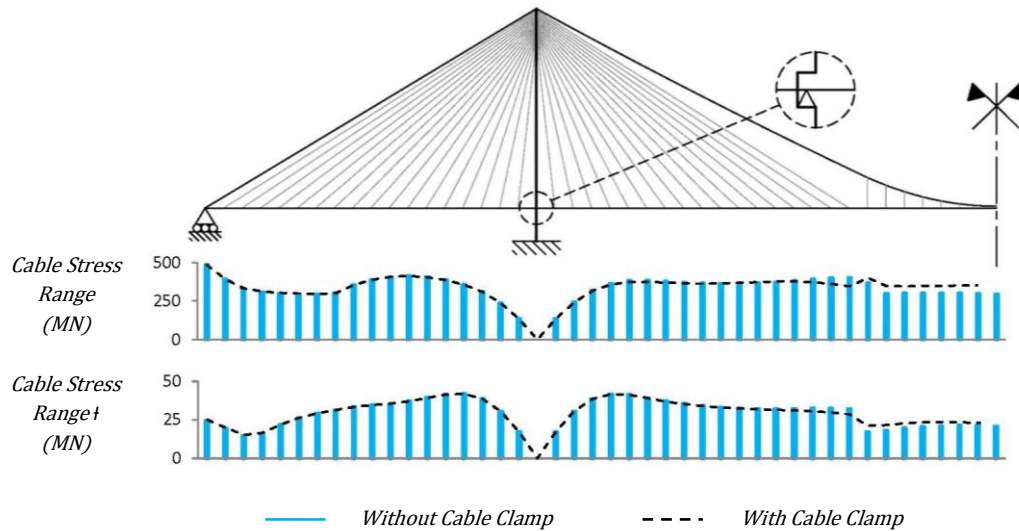
Figure 6.9: Cable Live Load Stress Range with Central Suspension Cable Clamp (AS2)
*Similar for AS1 and AS3
† Computed using the CHBDC FLS

The primary effect of the central suspension cable clamp is that the live load stress range is reduced for stay cables adjacent to the suspended region. However, this comes at the expense of a near uniform increase in the live load stress range for the hangers. Nevertheless, this is of little consequence when dealing with concentrated loads. Moreover, given that the peak live load stress range for all of the stay cables and hangers occurs in the side span, there is not a great deal of utility in employing a central suspension cable clamp when adhering to the recommended proportions specified in Chapter 5.

Although only the cable demands for AS2 are shown in Figure 6.9, the results are similar for AS1 and AS3. Normally, in suspension bridges, a central suspension cable clamp is only effective in mitigating static strain free deformations when the superstructure is longitudinally restrained. In that case, and in that respect, a central suspension cable clamp would be ineffective when used in conjunction with AS3. However, due to the restraining action of the anchor cable, longitudinal superstructure restraint at the towers is not a precondition in self-anchored hybrid cable bridges.

6.2.2 Cross Stays

Cross stays / hangers are adjunct members which, when added, form an overlap zone between the stayed and suspended regions of a discontinuous hybrid cable bridge (Figure 6.10). Their primary purpose is to facilitate a smoother stiffness transition at the junction. In this section, the effect of adding one, two, or three cross stays is examined. It is assumed that the axes of each cross stay and its

adjoining hanger intersect at the centroid of the superstructure. In addition, it is also assumed that each cross stay and its adjoining hanger shares an equal distribution of the superstructure dead load. As in previous sections, all other structural and geometric parameters are kept constant with the exception of the area of each cable which is recalculated based on the modified demands.

(Original Configuration)

(Modified Configuration with Cross Stays)
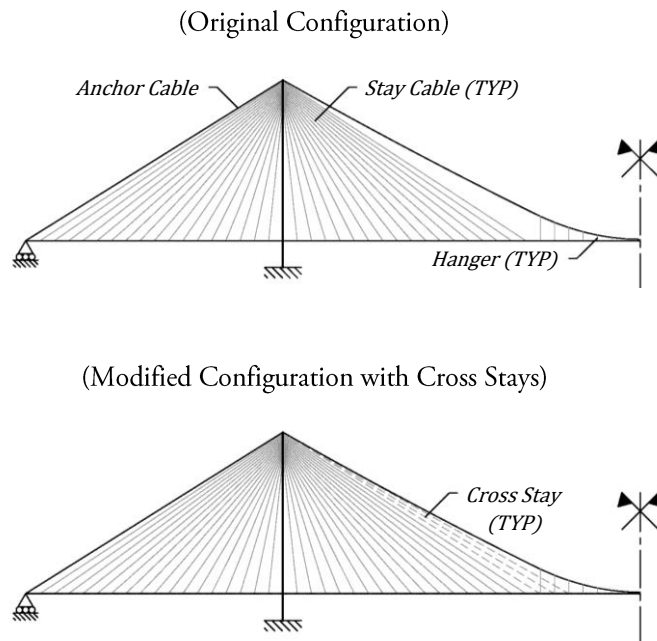
Figure 6.10: Discontinuous Hybrid Cable Bridge with Cross Stays

After compiling the analysis results it was discovered that the addition of cross stays has only a minor influence on superstructure and tower demands. Moreover, the influence on the superstructure demands is limited to the immediate vicinity of the stay cable-hanger junction. This is true regardless of the tower-superstructure articulation scheme. Still, the influence is beneficial in reducing the magnitude of the moment cusps near the junction (refer to Figure 6.3). Further details are included in Section 6.2.5.

The most pronounced effect of the cross stays is in relation to the live load cable stress ranges. The stress ranges are given in Table 6.6 for the single, double, and triple cross stay configurations. For each cable type, the peak stress range is emphasized in bold font. The percent change in the stress ranges is similar for all three tower-superstructure articulation schemes considered and, therefore, only the results for AS2 are displayed.

Table 6.6: Cable Live Load Demands with Cross Stay Configurations (AS2)
*Similar for AS1 and AS3

X Coord. at Deck (m)[1]	Cable Type[2]	Original (MPa)	1 Cross Stay		2 Cross Stays		3 Cross Stays	
			(MPa)	% Change[3]	(MPa)	% Change[3]	(MPa)	% Change[3]
0	CS	**485**	**486**	0	**487**	0	**487**	0
20	ST	392	393	0	393	0	394	1
40	ST	330	331	0	331	0	332	1
60	ST	308	308	0	308	0	309	0
80	ST	299	299	0	299	0	300	0
100	ST	296	296	0	296	0	296	0
120	ST	295	295	0	295	0	295	0
140	ST	300	300	0	300	0	300	0
160	ST	353	353	0	353	0	353	0
180	ST	389	389	0	389	0	389	0
200	ST	408	408	0	408	0	408	0
220	ST	**413**	**413**	0	**413**	0	**413**	0
240	ST	406	406	0	406	0	406	0
260	ST	386	386	0	387	0	387	0
280	ST	356	356	0	356	0	357	0
300	ST	310	310	0	310	0	310	0
320	ST	237	237	0	237	0	237	0
340	ST	135	135	0	135	0	135	0
TOWER								
380	ST	136	135	0	135	0	135	0
400	ST	243	242	0	242	-1	241	-1
420	ST	319	317	-1	316	-1	315	-1
440	ST	363	361	-1	359	-1	358	-1
460	ST	382	379	-1	377	-1	376	-1
480	ST	384	382	-1	380	-1	379	-1
500	ST	378	377	0	376	0	376	-1
520	ST	372	372	0	372	0	371	0
540	ST	367	367	0	367	0	367	0
560	ST	364	363	0	363	0	363	0
580	ST	364	361	-1	361	-1	361	-1
600	ST	367	362	-1	360	-2	360	-2
620	ST	373	364	-3	359	-4	358	-4
640	ST	382	369	-3	361	-5	356	-7
660	ST	392	375	-4	363	-7	356	-9
680	ST	399	381	-5	367	-8	357	-10
700	ST	403	384	-5	369	-8	358	-11
720	CST		384		370		359	
740	CST				371		363	
760	CST						374	
720	H	**367**	431	18	423	15	411	12
740	H	300	299	0	314	5	311	4
760	H	300	299	0	298	-1	308	3
780	H	301	300	0	298	-1	296	-2
800	H	301	300	0	298	-1	296	-2
820	H	300	299	0	298	-1	295	-2
840	H	298	297	0	295	-1	293	-2
860	H	295	294	0	292	-1	290	-2
MID SPAN								

Table Notes:
1. X Coordinate is measured with respect to end / anchor pier.
2. Cable types: 'CS' denotes anchor cable; 'ST' denotes stay cable; 'CST' denotes cross stay; 'H' denotes hanger.
3. Percent change is computed relative to original analysis results.

From Table 6.6, it is important to note that the addition of cross stays does not affect the stress range of the anchor cable. This is because the total force transferred by the cross stays is offset by a reduction in the total force transferred by the hangers (in conjunction with the suspension cable). In point of fact, similar to the superstructure demands, only cables situated near to the stay cable-hanger junction are markedly affected. To that end, the stress ranges of the adjoining stay cables are reduced, whereas, the stress ranges of the connecting hangers are increased. This may be confounding at first but it is important to consider that when cross stays are employed, the areas of the connecting hangers are substantially reduced in comparison to their original values on account of the dead load taken away by the cross stays. The stress range in the connecting hangers increases because the live load demands on those hangers were not reduced by the same proportion as the dead load demands.

The increase in the stress range of the connecting hangers may seem alarming given that their peak stress range exceeds, or is very near to, the peak stress range of the stay cables. However, the peak stress range of the connecting hangers can be reduced by tuning the dead load distribution between the cross stays and hangers. Nevertheless, this would increase the stress range in the cross stays, thereby negating the primary benefit.

When it comes to concentrated loading, the increase in the stress range of the connecting hangers is entirely inconsequential given the originally low stress range of the hangers (Table 6.7). Therefore, in said circumstance, the cross stays are helpful in reducing the stress range in the main span stays. However, again, the need to reduce the stress range of the main span stays is questionable given that the peak stress range of the stay cables generally occurs in the side spans. Furthermore, as demonstrated in Section 6.1.3, cable fatigue is unlikely to be an issue, thus further discussion of this matter is unwarranted for the purposes of this thesis.

All things considered, the structural benefits of employing cross stays are meager. It would be remiss though not to briefly mention the aesthetic benefit. There is undoubtedly a certain aesthetic appeal associated with cross stays because, with their presence, the cable system as a whole has a more uniform and harmonious appearance.

Table 6.7: Cable Live Load Demands Computed using the CHBDC FLS (AS2)
*Similar for AS1 and AS3

X Coord. at Deck (m)[1]	Cable Type[2]	CHBDC (MPa)	1 Cross Stay		2 Cross Stays		3 Cross Stays	
			(MPa)	% Change[3]	(MPa)	% Change[3]	(MPa)	% Change[3]
0	CS	**24.5**	**24.7**	1	**24.9**	1	**25.0**	2
20	ST	19.3	19.5	1	19.6	2	19.8	2
40	ST	14.7	14.8	1	14.9	2	15.0	2
60	ST	16.4	16.4	0	16.4	0	16.4	0
80	ST	21.9	21.8	0	21.8	0	21.8	0
100	ST	26.2	26.2	0	26.2	0	26.2	0
120	ST	29.3	29.3	0	29.3	0	29.3	0
140	ST	31.2	31.2	0	31.2	0	31.2	0
160	ST	33.3	33.4	0	33.4	0	33.4	0
180	ST	34.5	34.6	0	34.6	0	34.6	0
200	ST	35.4	35.4	0	35.4	0	35.5	0
220	ST	37.1	37.1	0	37.1	0	37.0	0
240	ST	39.4	39.4	0	39.4	0	39.4	0
260	ST	41.5	41.5	0	41.5	0	41.4	0
280	ST	**41.8**	**41.8**	0	**41.8**	0	**41.8**	0
300	ST	38.7	38.7	0	38.7	0	38.7	0
320	ST	30.6	30.6	0	30.6	0	30.6	0
340	ST	17.2	17.2	0	17.2	0	17.2	0
				TOWER				
380	ST	17.0	17.0	0	17.0	0	17.0	0
400	ST	30.5	30.5	0	30.5	0	30.5	0
420	ST	38.5	38.6	0	38.6	0	38.6	0
440	ST	41.7	41.7	0	41.7	0	41.7	0
460	ST	41.3	41.3	0	41.3	0	41.3	0
480	ST	39.2	39.2	0	39.2	0	39.2	0
500	ST	37.2	37.1	0	37.0	-1	36.9	-1
520	ST	35.6	35.6	0	35.5	0	35.4	-1
540	ST	34.2	34.1	0	34.1	0	34.0	0
560	ST	33.1	33.0	0	33.0	0	33.0	0
580	ST	32.4	32.3	0	32.3	-1	32.2	-1
600	ST	32.2	31.9	-1	31.7	-1	31.6	-2
620	ST	32.1	31.6	-2	31.3	-3	31.1	-3
640	ST	32.2	31.4	-3	30.8	-4	30.6	-5
660	ST	32.4	31.1	-4	30.3	-6	29.9	-7
680	ST	32.4	30.8	-5	29.7	-8	29.1	-10
700	ST	32.1	30.2	-6	28.9	-10	28.1	-12
720	CST		29.2		27.7		27.1	
740	CST				27.3		26.5	
760	CST						25.7	
720	H	17.1	**21.9**	28	21.0	23	20.0	17
740	H	18.1	17.8	-2	20.2	11	19.5	8
760	H	19.6	19.4	-1	19.2	-2	**21.9**	12
780	H	20.5	20.4	-1	20.1	-2	19.9	-3
800	H	21.1	21.0	0	20.9	-1	20.6	-2
820	H	**21.4**	21.4	0	21.3	0	21.1	-1
840	H	21.3	21.4	0	**21.4**	0	21.3	0
860	H	21.1	21.2	0	21.2	0	21.1	0
				MID SPAN				

Table Notes:
1. X Coordinate is measured with respect to end / anchor pier.
2. Cable types: 'CS' denotes anchor cable; 'ST' denotes stay cable; 'CST' denotes cross stay; 'H' denotes hanger.
3. Percent change is computed relative to original analysis results.

6.2.3   Single Intermediate Pier

Intermediate piers are auxiliary piers positioned in the side spans between the anchor piers and towers. Their general function is to act as additional anchor piers, which in turn, enables multiple cables to be engaged as anchor cables. As a secondary benefit, intermediate piers stiffen the side spans by reducing the distance between ground supports. In conventional cable-stayed bridges, single and multiple intermediate pier configurations have been used. Examples are provided in Figure 6.11 and Figure 6.12, respectively. The single intermediate pier configuration is examined in this section. Multiple intermediate pier configurations are covered in Section 6.2.4.

Figure 6.11: The Incheon Bridge, South Korea (Single Intermediate Pier)
Photo By Maarten Visser from Capelle aan den IJssel, Nederland (Seoul bridge & city)
[CC BY-SA 2.0 (http://creativecommons.org/licenses/by-sa/2.0)], via Wikimedia Commons

Figure 6.12: The Pont de Normandie, France (Multiple Intermediate Piers)
Photo By François Roche from Paris, France
[CC BY 2.0 (http://creativecommons.org/licenses/by/2.0)], via Wikimedia Commons

When employing a single intermediate pier, the location of the pier is a crucial parameter. To study the most favourable position, three different pier locations are examined. Specifically, the spacing of the intermediate pier with respect to the original anchor pier (x_{pi}), is set equal to 25%, 50%, and 75% of the side span length (L_s). In computing the demands, it is assumed that the intermediate pier is not engaged to support dead loads. In addition, the intermediate pier is assumed to have zero bending stiffness and an infinite axial stiffness. In other words, simple roller supports are used to model the intermediate pier. As in previous sections, all input parameters are kept constant with the exception of the area of each cable.

The demands for the three intermediate pier locations considered are displayed in Figure 6.13 and Figure 6.14. For the superstructure and cable demands, only the results for AS2 are displayed. Details for AS1 and AS3 are included in Section 6.2.5; however, the overall trends are similar.

With regards to the superstructure, the addition of an intermediate pier reduces deflections and deflections are smallest for the case when x_{pi}/L_s = 0.5. The same is also true for the axial force demands. In contrast, moment and shear force demands are not affected in a positive manner. Moment and shear force demands in the side spans increase with increasing values of x_{pi}/L_s, and in the main span, force demands are only marginally affected. Similarly, the stress range in the main span cables does not depend greatly on the value of x_{pi}/L_s. Nevertheless, due to the added vertical support provided by the intermediate pier the stress range in the side span cables is, in most cases, substantially reduced. The only exception is when x_{pi}/L_s = 0.25. In that case, the maximum stress range in the side span cables remains practically unchanged when the bridge is subjected to concentrated live loading.

From Figure 6.14, it is clear that the addition of an intermediate pier is highly beneficial with regards to the tower demands. Similar to the superstructure deflection demands, tower demands are generally smallest for the case when x_{pi}/L_s = 0.5. This result is undoubtedly related to the effect of cable inclination (refer to Chapter 3, Section 3.1.2.2). The cables near to the intermediate pier behave as supplementary anchor cables and when x_{pi}/L_s = 0.5, those cables are inclined at roughly the optimum inclination of 45 degrees to the horizon.

Considering all the above, the use of an intermediate pier is generally advantageous, although as a consequence, a portion of the side spans will likely need strengthening. In addition, when selecting the position of the intermediate pier, the most favourable value of x_{pi}/L_s lies between 0.25 and 0.5.
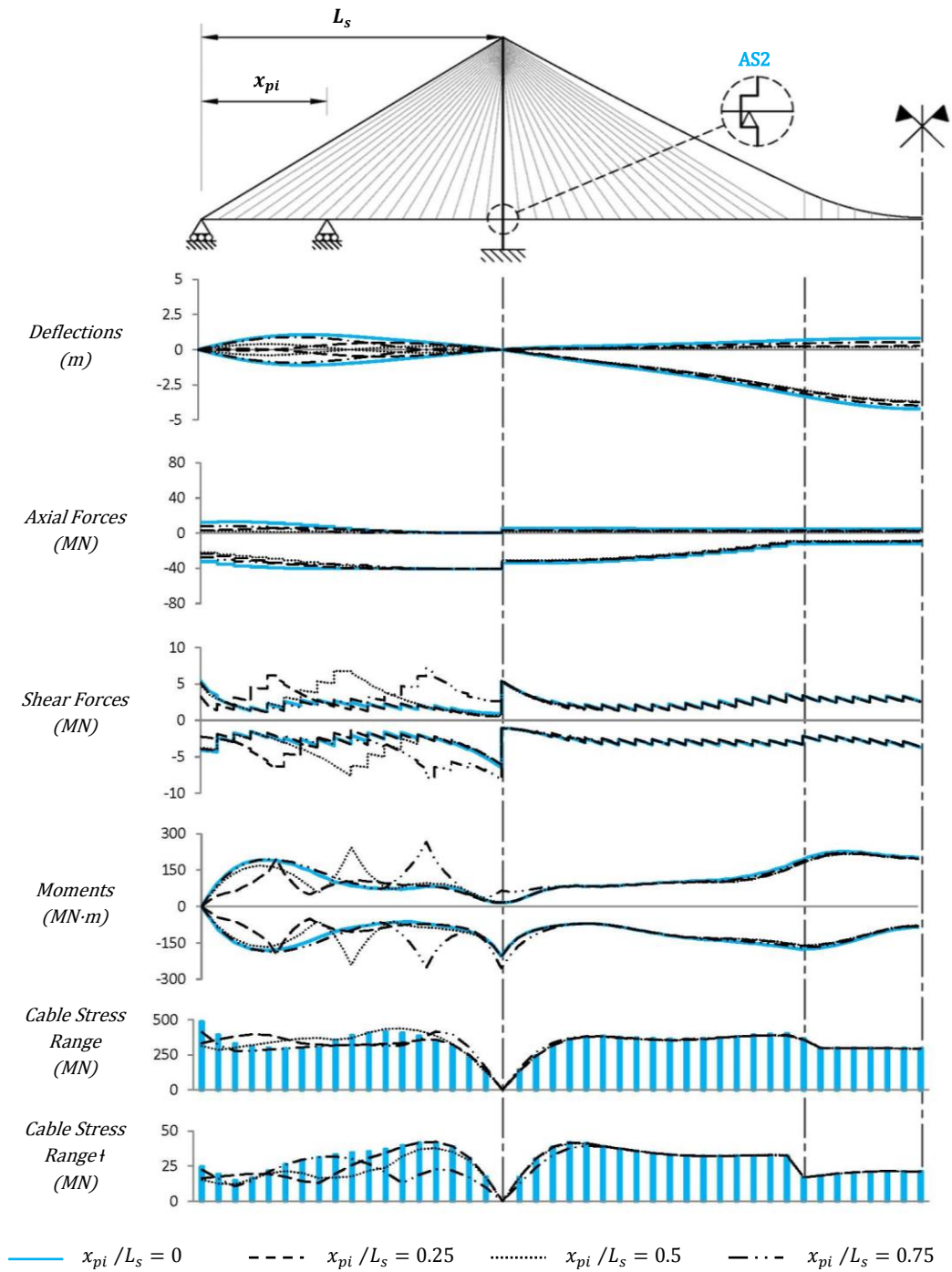
Figure 6.13: Superstructure and Cable Live Load Demands with Single Intermediate Pier
*Similar for AS1 and AS3
ⱡ Computed using the CHBDC FLS
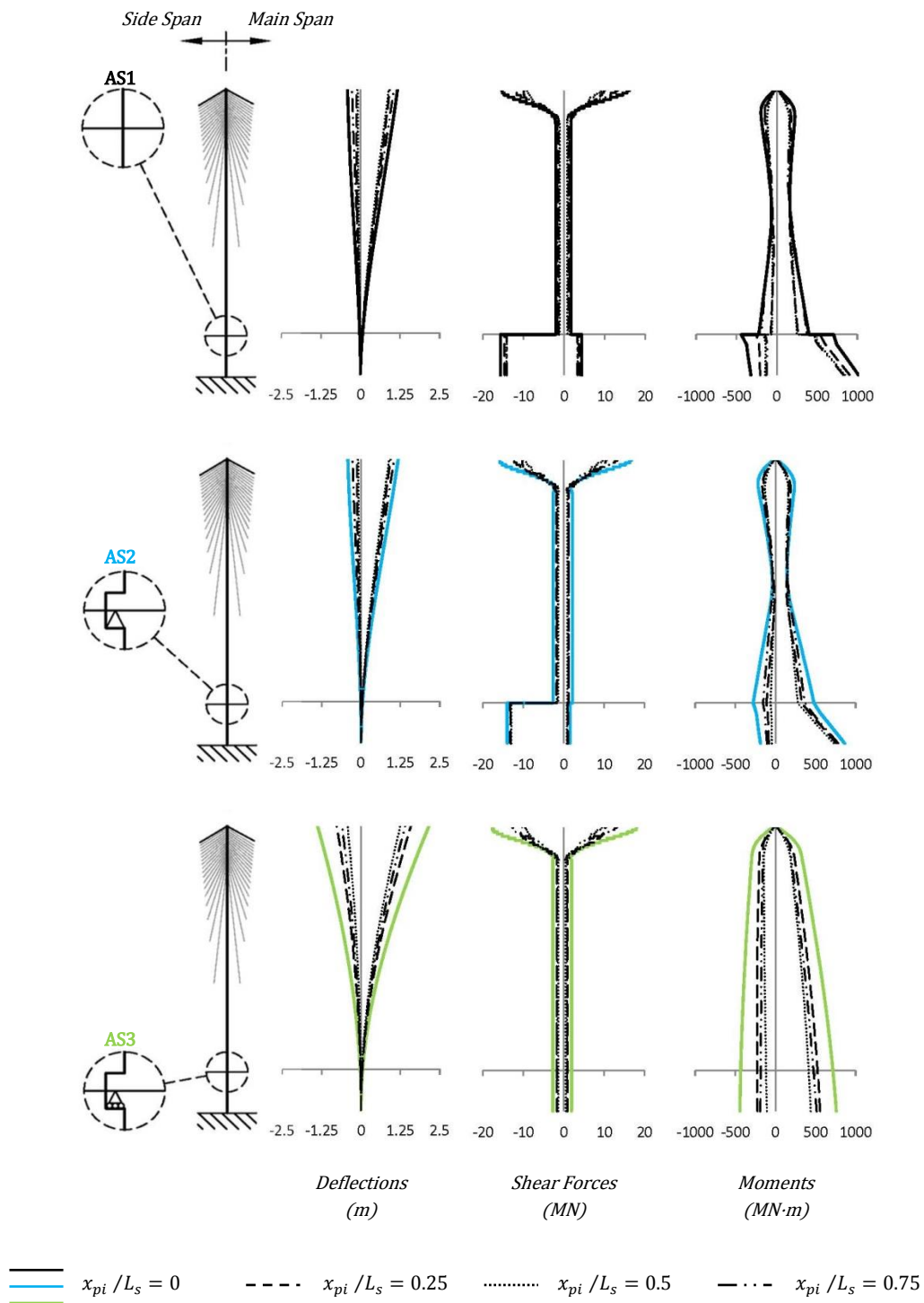
Figure 6.14: Tower Live Load Demands with Single Intermediate Pier

6.2.4 Multiple Intermediate Piers

Utilizing multiple intermediate piers is only a possibility when the topography of the bridge site does not preclude their construction. It is of interest in this section to study how demands vary with the number of intermediate piers included. Although numerous different configurations can theoretically be conceived, for simplicity, only the three basic configurations shown in Figure 6.15 are considered.

(2 Intermediate Pier Configuration)

3 Equal Spaces   *3 Equal Spaces*

(3 Intermediate Pier Configuration)

4 Equal Spaces   *4 Equal Spaces*

(4 Intermediate Pier Configuration)

5 Equal Spaces   *5 Equal Spaces*
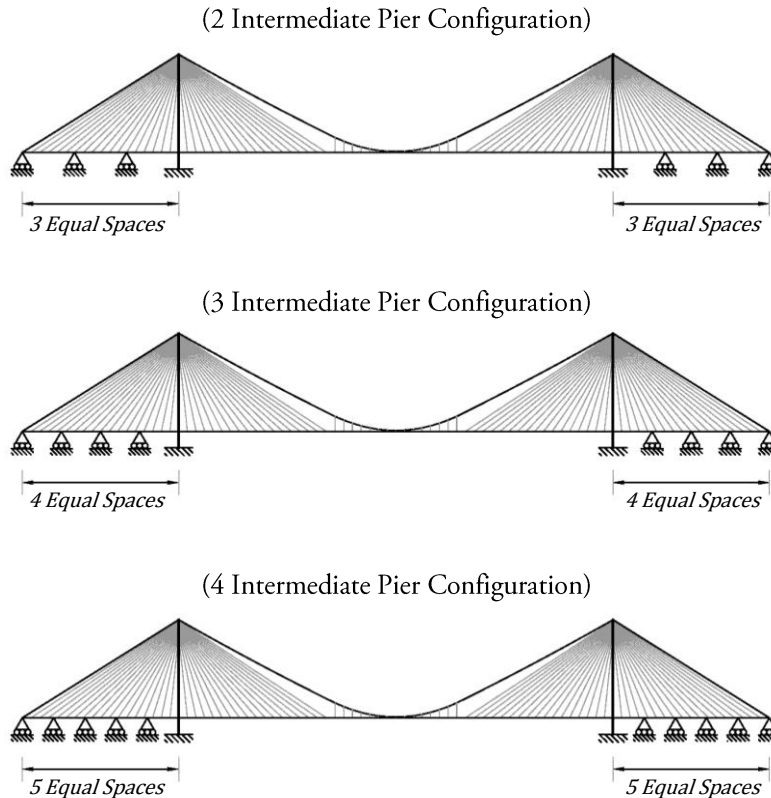
Figure 6.15: Multiple Intermediate Pier Configurations Considered

The results of the study are presented in Figure 6.16 and Figure 6.17. Clearly, the application of multiple intermediate piers is highly effective in universally reducing demands. It is interesting though that the superstructure and cable demands in the main span are not greatly affected by the number of intermediate piers included. The same is also true of the tower demands. Nevertheless, the amount of reduction in those demands is equal to or greater than that recorded for the single intermediate pier configuration. Moreover, there are even greater reductions in the superstructure and cable demands in the side spans. The large peaks in the side span force envelopes previously observed for the single intermediate pier configuration are, for the most part, abated when using

multiple intermediate piers. In addition, cables stresses in the side span become more uniform.

When examining the results for different pier configurations, demands generally decrease with increasing numbers of intermediate piers. Therefore, there are definite advantages to employing two or more intermediate piers in each side span. Notwithstanding, the gains are not without bounds. Consequently, there are substantially less benefits to be gained when shifting from three to four intermediate piers as there are when shifting from two to three intermediate piers. This is more clearly shown in the following section which gives a comparison of the results for all of the design components considered.
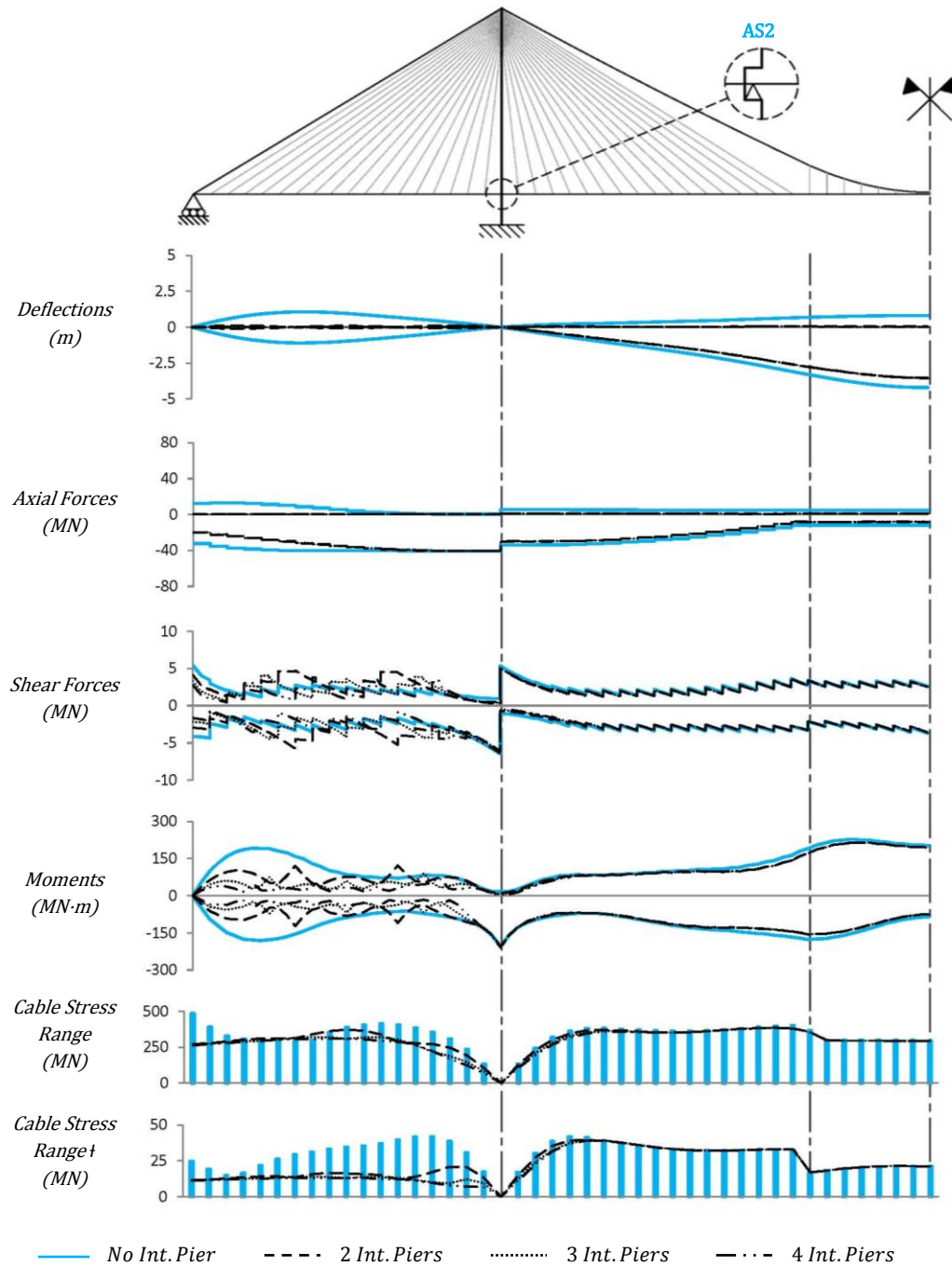
Figure 6.16: Superstructure and Cable Live Load Demands with Multiple Intermediate Piers
*Similar for AS1 and AS3
ᵻ Computed using the CHBDC FLS
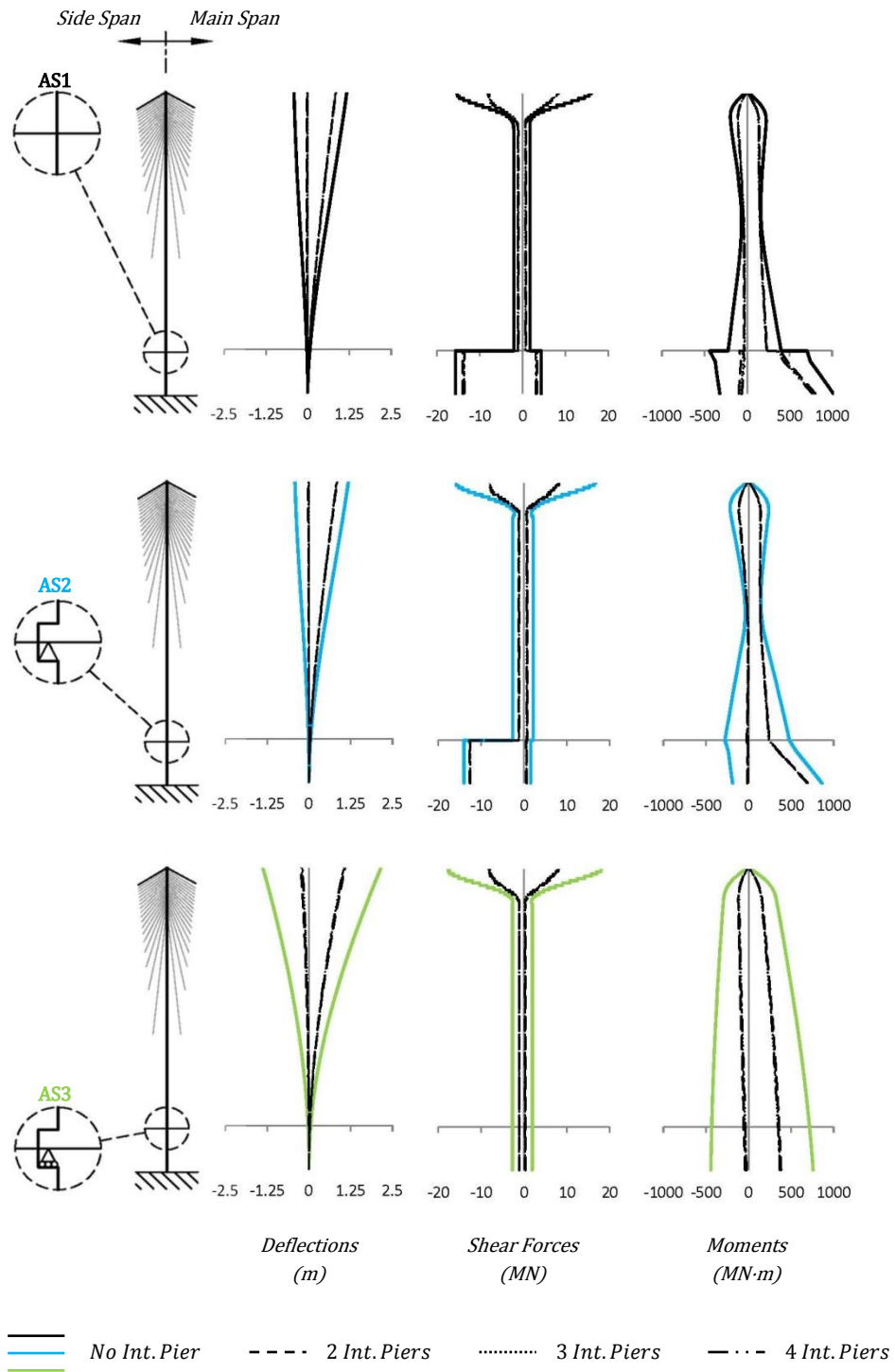
Figure 6.17: Tower Live Load Demands with Multiple Intermediate Piers

6.2.5   Comparison of Design Components

The results for all of the design components are compiled in Table 6.8. Sub-tables are provided for each of the tower-superstructure articulation schemes considered. In each sub-table, results are presented for numerous demand parameters in terms of percent change (percent change relative to the original/reference model). As per the convention established earlier in the chapter, negative numbers indicate a reduction in the demands whereas positive numbers indicate an increase in the demands.

It is clear from Table 6.8 that the addition of a central suspension cable clamp is not significantly effective and is, therefore, unwarranted. The application of cross stays is somewhat more practical although their influence is greatly overshadowed by that of the single and multiple intermediate pier configurations. Comparing Table 6.8 to Table 6.5, the utilization of intermediate piers is even more effective in reducing demands than member stiffness modifications. This is particularly true for horizontal deflections and their associated demands. In that regard, the use of intermediate piers effectively nullifies the negative characteristics associated with AS3.

Regardless of the tower-superstructure articulation scheme, the presence of intermediate piers also reduces the peak tension in the anchor cables to a value nearly equal to the peak tension in the suspension cable. This is because with intermediate piers, the original anchor cables are no longer solely responsible for resisting unbalanced loading in the stayed regions of the bridge. The majority of the unbalanced load is resisted by the intermediate piers and their associated anchor cables. Consequently, the same section properties for the suspension cable can be used continuously over the entire length of the bridge without incurring undue costs.

Table 6.8a: Comparison of Design Components (AS 1)
*Percent Change Relative to Original Demand Value (units: MN,m)

			Central Cable Clamp	Cross Stays (No. of Cross Stays)			Single Intermediate Pier (Distance from End Pier)			Multiple Intermediate Piers (No. of Equally Spaced Int. Piers)		
		Original Value		1	2	3	$0.25 \cdot L_s$	$0.5 \cdot L_s$	$0.75 \cdot L_s$	2	3	4
Superstructure	Negative Vertical Deflection at Mid-Span	-4.18	-1	0	0	0	-11	-13	-5	-15	-15	-15
	Absolute Maximum Horizontal Deflection at End Pier	0.120	-3	-1	-1	-2	-10	-17	-16	-20	-21	-22
	Maximum Negative Axial Force at Tower	-40.8	2	0	0	0	0	0	0	0	-1	-1
	Absolute Maximum Shear at Tower	6.08	0	0	0	0	1	1	32	-8	-8	-8
	Absolute Maximum Shear at End Pier	5.40	0	0	0	0	-38	-8	-3	-24	-38	-48
	Peak Negative Moment in Main Span	-176	1	-4	-6	-7	-8	-9	-4	-11	-11	-11
	Peak Positive Moment in Main Span	227	1	-3	-5	-7	-4	-5	-2	-6	-6	-6
	Maximum Negative Moment at Tower	-266	0	0	0	1	-7	-6	1	-7	-8	-8
	Peak Negative Moment in Side Span	-181	0	0	0	0	6	28	41	-33	-61	-74
	Peak Positive Moment in Side Span	192	0	0	0	0	0	19	34	-37	-62	-72
Towers	Positive Horizontal Deflection at Top of Tower	1.18	-1	0	0	0	-21	-23	-10	-28	-29	-29
	Negative Horizontal Deflection at Top of Tower	-0.410	-1	0	0	0	-69	-77	-34	-94	-98	-98
	Negative Axial Force at Base of Tower	-76.4	1	0	0	0	0	1	0	0	0	0
	Absolute Maximum Shear at Top of Tower	16.0	2	-3	-5	-5	-37	-41	-17	-47	-48	-48
	Absolute Maximum Shear at Base of Tower	15.7	0	-1	-3	-4	-6	-9	-10	-11	-13	-13
	Negative Moment at Base of Tower	-321	-7	0	0	0	-36	-55	-61	-69	-77	-81
	Positive Moment at Base of Tower	1016	-2	-1	-1	-2	-11	-17	-18	-21	-23	-24
Cables	Peak Tension in Main Span Suspension Cable	23.0	12	-6	-13	-20	-1	-1	0	-1	-1	-1
	Peak Tension in Anchor Cable	37.2	0	0	0	0	-28	-31	-12	-36	-37	-37
	Peak Stress Range in Side Span Cables (Inc. Anchor Cable)	475	0	0	0	0	-19	-8	-13	-23	-32	-34
	⮡ Computed using the CHBDC FLS	35	0	0	0	0	-1	-5	-12	-53	-60	-62
	Peak Stress Range in Main Span Stay Cables	399	-5	-5	-8	-7	-3	-3	-2	-4	-4	-4
	⮡ Computed using the CHBDC FLS	38	-1	0	-1	-1	0	0	0	0	0	0
	Peak Stress Range in Hangers	367	8	17	15	12	-2	-2	-1	-3	-3	-3
	⮡ Computed using the CHBDC FLS	21	11	2	0	3	0	0	0	0	0	0
	Total Cable Steel Volume	333	1.1	-0.7	-1.3	-1.8	-3.4	-3.6	-1.8	-4.9	-5.3	-5.4

Table 6.8b: Comparison of Design Components (AS 2)
*Percent Change Relative to Original Demand Value (units: MN,m)

		Original Value	Central Cable Clamp	Cross Stays (No. of Cross Stays)			Single Intermediate Pier (Distance from End Pier)			Multiple Intermediate Piers (No. of Equally Spaced Int. Piers)		
				1	2	3	$0.25 \cdot L_s$	$0.5 \cdot L_s$	$0.75 \cdot L_s$	2	3	4
Superstructure	Negative Vertical Deflection at Mid-Span	-4.22	-1	0	0	0	-12	-13	-6	-16	-16	-16
	Absolute Maximum Horizontal Deflection at End Pier	0.109	-3	0	-1	-1	-10	-16	-10	-18	-19	-19
	Maximum Negative Axial Force at Tower	-40.9	2	0	0	0	0	0	0	0	-1	-1
	Absolute Maximum Shear at Tower	6.50	0	0	0	0	-6	-5	25	-6	-6	-2
	Absolute Maximum Shear at End Pier	5.46	0	0	0	0	-39	-9	-4	-24	-39	-49
	Peak Negative Moment in Main Span	-176	2	-4	-6	-7	-8	-9	-4	-11	-12	-12
	Peak Positive Moment in Main Span	228	1	-3	-5	-7	-4	-5	-2	-6	-6	-6
	Maximum Negative Moment at Tower	-204	0	0	0	0	1	0	25	0	0	2
	Peak Negative Moment in Side Span	-181	0	0	0	0	8	33	39	-32	-60	-73
	Peak Positive Moment in Side Span	192	0	0	0	0	2	27	38	-37	-53	-61
Towers	Positive Horizontal Deflection at Top of Tower	1.19	0	0	0	0	-21	-24	-11	-29	-30	-30
	Negative Horizontal Deflection at Top of Tower	-0.418	0	0	0	0	-68	-78	-35	-95	-98	-99
	Negative Axial Force at Base of Tower	-76.6	1	0	0	0	0	1	0	0	0	1
	Absolute Maximum Shear at Top of Tower	16.7	1	-3	-5	-5	-37	-41	-20	-49	-50	-50
	Absolute Maximum Shear at Base of Tower	14.0	0	-2	-3	-4	-6	-7	-6	-10	-10	-11
	Negative Moment at Base of Tower	-188	-9	0	0	-1	-56	-76	-44	-91	-94	-95
	Positive Moment at Base of Tower	864	-2	-1	-1	-2	-12	-16	-9	-19	-20	-20
Cables	Peak Tension in Main Span Suspension Cable	23.0	13	-6	-13	-20	-1	-1	0	-1	-1	-1
	Peak Tension in Anchor Cable	38.2	0	0	0	0	-28	-31	-14	-38	-38	-39
	Peak Stress Range in Side Span Cables (Inc. Anchor Cable)	485	0	0	0	0	-18	-10	-14	-23	-34	-36
	↳ Computed using the CHBDC FLS	42	0	0	0	0	1	-10	-24	-50	-67	-68
	Peak Stress Range in Main Span Stay Cables	403	-6	-5	-6	-6	-3	-3	-2	-4	-4	-4
	↳ Computed using the CHBDC FLS	42	0	0	0	0	0	-1	-5	-5	-6	-6
	Peak Stress Range in Hangers	367	9	18	15	12	-2	-2	-1	-3	-3	-3
	↳ Computed using the CHBDC FLS	21	11	2	0	2	0	0	0	0	0	0
	Total Cable Steel Volume	336	1.2	-0.7	-1.2	-1.7	-3.4	-3.8	-2.3	-5.4	-5.9	-6.1

Table 6.8c: Comparison of Design Components (AS 3)
*Percent Change Relative to Original Demand Value (units: MN,m)

		Original Value	Central Cable Clamp	Cross Stays (No. of Cross Stays)			Single Intermediate Pier (Distance from End Pier)			Multiple Intermediate Piers (No. of Equally Spaced Int. Piers)		
				1	2	3	$0.25 \cdot L_s$	$0.5 \cdot L_s$	$0.75 \cdot L_s$	2	3	4
Superstructure	Negative Vertical Deflection at Mid-Span	-4.22	-1	0	0	0	-11	-12	-5	-15	-15	-15
	Absolute Maximum Horizontal Deflection at End Pier	2.18	0	0	0	0	-40	-63	-47	-72	-74	-74
	Maximum Negative Axial Force at Tower	-41.0	0	0	0	0	0	0	0	0	-1	-1
	Absolute Maximum Shear at Tower	6.51	0	0	0	0	-5	-4	28	-6	-5	-1
	Absolute Maximum Shear at End Pier	5.65	-3	0	0	0	-40	-11	-6	-27	-41	-51
	Peak Negative Moment in Main Span	-176	3	-4	-6	-7	-9	-10	-5	-12	-12	-12
	Peak Positive Moment in Main Span	229	3	-3	-5	-7	-5	-5	-2	-6	-6	-6
	Maximum Negative Moment at Tower	-204	0	0	0	0	2	1	32	1	2	4
	Peak Negative Moment in Side Span	-192	-4	0	0	0	14	33	46	-35	-62	-74
	Peak Positive Moment in Side Span	206	-4	0	0	0	5	25	42	-37	-54	-62
Towers	Positive Horizontal Deflection at Top of Tower	2.18	1	0	0	0	-26	-42	-35	-50	-52	-52
	Negative Horizontal Deflection at Top of Tower	-1.40	2	0	0	0	-44	-69	-56	-82	-85	-86
	Negative Axial Force at Base of Tower	-76.4	1	0	0	0	0	2	2	1	1	2
	Absolute Maximum Shear at Top of Tower	18.1	3	-3	-4	-4	-42	-47	-27	-53	-54	-54
	Absolute Maximum Shear at Base of Tower	2.7	0	0	0	0	-35	-51	-38	-57	-58	-59
	Negative Moment at Base of Tower	-442	2	0	0	0	-49	-76	-57	-91	-94	-95
	Positive Moment at Base of Tower	759	1	0	0	0	-27	-42	-32	-50	-51	-52
Cables	Peak Tension in Main Span Suspension Cable	23.0	14	-6	-13	-20	-1	-1	-1	-1	-1	-1
	Peak Tension in Anchor Cable	39.2	-3	0	-1	-1	-31	-34	-17	-40	-41	-41
	Peak Stress Range in Side Span Cables (Inc. Anchor Cable)	500	-3	0	0	0	-15	-7	2	-21	-30	-33
	↳ Computed using the CHBDC FLS	42	0	0	0	0	1	-11	-25	-51	-66	-66
	Peak Stress Range in Main Span Stay Cables	399	-5	-5	-5	-6	-3	-3	-2	-3	-4	-4
	↳ Computed using the CHBDC FLS	41	0	0	0	0	0	-1	-6	-5	-6	-6
	Peak Stress Range in Hangers	376	5	19	17	13	-4	-5	-2	-5	-5	-5
	↳ Computed using the CHBDC FLS	21	11	4	0	3	0	0	0	0	0	0
	Total Cable Steel Volume	337	0.9	-0.7	-1.3	-1.8	-3.6	-4.1	-2.5	-5.6	-6.1	-6.3

Design Component

Demand Parameter

6.3   End of Chapter Summary

This chapter presents the results of a comprehensive and detailed study on the behaviour of self-anchored discontinuous hybrid bridges subject to the confines of the optimum proportions specified in Chapter 5. The study commences with an examination into the effect of the tower-superstructure articulation scheme. In general, it was found that rotationally restraining the superstructure at the towers only affects local demands within the immediate vicinity of the towers. Moreover, the effect on the demands is minor. Similarly, when longitudinal movement of the superstructure is unrestrained at the towers, the superstructure and cable demands are not significantly altered. However, the longitudinal restraint of the superstructure at the towers does have a considerable impact on the tower demands and the longitudinal superstructure deflection demands. Based solely on live loading, the latter can be twenty times greater than in bridges where the superstructure is longitudinally restrained at the towers.

By comparing the behaviour of self-anchored hybrid and cable-stayed bridges it was discovered that the indifference the tower-superstructure articulation scheme has on superstructure and cable demands is not unique to self-anchored hybrid cable bridges. The same also applies to cable-stayed bridges. Furthermore, regardless of the tower-superstructure articulation scheme, both bridge types exhibit similar demands. This further confirms that the material costs of both bridge types should be at par with one another. It can also be inferred that live load induced cable fatigue should not be an issue in self-anchored hybrid cable bridges.

Nonlinearity in the hybrid system due to live load was examined once more and it was found that although a linearized influence analysis delivers, in most cases, a conservative estimate of the demands on the bridge, the safety of the method cannot always be relied upon. Application of the linearized influence analysis must be done judiciously. In a separate study, the effect of the cable, superstructure, and tower stiffness parameters were examined. Therein, it was found that when the superstructure is longitudinally restrained at the towers, increasing the flexural stiffness of the superstructure has the detrimental effect of increasing the force demands on the superstructure. Nevertheless, the longitudinal superstructure deflection, the positive moment and shear forces at the base of the tower, and the stress range of the cables (when subject to concentrated loading) are all reduced. On the other hand, no benefits were observed when increasing the flexural stiffness of the towers, whereas, there were only benefits observed when increasing the axial stiffness of the suspension and anchor cables. Two main differences result when the superstructure is longitudinally unrestrained at the towers. First, increasing the flexural stiffness of the superstructure yields no benefits, and second, increasing the flexural stiffness of the towers becomes highly beneficial.

The remainder of the chapter studied the advantages of applying various design components including central suspension cable clamps, cross stays, and intermediate piers. In discontinuous hybrid cable bridges, due to the condensed length of the suspended region, the application of central suspension cable clamps has only a minor, inconsequential effect. By comparison, cross stays have a more constructive influence on the demands; however, their influence is confined to the immediate vicinity surrounding the stay cable-hanger junction. In addition, their use to mitigate stress fluctuations in the adjoining stay cables is only practical when dealing with concentrated live loading.

Of all of the design components considered, the greatest advantages were observed with the addition of intermediate piers. When the topography of the bridge site permits, intermediate piers were observed to be most effective when three or more piers were included in each side span, whereupon, demands for the superstructure, towers, and cables are all significantly reduced. As a consequence, the peak tension in the anchor cable becomes comparable to the peak tension in the suspension cable and the same diameter of cable can be used cost-effectively on both sides of the towers. In addition, when the superstructure is longitudinally unrestrained at the towers, the longitudinal deflection of the superstructure is dramatically reduced to a much more manageable value.

The aforementioned conclusions were obtained for a reference model with a 1000 metre main span. However, so long as the bridge stiffness parameters are scaled in accordance with Section 4.2.1.6, the conclusions should be applicable to any span length. To that end, although not mentioned in Chapter 4, to maintain a consistent level of global stiffness, the tower stiffness parameters should be scaled in proportion to the superstructure stiffness parameters.

Chapter 7

CONSTRUCTABILITY

Thus far, considerable attention has been given in this thesis to studying the structural behaviour of self-anchored discontinuous hybrid cable bridges. As a result, the behaviour of the system under static service loading is now well researched and documented. However, the usefulness of such research is limited without considering the constructability of the system. This is because, unlike conventional cable bridges which have well-established construction schemes, self-anchored discontinuous hybrid cable bridges are fairly novel and their construction presents obstacles similar to those associated with self-anchored suspension bridges. As such, this chapter endeavours to address the constructability of the system so as to ease any concerns regarding its practicality.

In any type of self-anchored cable bridge, following construction, the horizontal components of the cable forces from dead load are efficiently balanced by internal axial forces within the superstructure. However, during construction, the system must inevitably cope with unbalanced forces. Conventional cable-stayed bridges have the advantage because the horizontal components of the cable forces are transferred to the superstructure from the stay cables at discrete intervals along the length of the bridge. As a result, construction methods can be employed which minimize the amount of unbalanced force introduced during construction. In contrast, in self-anchored suspension bridges the entire horizontal force from the cable system is transferred at the ends of the superstructure where the suspension cable is anchored. This presents certain complications. For context, some of the more common methods employed in the construction of conventional cable bridges are briefly discussed in Sections 7.1 and 7.2.

The latter half of this chapter discusses an innovative construction method proposed for self-anchored discontinuous hybrid cable bridges. The primary objectives of the proposed method are to reduce construction time and costs. This is made possible by building upon conventional construction techniques for cables bridges while capitalizing on the unique characteristics of self-anchored discontinuous hybrid cable bridges.

7.1   Standard Construction Methods for Self-Anchored Cable-Stayed Bridges

Conventional cable-stayed bridges are normally constructed using the double or one-sided free cantilever method (Figure 7.1 and Figure 7.2). In the double-sided free cantilever method, the superstructure is constructed in segments, where the length of each segment often corresponds to the spacing between stay cables. Commencing at the towers, segments are typically hoisted to deck level and sequentially added to the side and main spans. Consequently, during construction, the load is never more than one segment out of balance. Thus, unbalanced forces are kept small and any unbalanced load can normally be carried by the superstructure and towers in bending. Nonetheless, depending on the span proportions and weight distribution of the superstructure, if required, multiple cable stressing operations and/or guy lines can be used to lessen the burden on the superstructure and towers. Alternatively, it is also possible to construct the side spans on falsework and then progressively erect the main span using the one-sided free cantilever process. This alternate method is commonly employed when the side spans are composed of concrete. The addition of the falsework substantially increases the global stiffness the system during construction and further abates the unbalanced load which must be resisted by the superstructure and towers.
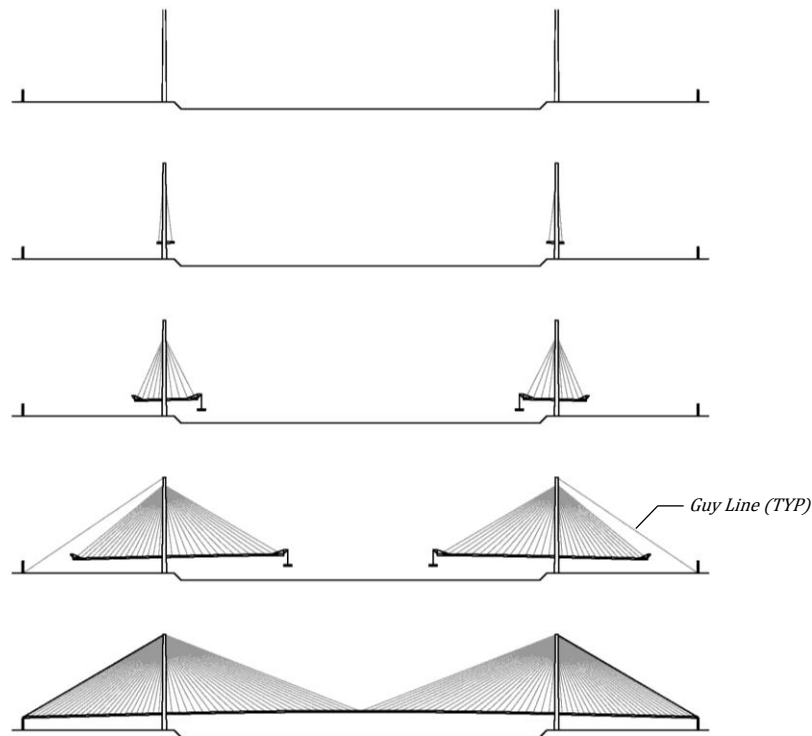
Figure 7.1: The Double-Sided Free Cantilever Method of Construction
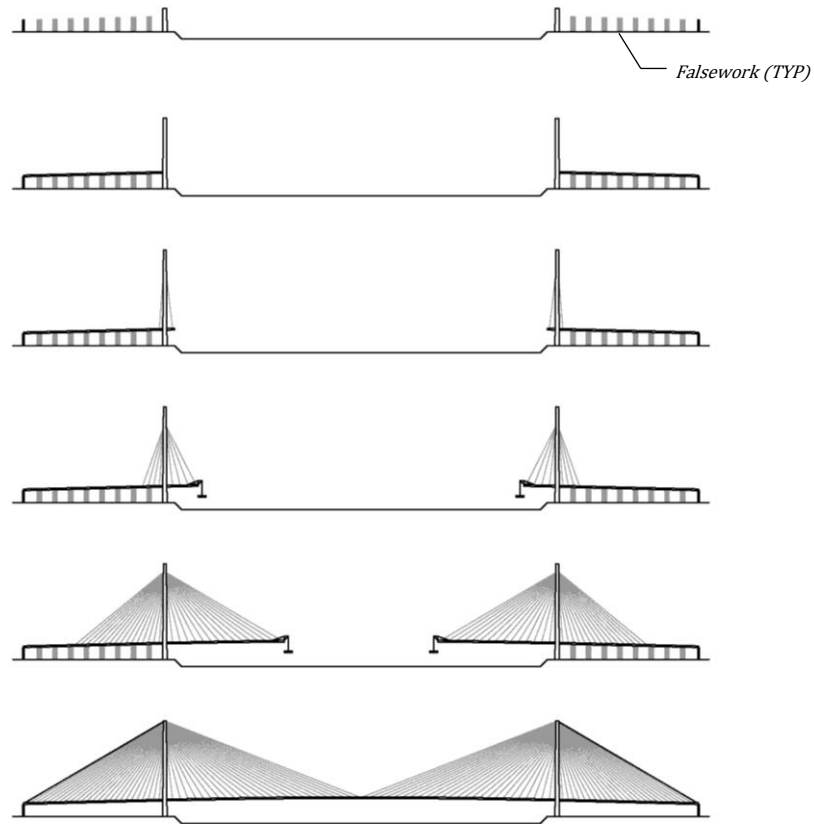
Figure 7.2: The One-Sided Free Cantilever Method of Construction

7.2 Standard Construction Methods for Self-Anchored Suspension Bridges

In self-anchored suspension bridges, because the entire horizontal force from the cable system is transferred to the superstructure at singular locations, there are, in general, only two possible approaches for construction. Either the suspension cables must be temporarily earth-anchored or, alternatively, the entire superstructure must be constructed on falsework. These approaches are illustrated in Figure 7.3 and Figure 7.4, respectively.

When constructing the superstructure on falsework the towers only need to resist the unbalanced force from the self-weight of the suspension cable and hangers; guy lines can be installed to aid if

necessary. However, the cost of constructing the falsework typically renders the approach economically nonviable for long spans, or for spans traversing deep canyons or waterways. On the other hand, the creation of a temporary earth-anchorage for the suspension cables enables long spans of superstructure to be constructed extremely efficiently using the traditional method for earth-anchored suspension bridges. This involves progressively hoisting and installing segments of superstructure using a crane mounted on top of the suspension cables. Still, the temporary earth-anchorage has to be highly robust to resist the dead load cable force from the self-weight of the superstructure and cables. Construction of an extrinsic temporary earth-anchorage therefore requires a substantial monetary investment which would have to be forfeited when construction completes. The construction of the anchorage is likely to also incur additional geotechnical concerns. Consequently, the construction of an extrinsic temporary earth-anchorage negates, to a large extent, the benefits associated with self-anchoring the cable system.
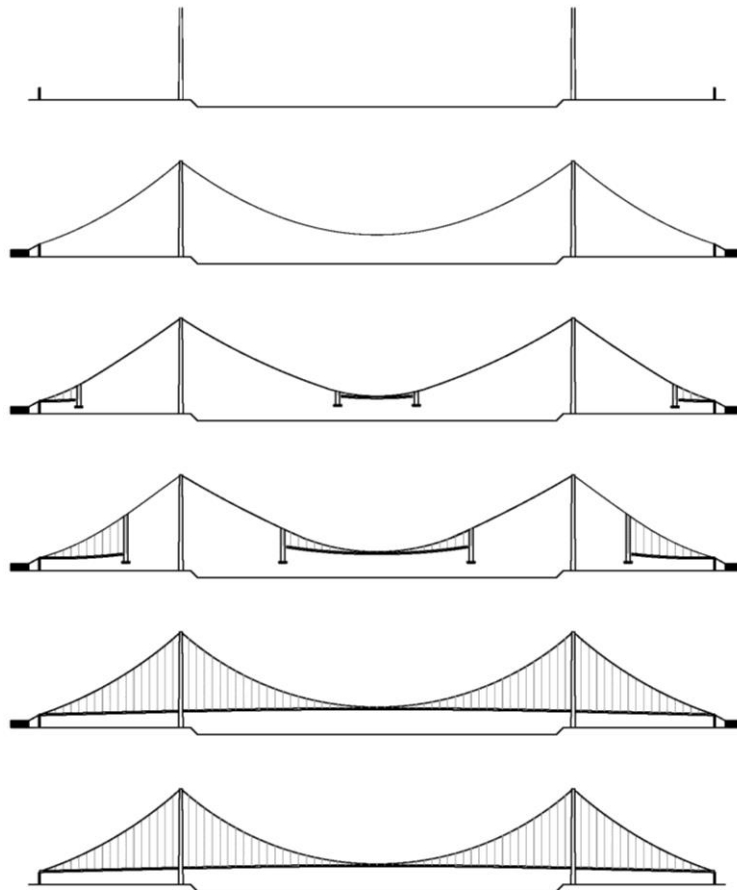
Figure 7.3: Using Extrinsic Earth-Anchorage to Construct Superstructure
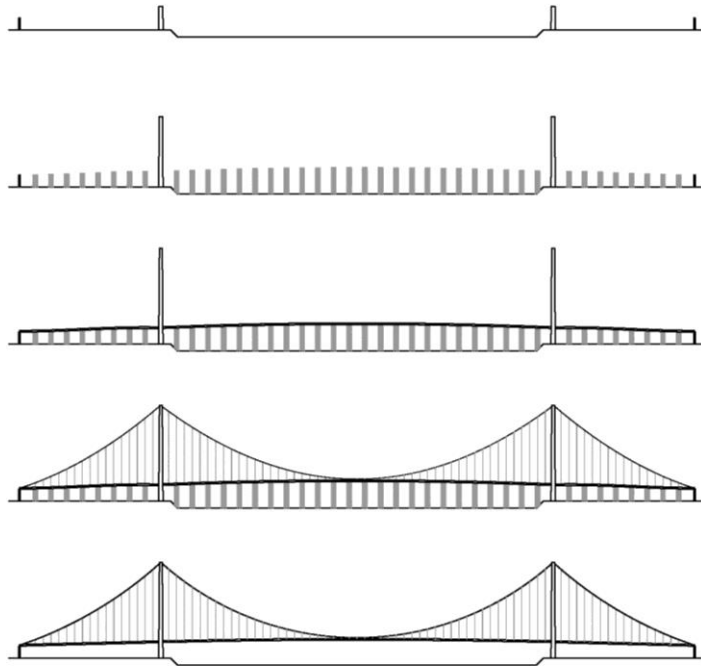
Figure 7.4: Constructing the Superstructure on Falsework

7.3 Proposed Construction Methods for Self-Anchored Discontinuous Hybrid Cable Bridges

Self-anchored discontinuous hybrid cable bridges are restricted to the same two general construction approaches discussed, in Section 7.2, for self-anchored suspension bridges. However, self-anchored discontinuous hybrid cable bridges possess two significant advantages over self-anchored suspension bridges which, when taken together, make their construction much more practical.

1. For a given main span length, the horizontal suspension cable force which must be temporarily earth-anchored during construction is significantly smaller in a discontinuous hybrid cable bridge in comparison to a self-anchored suspension bridge. Naturally, this is because in the former only a portion of the main span length is directly supported by the suspension cable.

2. As a result of the first advantage, it becomes feasible to use an intrinsic anchorage system to

temporarily restrain the suspension cable force during construction. This is further explained below.

Generally, the use of an intrinsic temporary anchorage system will be most convenient when intermediates piers are employed in conjunction with heavy side spans. It was already established in Chapter 6 that intermediate piers offer significant advantages when considering service loading. Similarly, heavy side spans are extremely effective in reducing unfavourable uplift forces from service loads and are a natural accompaniment to intermediate piers which in return provide supplemental support to the side spans. For these reasons, the combined use of intermediate piers with heavy side spans can be easily justified even prior to considering construction demands. Once more, during construction, under deck auxiliary stay cables can be further added to create a temporary earth-anchorage system from mainly permanent bridge components. As a result, the financial and geotechnical hindrances normally associated with the construction of a temporary earth-anchorage are all but removed. An illustration of one possible construction scheme is given in Figure 7.5.

Step 1   Commencement of tower and side span pier erection.
Step 2   Erection of side span falsework followed by erection of side span superstructure.
Step 3   Commencement of one-sided free cantilevering.
Step 4a   Installation and initial tensioning of below deck auxiliary stay cables.
Step 4b   Erection of suspension cable and anchor cables.
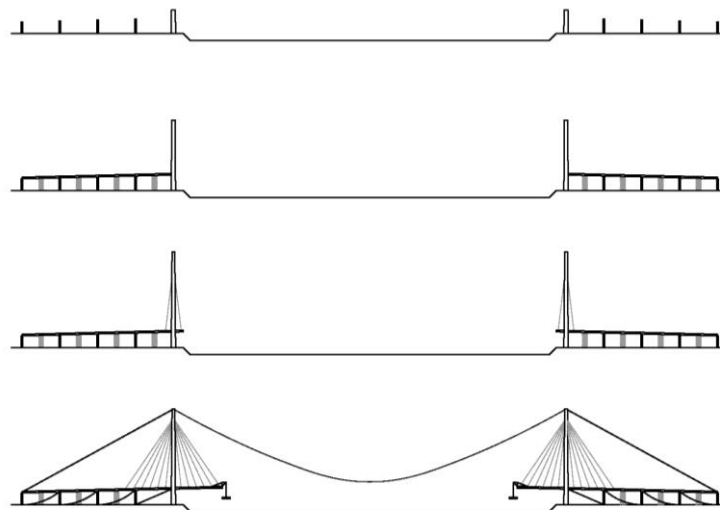
Figure 7.5: Possible Construction Scheme for Self-Anchored Discontinuous Hybrid Cable Bridges
*Continued on next page

Step 5a   Installation of hangers and hanger clamps.
Step 5b   Partial removal of side span falsework
Step 6a   Commencement of superstructure erection in suspended region.
Step 6b   Tension adjustment of below deck auxiliary stay cables as erection progresses.
Step 7a   Removal of side span falsework.
Step 7b   Completion of superstructure erection in suspended region.
Step 8   Installation of superstructure closure segment.
Step 9   Transfer of horizontal cable force via de-tensioning of auxiliary stay cables.
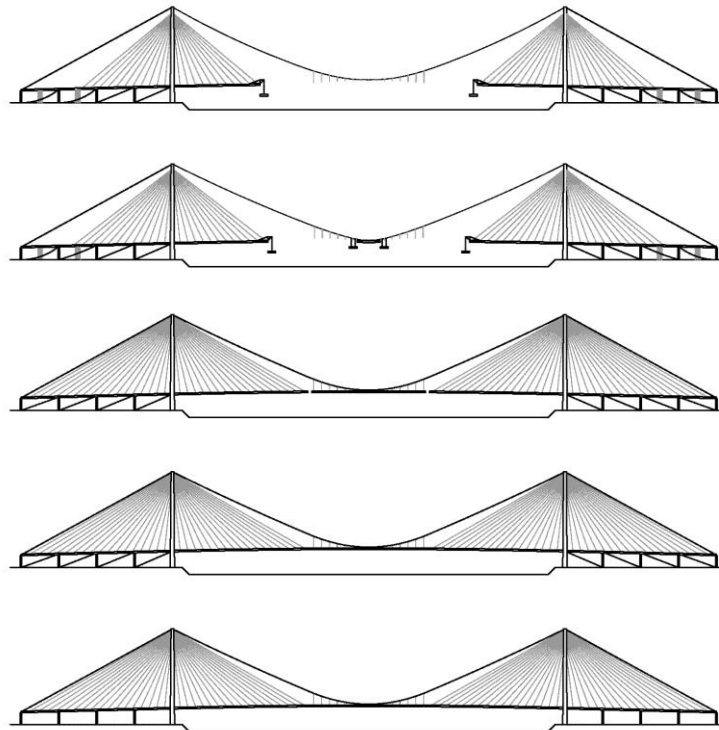
Figure 7.5 Continued

The intrinsic anchorage system clearly relies heavily on the frictional resistance provided between the side span pier foundations and the ground. The practicality of the proposed construction scheme can therefore be verified by comparing the available friction resistance to the horizontal suspension cable force which must be resisted. The latter can be approximated from Equation (5.72), which is repeated below for convenience,

$$(H_{cm})_{DL} \cong \frac{L_m \omega_{sm}}{8 S_R} \left[\frac{\omega_{cm}}{\omega_{sm}} + L_R (2 - L_R) \right] \qquad (7.1)$$

It should be noted that Equation (5.72) is relabel Equation (7.1) for the simple reason that the

variable ω_{sm} is used in Equation (7.1) as opposed to ω_s. This is so that the main span superstructure dead load (ω_{sm}) can be differentiated from the side span superstructure dead load (ω_{ss}). As per convention, L_m is the main span length, S_R is the global sag ratio, L_R is the suspension ratio, and ω_c is the uniformly distributed self-weight of the suspension cable.

During conceptual design it is common to approximate the magnitude of friction forces using the Coulomb model of friction. Accordingly, the frictional resistance provided at the base of the side span piers can be approximated as,

$$H_{SR} \cong \mu V_{pf} \tag{7.2}$$

where μ is the coefficient of static friction between the pier foundations and the ground, and V_{pf} is the total normal force acting on the pier foundations from dead load. V_{pf} is composed mainly of the portion of the side span superstructure dead load which is unbalanced by the main span superstructure dead load. However, the vertical component of the suspension cable force must be subtracted from whatever surplus exists. When it is assumed that the stay cables are symmetrically arranged about the centerline of the towers (i.e. $L_R = 1 - 2L_{SR}$), the following relationship can be easily derived,

$$V_{pf} \cong \underbrace{(\omega_{ss} - \omega_{sm})L_{SR}L_m}_{\substack{\text{Surplus Dead Load from} \\ \text{Side Span Superstructure}}} - \underbrace{(H_{cm})_{DL}\left(\frac{S_R}{L_{SR}}\right)}_{\substack{\text{Vertical Component of} \\ \text{Suspension Cable Force}}} \tag{7.3}$$

where L_{SR} is the side-to-main span length ratio. It is important to note that, for simplicity, Equation (7.3) does not account for the tributary portion of the surplus dead load that gets transferred to the main towers at deck level. However, this is offset by neglecting the weight of the side span piers and pier foundations.

The fraction of the suspension cable force which can be resisted through friction can, therefore, be expressed as,

$$\frac{H_{SR}}{(H_{cm})_{DL}} = \mu \frac{2S_R}{(1 - L_R)}\left[\frac{\frac{\omega_{cm}}{\omega_{sm}} + (1 - L_R)^2\left(1 - 2\frac{\omega_{ss}}{\omega_{sm}}\right) + 1}{\frac{\omega_{cm}}{\omega_{sm}} - (1 - L_R)^2 + 1}\right] \tag{7.4}$$

which can also be regarded as the safety margin against sliding. With the exception of ω_c it can be seen that the expression is independent of the main span length, and of the specific loading values. It is solely dependent on loading and geometric ratios.

Evidently, one of the most influential parameters in Equation (7.4) is the coefficient of static friction. Typical values range from 0.3 to 0.7 depending on the soil properties at the bridge site (Souder, 2015). Assuming a side-to-main span superstructure dead load ratio of 4.0, which is characteristic of concrete side spans used in conjunction with a steel main span, Figure 7.6 plots the safety margin against sliding for several coefficients of static friction. The passive resistance of the soil and the bending resistance of the intermediate piers and towers should both be taken into account when contemplating the calculated safety margins.

In most circumstances, it can be seen from Figure 7.6 that the friction force alone is enough to restrain the suspension cable force during construction. Nevertheless, the side-to-main span superstructure dead load ratio can vary markedly depending on a number of factors such as the width of the deck and the spacing of the stay cables and hangers. Therefore, a more general plot is also included in Figure 7.7 which gives the side-to-main span superstructure dead load ratio required to achieve a safety margin against sliding of 1.0.
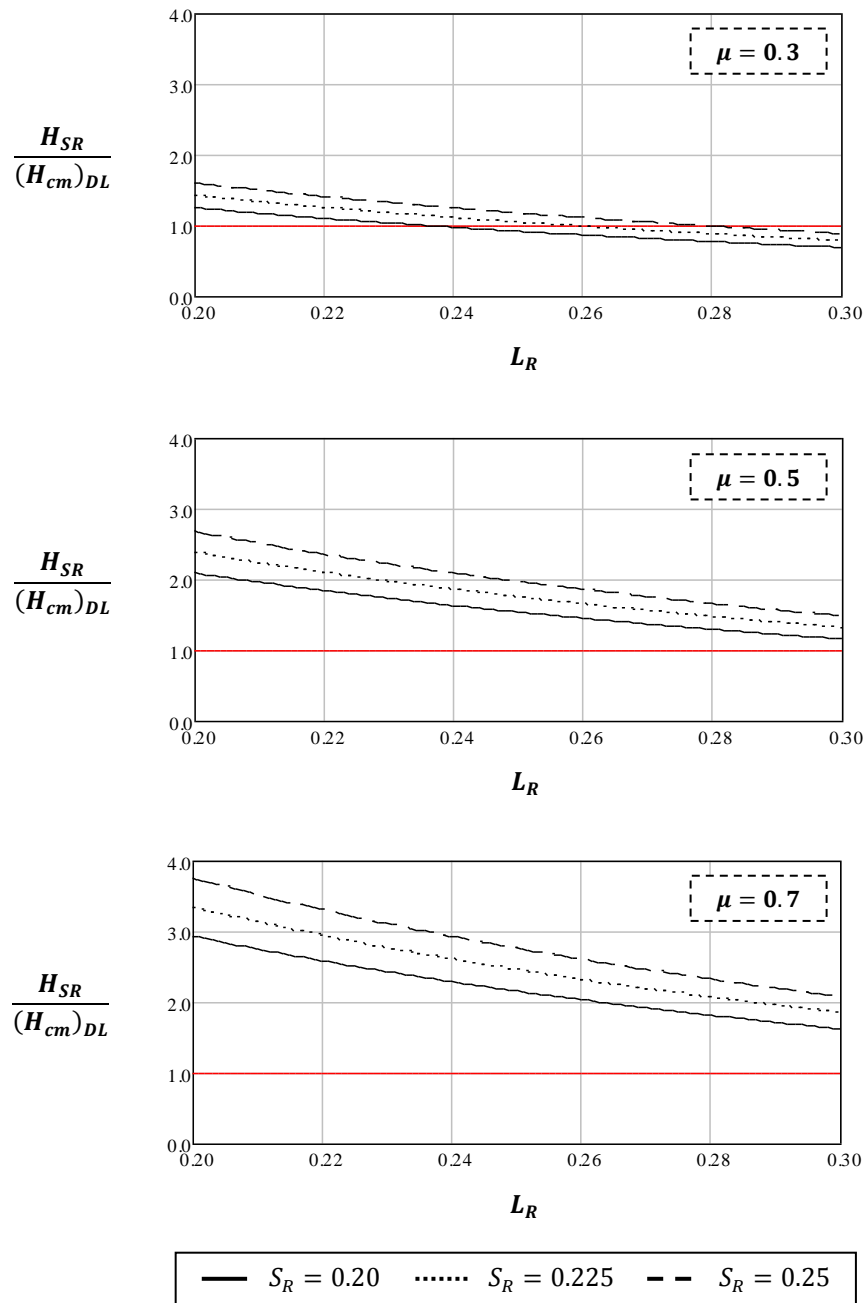
Figure 7.6: Margin of Safety Against Sliding as a Function of the Suspension Ratio
Parameters: L_m = 1000m, L_{SR} = 1 − 2·L_R, ω_R = 0.6, γ_c = 0.09MN/m³, σ_{allow} = 800MPa

Figure 7.7: Side-to-Main Span Superstructure Dead Load Ratio Required to Prevent Sliding
Parameters: $L_m = 1000$m, $L_{SR} = 1 - 2 \cdot L_R$, $\omega_R = 0.6$, $\gamma_c = 0.09$MN/m^3, $\sigma_{allow} = 800$MPa

In circumstances where the friction force cannot by solely relied upon to restrain the suspension cable force, additional ballast can be provided in the side spans so as to temporarily increase the side-to-main span superstructure dead load ratio. This could be readily achieved by ensuring that any permanent acting superimposed dead load is applied to the side spans, prior the main span. Heavy construction vehicles can also be parked in the side spans during critical construction operations.

If, for whatsoever reason, the superstructure must be designed to be homogeneous with a similar weight in the side and main spans, then it may be impractical to apply the amount of additional ballast required. Should this be the case, or should vehicular clearance requirements prohibit the use of auxiliary stay cables in some, or all of, the side span bays, there are a number of other more elaborate recourses available. These include:

- Using under deck auxiliary stay cables in conjunction with the approaches and approach piers to form the temporary intrinsic anchorage system. For bridges spanning major navigational channels, the approach length required to achieve the necessary elevation at mid-span will, in most cases, be much longer than that required for the anchorage system. Notwithstanding, the weight of the abutments can be conveniently exploited when the approach length is relatively small. Still, with any approach anchorage system, the axial continuity of the superstructure must be maintained over the entire length of the anchorage system. Accordingly, this necessitates the installation of temporary links at pertinent expansion joint locations.

- Engaging the intermediate piers and main towers (or alternatively the approach piers) to resist a portion of the horizontal suspension cable force in bending and shear. As the piers and towers normally have to be designed to withstand substantial shear and bending stresses from service temperature loading they will inevitably have an innate capacity to resist such loading without impairment. Moreover, during construction, jacking apart the superstructure prior to the main span closure would alleviate any potential locked-in stresses.

- Employing a combination of temporary intrinsic and extrinsic anchorage systems. With some of the force being taken by the intrinsic anchorage system, the extrinsic anchorage system would be considerably smaller than that which would normally be required for a conventional self-anchored suspension bridge.

It should be mentioned that these recourses also apply to situations where the side span topography inhibits the use of intermediate piers. With the use of any of the aforementioned recourses it also becomes feasible to erect the stayed regions of the bridge using the standard double-sided free cantilever method which would also obviate the need for falsework in the side spans.

Undoubtedly, the costs associated with each of the proposed construction alternatives discussed above may vary considerably depending on the bridge design, the materials chosen for the bridge structure, and the site conditions. However, the same can be said of any construction method. So long as large extrinsic anchorages are avoided, the proposed construction alternatives should not require any extraordinary means beyond those normally expected in the construction of conventional cable-stayed bridges. Therefore, in conjunction with the results from Chapter 5 and with all input parameters being equal, the direct material and labour costs resulting from the construction of a self-anchored discontinuous hybrid cable bridges are likely to be comparative to those which would result from the construction of a conventional cable-stayed bridge. Nevertheless, the former statement excludes the relationship between cost and construction duration.

For suspension ratios within the optimum range specified in Chapter 5 (i.e. $0.2 \leq L_R \leq 0.3$), assuming that the erection of the suspended region of the superstructure can occur concurrent with the erection of the stayed regions as depicted in Figure 7.5, the erection of the suspended region should not fall on the critical construction path. Rather, as in conventional cable-stayed bridges, a considerable portion of the construction timeline will inevitably be governed by the erection of the stayed regions. Since the stayed regions in a discontinuous hybrid cable bridge are much smaller in comparison to a conventional cable-stayed bridge, there is the potential for substantial construction time savings. This is important because construction time saved can translate into considerable economic gains.

In general, when the construction duration of a project is reduced through the creation of multiple work fronts as opposed to through the augmentation of the project's labour force and/or resources, there are savings associated with lower overhead costs. Also, when constructing in heavily congested areas, a shortened project duration can lead to fewer traffic disruptions and delays which has an indirect positive impact on the local economies of communities adjacent to and surrounding the project. A shortened construction period can also reduce service charges on project funding and improve cash flow where tolls are planned to generate income following construction. Such is the case in public private partnerships (PPPs) which are now a popular delivery option for major infrastructure projects.

All of the aforementioned factors have the potential to create an overall economic advantage for self-anchored discontinuous hybrid cable bridges over conventional cable supported bridges. Nevertheless, before self-anchored hybrid cable bridges gain acceptance world-wide, there will inevitably be a the large risk premium associated with their construction. In some cases, the risk premium may be offset by the desire for a unique or signature structure; however, in most cases, it will be vital to maximize the economic incentive in order to make self-anchored discontinuous hybrid cable bridges attractive.

As previously mentioned in Chapter 5, one possible way to maximize the economic incentive is to utilize an optimized superstructure system which exploits the continual compression force in the superstructure generated by the self-anchored hybrid cable system. This could theoretically generate direct savings in fabrication costs, and indirect savings associated with weight reduction. Another solution is to further shorten the critical construction path through a reordering of construction activities. Notwithstanding, this option is much less adaptable as it would be most advantageous when the approach spans can be used for the intrinsic anchorage system. In such cases, time savings may be achieved by erecting the suspension cable immediately following the tower construction and then utilizing the load capacity of the suspension cable to erect both the stayed and suspended regions of the superstructure. The utilization of the suspension cable would permit the simultaneous lifting of multiple superstructure segments and, theoretically, stay cable stressing operations for the lifted segments could be performed in a single stage. As a result, the erection time for the superstructure in the stayed regions would be greatly improved. This would however place the erection of the suspension cable back on the critical construction path and, therefore, in this scenario it would be particularly advantageous to use stay cable technology for the suspension cables in the form of lock-coil strands. The general advantages to using lock-coil strands are discussed in more detail below.

Normally, suspension cables are composed of parallel wires and the cables are assembled on-site using either the aerial spinning (AS) method, or the prefabricated parallel wire strand (PPWS) method. More information on these methods can be found in Gimsing & Georgakis (2012) and Jones & Howells (2008). In contrast, locked-coil strands are factory fabricated. They arrive on-site on reels, assembled in full length, with their sockets already attached. Furthermore, they do not need to be packaged into a single bundle; rather, they can be easily organized into an open rectangular array. Strand sizes up to 140 millimetres in diameter are common and each strand is designed with an outer layer(s) of Z-shaped wires which, when tensioned longitudinally, form a compression ring that inhibits water penetration. When combined with modern wire and surface treatments, no further corrosion protection is required. For these reasons, the erection time of suspension cables composed of lock-coil strands is generally much quicker compared to suspension cables fabricated using the AS or PPWS methods.

It should also be mentioned that locked-coil strand suspension cables have been used on prior occasions in conventional earth-anchored suspension bridges. Therefore, their use should not be associated with a substantial risk premium. In fact, locked-coil strand suspension cables have long been the preferred cable type for suspension bridges in Norway. Over twenty such bridges have been built in Norway with main spans ranging from 225 to 850 metres (Larsen & Valen, 2000). The most prominent is the Askøy Suspension Bridge which opened to traffic in 1992. Moreover, in North America, contractors are usually familiar with either cable-stayed bridge construction or suspension

bridge construction. There are few contractors with experience in both bridge types. Consequently, for hybrid cable bridges, a lock-coil strand suspension cable should offer an advantage since contractors familiar with cable-stayed bridge construction will normally have experience erecting locked-coil strands.

The reasons why locked-coil strand suspension cables have not been more readily employed in North America mainly relate to tradition and practicality. The AS method was first automated and popularized in America in the mid-1800s, by renowned bridge engineer John A. Roebling (Peters, 1987). Although some improvements have been made over the years, the principle and basic method are still largely the same. On that account the AS method is well-established. Still, more critical are the practical aspects associated with using locked-coil strand suspension cables for earth-anchored suspension bridges. Due to the relatively low sag ratio conventionally employed in earth-anchored suspension bridges an exorbitant number of strands are required, and accommodating the strands in any open array becomes impractical. This is not the case for discontinuous hybrid cable bridges. As confirmation, using Equations (3.67) and (4.21), Figure 7.8 compares the cable area required in an earth-anchored suspension bridge to the area required in a discontinuous hybrid cable bridge of equal span. The sag ratio of the earth-anchored suspension bridge is set equal to the conventional value of 0.1, while the global sag ratio of the discontinuous hybrid cable bridge is varied within the optimal interval specified in Chapter 5. Because a relative comparison is made, the relationship plotted is independent of the loading parameters, and is only marginally dependent on the span length.
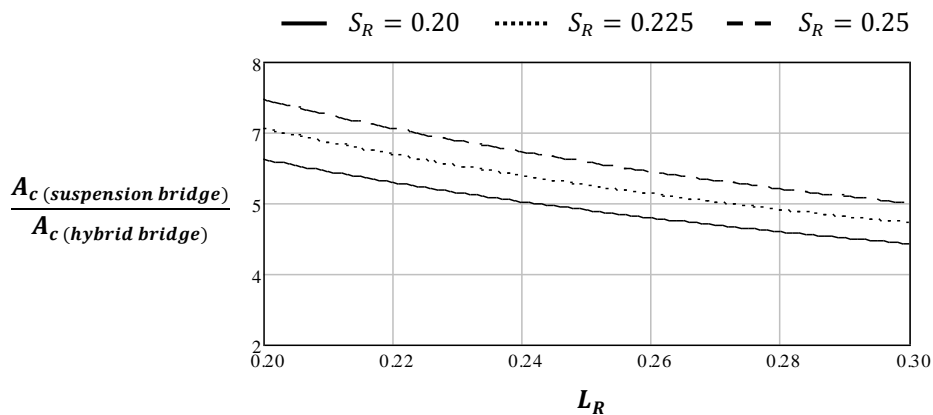
Figure 7.8: Suspension Cable Size Comparison
(Conventional Earth-Anchored Suspension Bridge versus Discontinuous Hybrid Cable Bridge)
Parameters: L_m = 1000m, γ_c = 0.09MN/m^3, σ_{allow} = 800MPa

To demonstrate the difference in the cable sizes required, the Askøy Suspension Bridge, with a main span of 850 metres, approaches the practical limit for the application of locked-coil strand cables in

suspension bridges. Each of its two suspension cables are comprised of 21, 99 millimetre diameter strands, organized in a 7x3 array (Jones & Howells, 2008). From Figure 7.8, a comparable discontinuous hybrid cable bridge with a global sag ratio of 0.2 and a suspension ratio of 0.3 would have only required 5, 99 millimetre strands per cable. The reduced number of strands required in discontinuous hybrid cable bridges produces two significant benefits:

1. It easier to inspect and maintain the cables when there are fewer strands; and

2. It becomes feasible to detail hanger clamps which permit each locked-coil strand to be replaced over the lifetime of the bridge. One possible example is provided in Figure 7.9 for an extreme case involving a 2x6 array of locked-coil strands.

The second benefit is clearly of consequence for improving longevity and reducing lifetime costs of the structure. Traditional parallel wire suspension cables assembled using the AS or PPWS method cannot be economically replaced. Thus, this is one more aspect for decision makers to consider when contemplating the potential advantages associated with constructing a self-anchored discontinuous hybrid cable bridge.
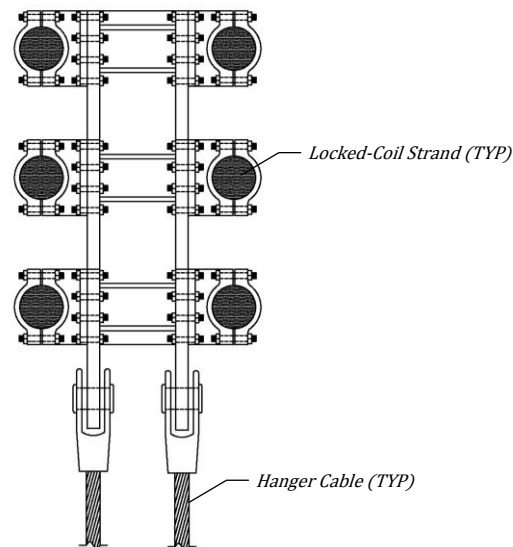
Figure 7.9: Example of Hanger Clamp Detail that Allows for Suspension Cable Replacement

7.4   End of Chapter Summary

Common construction methods for conventional self-anchored cable supported bridges were discussed at the beginning of this chapter. For cable-stayed bridges, the two most common methods of construction are the double and one-sided cantilever techniques. For self-anchored suspension bridges, construction methods are much more limited due to the large temporary works they require. In general, the superstructure of a self-anchored suspension bridge can be erected using a continuous system of temporary falsework or, alternatively, using a crane mounted on the suspension cables. In the latter case, a large extrinsic temporary anchorage system is required to restrain the suspension cables until the erection of the superstructure is complete. Accordingly, the construction of self-anchored suspension bridges is in most cases uneconomical.

Construction of self-anchored discontinuous hybrid cable bridges presents similar obstacles in comparison to self-anchored suspension bridges and has, therefore, thus far been plagued with misconceptions. However, due to the innate features of self-anchored discontinuous hybrid bridges, the obstacles which manifest out of a need for temporary works reduce to mere hurdles. This is mainly because the suspension system in a discontinuous hybrid cable bridge carries only a fraction of the load in comparison to a suspension bridge with equal span. As a result, devising a temporary anchorage system for the suspension cable becomes much more practical. On those grounds, the constructability of self-anchored discontinuous hybrid cable bridges was addressed in this chapter through the proposal of several innovative and economically viable construction schemes. Basic calculations were also included to demonstrate the structural feasibility of the proposed schemes. The primary advantages of the proposed schemes are that they:

1)   Eliminate the need for large temporary works by exploiting the convenience and versatility of permanent bridge components; and

2)   Achieve overall construction time savings through the creation of multiple work fronts.

The latter advantage has the potential to generate substantial economic benefits which have the potential to render self-anchored discontinuous hybrid cable bridges very competitive in comparison to all other conventional cable supported bridges. It was also reported how such benefits can be maximized when clearance requirements mandate lengthy approach structures and when stay cable technology is used in lieu of standard cable technology for the suspension cables. To that end, the general advantages associated with using stay cable technology in the form of lock-coil strands for the suspension cables were discussed in more detail. Generally, in contrast to conventional earth-anchored suspension bridges, lock-coil strand suspension cables can be more readily and rapidly

employed on discontinuous hybrid cable bridges. In addition, through their use, suspension cable replacement becomes practical, thereby improving structural longevity.

Chapter 8

SIGNIFICANCE OF FINDINGS AND

SUGGESTED FUTURE WORK

To gain better insight into the current level of development of the hybrid system, a comprehensive review of the research conducted to date was provided in Chapter 2. Both current designs and past proposals were discussed in detail and all pertinent research was scrutinized. Such a review cannot be found elsewhere, and from the information available, several key areas in need of further study were identified. Specifically, it became evident that there have been no generalized studies on the structural behaviour of self-anchored discontinuous hybrid cable bridges. As a result, there is a large degree of uncertainty as to how the system's behaviour changes when common design parameters are altered. In addition, no study has examined the optimum proportions of the system, and based on the current designs and past proposals, no consensus has thus far been reached. Lastly, no study has attempted to address the constructability of the system which is central in demonstrating its practicality. Accordingly, the research objectives of this thesis were:

1) To evaluate the structural and economic attributes of self-anchored discontinuous hybrid cable bridges;

2) To develop and optimize the general design of self-anchored discontinuous hybrid cable bridges; and

3) To address and resolve the foremost concerns regarding the constructability of self-anchored discontinuous hybrid cable bridges.

To achieve these research objectives a unique, systematic, step-by-step approach was employed. Models were first created to study the isolated behaviour of the basic cable systems which form a self-anchored discontinuous hybrid cable bridge. Then, starting with a bare model of the hybrid system, detail was progressively incorporated into the model while the impact of different design parameters was constantly reassessed. This allowed different behavioural effects and their associated causes to be identified and investigated, permitting a generalized study of the research objectives. Ultimately, the

information contained within this thesis represents an accumulation of analyses undertaken on numerous different structural models. Results for each chapter have been thoroughly summarized in the following sections: 2.4, 3.3, 4.3, 5.5, 6.3, and 7.4. As a result, only a concise report on the significance of the findings is included here. This is followed by some suggestions for future work.

The basic cable systems of a self-anchored discontinuous hybrid cable bridge are comprised of stay cables and suspension cables; however, their behaviour is a specialized topic for which only a limited amount of pertinent information is available. A significant amount of original research was, therefore, conducted and presented in Chapter 3 in order to provide context and to expand on the information currently available. This includes the development of an algorithm that is able to determine the near exact coordinates of a suspension cable lying in any three-dimensional space. Improvements were also made to an existing two-dimensional algorithm in order to simplify the solution process. Using these algorithms, near exact and approximate methods for computing the dead load coordinates of a suspension cable were compared under a wide range of design parameters. To the author's knowledge, such a comparison has never before been made and, from this comparison, designers may quickly evaluate the error associated with using the more traditional, approximate, methods.

A parametric study was also presented in Chapter 3 which examined the deformation characteristics of suspension cables subject to changes in span length, dead and live loading, and cable sag. Thereafter, the study was further expanded to include the effects resulting from self-anchoring the suspension cable and the effects the superstructure's stiffness has on live load demands. Designers will find the data presented useful as a reference during conceptual design. In carrying out the study, a number of insights also emerged. Most notably, the incorporation of a longitudinal superstructure restraint was shown to be highly beneficial in reducing live load demands in both earth and self-anchored suspension bridges. Through its inclusion, strain-free deformations were limited to such a degree that increasing the sag ratio did not greatly impact the level of global stiffness exhibited. As a result, this observation could have implications for the historically established optimum sag ratio of conventional earth-anchored suspension bridges.

Chapter 4 follows much of the same form as Chapter 3, except that the focus is on partially-laden suspension cables and hybrid cable bridges. Firstly, it was demonstrated how the algorithms developed in Chapter 3 could be used to determine the near exact cable coordinates of a partially-laden suspension cable. Formulas which can be more readily employed to determine an approximate set of coordinates were also derived, and their error evaluated. Through the use of the presented graphs and tables, designers may quickly evaluate the most appropriate method to obtain cable coordinates for any specific set of design parameters. A useful non-iterative equation was also developed to approximate the cable area required for a partially-laden suspension cable subject to

general loading and geometric parameters.

Secondly, the deformation characteristics of a single, isolated, partially-laden suspension cable were examined. From the results, it is clear that the addition of stayed regions has a greater amplifying effect on deflections resulting from asymmetrical loading scenarios in comparison to deflections resulting from symmetrical loading scenarios. Nevertheless, it was determined that the deflection of a partially-laden suspension cable is always less than that of a fully-laden suspension cable when the two cables have equal global sag and equal loading conditions.

Lastly, using finite element analysis, a parametric study was performed on a basic model of a self-anchored discontinuous hybrid cable bridge. A wide range of parameters was varied, including the global sag ratio, the suspension ratio, the superstructure flexural stiffness, the span length, and the superstructure dead load. Through these variations, the relationship these parameters have on demand values was ascertained. The error associated with utilizing a second order influence analysis was also studied, in addition to the effect the anchor cable has on the overall bridge behaviour. One key observation was that demand values in self-anchored discontinuous hybrid cable bridges are not greatly dependent on the global sag ratio when its value exceeds 0.2. Similarly, there is only a small variance in demand values when the suspension ratio is kept below a value of 0.4. Notwithstanding, all of the trends that emerged from the parametric study are valuable as they are all without precedent. No other generalized study of this nature appears to have been conducted to date. Moreover, from the results, it is possible to infer what structural behaviour can be expected for any given set of design parameters, and which parameters have the most influence on certain demand values. In essence, a design model has been created that can efficiently evaluate and confirm the structural attributes of any self-anchored discontinuous hybrid cable bridge.

In Chapter 5, the design model was expanded to include economic considerations. Simple analytical expressions were derived to estimate the quantity of material required in the various principal components of a self-anchored discontinuous hybrid cable bridge. The validity of the expressions was verified through a number of analyses and, from the expressions, a cost function was created. The cost function was then examined in conjunction with different aesthetic and structural criterion to arrive at several conclusions regarding the most efficient span proportions for the bridge system. The following ranges were ultimately recommended for design: 0.2 to 0.25 for the global sag ratio, 0.35 to 0.4 for the side-to-main span ratio, and 0.2 to 0.3 for the suspension ratio.

In combination with the results from Chapter 4, a sensitivity analysis confirmed that the recommended span proportions are fairly robust to changes in the material, cost, and loading parameters. As such, it can be concluded that an important optimal design space has been identified

which can be applied universally to any design scenario. This is of great benefit to designers as it allows any design to be rapidly optimized. By providing a constraint window, the recommended design space can also be used to significantly improve the speed with which more rigorous, site specific optimizations studies are performed.

At the end of Chapter 5, the previously defined cost function was further utilized to evaluate the direct costs associated with the construction of self-anchored discontinuous hybrid cable bridges. Within the recommended design space, the direct costs associated with a self-anchored discontinuous hybrid cable bridge were shown to be comparable to a conventional cable-stayed bridge. This is an important step in demonstrating the utility of the system. In addition, from the results, it can be inferred that the economic span range of the system is similar to that historically established for conventional cable-stayed bridges.

In Chapter 6, the results from Chapter 5 were applied to narrow the range of design parameters considered. This enabled a more detailed investigation into how additional structural parameters and design components affect the structural attributes of self-anchored discontinuous hybrid cable bridges. Specifically, different tower-superstructure articulation schemes were investigated to determine their influence on deflection and force demands. Similarly, the stiffnesses of key structural members were varied to ascertain their influence. Nonlinear effects resulting from the application of live load were also re-examined, and by comparing the results from a second order influence analysis with the results from a full nonlinear analysis, important areas of the structure which require a higher order analysis during final design were identified.

The advantages of using specific design components, such as a central suspension cable clamp, cross stays, and intermediate piers were also appraised. Within the recommended design space, the use of a central suspension cable clamp proved ineffective. Cross stays were similarly ineffectual except at the stay cable-hanger junction. In contrast, intermediate piers proved the most advantageous and there was clear rationale for the use of multiple, as opposed to single, intermediate piers.

It was also established in Chapter 6 that, within the recommended design space, cable-stayed bridges and self-anchored discontinuous hybrid cable bridges exhibit very comparable service demands. This outcome once again confirms the utility of the hybrid system. Nonetheless, all of the content provided in Chapter 6 is significant as it serves to further extend and enhance the design model originally developed in Chapter 4.

The constructability of the bridge system was addressed in Chapter 7. Several innovative and economically viable construction approaches were presented which function for a wide range of site

conditions. The structural feasibility of the approaches was verified using simple analytical methods. The primary significance of the approaches is that they overcome the need to construct and de-construct large, and often costly, temporary works. In some instances, overall construction time savings may be achieved through the creation of multiple work fronts. Consequently, the approaches discussed have the potential to create a substantial economic incentive for the construction of self-anchored discontinuous hybrid cable bridges. As an added consideration, it was also demonstrated how longevity could be improved relative to conventional suspension bridges through the global application of stay cable technology.

In summary, this thesis has demonstrated that self-anchored discontinuous hybrid cable bridges have the potential to be highly competitive with standard cable bridges. This information should alleviate many of the present concerns regarding the structural and/or economic feasibility of self-anchored discontinuous hybrid cable bridges. Moreover, should a designer wish to advance a self-anchored discontinuous hybrid cable bridge for a specific application, this thesis provides the tools necessary to achieve both an effective and optimal design.

8.1 Suggested Future Work

The aforementioned contributions represent an important step in the development of self-anchored discontinuous hybrid cable bridges. Nevertheless, there remain additional opportunities to investigate aspects of self-anchored discontinuous hybrid cable bridges not covered in this thesis. Areas of suggested future work lying outside the scope of this thesis are briefly discussed below. It is not expected that any of the results derived therefrom will negate the findings contained within this thesis. Rather, this work is being suggested to augment, support, or complement the information already provided.

First, it would be of value to extend the scope of information in this thesis to include alternate forms of loading such as pedestrian and rail, both of which are subject to different serviceability requirements. Second, much remains to be learned about the dynamic behaviour of self-anchored discontinuous hybrid cable bridges. Although it is not anticipated that significant complications will emerge, such research would reassure designers that the system is adaptable to different seismic and climatic environments. Third, detailed case studies are required to fully assess the circumstances in which self-anchored discontinuous hybrid cable bridges are most cost-effective. These case studies should include a three-dimensional structural assessment along with a full staged analysis of the construction approaches presented in Chapter 7, with an accurate estimate of their expected costs. It is important that the costs take into account lifetime costs and impacts attributable to a shortened

construction schedule – such as cost savings or revenues if bridge tolls are envisaged. Furthermore, it would be beneficial to investigate the extent to which the uniform compression force applied to the superstructure from the suspension cable can be exploited in the superstructure design to reduce overall costs.

REFERENCES

Ammann, O. H., Von Kármán, T. & Woodruff, G. B., 1941. *The Failure of the Tacoma Narrows Bridge: A Report to the Honorable John M. Carmody, Administrator, Federal Works Agency, Washington D.C.,* Pasadena: s.n.

Bradley, E. T., 2010. Crossing the Severn Estuary, UK: Challenges Past and Present. *Proceedings of the Institution of Civil Engineers: Engineering History and Heritage,* November, 163(4), pp. 219-229.

Brown, J. L., 2006. Hybrid Span Combines Suspension, Cable-Stayed Systems. *Civil Engineering (ASCE),* 76(9), pp. 16-17.

Buonopane, S. G. & Billington, D. P., 1993. Theory and History in Suspension Bridge Design from 1823 to 1940. *Journal of Structural Engineering,* 119(3), pp. 954-977.

City of Portland Design Commission, 2009. *Letter to Portland-Milwaukie Light Rail Project Committee.* [Online] Available at: http://rim.metro-region.org [Accessed 9 July 2015].

Colford, B. R. & Clark, C. A., 2010. Forth Road Bridge Main Cables: Replacement/Augmentation Study. *Bridge Engineering,* 163(2), pp. 79-89.

Epperson, J. F., 2013. *An Introduction to Numerical Methods and Analysis.* 2nd ed. Hoboken, New Jersey: John Wiley & Sons.

Ernst, H. -J., 1965. Der E-Modul von Seilen unter Berücksichtigung des Durchhanges. *Bauingenieur,* pp. 52-55.

Farquhar, D. J., 2008. Cable Stayed Bridges. In: G. Parke & N. Hewson, eds. *ICE Manual of Bridge Engineering.* 2nd ed. London: Thomas Telford Ltd.

Feng, G., Liu, R. & Chen, B., 2013. Static Characteristics Analysis of Cable-Stayed Suspension Bridges Using CFRP Cables. *International Journal of Computer Trends and Technology,* 4(4), pp. 861-866.

Flint, A. R. & Smith, B. W., 1992. Strengthening and Refurbishment of Severn Crossing Part 5: Other Background Research and Development. *Proceedings of the Institution of Civil Engineers: Structures and Buildings,* February, 94(1), pp. 51-60.

Ghali, A., Neville, A. M. & Brown, T. G., 2003. *Structural Analysis: A Unified Classical and Matrix Approach.* Fifth ed. Abingdon, Oxon: Spon Press.

Gimsing, N. J., 1996. Cables. In: *Congress Report.* Zurich: s.n.

Gimsing, N. J. & Georgakis, C. T., 2012. *Cable Supported Bridges: Concept and Design.* 3rd ed. Chichester: John Wiley & Sons.

Goodyear, D. W., 1987. Stay Cable Fatigue Design Loading. *PCI Journal,* 32(3).

Goolen, D. v., 2006. *Self-Anchored Suspension Bridges,* Delft, Netherlands: s.n.

Hauge, L. & Petersen, A., 1999. *To Bridge the Scandinavian Way.* Singapore, s.n., pp. 59-70.

Irvine, M. H., 1981. *Cable Structures.* Cambridge, MA: MIT Press.

Janjic, D., 2008. *Experience from the Global Analysis of Stonecutter's Bridge and Sutong Bridge.* Pittsburgh, Pennsylvania, USA, Engineers Society of Western Pennsylvania, pp. 270-277.

Jones, V. & Howells, J., 2008. Suspension Bridges. In: G. Parke & N. Hewson, eds. *ICE Manual of Bridge Engineering.* London: Thomas Telford Ltd, pp. 383-419.

Kawada, T., 2010. *History of the Modern Suspension Bridge: Solving the Dilemma between Economy and Stiffness.* Reston: American Society of Civil Engineers.

LARSA, Inc., 2011. *LARSA 4D Reference Manual.* Melville, NY: LARSA, Inc..

Larsen, J. & Valen, A., 2000. Comparison of Aerial Spinning versus Locked-Coil Cables for Two Suspension Bridges. *Structural Engineering International,* Volume 2, pp. 128-131.

Leet, K. M. & Uang, C.-M., 2005. *Fundamentals of Structural Analysis.* 2nd ed. New York: McGraw-Hill.

Leonhardt, F., 1991. Developing Guidelines for Aesthetic Design. In: *Bridge Aesthetics Around the World.* Washington, D.C.: Transportation Research Board, pp. 32-57.

Leonhardt, F. & Zellner, W., 1980. Cable-Stayed Bridges. *IABSE Surveys S-13/80,* pp. 21-48.

Li, F. & Zhang, Z., 2010. Jianshe Self-Anchored Cable-Stayed-Suspension Bridge, China. *Structural Engineering International,* Issue 3, pp. 317-320.

Machol, R. E., 1965. *System Engineering Handbook.* New York: McGraw Hill.

Miao, F., 2014. Development of Self-Anchored Cable-Stayed Suspension Bridge in China. *Advanced Materials Research,* Volume 898, pp. 387-390.

Miao, F., Shi, L. & Zhang, Z., 2011. Elastic-Plastic Time History Analysis of Self-Anchored Cable-Stayed Suspension Bridge. *Advanced Materials Research,* Volume 163-167, pp. 4295-4300.

Miller, I. R. S., 1971. *Analysis of Cable Structures by Newton's Method,* Vancouver, Canada: s.n.

Ochsendorf, J. A. & Billington, D. P., 1999. Self-Anchored Suspension Bridges. *Journal of Bridge Engineering,* August, 4(3), pp. 161-168.

Parsons, 2008. *Partnership Border Study.* [Online] Available at: http://www.partnershipborderstudy.com/pdf/Engineering-Report-081124/DRIC%20ER%20Volume%205_Main%20Bridge%20Struct%20Study.pdf [Accessed 26 April 2016].

Peters, T. F., 1987. *Transitions in Engineering: Guillaume Henri Dufour and the Early 19th Century Cable Suspension Bridges.* Basel: Birkhauser Verlag.

Podolny, W. & Scalzi, J. B., 1976. *Construction and Design of Cable-Stayed Bridges.* New York: John Wiley & Sons.

Powers, T. et al., 2005. Reconstruction of North Avenue Bridge over the Chicago River, Chicago, Illinois. *Journal of the Transportation Research Board,* pp. 459-464.

Pugsley, S. A., 1957. *The Theory of Suspension Bridges.* London: Edward Arnold Ltd..

Romeijn, A., Sarkhosh, R. & Goolen, D. v., 2008. Parametric Study on Static Behaviour of Self-Anchored Suspension Bridges. *International Journal of Steel Structures,* Issue 8, pp. 91-108.

Ross, C. T. F., 1998. *Advanced Applied Finite Element Methods.* Chichester, West Sussex: Horwood Publishing.

Schüller, M., 1998. *Das Tragverhalten von Seilbrücken unter dem Aspekt der Ermüdung.* Darmstadt: Druck und Verlag.

Smith, A., 2008. North Avenue Bridge Reconstruction - A Modern High Performance Structure. *HPC Bridge Views*, Mar/April, pp. 9-11.

Souder, C., 2015. *Temporary Structure Design.* New Jersey: John Wiley & Sons Inc..

Steinman, D. B., 1911. *Suspension Bridges and Cantilevers, Their Economic Proportions and Limiting Spans.* New York: D. Van Nostrand Company.

Steinman, D. B., 1922. *A Practical Treatise on Suspension Bridges: Their Design, Construction and Erection.* New York: John Wiley & Sons.

Stewart, J., 2012. *Multivariable Calculus.* 7th ed. Belmont(CA): Brooks/Cole Cengage Learning.

Svensson, H., 2012. *Cable-Stayed Bridges: 40 Years of Experience Worldwide.* Berlin: Ernst & Sohn.

TriMet, 2009. *Portland-Milwaukie Light Rail Project - Willamette River Bridge Type Selection Process.* [Online] Available at: http://trimet.org/pm/library/bridge.htm [Accessed 9 July 2015].

Troitsky, M. S., 1988. *Cable-Stayed Bridges.* London: BSP Professional Books.

Virlogeux, M., 1999. Replacement of the Suspension System of the Tancarville Bridge. *Transportation Research Board,* Volume 1654, pp. 113-120.

Wang, H.-L., Ma, X.-L. & Qin, S.-F., 2013b. Study on the Joint Part of Self-Anchored Cable-Stayed Suspension Bridge with Hybrid Girder. *International Journal of Advancements in Computing Technology,* February, 5(4), pp. 158-163.

Wang, H., Qin, S. & Jiang, R., 2011. The Design of the Jianshe Bridge. *Advances in Civil Engineering,* Volume 255-260, pp. 792-796.

Wang, H.-L.et al., 2010. The Basic Differential Equations of Self-Anchored Cable-Stayed Suspension Bridge. *Mathematical Problems in Engineering,* Issue 6, pp. 1-12.

Wang, H.-L., Tan, Y.-B., Qin, S.-F. & Zhang, Z., 2013a. Geometric Nonlinear Analysis of Self-Anchored Cable-Stayed Suspension Bridges. *The Scientific World Journal.*

Wenzel, H., 1991. Cable-Stayed Bridge in a Typhoon Area. *IABSE Reports,* Volume 64, pp. 425-430.

West, H. H. & Robinson, A. R., 1967. *A Re-Examination of the Theory of Suspension Bridges,*

Urbana, Illinois: s.n.

Willamette River Bridge Advisory Committee, 2009. *Portland-Milwaukie Light Rail Project (Presentation)*. [Online] Available at: http://trimet.org/pm/library/bridge.htm [Accessed 9 July 2015].

Yanev, B., 2010. *Suspension Bridge Cables: 200 Years of Empiricism, Analysis and Management*. New Jersey, 6th US - China Bridge Engineering Workshop.

Zhang, X. & Sun, B., 2004. Parametric Study on the Aerodynamic Stability of a Long-Span Suspension Bridge. *Journal of Wind Engineering,* Volume 92, pp. 431-439.

Zhang, Z., Li, F.-R., Kou, C.-H. & Tsai, J.-L., 2010. Static Analysis of a Self-Anchored Cable-Stayed-Suspension Bridge with Optimal Cable Tensions. *Journal of C.C.I.T.,* November, 39(2), pp. 1-9.

Zhang, Z., Teng, Q.-J. & Qiu, W.-L., 2006. Recent Concrete, Self-Anchored Suspension Bridges in China. *Bridge Engineering,* December, Issue BE4, pp. 169-177.

Zhang, Z., Wang, H.-L., Qin, S.-F. & Ge, X., 2009. Limit Span of Self-Anchored Cable-Stayed Suspension Cooperation System Bridge Based on Strength. *Frontiers of Architecture and Civil Engineering in China,* September, 3(3), pp. 286-291.

Appendix A
PROCEDURE TO DETERMINE CABLE
SHAPE IN THREE DIMENSIONS

Figure A1 displays a three dimensional view of a suspension cable whose ends, according to the prescribed global Cartesian coordinate system, are offset in the X (longitudinal), Y (vertical), and Z (transverse) directions by the vectors ΔX_T, ΔY_T, and ΔZ_T respectively. The cable is further represented as a series of cable segments, where each segment is bounded by nodes which have been placed at the ends of the cable and at hanger locations.
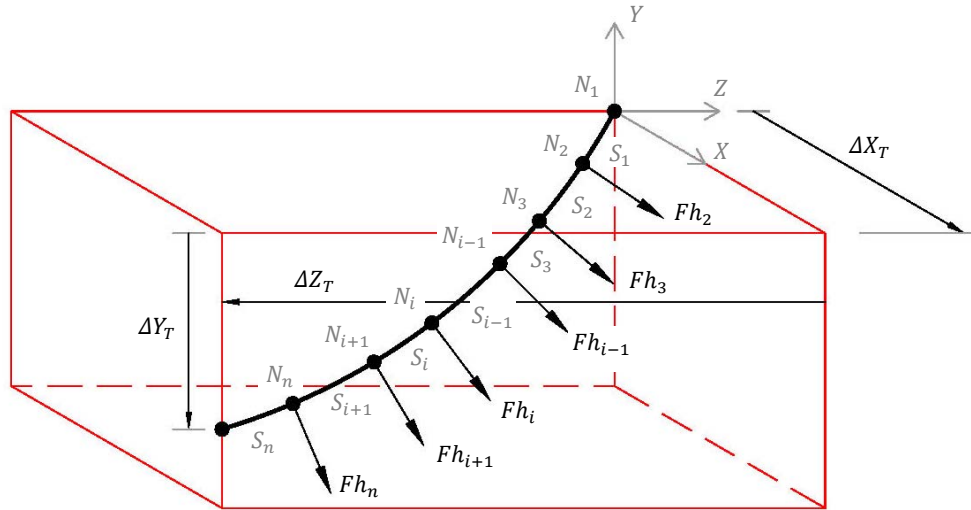
$N_{1...n}$	Nodal Numbering Scheme	ΔX_T	Projected Length of Cable in 'x' Direction
$S_{1...n}$	Segment Numbering Scheme	ΔY_T	Projected Length of Cable in 'y' Direction
ω_c	‡Self-Weight of Suspension Cable	ΔZ_T	Projected Length of Cable in 'z' Direction
Fh_i	Hanger Force Acting at Node i	n	Number of Cable Segments

‡Not Shown for Clarity

Figure A1: 3D View of a Suspension Cable

A free body diagram for a given segment i, is depicted in Figure A2. Assuming that the cable is only subjected to gravity loads, then the only forces acting along the length of each cable segment are those due to the self-weight of the cable (hanger forces are considered to act at nodal locations). Hence, between nodes, the local curve of each cable segment takes the form of a catenary whose local coordinates lie in a two dimensional plane characterized by the x^* and y axes. It should be noted that lowercase letters will be used throughout to represent the local axes of the individual cable segments in order to avoid confusion with the global axes which are denoted by uppercase letters.
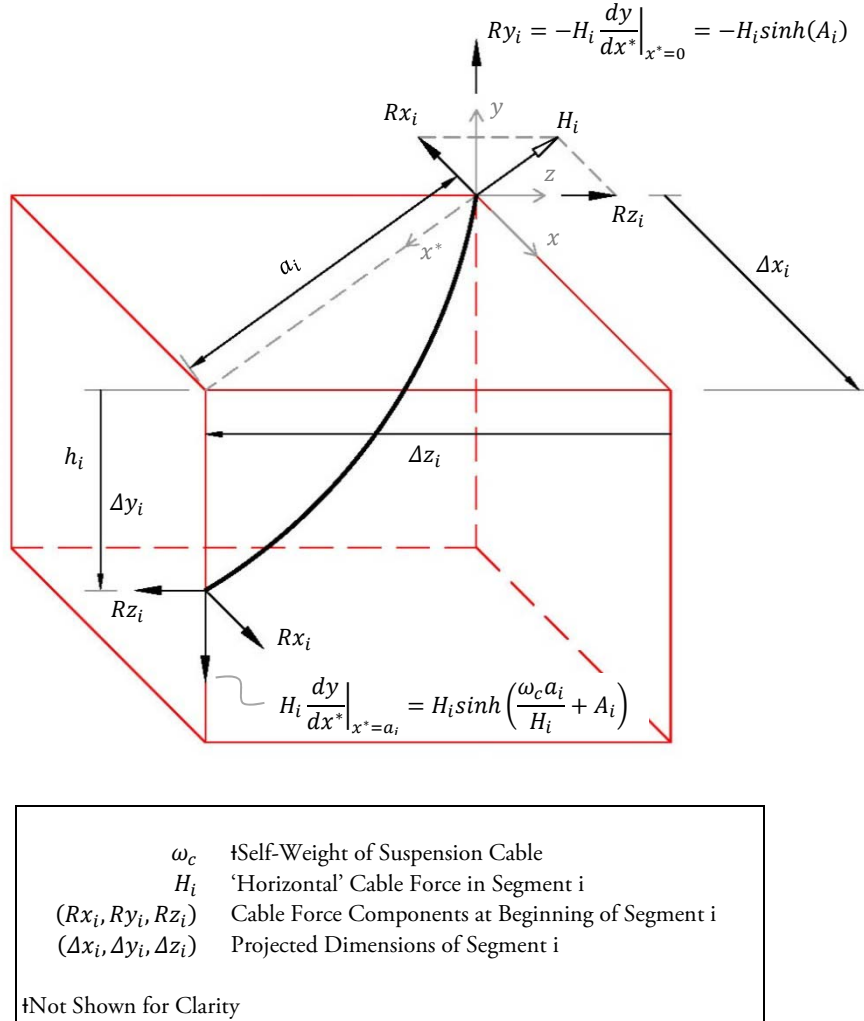
Figure A2: Free Body Diagram of Segment i

Using the Equations already established in Section 3.1.1.1, the local ordinates of a given cable segment i may thereby be expressed as (from Figure 3.1 and Equation 3.3),

$$y_i = \frac{H_i}{\omega_c} cosh \left(\frac{\omega_c x_i^*}{H_i} + A_i \right) + B_i \qquad (A1)$$

where,

$$A_i = asinh \left[\frac{\omega_c h_i}{2 H_i sinh \left(\frac{\omega_c a_i}{2 H_i} \right)} \right] - \frac{\omega_c a_i}{2 H_i} \quad and \quad B_i = -\frac{H_i}{\omega_c} cosh(A_i)$$

The direction of the x^* axis may vary from segment to segment depending upon the line of action of the hanger forces. As such, Equation (A1) needs to be transformed to a consistent local three dimensional coordinate system by making the following substitutions (with reference to Figure A2),

$$H_i = \sqrt{(Rx_i)^2 + (Rz_i)^2} \tag{A2}$$

$$a_i = \sqrt{(\Delta x_i)^2 + (\Delta z_i)^2} \tag{A3}$$

$$h_i = \Delta y_i \tag{A4}$$

$$x_i^* = x_i \sqrt{1 + \left(\frac{\Delta z_i}{\Delta x_i}\right)^2} \tag{A5}$$

3D TRANSFORMATION EQUATIONS

where, the local z and x axes are related through the following relationship,

$$z_i = x_i \left(\frac{\Delta z_i}{\Delta x_i}\right) \tag{A6}$$

Equations (A1)-(A6) describe the three dimensional catenary curve of an individual cable segment with respect to a local Cartesian coordinate system positioned at the beginning of the segment. Considering all cable segments, assuming the self-weight of the suspension cable and the projected length of each cable segment in the x direction are known parameters, there remain $5 \times n$ unknowns in the form of $Rx_{1...n}$, $Ry_{1...n}$, $Rz_{1...n}$, $\Delta y_{1...n}$, and $\Delta z_{1...n}$. However, given the support reactions at Node 1 (Rx_1, Ry_1, Rz_1), the transverse and vertical projected dimensions of Segment 1 can be determined from the geometrical conditions upon which,

$$\Delta z_i = \Delta x_i \left(\frac{Rz_i}{Rx_i}\right) \tag{A7}$$

and

$$Ry_i = -H_i \sinh(A_i) \tag{A8}$$

where, A_i is a function of Δy_i. Thereafter, the parameters of all subsequent cable segments can be derived via the following equilibrium equations,

$$\left.\begin{array}{l} Rx_{i+1} = Rx_i + Fh_{x_{i+1}} \qquad\qquad\qquad (A9) \\[2em] Ry_{i+1} = Fh_{y_{i+1}} - H_i sinh\left(\dfrac{\omega_c a_i}{H_i} + A_i\right) \quad (A10) \\[2em] Rz_{i+1} = Rz_i + Fh_{z_{i+1}} \qquad\qquad\qquad (A11) \end{array}\right\} \begin{array}{c} \text{JOINT} \\ \text{EQUILIBRIUM} \\ \text{EQUATIONS} \end{array}$$

where, Fh_{x_i}, Fh_{y_i}, and Fh_{z_i} denote the respective longitudinal, vertical, and transverse components of the hanger force acting at node i.

The line of action of each hanger force depends upon the shape of the cable. Consequently, the hanger force components cannot be determined independent to the cable coordinates. Nonetheless, using the geometric parameters obtained from Equations (A1)- (A11) and given the magnitude of the tensile force in each hanger $|Fh|$, the hanger force components at a given node i can be computed as (neglecting the sag effect of the hangers),

$$Fh_{x_i} = |Fh_i| \left(\frac{\delta h_x}{\sqrt{\delta h_x{}^2 + \delta h_y{}^2 + \delta h_z{}^2}}\right)_i \qquad (A12)$$

$$Fh_{y_i} = |Fh_i| \left(\frac{\delta h_y}{\sqrt{\delta h_x{}^2 + \delta h_y{}^2 + \delta h_z{}^2}}\right)_i \qquad (A13)$$

$$Fh_{z_i} = |Fh_i| \left(\frac{\delta h_z}{\sqrt{\delta h_x{}^2 + \delta h_y{}^2 + \delta h_z{}^2}}\right)_i \qquad (A14)$$

where,

$$\delta h_{x_i} = h_{x_i} - \sum_{m=1}^{i-1} \Delta x_m$$

$$\delta h_{y_i} = h_{y_i} - \sum_{m=1}^{i-1} \Delta y_m$$

$$\delta h_{z_i} = h_{z_i} - \sum_{m=1}^{i-1} \Delta z_m$$

As shown in Figure A3, δh_x, δh_y, and δh_z represent the projected dimensions of the hanger in the x, y, and z directions, respectively. And, $(h_x, h_y, h_z)_i$ denote a set of specified coordinates for the end node of hanger i, opposite the cable, measured with respect to the global coordinate system assigned in Figure A1.
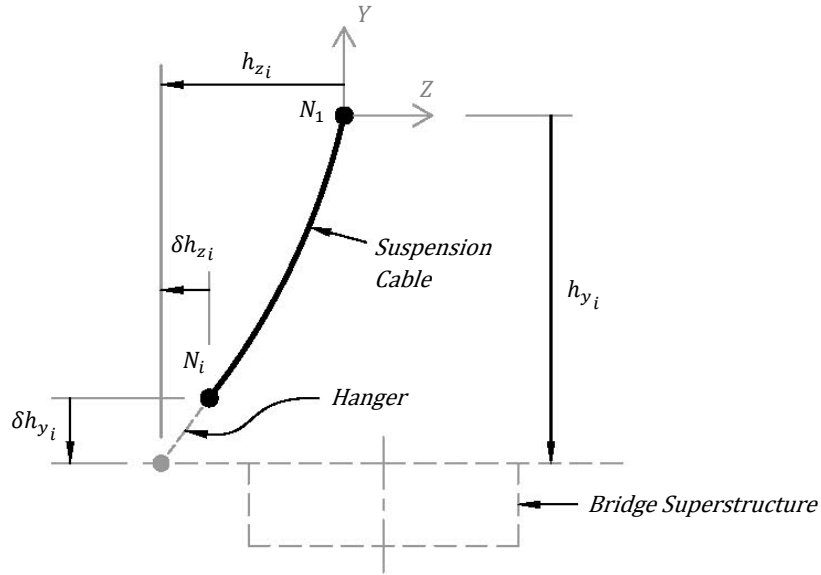
Figure A3: YZ Section at Node i
*Nodes (2… i-1) not shown for clarity

If, on the other hand, the component of the hanger force in the direction of gravity is known, as opposed to the magnitude of the tensile force, then the other components of the force may be alternatively computed as,

$$Fh_{x_i} = Fh_{y_i} \left(\frac{\delta h_x}{\delta h_y} \right)_i \tag{A15}$$

$$Fh_{z_i} = Fh_{y_i} \left(\frac{\delta h_z}{\delta h_y} \right)_i \tag{A16}$$

Equations (A1)-(A16) allow for the determination of the coordinates of a general three dimensional suspension cable with support reactions at one end equal to Rx_1, Ry_1, and Rz_1. However, since these

support reactions are typically unknown, iteration is required in order to obtain the correct values of the support reactions, for a given longitudinal span ΔX_T, which yield the specified end offsets of the cable (see Figure A1).

$$\Delta Y_T = \sum_{i=1}^{n} \Delta y_i = Specified\ Value \tag{A17}$$

$$\Delta Z_T = \sum_{i=1}^{n} \Delta z_i = Specified\ Value \tag{A18}$$

Still, there exist an infinite number of solutions which satisfy the support boundary conditions, and as such, an added parameter must be specified which dictates the sag of the cable curve. For this purpose, with respect to the global coordinate system in Figure A1, the vertical distance (distance in the 'Y' direction) from the origin to the cable at,

$$X = \frac{\Delta X_T}{2}$$

is chosen. This value, referred to hereon as the vertical cable sag, f_y, is computed for given set of support reactions as.

$$f_y = \begin{cases} \sum_{i=1}^{q} \Delta y_i & \text{if there is a hanger at midspan} \\ \\ \sum_{i=1}^{p-1} \Delta y_i + y_p \left(x_p = \frac{\Delta x_p}{2} \right) & \text{if there is no hanger at midspan} \end{cases} \tag{A19}$$

where,

$$q = \frac{n}{2} \qquad \text{and} \qquad p = \frac{n+1}{2}$$

Thus, the correct cable coordinates are obtained only when Equations (A17)-(A19) all converge to their desired target values. The entire iterative process is described in the following algorithm which uses a multi-dimensional form of Newton's Method.

<center>MULTI-DIMENISONAL CABLE SHAPE FINDING ALGORITHM</center>

Assumptions:

1. The cable has negligible bending stiffness.
2. The material of the cable obeys Hooke's Law.
3. Infinitesimal strain theory applies.
4. The sag effect of the hangers is neglected.

Initial Inputs:

1. The self-weight of the suspension cable, $\omega_c = \gamma_c A_c$.
2. An array containing $\Delta x_{1...n}$
3. An array containing $Fh_{1...n}$, or alternatively $Fh_{y_{1...n}}$ $\Big\}$ See Figure A1
4. Target values for f_y, ΔY_T, and ΔZ_T. Also, the tolerance accepted in achieving the target values, denoted as TOL.
5. An initial guess for the support reactions at Node 1, denoted as Rxa_1, Rya_1, and Rza_1.

Steps:

1. Set the support reactions at Node 1 equal to (Rxa_1, Rya_1, Rza_1).
2. Compute Δz_i using Equation (A7).
3. Solve for Δy_i using Equation (A8).
4. Decompose Fh_i using Equations (A12)-(A14).
5. Compute Rx_{i+1}, Ry_{i+1}, and Rz_{i+1} using the joint equilibrium equations, (A9)-(A11).
6. Repeat Steps 2 through 5 for $i = 1 ... n$.
7. Compute the vertical cable end offset (denoted as ΔY_{Ta}), the transverse cable end offset (denoted as ΔZ_{Ta}), and the vertical cable sag (denoted as f_{ya}) corresponding to (Rxa_1, Rya_1, Rza_1) using Equations (A17)-(A19) combined with the geometric parameters obtained in Steps 2 through 6.
8. Determine the error in the target parameters,
   $\Delta Y_{T\,Error} = \Delta Y_T - \Delta Y_{Ta}$, $\Delta Z_{T\,Error} = \Delta Z_T - \Delta Z_{Ta}$, and $f_{y\,Error} = f_y - f_{ya}$
9. Check convergence
   a. If $\left(\left| \Delta Y_{T\,Error} \right| \wedge \left| \Delta Z_{T\,Error} \right| \wedge \left| f_{y\,Error} \right| \right) > TOL$ advance to Step 10.
   b. If $\left(\left| \Delta Y_{T\,Error} \right| \wedge \left| \Delta Z_{T\,Error} \right| \wedge \left| f_{y\,Error} \right| \right) \le TOL$ advance to Step 13.

10. Numerically compute the Jacobian Matrix, $[J] = \begin{bmatrix} \dfrac{df_{yab}}{dRx_{ab}} & \dfrac{df_{yac}}{dRy_{ac}} & \dfrac{df_{yad}}{dRz_{ad}} \\[2mm] \dfrac{d\Delta Y_{Tab}}{dRx_{ab}} & \dfrac{d\Delta Y_{Tac}}{dRy_{ac}} & \dfrac{d\Delta Y_{Tad}}{dRz_{ad}} \\[2mm] \dfrac{d\Delta Z_{Tab}}{dRx_{ab}} & \dfrac{d\Delta Z_{Tac}}{dRy_{ac}} & \dfrac{d\Delta Z_{Tad}}{dRz_{ad}} \end{bmatrix}$

   a. Set, $Rxb_1 = (1 - TOL)Rxa_1$, $Ryc_1 = (1 - TOL)Rya_1$, and $Rzd_1 = (1 - TOL)Rza_1$.

   b. Repeat Steps 2 through 6 except with the support reactions at Node 1 equal to (Rxb_1, Rya_1, Rza_1) and label the cable parameters in Step 7 $(\Delta Y_{Tb}, \Delta Z_{Tb}, f_{yb})$.

   c. Compute first column of the Jacobian Matrix,

$$\frac{df_{yab}}{dRx_{ab}} = \frac{f_{ya} - f_{yb}}{Rxa_1 - Rxb_1} \; ; \; \frac{d\Delta Y_{Tab}}{dRx_{ab}} = \frac{\Delta Y_{Ta} - \Delta Y_{Tb}}{Rxa_1 - Rxb_1} \; ; \; \frac{d\Delta Z_{Tab}}{dRx_{ab}} = \frac{\Delta Z_{Ta} - \Delta Z_{Tb}}{Rxa_1 - Rxb_1}$$

   d. Repeat Steps 2 through 6 except with the support reactions at Node 1 equal to (Rxa_1, Ryc_1, Rza_1) and label the cable parameters in Step 7 $(\Delta Y_{Tc}, \Delta Z_{Tc}, f_{yc})$.

   e. Compute second column of the Jacobian Matrix,

$$\frac{df_{yac}}{dRy_{ac}} = \frac{f_{ya} - f_{yc}}{Rya_1 - Ryc_1} \; ; \; \frac{d\Delta Y_{Tac}}{dRy_{ac}} = \frac{\Delta Y_{Ta} - \Delta Y_{Tc}}{Rya_1 - Ryc_1} \; ; \; \frac{d\Delta Z_{Tac}}{dRy_{ac}} = \frac{\Delta Z_{Ta} - \Delta Z_{Tc}}{Rya_1 - Ryc_1}$$

   f. Repeat Steps 2 through 6 except with the support reactions at Node 1 equal to (Rxa_1, Rya_1, Rzd_1) and label the cable parameters in Step 7 $(\Delta Y_{Td}, \Delta Z_{Td}, f_{yd})$.

   g. Compute third column of Jacobian Matrix,

$$\frac{df_{yad}}{dRz_{ad}} = \frac{f_{ya} - f_{yd}}{Rza_1 - Rzd_1} \; ; \; \frac{d\Delta Y_{Tad}}{dRz_{ad}} = \frac{\Delta Y_{Ta} - \Delta Y_{Td}}{Rza_1 - Rzd_1} \; ; \; \frac{d\Delta Z_{Tad}}{dRz_{ad}} = \frac{\Delta Z_{Ta} - \Delta Z_{Td}}{Rza_1 - Rzd_1}$$

11. Update the initial guess values for the support reactions at Node 1, $[Ra]_{NEW} = [Ra] + [\Delta Ra]$

   a. Set, $[Ra] = \begin{bmatrix} Rxa_1 \\ Rya_1 \\ Rza_1 \end{bmatrix}$

   b. Compute the requisite change in the support reactions,

$$[\Delta Ra] = [J]^{-1} \begin{bmatrix} f_{y_{Error}} \\ \Delta Y_{T_{Error}} \\ \Delta Z_{T_{Error}} \end{bmatrix}$$

12. Repeat Steps 1 through 11 until the convergence criterion in Step 9b is met.

13. With (Rxa_1, Rya_1, Rza_1) set as the end support reactions at Node 1, compute the local cable coordinates for each cable segment using Equations (A1)-(A16) combined with the geometric parameters obtained in Steps 2 through 6.

14. Convert the local coordinates of each cable segment to the global coordinate system shown in Figure A1.

ADDITIONAL NOTES

- All initial inputs should be entered as positive or negative values according to the coordinate systems specified in Figure A1 and Figure A2.

- As Fh_1 acts at a support node, its value should be set equal to zero.

- The convergence of Newton's Method is sensitive to the initial guess values provided. For general bridge engineering applications, it is recommended that the parabolic approximation be used as a basis when determining the starting values for Rxa_1, Rya_1, and Rza_1.

- If the transverse force component of all hangers is zero $\left(Fh_{z1...n} = 0\right)$, then the third row and third column of the Jacobian Matrix must be omitted to prevent the matrix from becoming singular.

- To avoid possible convergence problems, the updated guess values for the support reactions at Node 1 should be prevented from changing signs. As such, it is recommended that the following limit, $\left|[\Delta Ra]_j\right| \leq 0.5\left|[Ra]_j\right|$ be placed on Step 11 for $j = 1 \dots rows([\Delta Ra])$.

GENERAL COMMENTS

- Once the correct cable shape has been established using the algorithm presented, other geometric and force parameters can be determined. The magnitude of the tensile force at each end of the cable can be found using Equations (A20) & (A21).

$$T_1 = \sqrt{Rx_1{}^2 + Ry_1{}^2 + Ry_1{}^2} \tag{A20}$$

$$T_{n+1} = \sqrt{Rx_{n+1}{}^2 + Ry_{n+1}{}^2 + Ry_{n+1}{}^2} \tag{A21}$$

Also, the angles formed between the ends of the cable and the x, y, and z axes are given by,

$$\theta_{x_1} = acos\left(\frac{|Rx_1|}{T_1}\right) \quad \text{and} \quad \theta_{x_{n+1}} = acos\left(\frac{|Rx_{n+1}|}{T_{n+1}}\right) \tag{A22}$$

$$\theta_{y_1} = acos\left(\frac{|Rx_1|}{T_1}\right) \quad \text{and} \quad \theta_{y_{n+1}} = acos\left(\frac{|Ry_{n+1}|}{T_{n+1}}\right) \tag{A23}$$

$$\theta_{z_1} = acos\left(\frac{|Rz_1|}{T_1}\right) \quad \text{and} \quad \theta_{z_{n+1}} = acos\left(\frac{|Rz_{n+1}|}{T_{n+1}}\right) \tag{A24}$$

And, the unstressed length of the cable may be computed as (refer to Equations (3.10), (3.12) and (3.13)),

$$USL = \left[\sum_{i=1}^{n} C_i - \Delta_i \right] \tag{A25}$$

where,

$$C_i = \frac{H_i}{\omega_c} \left[sinh \left(\frac{\omega_c a_i}{H_i} + A_i \right) - sinh(A_i) \right] \tag{A26}$$

and,

$$\Delta_i = \frac{H_i a_i}{E_c A_c} \left[\frac{\omega_c \Delta y_i^2}{2 H_i a_i} coth \left(\frac{\omega_c a_i}{2 H_i} \right) + \frac{1}{2} + \frac{H_i}{2 \omega_c a_i} sinh \left(\frac{\omega_c a_i}{H_i} \right) \right] \tag{A27}$$

- In some cases, prior to computing the cable shape, it may be desirable to use the unstressed length of the cable as a target parameter rather than the vertical sag in the cable. In those scenarios, the algorithm presented may be easily modified using Equations (A25) to (A27).

- If desired, the sag effect of the hangers may be factored into Equations (A12) to (A16) by utilizing the equations given in Section 3.1.1.

- In terms of calculating updated guess values for the support reactions, other multi-dimensional numerical techniques exist which may offer improved convergence and/or computational efficiency. Notwithstanding, for most practical cases, the aforementioned method was found to converge, within a tolerance of 1×10^{-10}, in less than ten iterations.